Modeling and Control of the Falling Film Evaporator Process

Zur Erlangung des akademischen Grades eines

Doktors der Ingenieurwissenschaften (Dr.-Ing.)

von der KIT-Fakultät für Maschinenbau des
Karlsruher Instituts für Technologie (KIT)

angenommene

DISSERTATION

von

M. Sc. Julian Hofmann

Acknowledgment

The present thesis is a child of my work at the Institute for Automation and Applied Informatics (IAI), Karlsruhe Institute of Technology.

Other people from IAI whom I would like to thank are (alphabetical order): Moritz Böhland, Jürgen Engelmann, Claudia Greceanu, Andreas Hofmann, Prof. Jörg Matthes, Prof. Markus Reischl, and Dr. Markus Vogelbacher. Additionally, I want to express my gratitude to all the students I supervised during the last years. In particular, the contributions of Stephanie Gießler and Jan Schaßberger are to be emphasized.

Finally, I would like to point out that the last four years were an emotional roller-coaster ride. Especially, at the bottom of each valley I felt what it means to have a family – thank you Mama, Papa, Oma, and Kilian for all your love and support. However, there is one person who has been spending every day at my side for almost 10 years now: Sina, I can always rely on you and words cannot express how thankful I am to have you as my girlfriend. I hope that the house we have just bought is only a single highlight in our common future and that many more will follow.

May 2021   Julian Hofmann

Abstract

Due to their energy efficient operation and flexible designs, falling film evaporators (FFEs) have a wide field of application in the industry. Besides questions about construction, dominant time delays pose a large challenge to modeling and control of this process. Especially, the automation of production system requires digital twins, i.e., plant models to teach operators or to accelerate the design process.

The heart of an FFE consists in tubes, where a partially evaporating liquid film flows down on their insides. Hence, the tubes represent the main source of delays being primarily related to the transport of important process factors, such as the liquid's concentration and mass flow. Nevertheless, modeling of the corresponding dynamic behavior is challenging. From the control perspective, time delays cause oscillations of the output concentration – in particular, during ramp-up processes. Additionally, strong couplings between output mass flow and concentration further complicate multivariable control which, however, is required by modern production systems.

The present thesis presents solutions to all aforementioned challenges. By dividing the FFE process into subsystems, different designs can be simulated in a simple manner. In this context, a certain plant model is validated based on real-world data leading to a digital twin. To develop new transport models of evaporating liquid film, fundamental balance equations are evaluated, which yields systems of hyperbolic partial differential equations. Via the method of characteristics, a transformation into time-delay equations succeeds; the latter are advantageous regarding simulation and controller design. Pilot plant experiments to identify and validate a chosen model underline the ability of our approach to map the measured input-output behavior. To answer control-related questions, a simplified process model is developed, the loop pairing problem is solved, and a multivariable control concept is designed.

Deutsche Kurzfassung

Wegen ihres energieeffizienten Betriebs und flexiblen Designs haben Fallfilmverdampfer (FFV) eine breite Anwendung in der Industrie. Neben Fragen zur Konstruktion sind dominante Totzeiten herausfordernd bzgl. Prozessmodellierung und -regelung. Insbesondere erfordert die Automatisierung von Produktionssystemen digitale Zwillinge, d.h. Anlagenmodelle, um Betreiber zu schulen oder den Designprozess zu beschleunigen.

Das Herz eines FFV besteht aus Rohren, an deren Innenseiten verdampfender Flüssigkeitsfilm hinabläuft. Daher sind die Rohre primäre Quelle für Totzeiten, welche sich vornehmlich auf den Transport wichtiger Prozessgrößen wie Liquidkonzentration und Massenstrom beziehen. Allerdings ist die Modellierung des entsprechenden dynamischen Verhaltens schwierig. Aus Sicht der Regelung erzeugen Totzeiten Schwingungen der Ausgangskonzentration – im Speziellen während der Anfahrprozesse. Zusätzlich verkomplizieren starke Kopplungen zwischen Ausgangsmassenstrom und -konzentration die in modernen Produktionen erforderliche Mehrgrößenregelung.

Die vorliegende Arbeit präsentiert Lösungen für alle genannten Herausforderungen. Durch Gliederung des FFV-Prozesses in Teilsysteme sind verschiedene Designs in einfacher Weise simulierbar. In diesem Kontext erfolgt die Validierung eines bestimmtes Anlagenmodell auf Basis von Realdaten, was zum digitalen Zwilling führt. Zur Entwicklung neuer Transportmodelle verdampfender Flüssigkeitsfilme werden Bilanzgleichungen ausgewertet, sodass Systeme hyperbolischer partieller Differentialgleichungen entstehen. Mittels des Charakteristikenverfahrens gelingt eine Transformation in Totzeitgleichungen; letztere sind für Simulation und Reglerentwurf vorteilhaft. Pilotanlagenexperimente zur Identifikation und Validierung eines ausgewählten Modells unterstreichen die Eignung des Ansatzes, das gemessene Ein-/Ausgangsverhalten abzubilden. Zur Beantwortung regelungstechnischer Fragen wird ein einfaches Prozessmodell entwickelt, das Zuordnungsproblem gelöst und ein Mehrgrößenregelungskonzept entworfen.

Content

List of Figures

List of Tables

Notation

Abbreviations

BC	boundary condition
DIC	decentralized integral controllability
DPF	dynamic plug flow
DRGA	dynamic relative gain array
FFE	falling film evaporator
FIFO	first-in-first-out
HIIA	Hankel interaction index array
i/o	input-output
IAI	Institute for Automation and Applied Informatics
IC	initial condition
IMC	internal model controller
KIT	Karlsruhe Institute of Technology
MIMO	multiple-inputs-multiple-outputs
MPC	model predictive controller
MVR	mechanical vapor recompression
NI	Niederlinski index
NSE	Navier-Stokes equation
ODE	ordinary differential equation
OP	operation point
OPF	overtaking particle flow

PDE	partial differential equation
PM	participation matrix
RGA	relative gain array
RHP	right half-plane
SISO	single-input-single-output
TITO	two-inputs-two-outputs

Constants

π	circle constant: $3.14159\ldots$
$\bar{R}$	universal gas constant: $8.3144598\ldots \mathrm{J\,mol^{-1}\,K^{-1}}$

Latin Symbols and Variables

Lowercase Letters

c	velocity
c_p	specific heat capacity
d	diameter
g	gravity acceleration
h	filling level
Δh_v	enthalpy of evaporation
k	heat transfer coefficient
ℓ	length
m	mass
$\dot{m}$	mass flow rate
n	number

p	pressure
$\dot{q}$	heat flow rate
s	film thickness
t	time
v	specific volume
w	dry matter content

Uppercase Letters

A	area
C_p	heat capacity
D_f	diffusion coefficient
K_v	valve flow factor
$K_{v,s}$	open valve flow factor
M	molar mass
N	rotational speed
P	power
Re	Reynolds number
T	time constant
V	volume
$\dot{V}$	volumetric flow rate

Greek Symbols and Variables

$\Delta\vartheta$	boiling point elevation
η	dynamic viscosity
ϑ	temperature

κ	discharge coefficient
ν	kinematic viscosity
ϱ	volumetric mass density
τ	time delay
φ	valve position

Operators and Mathematical Symbols

e	Euler's number
i	imaginary unit
max	maximum operator
min	minimum operator
mod	modulo operator
round	round operator
sat	saturation operator

Subscripts

A	Ambience
C	Compressor
con	control
crit	critical
d	desired
d	dry matter
E	Effect
f	filter
ff	feedforward

fsh	flash
h	homogeneous
H	Heat Chamber
i	input
init	initial
lin	linear
liq	liquid
max	maximum
met	metal
min	minimum
NS	Navier-Stokes
o	output
o	orifices
p	particular
P	Plate
R	Reservoir
red	reduced
surf	surface
T	Tubes
v	vapor
V	Valve
w	water

1 Introduction

All models are wrong, but some are useful.

(George Box, British statistician)

The present thesis deals with modeling and control of falling film evaporators (FFEs). Since the underlying process is built of many Pipes and Tubes[1], where some liquid[2] is concentrated, large transport delays occur. The latter are challenging to both, modeling and control of the process. To solve the most important modeling challenges, this thesis presents new models for evaporating liquid films in the Tubes; the latter may be interpreted as the "heart" of an FFE. Regarding major control challenges, strong couplings of the controlled variables require a multivariable controller, which is developed in this thesis. In general, all related works are based on a cooperation between the IAI as part of KIT and GEA Wiegand GmbH[3].

1.1 Falling Film Evaporators

Falling film evaporators are industrial heat exchangers to concentrate temperature-sensitive solutions of liquids, where Fig. 1.1 shows a real-world example. Thus, FFEs are widely used in the food, chemical, or pharmaceutical industries, where flow capacities up to 150 tons per hour are possible [134].

Parts of this chapter are reproduced from [161, 155, 160, 157].

[1] For the sake of consistency, subsystems of an FFE, such as Pipes, Tubes, etc., begin with a capital letter.

[2] The terms "liquid" and "product" are used synonymously.

[3] Postal address: GEA Wiegand GmbH, Am Hardtwald 1, 76275 Ettlingen, Germany

Figure 1.1: One-Effect FFE with MVR to concentrate wheat starch effluent

More precisely, the main purpose of FFEs is to thermally separate the volatile liquid – usually water – from the desired liquid, e.g., concentrated milk, drugs, or bioethanol [155, 160]. Due to a large product diversity and other technical requirements, a variety of different FFE designs and operational modes exists. To this end, let us mention two examples: Firstly, the number of product passes can vary, which is detailed in Sec. 1.1.2. Secondly, there are different possibilities w.r.t. the heating source providing the energy to initiate evaporation. In this context, mechanical vapor recompression (MVR), cf. [142, 1] and Sec. 1.1.2, is a commonly used method. Other heating options are direct live steam induction, cf. [72, 74] and Sec. 4.2, or thermal vapor recompression [102, 50]. Finally, let us summarize some special features of the FFE process [134]:

– *Good product quality* is ensured via evaporation at low temperatures due to partial vacuum in the plant.

– *High energy efficiency* is achieved by multiple product passes and mechanical vapor recompression enabling small temperature differences between the Compressor's suction and pressure side.

– *Flexible mode of operation* is possible since different liquids can be concentrated by the same FFE. Additionally, switching between cleaning and standard operation is simple.

1.1.1 Role in the Food Industry

Especially in the food industry, the concentrate is often further processed in a spray dryer to produce, e.g., milk powder [41]. The application of a downstream spray dryer is necessary since FFEs are not able to remove the whole water content from the product to avoid, e.g., sedimentation [81, 74] which requires cleaning. Therefore, the last stage in powder production systems is always a drying process. However, the energy consumption of a spray dryer is 10-20 times higher per kg of removed water compared to an FFE [108]. Thus, due to the high energy efficiency of the FFE process, it is desired to pre-concentrate the liquid as much as possible in FFEs while hygienic and safety constraints or fouling [12, 35, 103] should be taken into account. As pre-stage of the drying process, FFEs can have different purposes, such as pre-concentration of raw product, high-concentration of pre-concentrated product, or even serial connections of FFEs are possible.

1.1.2 Process Description

In the present thesis, FFEs with one Effect, multiple passes and MVR are basically considered.[4] To keep the process description as simple as possible, the flow diagram of a one-Effect FFE with two passes and MVR is discussed and shown in Fig. 1.2. Before this process is detailed, let us make some basic remarks on Fig. 1.2:

- While the first pass is visualized in detail, the second one is only sketched roughly.

- Bold lines are attributed to the suction side (Effect) of the Compressor.

- Thin lines are attributed to the pressure side (Heat Chamber) of the Compressor.

In general, a pass of an FFE consists of a Plate and Tubes, and a Reservoir. At first, input liquid with mass flow $\dot{m}_i$ and dry matter content[5] w_i is pumped

---

[4] The pilot plant from Ch. 4 represents an exception since it has only one Tube, where live steam acts as heating source.

[5] The terms "dry matter content" and "concentration" are used synonymously.
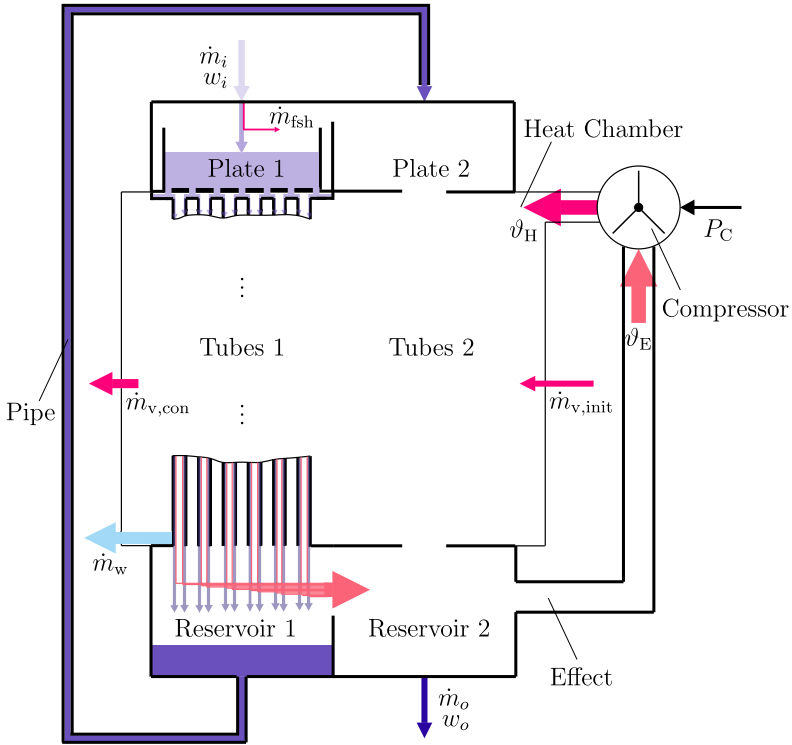
Figure 1.2: Flow diagram of a one-Effect FFE with two passes

onto the Plate 1 which distributes the liquid over the Tubes 1. Additionally, a small mass flow $\dot{m}_{\text{fsh}}$ evaporates from the entering liquid due to the partial vacuum conditions inside the FFE (so called "flash evaporation"), cf. [102] and Sec. 2.2.1. From there, the liquid falls down the narrow vertical Tubes 1, uniformly covering their inner walls as a thin falling film. The Tubes of both passes are heated from outside by the vapor in the Heat Chamber which causes some water content to evaporate from the liquid film inside the Tubes. This vapor is sucked by the Compressor, which increases the vapor's energy level from the temperature ϑ_{E} to the higher temperature ϑ_{H} due to the additional electrical power P_{C} supplied to the Compressor. Meanwhile, the product coming out of the Tubes 1 drops into the Reservoir 1, which collects

the intermediate product. Downstream to the Reservoir 1, a pump conveys the intermediate product via a Pipe onto the Plate 2. From there, the product undergoes a similar process as in the first pass such that the output of the second pass represents the final concentrated product with mass flow $\dot{m}_o$ and dry matter content w_o. Hence, in each pass, the concentration increases while being limited by viscosity constraints. If viscosity becomes too high, deposits on the inner walls of the Tubes cause undesired sedimentation and fouling, cf. [81, 74, 35, 12, 103]. The Compressor's action makes the FFE a particularly exquisite process. To understand its role, let us adopt the energetic point of view. The electrical power P_C supplied to the system via the Compressor forms vapor with higher temperature ϑ_H outside the Tubes compared to the inside. It causes partial condensation of the vapor outside the Tubes, thus releasing its enthalpy of condensation. Therefore, the mass flow of condensated water $\dot{m}_w$ is released from the Heat Chamber. To keep the temperature ϑ_E at a desired equilibrium, the excess vapor flow $\dot{m}_{v,con}$ is released from the Heat Chamber, which compensates the energy excess due to P_C. The process is ramped up by the live steam mass flow $\dot{m}_{v,init}$, which additionally helps to keep the energy in Effect and Heat Chamber balanced, see Ch. 2 for further details.

1.1.3 Challenges

Due to the described complexity of the FFE process, many challenges arise, which, in the following, are attributed to the relevant domains, namely, economy, process engineering, and control engineering.

From the economic perspective, process shut-downs, cleanings, and ramp-ups should occur as rare as possible. Nevertheless, if such actions are necessary, they should be finished as fast as possible. The background is that production breakdowns should be avoided. Therefore, a practitioner might conclude that the FFE should be cleaned less often. However, such argumentation is dangerous since less cleaning would increase the risk for fouling of the Tubes and Pipes. At the same time, the product quality would decrease since fouling and sedimentation decreases the heat transfer through the Tubes and, in the worst case, leads to undesired film break-up [103].
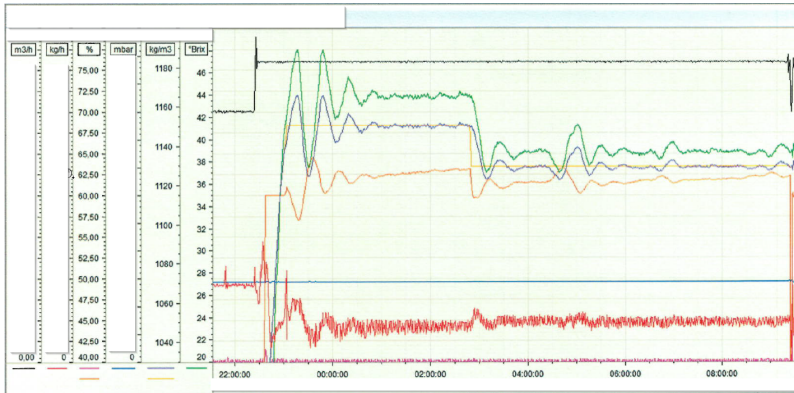
Figure 1.3: Ramp-up of an FFE to concentrate coffee with "aggressive" PI controller observed via oscillations of the output °Brix (green curve)

While the economist mitigates the aforementioned conflict by optimizing the planning of process breakdowns, the process engineer develops practical countermeasures. For example, to avoid sedimentation of the liquid on the inner walls of the Tubes, the falling film's turbulence and thickness should be sufficiently high [12]. Higher film turbulence and thickness is achieved by increasing the Re number, see (2.16), which itself is achieved by increasing the liquid's mass flow $\dot{m}$ and/or decreasing its dynamic viscosity η. However, both of these measures yield the same problem, namely, less evaporation and thus less concentration of the liquid, which thwarts the original purpose of an FFE. Hence, the process engineer should, e.g., have this conflict in mind when designing FFEs.

Since the control engineer is asked by the economist to accelerate process ramp-ups and shut-downs, the next area of conflict arises. As discussed in Sec. 1.2.2, PI control is still standard in the industry. Hence, the control engineer tends to too aggressive tuning of controllers – the result is shown in Fig. 1.3. Since there exists a linear relation [102] between the output °Brix, see green curve in Fig. 1.3, and output dry matter content w_o, which is the primary controlled variable, it is obvious that too aggressive tuning of the corresponding PI controller leads to large oscillations of w_o. The culprit is the dominant transport delay w.r.t. dry matter content w which cannot be satisfactorily handled by a single PI controller, see also Sec. 1.2.2. Thus, the

control engineer optimizes the PI controller's parameters to handle the balance between the duration of ramp-ups and amount of waste product caused by long-lasting oscillations. However, better control can already be achieved by applying additional structural features to "support" the PI controller.

The present thesis is basically dedicated to the challenges of the control engineer, where the general solution strategy consists in advanced modeling. The reasons are ass follows: Firstly, models form the basis to design the aforementioned structural control features, such as feedforward or decoupling compensators. Secondly, the process understanding is enhanced via models and digital twins of plants can be readily developed for, e.g., operator teaching. Nevertheless, the process engineer can also profit from the conducted results, especially from the experiments in Ch. 4.

1.2   Stage of Development

Since the present thesis aims at *modeling* and *control* of the FFE process, the literature review is split accordingly.

1.2.1 Modeling

Broadly speaking, models of FFEs[6] are developed to get a deeper understanding of the process. In this context, costs and process breakdowns can be efficiently reduced as operators are educated by controlling a digital twin instead of the real plant. Moreover, new developments concerning control concepts or system designs can be easily tested since there is less need for extensive and expensive experiments.

In the 1960's, first empirically-motivated [68] and ordinary differential equation (ODE) based [5] simulation approaches were started. While other early computer programs to simulate FFEs were considered unsuitable and gathered only few attention [67], first simple physically-motivated FFE models were implemented on digital computers [65, 22]. In this context, the nonlin-

---

[6] In many publications referenced in this subsection, the term "multiple effect evaporator" is used which may be regarded as synonym for "falling film evaporator".

ear and linear simulation models of Newell and Fisher [95] could be experimentally validated. Another famous work in this early period was published by Andre and Ritter [6] who developed a dynamic model of a two-Effect FFE based on material and energy balances. However, most of these early works only consider strongly simplified behavior since fast dynamics or time delays are neglected. Additionally, the obtained equations were linearized about a specific operation point (OP), cf. [95], and could therefore only describe small deviations from the OP.

In 1990, Tonelli et al. [132] presented a computer package, where constant time delays in and between the effects could be included into the simulation model. Further recent studies on dynamic FFE simulation focus on detailed subsystem modeling [141, 102], usage of dynamic models for control design [142, 13, 129] or distributed-parameter effect models [128, 21]. In all of these plant simulation models, constant transport velocities and thus constant transport delays are assumed.

Regarding FFEs, two types of transport delays are crucial: the flow of liquid through the completely filled Pipes and the flow of partially evaporating liquid film down the Tubes [102, 141]. The flow through the Pipes is the easier case since the density, concentration, or temperature transport can be well described by classical transport models with time-varying velocities [23, 37, 112, 146]. As for the transport of evaporating falling films, it is often modeled by assuming that *velocity is constant* and *evaporation is uniformly distributed* along the Tubes [21, 102, 107, 127, 142]. In reality, though, the velocity of liquid films depends on time-varying quantities, such as mass flow or viscosity [33], which causes *time-varying* transport delays of the liquid elements in the Tubes. Moreover, there are wave phenomena affecting the dynamics of the liquid film and thus lead to accumulations of liquid elements at different points in the Tubes [4, 14, 116]. Therefore, the aforementioned transport models with constant velocities are only rough approximations of the real behavior. To model more realistic scenarios, there exist computational fluid dynamics simulations which are based on coupled Navier-Stokes equations for the liquid and vapor phase [38, 77]. However, such detailed models, see also [4, 14, 116], are too complex for control design and hard to embed in a digital twin of a plant.

In general, to describe transport mathematically, there are two options: partial differential equations (PDEs) and time-delay equations. The PDE-based

approach commonly uses fundamental balance equations of mass, momentum, and energy, which form the basis for various kinds of transport [52, 135, 148, 150]. Time-delay equations, on the other hand, are often phenomenologically motivated [27] and are based on the continuity equation of, e.g., liquid elements, such as plugs [78, 97, 146]. The relation between certain PDE and time-delay models was investigated by Karafyllis et al. [69, 70]. While the focus of [69, 70] is on system-theoretic aspects of the two kinds of models, the author's research is motivated by the control-oriented advantages of the *time-delay* representations: They enjoy a wider range of common analysis techniques and control algorithms, including adaptive ones [44, 152], and are easier to implement in simulation environments, such as Simulink, where time-delay blocks are standard.

Besides dynamic models, there are numerous publications concerning evaporators with different focuses, e.g., an estimation of the overall heat transfer coefficient [7], computational aspects [145, 79], multiple stream concepts [140, 76], usage of commercial software [94, 149], energy saving mechanisms in counterflow FFEs [113], FFEs in the sugar industry [126], fouling [35, 12, 103], pressure drop along the Tubes and interactions between vapor and liquid phase [50], energy reduction schemes [75], or turbulence in evaporating falling films [77].

Apart from physical modeling, pure empirically motivated FFE models can be obtained by applying neural networks [115, 31] or identification-based black box approaches [107]. New experimental insights are given in [51].

1.2.2 Control

PI controllers are still standard in the industry [98]. However, it is commonly known that a PI controller is unable to adequately cope with dominant time delays since it typically leads to large-amplitude, long-lasting oscillations of the output dry matter content w_o, see Sec. 1.1.3. In particular, Winchester et al. [142] conclude that pure single-loop PI control is insufficient to reject disturbances due to the input dry matter content w_i.

Therefore, in the last decades, more advanced methods have been proposed and applied to enhance the w_o-loop. In [102, 13], a cascade controller based on a transfer function model is designed, where w_o is controlled via steam

pressure. A similar approach based on a nonlinear process model is studied in [72] and an advanced triple loop cascade controller is developed in [45]. Moreover, Haasbroek et al. [57] design an LQR controller with Kalman state estimator and thereby evaluate the performance of different kinds of models. Since measurements of the liquid's density, which essentially determines the dry matter content, and mass flow are usually available only at the FFE's input and output, there exist further Kalman-based approaches to estimate states between the FFE passes. In this line, Karimi et al. [73] use a linear Kalman filter to estimate the dry matter content inside the FFE (between two passes) and thus are able to design an inferential cascade controller for w_o. Another observer-based approach is treated in [139], where the observer estimates nonmeasurable disturbances, while the Effect temperature ϑ_E and output dry matter content w_o are controlled by a model predictive controller (MPC). Similarly, Stefanov et al. [129] present an MPC strategy and compare it to PI control via a partial differential equation based process model, whereas Russel [114] applies MPC to control the input mass flow $\dot{m}_i$ and Effect temperature ϑ_E. A different approach is considered by Lahtinen [84], who develops a fuzzy controller. In [56], existing techniques, namely, PI, fuzzy, cascade, and LQR control are compared w.r.t. disturbance rejection of w_i-steps, where the cascade controller revealed the best performance. Recently, Meng et al. [91] proposed auto-tuning PID controllers to control the output dry matter content of each pass. Such an approach requires additional measurements, which are, however, rarely available in most FFE plants due to cost restrictions [13].

Although modern predictor-based control techniques for uncertain time-delay systems [17, 24, 86] or systems with distributed delay [18, 106] have been developed, these methods are not suitable for the considered application. The reasons are of practical nature. Firstly, implementation of such advanced techniques in digital control systems may be hard to do correctly, reliably, and cost-effectively on the industrial level. Secondly, it is debatable if those solutions acquire acceptance among the operators. Recalling rather classical approaches such as the Smith predictor [124] and its modifications, e.g. [90, 88], these approaches often lack robustness against structural model uncertainties or large variations of time delays [53, 92].

1.3 Open Problems and Objectives

As already done in Sec. 1.2, the open problems and objectives are divided into a subsection on *modeling* and another one on *control* of the FFE process.

1.3.1 Modeling

Based on the corresponding literature review, it is required to develop enhanced dynamic models of FFE subsystems to simulate scenarios beyond static operating points and to consider time-varying delays. Additionally, these subsystem models should have a user-friendly implementation so that large FFE plants with multiple passes can be easily built up by connecting blocks of subsystems. The latter should have a user interface which enables the setting block-specific parameters in a simple manner. To this end, application of *Simulink's block masks*[7] is a promising option. Practical relevance of the implementation is to be shown by comparing modeled and measured outputs of a real-world FFE design such that a digital twin of a plant is obtained.

As detailed in Sec. 1.2.1, there are two approaches in the literature to model the behavior of evaporating liquid film in the Tubes: Firstly, there is the "plant model community" [21, 102, 107, 127, 142] working with strong simplifications of the real behavior. Secondly, there is the "computational fluid dynamics community" [4, 14, 38, 77, 116] who develops detailed models based on multiphase Navier-Stokes equations. However, the control engineer is mainly interested in models with a good mapping of the observed input-output behavior. Moreover, the models should be part of a system class where well-developed control algorithms exist, such as time-delay systems [110, 44, 152].

Finally, practical relevance of the models for evaporating liquid film should be shown by designing suitable pilot plant experiments for the purpose of identification and experimental proof. In this context, the identification of systems with distributed delay is of special interest. As corresponding algo-

---

[7] https://de.mathworks.com/help/simulink/block-masks.html, retrieved May 13, 2021, 16:21.

rithms are only tested via academic examples [40], a practical way to identify the distributed delay behavior is desired.

1.3.2 Control

Abstractly speaking, the FFE process is a multiple-inputs-multiple-outputs (MIMO) process. Thus, before designing a control concept, there are preliminary questions to be answered, such as:

– Which disturbances exist and which process quantities are measured?

– Which quantities should be controlled and which ones can be manipulated?

– How to solve the pairing problem of manipulated and controlled variables?

– May a multivariable controller be better than a multiloop single-input-single-output (SISO) controller?

By reviewing and applying suitable methods to a control-oriented process model, these questions can be answered.

As discussed in Sec. 1.2.2, all of the studies on FFE control consider either single-loop control of the output dry matter content w_o or multiloop control of w_o and Effect temperature ϑ_{E}. Nevertheless, besides w_o and ϑ_{E}, modern FFE plants should additionally enable the control of the output mass flow $\dot{m}_o$. Based on the results in [142], this task is challenging since w_o and $\dot{m}_o$ are strongly coupled, which requires multivariable control design. To the best of the author's knowledge, the only paper addressing this problem is [136], where an internal model controller (IMC) is proposed based on the models in [107]. However, the design of this IMC is not explicitly discussed therein. Furthermore, the challenge of decoupling w_o and $\dot{m}_o$ is only solved implicitly by configuring the controller in such a way that the corresponding loops have different response speeds. Therefore, based on the answers to the aforementioned questions, a new multivariable control concept should be designed, implemented, and tested. In particular, the problems originating

from dominant transport delays, see Sec. 1.1.3, should be solved so that a novel ramp-up strategy can be readily developed.

1.4 Outline

An overview of the present thesis' structure is shown in Fig. 1.4, which visualizes the relations between all chapters. Their contents[8] are summarized in the following.

Chapter 2
A Digital Twin for a Falling Film Evaporator

– Models of FFE subsystems
– Validation via plant data
⇒ Digital twin

Modeling

Control

Chapter 3
New Models for Evaporating Liquid Films

– PDE-based flow models
– Evaporaration via sink term
⇒ Time-delay models

Chapter 5
A New Multivariable Conrol Concept for Falling Film Evaporators

– Control-oriented plant model
– Pairing and interaction analyses
⇒ Multivariable control concept

Chapter 4
Identification of Distributed Delays and Experimental Proof of a New Model

– Choice of a model
– Pilot plant experiments
⇒ Identification and exp. proof

Figure 1.4: Structure of the present thesis

---

[8] If there are contents, that can be skipped by a familiar reader, corresponding advice is given at the beginning of each chapter.

In **Chapter 2**, a certain FFE plant is modeled and validated which generates a digital twin. To this end, the FFE process is divided into subsystems and corresponding dynamic models are presented. In this context, modeling the time-varying delay behavior in the Tubes and Pipes is particularly focused. Subsequently, the subsystem models are implemented under Simulink masks as user interfaces. By combining the subsystems models, a plant model of the considered FFE design is obtained. For the purpose of validation, the plant model is fed by measured inputs so that its outputs can be compared to the measured ones, which leads to a digital twin of the plant.

The results of Ch. 2 motivate further research on modeling the transport of evaporating liquid films in the FFE's Tubes. Therefore, in **Chapter 3**, new flow and evaporation models are derived such that first-order quasilinear partial differential equations (PDEs) are obtained, where evaporation is included as sink term. Technically meaningful combinations of flow and evaporation models are then transformed into time-delay equations via the method of characteristics. By considering simulations, the general behavior of these time-delay models is studied.

One of these models is then chosen for the detailed investigations in **Chapter 4**. Based on pilot plant experiments, the distributed delay behavior of this model is identified. Subsequently, the identified model is experimentally proven, i.e., the measured and simulated outputs are compared under realistic FFE conditions. Hence, Ch. 4 concludes the *modeling* part of the present thesis.

The *control* part is treated in **Chapter 5** and is basically motivated by the lack of multivariable control and problems with the ramp-up process, see Sec. 1.1.3. For this purpose, control-oriented plant models based on simplifications of the digital twin from Ch. 2 are derived. To sum up, the aim of Ch. 5 is twofold: Firstly, the loop pairing problem is solved and plant interactions are analyzed. Secondly, a new multivariable concept is developed, which enables control of the output concentration *and* output mass flow. The concept is validated by connecting it to the digital twin of the plant.

2 A Digital Twin of a Falling Film Evaporator

In this chapter, an FFE being part of a milk powder production system is modeled and validated. Nevertheless, let us emphasize that the subsystem models presented in this chapter can also be used to simulate other FFE designs. Compared to the literature, see Sec. 1.2.1, where mostly process models with constant delays are presented, the main challenge is mapping of *time-varying* delay behavior. The latter is basically affected by the product transport in the Tubes and Pipes of an FFE.

The plan of this chapter is as follows. In Sec. 2.1, the considered plant is introduced, where readers being unfamiliar with the FFE process are recommended to recall Sec. 1.1.2. Subsequently, Sec. 2.2 presents models of subsystems which typically appear in FFE plants. These models are either borrowed from the literature and suitably modified or they are deduced from scratch. In Sec. 2.3, a plant model of the FFE introduced in Sec. 2.1 is implemented in Simulink and, in Sec. 2.4, this model is validated based on measurement data so that a digital twin of the plant is obtained.

Readers being familiar with dynamic modeling of FFEs may skip most of the parts of Sec. 2.2. Nevertheless, the author recommends to take a closer look at Sec. 2.2.2, where a first approach to model the time-varying delay behavior in the Tubes is presented.

Parts of this chapter are reproduced from [161].

2.1 Preliminaries

The FFE considered in this chapter is sketched in Fig. 2.1, where mass flow measurements are indicated by FI, density by DI, temperature by TI, and pressure by PI. The Compressor's variable frequency drive (VFD) enables measurements of the desired electrical power $P_{C,d}$ and desired rotational speed $N_{C,d}$, which is generated by some controller, see Sec. 2.2.7.

In general, this FFE is built of one Effect with four passes each consisting of a Plate, Tubes, and a Reservoir. These four passes are connected by three Pipes. The purpose of this FFE is to increase the dry matter content of pre-concentrated milk with approximately $0.35\,\text{kg kg}^{-1}$. More precisely, the aim of this process is to produce highly concentrated liquid milk, whereas a down-stream spray dryer completely dries the FFE's output product.

The properties (density ϱ, enthalpy of evaporation Δh_v, specific heat capacity c_p, dynamic viscosity η, and boiling point elevation $\Delta\vartheta$) of a product depend on the product's temperature ϑ and dry matter content w so that the following quantity equations[1] hold:

$$\varrho(\vartheta, w) = \underbrace{\left(A_{\varrho,\text{w}} + B_{\varrho,\text{w}}\vartheta + C_{\varrho,\text{w}}\vartheta^2\right) \tfrac{\text{kg}}{\text{m}^3}}_{=\varrho_\text{w}(\vartheta)} \left(1 + A_\varrho w^{B_\varrho}\right), \qquad (2.1a)$$

$$\Delta h_v(\vartheta) = B_h \left(\frac{1 - \frac{\vartheta}{C_h}}{1 - \frac{A_h}{C_h}}\right)^{0.38} \frac{\text{kJ}}{\text{kg}}, \qquad (2.1b)$$

$$c_p(\vartheta, w) = (A_c + B_c\vartheta)\, w \tfrac{\text{kJ}}{\text{kg K}}$$
$$+ \underbrace{\left(A_{c,\text{w}} + B_{c,\text{w}}\vartheta + C_{c,\text{w}}\vartheta^2\right) \tfrac{\text{kJ}}{\text{kg K}}}_{=c_{p,\text{w}}(\vartheta)} (1 - w), \qquad (2.1c)$$

$$\eta(\vartheta, w) = \exp\Big(E_\eta + \frac{F_\eta}{C_\eta w + 1} + A_\eta w^{D_\eta}$$
$$- (B_\eta w + G_\eta)(\vartheta - \vartheta_\text{A})\Big)\text{Pa s}, \qquad (2.1d)$$

$$\Delta\vartheta(\vartheta, w) = \left(A_\Delta w^{B_\Delta} + C_\Delta w \frac{\vartheta - 343.15}{100}\right) \text{K}, \qquad (2.1e)$$

---

[1] The quantity equations (2.1) are provided by GEA Wiegand GmbH, where the coefficients of (2.1) specify the considered product. In App. A.6, the coefficients for milk are given.

where ϑ in K and w in $\mathrm{kg\,kg^{-1}}$. Additional information on (2.1a), (2.1b), and (2.1e) is given in the Remarks 2.1, 2.2, and 2.3, respectively.

Remark 2.1. Since densities ϱ and temperatures ϑ are directly measured, see Fig. 2.1, the liquid's dry matter contents w can be indirectly measured by solving (2.1a) w.r.t. w, which yields the static estimator

$$w(\varrho, \vartheta) = \left(\frac{1}{A_\varrho} \left(\frac{\varrho}{A_{\varrho,\mathrm{w}} + B_{\varrho,\mathrm{w}}\vartheta + C_{\varrho,\mathrm{w}}\vartheta^2} - 1 \right) \right)^{1/B_\varrho} \frac{\mathrm{kg}}{\mathrm{kg}}. \qquad (2.2)$$

Note that w is an important process quantity for control and design.

Remark 2.2. Strictly speaking, the enthalpy of evaporation Δh_v, see (2.1b), is not a product property. In fact, it is a property of the product's water content. Hence, the corresponding temperature ϑ is attributed to the product's water content, which is approximately equal to the product's temperature.

Remark 2.3. The boiling point elevation $\Delta\vartheta$, see (2.1e), essentially determines the product's temperature, which is motivated by the fact that increasing w leads to an increase of the product's boiling point [74].

2.2   Dynamics of Subsystems

In this section, the models of an FFE's subsystems are specified. At first, let us make some general remarks:

- In most of the equations in this section, subscript $j = 1, \ldots, 4$ over the FFE's passes is dropped for the sake of compact notation.

- Temperatures and other relevant properties of the product (ϱ, c_p, etc.) are specified at the end of each subsection.

- In most of the physical balance equations, it is assumed that changes of liquid properties are small and slow so that $\frac{\mathrm{d}\varrho}{\mathrm{d}t} \approx 0$, $\frac{\mathrm{d}c_p}{\mathrm{d}t} \approx 0$, etc.

- By assuming uniformly distributed vapor, the vapor in the Effect has the temperature ϑ_E and the vapor in the Heat Chamber has the temperature ϑ_H.
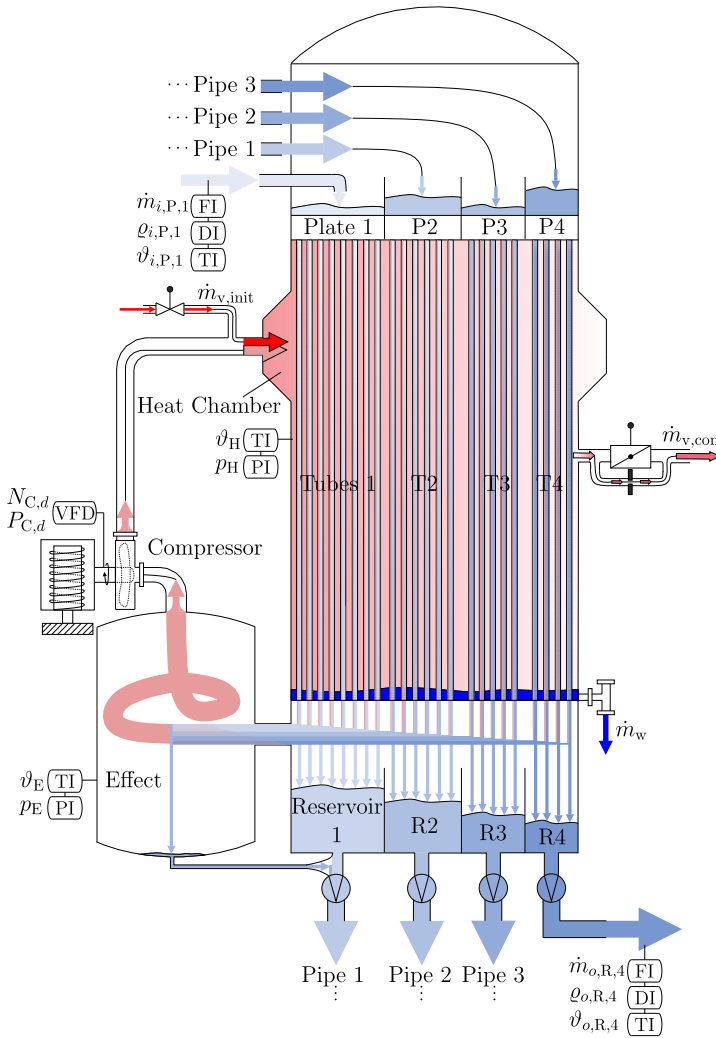
Figure 2.1: Sketch of a one-Effect FFE with four passes and MVR

2.2.1 Plate
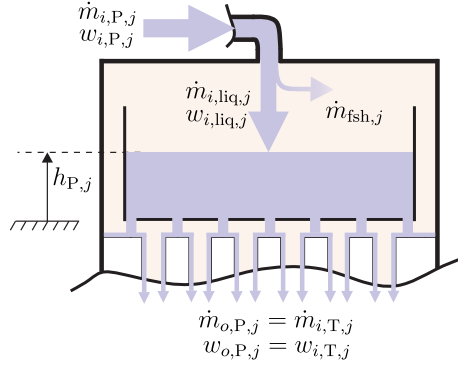
Figure 2.2: Plate

Essentially, the Plate is a tank with orifices at its bottom to distribute the product over the downstream Tubes, see Fig. 2.2. To treat the product with care, evaporation at low temperatures and pressures is desired. Therefore, before the process is ramped up, partial vacuum is generated by a vacuum pump.[2] Due to the low pressure inside the FFE and the fact that the product is superheated with temperature $\vartheta_{i,P}$, a small amount of water content $\dot{m}_{fsh}$ evaporates (so called "flash evaporation") when product enters the FFE [102]. Thus, the product *rapidly* cools down to the temperature $\vartheta_{i,liq,P} = \vartheta_E + \Delta\vartheta_{i,P} < \vartheta_{i,P}$.

Mass Balance
The derivation of the Plate's model is detailed in [102]. While the influence of the Plate's tank thickness on the filling level can be neglected, the shape of the orifices is considered via the discharge coefficient κ_o, cf. [141]. Based on Torricelli's law, see Remark 2.4, the output mass flow gets

$$\dot{m}_{o,P}(t) = \varrho_{i,P}(t)\bar{A}\sqrt{2g\max\{h_P(t), 0\}} \tag{2.3}$$

---

[2] Partial vacuum generation is not modeled since it is not relevant w.r.t. control of this process.

with

$$\bar{A} = \frac{A_{\mathrm{o}} n_{\mathrm{o}} \kappa_{\mathrm{o}}}{1 - \left(\frac{A_{\mathrm{o}} n_{\mathrm{o}}}{A_{\mathrm{P}}}\right)^2}. \tag{2.4}$$

Then, the filling level h_{P} follows from the mass balance over the Plate, i.e.,

$$\frac{\mathrm{d}}{\mathrm{d}t} h_{\mathrm{P}}(t) = \frac{\dot{m}_{i,\mathrm{liq}}(t)}{\varrho_{i,\mathrm{P}}(t) A_{\mathrm{P}}} - \frac{\bar{A}}{A_{\mathrm{P}}} \sqrt{2g \max\{h_{\mathrm{P}}(t), 0\}}, \tag{2.5}$$

where the input mass flow is determined by

$$\dot{m}_{i,\mathrm{liq}}(t) = \dot{m}_{i,\mathrm{P}}(t) - \dot{m}_{\mathrm{fsh}}(t). \tag{2.6}$$

To this end, the vapor mass flow $\dot{m}_{\mathrm{fsh}}$ due to flash evaporation follows from

$$\begin{aligned} \dot{m}_{i,\mathrm{P}}(t) c_{p,\mathrm{feed}}(t) \vartheta_{i,\mathrm{P}}(t) = {}& \dot{m}_{i,\mathrm{liq}}(t) c_{p,i,\mathrm{P}}(t) \vartheta_{i,\mathrm{liq},\mathrm{P}}(t) \\ & + \dot{m}_{\mathrm{fsh}}(t) \big(c_{p,\mathrm{w},\mathrm{E}}(t) \vartheta_{\mathrm{E}}(t) + \Delta h_{v,\mathrm{E}}(t) \big) \end{aligned} \tag{2.7}$$

such that, with (2.6),

$$\dot{m}_{\mathrm{fsh}}(t) = \max \left\{ \frac{\dot{m}_{i,\mathrm{P}}(t) \left(c_{p,\mathrm{feed}}(t) \vartheta_{i,\mathrm{P}}(t) - c_{p,i,\mathrm{P}}(t) \vartheta_{i,\mathrm{liq},\mathrm{P}}(t) \right)}{c_{p,\mathrm{w},\mathrm{E}}(t) \vartheta_{\mathrm{E}}(t) + \Delta h_{v,\mathrm{E}}(t) - c_{p,i,\mathrm{P}}(t) \vartheta_{i,\mathrm{liq},\mathrm{P}}(t)}, 0 \right\} \tag{2.8}$$

is obtained.[3] Note that, in (2.3), (2.5), changes of density due to flash evaporation are neglected so that $\varrho_{i,\mathrm{P}} = \varrho_{o,\mathrm{P}}$ holds, since $\dot{m}_{\mathrm{fsh}}$ is small compared to other mass flows.

Remark 2.4. Of course, in the original version of Torricelli's law [119], there is no max operator under the square root of (2.3). Physically, this max operator models draining of the tank so that the filling level cannot get smaller than zero. From the numerical perspective, a negative argument of the square root in (2.3) and (2.5) is avoided. As an alternative to the max operator, it is possible to formulate (2.3), (2.5) via distinction of cases. However, the max operator leads to a more compact notation and simplifies the implementation in simulation environments, such as Simulink.

---

[3] In case of (2.8), the max operator ensures nonnegative $\dot{m}_{\mathrm{fsh}}$.

Dry Matter Balance

By assuming perfect mixing of the liquid's water and dry matter content, the dry matter balance over the Plate yields[4]

$$\frac{\mathrm{d}}{\mathrm{d}t} w_{o,\mathrm{P}}(t) = \frac{\dot{m}_{i,\mathrm{liq}}(t)}{\varrho_{i,\mathrm{P}}(t) A_{\mathrm{P}} \max\{h_{\mathrm{P}}(t), \varepsilon\}} \big(w_{i,\mathrm{liq}}(t) - w_{o,\mathrm{P}}(t)\big) \qquad (2.9)$$

with $0 < \varepsilon \ll 1$ and

$$w_{i,\mathrm{liq}}(t) = \frac{w_{i,\mathrm{P}}(t)\dot{m}_{i,\mathrm{P}}(t)}{\dot{m}_{i,\mathrm{liq}}(t)}. \qquad (2.10)$$

Based on (2.1), the liquid's temperatures and properties are determined by

$$\vartheta_{i,\mathrm{liq},\mathrm{P}}(t) := \vartheta_{\mathrm{E}}(t) + \Delta\vartheta_{i,\mathrm{P}}(t), \qquad \Delta\vartheta_{i,\mathrm{P}}(t) := \Delta\vartheta(\vartheta_{\mathrm{E}}(t), w_{i,\mathrm{P}}(t)),$$

$$c_{p,\mathrm{feed}}(t) := c_p(\vartheta_{i,\mathrm{P}}(t), w_{i,\mathrm{P}}(t)), \qquad c_{p,i,\mathrm{P}}(t) := c_p(\vartheta_{i,\mathrm{liq},\mathrm{P}}(t), w_{i,\mathrm{P}}(t)),$$

$$c_{p,\mathrm{w},\mathrm{E}}(t) := c_{p,\mathrm{w}}(\vartheta_{\mathrm{E}}(t)), \qquad \Delta h_{v,\mathrm{E}}(t) := \Delta h_v(\vartheta_{\mathrm{E}}(t)),$$

$$\varrho_{i,\mathrm{P}}(t) := \varrho(\vartheta_{i,\mathrm{liq},\mathrm{P}}(t), w_{i,\mathrm{P}}(t)).$$

2.2.2 Effect with Tubes

The product exiting the Plate is distributed over the Tubes, where it flows down on their insides as a thin liquid film. Additionally, there is a heat flow through the walls of the Tubes so that the liquid partially evaporates, which affects increasing dry matter content as shown in Fig. 2.3.

Discrete Conveyor Flow

A classical model to describe the flow of liquid film in Tubes assumes constant flow velocity and uniform evaporation along the Tubes. While classical models are detailed in, e.g. [107, 141, 102], the Discrete Conveyor Flow model is introduced in this section. In general, it models overtaking of liquid particles and has a discrete-time nature. The latter causes some drawbacks that are discussed in Sec. 2.4.2 and resolved in Ch. 3.

---

[4] In case of (2.9), the max operator avoids division by zero.
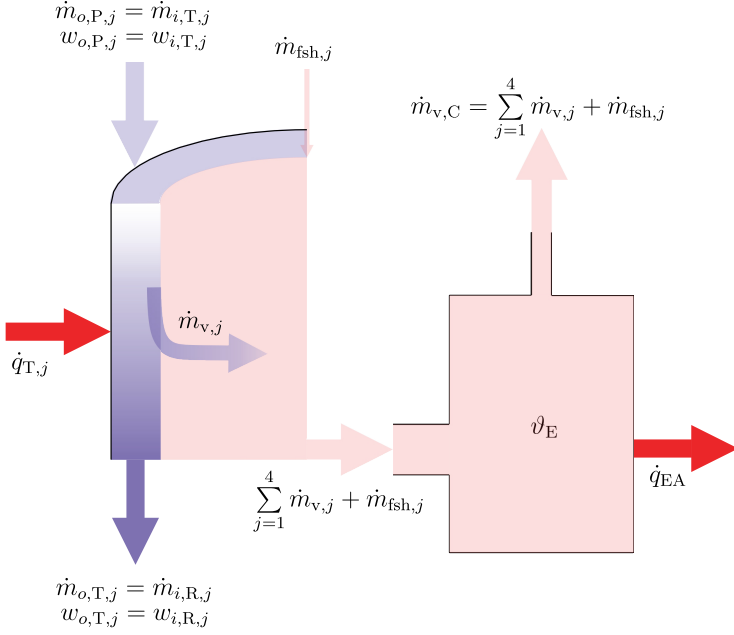
Figure 2.3: Effect with Tubes, where only a part of a single Tube is sketched

Based on Fig. 2.4, let us discuss the general behavior of this model. As can be seen, the model consists of a shift register at the top of Fig. 2.4 to distribute the input flow. Additionally, there are two conveyors where each of them moves with the sampling interval $\Delta t \in \mathbb{R}_+$. The first conveyor is attributed to the water flow, whereas the second conveyor describes the dry mass flow. For this purpose, the input mass flow $\dot{m}_{i,\mathrm{T}}$ with dry matter content $w_{i,\mathrm{T}}$ is split into the water mass[5]

$$m_{\mathrm{w},k} := m_{\mathrm{w}}(t_k) = \int\limits_{t_k}^{t_k+\Delta t} \big(1 - w_{i,\mathrm{T}}(\theta)\big)\dot{m}_{i,\mathrm{T}}(\theta)\,\mathrm{d}\theta \qquad (2.11)$$

---

[5] The notation $(\cdot)_k$ to evaluate the variable $(\cdot)$ at $t = t_k$ is introduced in (2.11), (2.12) and used throughout this subsection.
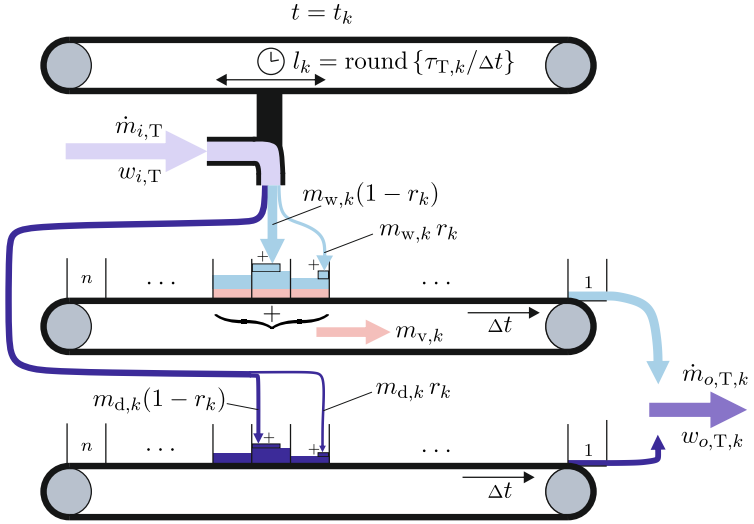
Figure 2.4: Discrete Conveyor Flow model

and dry mass

$$m_{\mathrm{d},k} := m_{\mathrm{d}}(t_k) = \int\limits_{t_k}^{t_k+\Delta t} w_{i,\mathrm{T}}(\theta)\dot{m}_{i,\mathrm{T}}(\theta)\,\mathrm{d}\theta. \qquad (2.12)$$

Each conveyor has n registers which are defined by

$$n = \frac{\tau_{\mathrm{T,max}}}{\Delta t}. \qquad (2.13)$$

Note that $\tau_{\mathrm{T,max}} \in \mathbb{R}_+$ denotes the maximum travel time of liquid particles from the input to the output of the Tubes. Both parameters, $\tau_{\mathrm{T,max}}$ and Δt, are constants and chosen by the user[6] based on preliminary knowledge about the considered application. Furthermore, we need a relation for the

---

[6] Of course, the user must ensure that $\tau_{\mathrm{T,max}}$ is an integer multiple of Δt such that n is an integer.

instantaneous travel time $\tau_{\mathrm{T}}(t)$ of liquid particles through the Tubes. To this end, let us consider

$$\tau_{\mathrm{T}}(t) = \frac{V_{\mathrm{T}}(t)}{\dot{V}_{\mathrm{T}}(t)} = \frac{n_{\mathrm{T}}\pi \ell_{\mathrm{T}}(d_{\mathrm{T}} - \bar{s}_{\mathrm{T}}(t))\bar{s}_{\mathrm{T}}(t)\varrho_{i,\mathrm{T}}(t)}{\dot{m}_{i,\mathrm{T}}(t)} \tag{2.14}$$

which relates $\tau_{\mathrm{T}}(t)$ to the the average film thickness $\bar{s}_{\mathrm{T}}(t)$. The latter is based on Nusselt's thin film theory [137] and calculated by

$$\bar{s}_{\mathrm{T}}(t) = \left(\frac{3\eta_{i,\mathrm{T}}^2(t)}{g\varrho_{i,\mathrm{T}}^2(t)} \right)^{1/3} Re^{1/3}(t), \tag{2.15}$$

$$Re(t) = \frac{\dot{m}_{i,\mathrm{T}}(t)}{n_{\mathrm{T}}\pi d_{\mathrm{T}}\eta_{i,\mathrm{T}}(t)}. \tag{2.16}$$

Note that n_{T} denotes the number of Tubes in an FFE pass and should not be confused with the number of registers n on the conveyor.

To simplify the explanation, let us, at first, only focus on the water conveyor. The register, that is filled with the water mass $m_{\mathrm{w},k}$, see (2.11), is, according to (2.13), determined by the quotient $\tau_{\mathrm{T},k}/\Delta t$. The latter is commonly not an integer which is, however, required since noninteger numbered registers do not exist. Therefore, with the residual (noninteger) part

$$r_k = \frac{\tau_{\mathrm{T},k}}{\Delta t} \bmod 1, \tag{2.17}$$

integer part

$$l_k = \mathrm{round}\left\{ \frac{\tau_{\mathrm{T},k}}{\Delta t} \right\}, \tag{2.18}$$

and for $\nu = 1, 2, \ldots, n$, let us consider the following distinction of cases:

$$\text{if } 0 \leq r_k < 0.5: \quad b_{\nu,k} = \begin{cases} 1 - r_k, & \text{if } \nu = l_k, \\ r_k, & \text{if } \nu = l_k + 1, \\ 0, & \text{otherwise,} \end{cases} \tag{2.19a}$$

$$\text{if } 0.5 \leq r_k < 1: \quad b_{\nu,k} = \begin{cases} r_k, & \text{if } \nu = l_k, \\ 1 - r_k, & \text{if } \nu = l_k - 1, \\ 0, & \text{otherwise,} \end{cases} \tag{2.19b}$$

which determines the input vector

$$b_k := \begin{bmatrix} b_1, & b_2, & \ldots, b_n \end{bmatrix}_k^\top. \tag{2.20}$$

Note that, in Fig. 2.4, the upper case (2.19a) is sketched. As the conveyor moves with sampling Δt and since x_1 represents the last register on the conveyor, the superdiagonal of the corresponding discrete-time state matrix must be filled with ones. However, to model diffusion amongst adjacent states, the mass distribution coefficient $\xi = \text{const}$ is introduced and will be specified later. Thus, the discrete-time state space model of the water conveyor reads

$$\begin{bmatrix} x_1 \\ x_2 \\ \vdots \\ x_n \end{bmatrix}_{k+1} = \begin{bmatrix} \xi & 1-2\xi & \xi & 0 & \cdots & 0 \\ 0 & \xi & 1-2\xi & \xi & \cdots & 0 \\ \vdots & \vdots & \vdots & \vdots & \ddots & \vdots \\ 0 & 0 & 0 & 0 & \cdots & \xi \end{bmatrix} \begin{bmatrix} x_1 \\ x_2 \\ \vdots \\ x_n \end{bmatrix}_k +$$

$$\begin{bmatrix} b_1 \\ b_2 \\ \vdots \\ b_n \end{bmatrix}_k m_{\text{w},k} - \begin{bmatrix} v_1 \\ v_2 \\ \vdots \\ v_n \end{bmatrix}_k m_{\text{v},k} \tag{2.21}$$

$$y_{\text{w},k} = \begin{bmatrix} 1 & 0 & 0 & \ldots & 0 \end{bmatrix} x_k \tag{2.22}$$

with

$$x_k := \begin{bmatrix} x_1, & x_2, & \ldots, & x_n \end{bmatrix}_k^\top. \tag{2.23}$$

As the reader might have noticed, besides the water input $b_k m_{\text{w},k}$, the mass $v_k m_{\text{v},k}$ is subtracted to model evaporation. Analogous to (2.11), (2.12), the vapor mass is determined by

$$m_{\text{v},k} = \int_{t_k}^{t_k+\Delta t} \dot{m}_{\text{v}}(\theta) \, d\theta. \tag{2.24}$$

25

While subscript j over the FFE passes is skipped in most of the equations for better readability, it must be considered to calculate the instantaneously evaporating mass flow $\dot{m}_{v,j}$ from the Tubes of pass j. This mass flow is given by

$$\dot{m}_{v,j}(t) = \gamma_j(t)\dot{m}_{v,C}(t) - \dot{m}_{\text{fsh},j}(t), \tag{2.25}$$

where $\dot{m}_{v,C}$ is specified in Sec. 2.2.5 and γ_j are coefficients to back-calculate $\dot{m}_{v,C}$ to the j-th pass, see also Remark 2.5. These coefficients are obtained by relating the heat flow into pass j to the summed heat flow into all four passes, i.e.,

$$\gamma_j(t) = \frac{\dot{q}_{T,j}(t)}{\sum\limits_{j=1}^{4} \dot{q}_{T,j}(t)}, \tag{2.26}$$

where $\dot{q}_{T,j}$ is calculated according to (2.36b). To uniformly distribute the mass of vapor among the filled registers[7], the vector

$$v_k := \begin{bmatrix} v_1, & v_2, & \ldots, & v_n \end{bmatrix}_k^{\top} \tag{2.27}$$

is, for $\nu = 1, 2, \ldots, n$, calculated by

$$v_{\nu,k} = \begin{cases} \frac{1}{n_{\text{filled},k}}, & \text{if } x_{\nu,k} > 0, \\ 0, & \text{otherwise,} \end{cases} \tag{2.28}$$

where $n_{\text{filled},k}$ is the number of filled registers at $t = t_k$. Hence, the vapor mass $m_{v,k}/n_{\text{filled},k}$ is taken out of each filled register. However, it is ensured that the mass of water within a filled register cannot get smaller than zero, i.e., if $v_{\nu,k}m_{v,k} > x_{\nu,k}$, the register $x_{\nu,k}$ is emptied and the residual vapor mass is distributed amongst the remaining filled registers.

Remark 2.5. By modeling $\dot{m}_{v,j}$ via (2.25), (2.26), it is assumed that the mass flow of vapor $\dot{m}_{v,C}$ through the Compressor is equal to the total amount of evaporated water $\sum\limits_{j=1}^{4} \dot{m}_{v,j} + \dot{m}_{\text{fsh},j}$ from the liquid, see Fig. 2.3. Physically,

---

[7] More precisely, the register numbered ν is defined as "filled register" if its mass x_ν is greater than zero.

this assumption is justified since it represents the stationary mass balance of vapor over the Effect.

The dry mass conveyor gets $m_{\mathrm{d},k}$ as input, see (2.12), and the corresponding b_k-vector is determined in the same manner as for the water conveyor, cf. (2.17)–(2.20). Hence, the discrete-time state space model for dry mass is

$$
\begin{bmatrix} x_1 \\ x_2 \\ \vdots \\ x_n \end{bmatrix}_{k+1} = \begin{bmatrix} \xi & 1-2\xi & \xi & 0 & \cdots & 0 \\ 0 & \xi & 1-2\xi & \xi & \cdots & 0 \\ \vdots & \vdots & \vdots & \vdots & \ddots & \vdots \\ 0 & 0 & 0 & 0 & \cdots & \xi \end{bmatrix} \begin{bmatrix} x_1 \\ x_2 \\ \vdots \\ x_n \end{bmatrix}_k + \begin{bmatrix} b_1 \\ b_2 \\ \vdots \\ b_n \end{bmatrix}_k m_{\mathrm{d},k}
$$

(2.29)

$$
y_{\mathrm{d},k} = \begin{bmatrix} 1 & 0 & 0 & \ldots & 0 \end{bmatrix} x_k.
$$

(2.30)

To obtain the output mass flow $\dot{m}_{o,\mathrm{T}}$, the masses of dry matter and water content in the last register are summed and divided by Δt, i.e.,

$$
\dot{m}_{o,\mathrm{T},k} = \frac{y_{\mathrm{d},k} + y_{\mathrm{w},k}}{\Delta t}.
$$

(2.31)

The output dry matter content $w_{o,\mathrm{T},k}$ is determined by

$$
w_{o,\mathrm{T},k} = \frac{y_{\mathrm{d},k}}{y_{\mathrm{d},k} + y_{\mathrm{w},k}}.
$$

(2.32)

The discrete values $\dot{m}_{o,\mathrm{T},k}$ and $w_{o,\mathrm{T},k}$ can be back-converted into corresponding continuous-time signals via hold elements. In this case, the standard back-conversion from Simulink is used, i.e., a zero-order hold block over the sampling interval Δt.

With the spatial discretization $\Delta x = \ell_{\mathrm{T}}/n$, the mass distribution coefficient ξ, see (2.21) and (2.29), is modeled by

$$
\xi = \frac{D_f \Delta t}{\Delta x^2}.
$$

(2.33)

Note that von Neumann's stability analysis [59], which is used to check the stability of finite difference schemes, requires

$$\xi < \frac{1}{2}. \tag{2.34}$$

Since this notion of modeling diffusion is not diffusion per se, but rather a mass distribution within the Tubes, the value of the diffusion coefficient D_f cannot be found in literature. Therefore, D_f is used as tuning parameter and must satisfy (2.34).
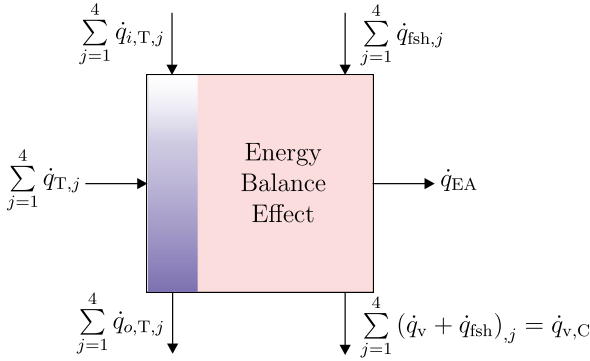
Figure 2.5: Energy balance over the Effect

Energy Balance
The heat flows into and out of the Effect are depicted in Fig. 2.5 such that evaluating the corresponding energy balance yields

$$\frac{\mathrm{d}}{\mathrm{d}t}\vartheta_{\mathrm{E}} = \frac{\sum_{j=1}^{4}(\dot{q}_{i,\mathrm{T}} + \dot{q}_{\mathrm{T}})_{,j} - \sum_{j=1}^{4}(\dot{q}_{o,\mathrm{T}} + \dot{q}_{\mathrm{v}})_{,j} - \dot{q}_{\mathrm{EA}} - \vartheta_{\mathrm{E}}\frac{\mathrm{d}m_{\mathrm{E}}}{\mathrm{d}t}\bar{c}_{p,\mathrm{T}}}{m_{\mathrm{E}}\bar{c}_{p,\mathrm{T}} + m_{\mathrm{met},\mathrm{E}}c_{p,\mathrm{met}}}. \tag{2.35}$$

Firstly, note that in (2.35), time dependencies of all variables are dropped[8] for the sake of compactness and the relations for the heat flows are

$$\dot{q}_{i,\mathrm{T},j}(t) = \left(\dot{m}_{i,\mathrm{T}}(t) c_{p,i,\mathrm{T}}(t) \vartheta_{i,\mathrm{liq},\mathrm{T}}(t)\right)_j \tag{2.36a}$$

$$\dot{q}_{\mathrm{T},j}(t) = k_{\mathrm{T},j} A_{\mathrm{T},j} \left(\vartheta_{\mathrm{H}}(t) - \bar{\vartheta}_{\mathrm{liq},\mathrm{T},j}(t)\right) \tag{2.36b}$$

$$\dot{q}_{o,\mathrm{T},j}(t) = \left(\dot{m}_{o,\mathrm{T}}(t) c_{p,o,\mathrm{T}}(t) \vartheta_{o,\mathrm{liq},\mathrm{T}}(t)\right)_j \tag{2.36c}$$

$$\dot{q}_{v,j}(t) = \dot{m}_{v,j}(t) \left(c_{p,w,\mathrm{E}}(t) \vartheta_{\mathrm{E}}(t) + \Delta h_{v,\mathrm{E}}(t)\right) \tag{2.36d}$$

$$\dot{q}_{\mathrm{EA}}(t) = k_{\mathrm{EA}} A_{\mathrm{EA}} \left(\vartheta_{\mathrm{E}}(t) - \vartheta_{\mathrm{A}}\right). \tag{2.36e}$$

Secondly, note that the heat flow $\dot{q}_{\mathrm{fsh},j}$ due to flash evaporation does not have to be specified since it is canceled by the energy balance over the Effect, which gets evident in Fig. 2.5. While the heat capacity of vapor can be neglected in (2.35), cf. Remark 2.5, the heat capacity of product within the Effect is determined by

$$m_{\mathrm{E}}(t) \bar{c}_{p,\mathrm{T}}(t) = \sum_{j=1}^{4} m_{\mathrm{T},j}(t) \bar{c}_{p,\mathrm{T},j}(t), \tag{2.37}$$

where $m_{\mathrm{T},j}$ follows from integrating the mass balances over the Tubes of each pass j, i.e.,

$$\frac{\mathrm{d}}{\mathrm{d}t} m_{\mathrm{T},j}(t) = \left(\dot{m}_{i,\mathrm{T}}(t) - \dot{m}_{v}(t) - \dot{m}_{o,\mathrm{T}}(t)\right)_j. \tag{2.38}$$

Thus, the derivative term on the right-hand side of (2.35) is given by

$$\frac{\mathrm{d}m_{\mathrm{E}}(t)}{\mathrm{d}t} \bar{c}_{p,\mathrm{T}}(t) = \sum_{j=1}^{4} \frac{\mathrm{d}m_{\mathrm{T},j}(t)}{\mathrm{d}t} \bar{c}_{p,\mathrm{T},j}(t). \tag{2.39}$$

Based on (2.1), the liquid's temperatures and properties are determined by

$$\vartheta_{i,\mathrm{liq},\mathrm{T}}(t) := \vartheta_{\mathrm{E}}(t) + \Delta\vartheta_{i,\mathrm{T}}(t), \qquad \Delta\vartheta_{i,\mathrm{T}}(t) := \Delta\vartheta(\vartheta_{\mathrm{E}}(t), w_{i,\mathrm{T}}(t)),$$

$$c_{p,i,\mathrm{T}}(t) := c_p(\vartheta_{i,\mathrm{liq},\mathrm{T}}(t), w_{i,\mathrm{T}}(t)),$$

$$\varrho_{i,\mathrm{T}}(t) := \varrho(\vartheta_{i,\mathrm{liq},\mathrm{T}}(t), w_{i,\mathrm{T}}(t)),$$

---

[8] Besides $m_{\mathrm{met},\mathrm{E}}$ and $c_{p,\mathrm{met}}$, all quantities in (2.35) depend on time t.

$$\eta_{i,\mathrm{T}}(t) := \eta(\vartheta_{i,\mathrm{liq},\mathrm{T}}(t), w_{i,\mathrm{T}}(t)),$$

$$\vartheta_{o,\mathrm{liq},\mathrm{T}}(t) := \vartheta_{\mathrm{E}}(t) + \Delta\vartheta_{o,\mathrm{T}}(t), \qquad \Delta\vartheta_{o,\mathrm{T}}(t) := \Delta\vartheta(\vartheta_{\mathrm{E}}(t), w_{o,\mathrm{T}}(t)),$$

$$c_{p,o,\mathrm{T}}(t) := c_p(\vartheta_{o,\mathrm{liq},\mathrm{T}}(t), w_{o,\mathrm{T}}(t)),$$

$$\bar{\vartheta}_{\mathrm{liq},\mathrm{T}}(t) := \vartheta_{\mathrm{E}}(t) + \Delta\bar{\vartheta}_{\mathrm{T}}(t),$$

$$\Delta\bar{\vartheta}_{\mathrm{T}}(t) := \Delta\vartheta\left(\vartheta_{\mathrm{E}}(t), \frac{w_{i,\mathrm{T}}(t) + w_{o,\mathrm{T}}(t)}{2}\right),$$

$$\bar{c}_{p,\mathrm{T}}(t) := c_p\left(\bar{\vartheta}_{\mathrm{liq},\mathrm{T}}(t), \frac{w_{i,\mathrm{T}}(t) + w_{o,\mathrm{T}}(t)}{2}\right),$$

$$c_{p,\mathrm{w},\mathrm{E}}(t) := c_{p,\mathrm{w}}(\vartheta_{\mathrm{E}}(t)),$$

$$\Delta h_{v,\mathrm{E}}(t) := \Delta h_v(\vartheta_{\mathrm{E}}(t)),$$

where the index j is skipped.

2.2.3 Reservoir
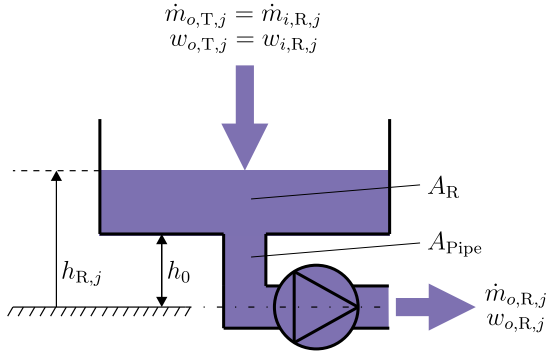
Figure 2.6: Reservoir

The concentrated product drops from the Tubes of pass j into the corresponding Reservoir and a pump conveys the product through the downstream Pipe, see Fig. 2.6. In this context, two cases must be distinguished: In the first case, the filling level does not reach the bottom of the Reservoir so that there is

only product in the cross-sectional area A_{Pipe}. In the second case, the product additionally fills the Reservoir with cross-sectional area A_{R}.

Furthermore, two phenomena must be distinguished: firstly, the case of perfect mixing, which holds for products with rather small viscosity; secondly, the case of layering, which occurs due to imperfect mixing and is rather observed with high-viscous products. Both cases can occur simultaneously within one plant, e.g., there is mixing in the first few passes and, as the viscosity increases in downstream passes, layering dominates. For convenience, only the case of perfect mixing is considered in the frame of this chapter; a more detailed discussion is given in Remark 2.6. However, let us keep in mind that, by assuming perfect mixing, a "source of delay" is neglected, which is also discussed in Sec. 2.4.3. Since there are no significant temperature changes along Pipes and Reservoirs due to a good insulation, the product temperature is assumed constant in both of these subsystems.

Remark 2.6. A possibility to model layering in the Reservoir via the concept of *variable transport delay* [147] is discussed in [161]. However, in experiments with the Reservoir, the author made the experience that this model is inadequate. Instead, it is more convenient to introduce the empirically motivated factor ζ_{mix} into the Reservoir's dry matter balance which roughly models layering, see Sec. 4.4.2. More elaborate PDE-based approaches to model imperfect mixing are given in [89].

Mass Balance
The mass balance over the Reservoir is given by

$$
\frac{\mathrm{d}}{\mathrm{d}t} h_{\text{R}}(t) = \begin{cases} \dfrac{1}{\varrho_{i,\text{R}}(t) A_{\text{Pipe}}} \big(\dot{m}_{i,\text{R}}(t) - \dot{m}_{o,\text{R}}(t) \big), & h_{\text{R}}(t) \in (0, h_0], \\ \dfrac{1}{\varrho_{i,\text{R}}(t) A_{\text{R}}} \big(\dot{m}_{i,\text{R}}(t) - \dot{m}_{o,\text{R}}(t) \big), & h_{\text{R}}(t) > h_0. \end{cases} \tag{2.40}
$$

Note that, generally, A_{R} can depend on the level in the Reservoir, i.e., $A_{\text{R}} = A_{\text{R}}(h_{\text{R}})$ if the Reservoir has, e.g., a conical shape instead of a cylindrical one.

The output mass flow is determined by a PI controller which controls the level in the Reservoir to a constant setpoint h_d such that[9]

$$\dot{m}_{o,\text{R}}(t) = \max\left\{ k_{p,\text{R}}(h_{\text{R}}(t) - h_d) + k_{i,\text{R}} \int_0^t (h_{\text{R}}(\theta) - h_d)\,\mathrm{d}\theta, 0 \right\} \quad (2.41)$$

with $k_{p,\text{R}}, k_{i,\text{R}} > 0$.

Dry Matter Balance
To evaluate the dry matter balance in case of perfect mixing, the same approach as in Sec. 2.2.1 is applied, which yields

$$\frac{\mathrm{d}w_{o,\text{R}}(t)}{\mathrm{d}t} = \begin{cases} \dfrac{\dot{m}_{i,\text{R}}(t)\left(w_{i,\text{R}}(t) - w_{o,\text{R}}(t)\right)}{h_{\text{R}}(t)\varrho_{i,\text{R}}(t)A_{\text{Pipe}}}, & h_{\text{R}}(t) \in (0, h_0], \\[2ex] \dfrac{\dot{m}_{i,\text{R}}(t)\left(w_{i,\text{R}}(t) - w_{o,\text{R}}(t)\right)}{(h_{\text{R}}(t) - h_0)\varrho_{i,\text{R}}(t)A_{\text{R}}}, & h_{\text{R}}(t) > h_0. \end{cases} \quad (2.42)$$

Based on (2.1), the liquid's temperature and density are given by

$$\vartheta_{i,\text{liq},\text{R}}(t) := \vartheta_{\text{E}}(t) + \Delta\vartheta_{i,\text{R}}(t), \quad \Delta\vartheta_{i,\text{R}}(t) := \Delta\vartheta(\vartheta_{\text{E}}(t), w_{i,\text{R}}(t)),$$
$$\varrho_{i,\text{R}}(t) := \varrho(\vartheta_{i,\text{liq},\text{R}}(t), w_{i,\text{R}}(t)).$$

2.2.4 Pipe

Besides the transport of product in the Tubes, there are also transport processes in the Pipes between passes, i.e., from the Reservoir to the Plate of the subsequent pass.

---

[9] In case of (2.41), the max operator ensures nonnegative $\dot{m}_{o,\text{R}}$. Moreover, the control error $(h_{\text{R}} - h_d)$ is considered in (2.41) since increasing $\dot{m}_{o,\text{R}}$ leads to decreasing h_{R} and vice versa.

Mass Balance

The Pipe can be modeled as feedthrough w.r.t. mass flow.[10] However, to simulate ramp-up processes, the filling of the Pipe must additionally be considered, which is modeled by the upper case in the following i/o relation:

$$
\dot{m}_{o,\text{Pipe}}(t) = \begin{cases} 0, & \text{if } \int_{t_0}^{t} \frac{\dot{m}_{i,\text{Pipe}}(\theta)}{\varrho_{i,\text{Pipe}}(\theta)}\,\mathrm{d}\theta < V_{\text{Pipe}}, \\ \dot{m}_{i,\text{Pipe}}(t), & \text{otherwise} \end{cases} \tag{2.43}
$$

with $V_{\text{Pipe}} = (\ell_{\text{Pipe}}\pi d_{\text{Pipe}}^2)/4$ and the initial time of the simulation is denoted by t_0.

Dry Matter Balance

In contrast to $\dot{m}_{o,\text{Pipe}}$, the output dry matter content $w_{o,\text{Pipe}}$ is determined via the corresponding input $w_{i,\text{Pipe}}$ delayed by the variable transport delay $\tau_{\text{Pipe}}(t)$, i.e,

$$
w_{o,\text{Pipe}}(t) = w_{i,\text{Pipe}}(t - \tau_{\text{Pipe}}(t)) \tag{2.44a}
$$

$$
\frac{\mathrm{d}}{\mathrm{d}t}\tau_{\text{Pipe}}(t) = 1 - \frac{c_{\text{Pipe}}(t)}{c_{\text{Pipe}}\big(t - \tau_{\text{Pipe}}(t)\big)},
$$

$$
\tau_{\text{Pipe}}(t_f) = t_f - t_0, \quad \int_{t_0}^{t_f} c_{\text{Pipe}}(\theta)\,\mathrm{d}\theta = \ell_{\text{Pipe}} \tag{2.44b}
$$

which is derived[11] in [146] based on

$$
\int_{t-\tau_{\text{Pipe}}(t)}^{t} c_{\text{Pipe}}(\theta)\,\mathrm{d}\theta = V_{\text{Pipe}}. \tag{2.45}
$$

---

[10] More precisely, the Pipe is a feedthrough w.r.t. volume flow $\dot{V}$ as it is modeled as plug flow vessel [146, 49]. Since the Pipe's cross-sectional area $A_{\text{Pipe}} = (\pi d_{\text{Pipe}}^2)/4$ is constant, it follows that the velocity is also a feedthrough, i.e., $c_{i,\text{Pipe}}(t) = c_{o,\text{Pipe}}(t) =: c_{\text{Pipe}}(t)$. By assuming that changes of the input density $\varrho_{i,\text{Pipe}}(t)$ are small, which is realistic in most relevant cases, the mass flow can also be modeled as feedthrough, see lower case of (2.43).

[11] The differential equation (2.44b) is obtained by calculating the derivative of the integral equation (2.45) w.r.t. time t.

Alternatively, (2.44) can be deduced by applying the method of characteristics to a simplified formulation of the transport PDE [155].[12] The Simulink implementation of (2.44) is given by the *variable transport delay* block [147]. If no direct measurement of the velocity c_{Pipe} is available, it can be calculated by

$$c_{\mathrm{Pipe}}(t) = \frac{4\,\dot{m}_{i,\mathrm{Pipe}}(t)}{\varrho_{i,\mathrm{Pipe}}(t)\pi d_{\mathrm{Pipe}}^2}. \tag{2.46}$$

Note that measurements of $\dot{m}_{i,\mathrm{Pipe}}(t)$ and $\varrho_{i,\mathrm{Pipe}}(t)$ are often known via a Coriolis flow meter in front of a Pipe.
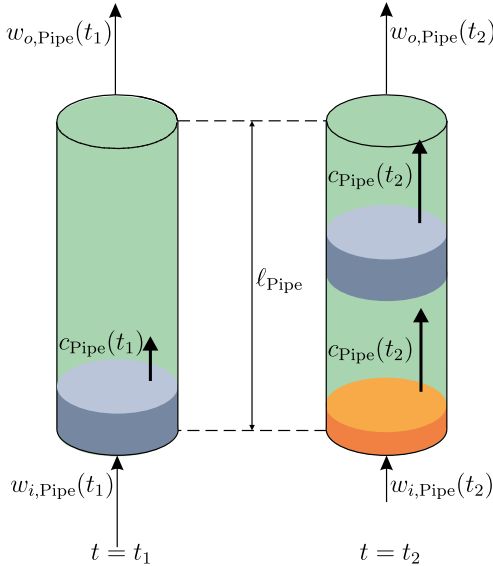
Figure 2.7: Sketch of the variable transport delay concept

A sketch of the variable transport delay concept (2.44) is shown in Fig. 2.7. The gray plug with high dry matter content $w_{i,\mathrm{Pipe}}(t_1)$ enters the Pipe at the time $t = t_1$. At the time $t = t_2$, the orange plug with lower dry matter

---

[12] Note that in [155], this notion is demonstrated w.r.t. the transport of density ϱ, but the same procedure also applies for the transport of concentration w since the transport of both, w and ϱ, follows the same principles [143].

content $w_{i,\mathrm{Pipe}}(t_2)$ enters the Pipe, which directly (without delay) increases the transport velocity c_{Pipe} of all plugs in the Pipe. However, the output dry matter content $w_{o,\mathrm{Pipe}}(t_2)$ is still the same as it was at $t = t_1$. A change of the output dry matter content is observed when the front orange plug arrives at the Pipe's output.

Based on (2.1), the product's temperature and density are determined by

$$\vartheta_{i,\mathrm{liq,Pipe}}(t) := \vartheta_{\mathrm{E}}(t) + \Delta\vartheta_{i,\mathrm{Pipe}}(t), \ \ \Delta\vartheta_{i,\mathrm{Pipe}}(t) := \Delta\vartheta(\vartheta_{\mathrm{E}}(t), w_{i,\mathrm{Pipe}}(t)),$$
$$\varrho_{i,\mathrm{Pipe}}(t) := \varrho(\vartheta_{i,\mathrm{liq,Pipe}}(t), w_{i,\mathrm{Pipe}}(t)).$$

2.2.5 Heat Chamber with Compressor

The vapor in the Effect is absorbed by the Compressor, which affects a pressure difference between the suction side (Effect) and pressure side (Heat Chamber). This pressure difference leads to a temperature difference and thus causes heat flow through the walls of the Tubes as shown in Fig. 2.8. Within the Heat Chamber, the vapor condenses at the outside of the Tubes by releasing its enthalpy of condensation.

The Compressor is basically modeled by its map which consists of two diagrams, see Fig. 2.9. The first diagram relates the pressure difference $p_{\mathrm{H}} - p_{\mathrm{E}}$ to the Compressor's speed N_{C} and vapor volume flow $\dot{V}_{\mathrm{v,C}}$. The second diagram relates the electrical power P_{C} to N_{C} and $\dot{V}_{\mathrm{v,C}}$. Based on the model in [142], the first diagram, see Fig. 2.9a, is obtained by fitting the coefficients a, b, and c of the relation

$$\frac{p_{\mathrm{H}}(t) - p_{\mathrm{E}}(t)}{\varrho_{\mathrm{v,E}}(t)} = aN_{\mathrm{C}}^2(t) + bN_{\mathrm{C}}(t)\dot{V}_{\mathrm{v,C}}(t) + c\dot{V}_{\mathrm{v,C}}^2(t). \tag{2.47}$$

to data of the real-world compressor map in the least-squares sense. Normally, the pressures p_{E} and p_{H} are directly measured, see Fig. 2.1. However, if this is not the case, Remark 2.7 shows a way to indirectly measure these pressures.
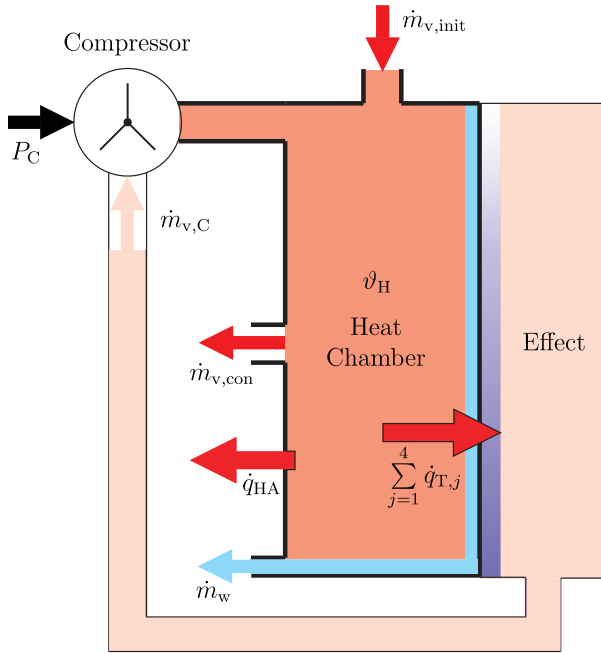
Figure 2.8: Heat Chamber

Remark 2.7. By assuming saturated vapor conditions in the Effect and Heat Chamber, the corresponding pressures $p_E = p(\vartheta_E)$ and $p_H = p(\vartheta_H)$ can be determined by Antoine's equation, cf. [125], so that

$$p(\vartheta) = \exp\left(16.57 - \frac{3984.92}{\vartheta - 39.72}\right), \tag{2.48}$$

where ϑ in K denotes the saturated vapor temperature and p in kPa the saturated vapor pressure.

(a) Pressure difference over volume flow

(b) Power over volume flow
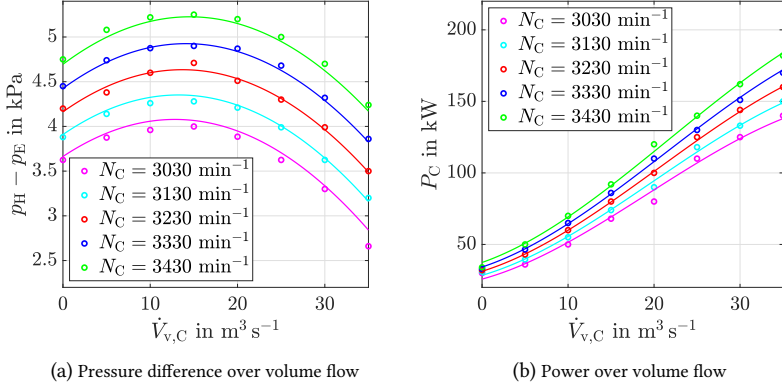
Figure 2.9: Comperessor map as fit of (2.47), (2.53) to data of the real-world map

Since the Compressor speed is measured by the variable frequency drive[13], (2.47) can be solved w.r.t. $\dot{V}_{\mathrm{v,C}}$ such that

$$\dot{V}_{\mathrm{v,C}}(t) = \left(\frac{p_{\mathrm{H}}(t) - p_{\mathrm{E}}(t)}{\varrho_{\mathrm{v,E}}(t)c} + \left(\frac{b^2 - 4ac}{4c^2} \right) N_{\mathrm{C}}^2(t) \right)^{1/2} - \frac{b}{2c} N_{\mathrm{C}}(t) \quad (2.49)$$

is obtained. However, note that (2.47) and (2.49) originate from the Compressor's steady-state behavior and are therefore limited w.r.t. modeling of dynamic behavior. Particularly during ramp-up and shut-down processes, there may be situations affecting negative values under the square root in (2.49). Thus, let us modify (2.49) as follows:

$$\dot{V}_{\mathrm{v,C}}(t) = \begin{cases} \underbrace{\left(\frac{p_{\mathrm{H}}(t) - p_{\mathrm{E}}(t)}{\varrho_{\mathrm{v,E}}(t)c} + \frac{b^2 - 4ac}{4c^2} N_{\mathrm{C}}^2(t) \right)^{1/2}}_{:=\alpha} - \frac{b}{2c} N_{\mathrm{C}}(t), & \alpha > 0, \\ -\frac{b}{2c} N_{\mathrm{C}}(t) & \alpha \leq 0, \end{cases}$$

$$(2.50)$$

---

[13] More precisely, the variable frequency drive measures the PI controller's signal $N_{\mathrm{C},d}$ which is converted into the actuated signal N_{C} via a slew rate limiter, see also Remark 2.8.

where $a, b > 0$ and $c < 0$. From the physical perspective, negative values of α in (2.50) correspond to operation below the Compressor's critical point $\dot{V}_{v,C} = -bN_C/(2c)$ which is not recommended. To avoid simulation breakdowns in such situations, (2.50) maps operation below the critical point to the latter.

With the assumption that vapor behaves like an ideal gas, the vapor mass flow is given by

$$\dot{m}_{v,C}(t) = \dot{V}_{v,C}(t)\varrho_{v,E}(t), \tag{2.51}$$

where

$$\varrho_{v,E}(t) = \frac{p_E(t)M_w}{\bar{R}\vartheta_E(t)}. \tag{2.52}$$

The second diagram of the Compressor map, see Fig. 2.9b, is modeled by

$$\frac{P_C(t)}{\varrho_{v,E}(t)} = dN_C^3(t) + eN_C^2(t)\dot{V}_{v,C}(t) + fN_C(t)\dot{V}_{v,C}^2(t) + g\dot{V}_{v,C}^3(t) \tag{2.53}$$

with the additional fitting coefficients $d, e, f > 0$, and $g < 0$.

Remark 2.8. On the one hand, in standard FFE plants, the Compressor speed is manipulated by a PI controller which outputs the desired signal $N_{C,d}$ (measured via the variable frequency drive) but, on the other, the corresponding actuator dynamics – a slew rate limiter – must additionally be considered. The latter is modeled by

$$\frac{\mathrm{d}}{\mathrm{d}t}N_C(t) = \begin{cases} \upsilon, & \text{if } N_{C,d}(t) > N_C(t), \\ -\upsilon, & \text{if } N_{C,d}(t) < N_C(t), \\ \text{sat}_\upsilon\left(\frac{\mathrm{d}}{\mathrm{d}t}N_{C,d}(t)\right), & \text{otherwise,} \end{cases} \tag{2.54}$$

where $\upsilon > 0$ denotes the slew rate limit and sat_υ symmetric saturation, i.e.,

$$\text{sat}_\upsilon(u) = \begin{cases} \upsilon, & \text{if } u > \upsilon, \\ -\upsilon, & \text{if } u < -\upsilon, \\ u, & \text{otherwise.} \end{cases}$$

Mass Balance

Since water is the only liquid in the Heat Chamber, the corresponding mass balance considers both, the vapor flows ($\dot{m}_{\mathrm{v,C}}$, $\dot{m}_{\mathrm{v,init}}$, $\dot{m}_{\mathrm{v,con}}$) and the condensate flow ($\dot{m}_{\mathrm{w}}$), which yields

$$\frac{\mathrm{d}}{\mathrm{d}t}\big(\underbrace{\varrho_{\mathrm{w,H}}(t)A(\bar{s}_{\mathrm{H}}(t))\ell_{\mathrm{T}}}_{=m_{\mathrm{w,H}}(t)}\big) = \dot{m}_{\mathrm{v,C}}(t) + \dot{m}_{\mathrm{v,init}}(t) - \dot{m}_{\mathrm{v,con}}(t) - \dot{m}_{\mathrm{w}}(t)$$

(2.55)

with

$$A(\bar{s}_{\mathrm{H}}(t)) = \pi\big(d_{\mathrm{T}} + \bar{s}_{\mathrm{H}}(t)\big)\bar{s}_{\mathrm{H}}(t)\sum_{j=1}^{4} n_{\mathrm{T},j}. \tag{2.56}$$

Substituting (2.56) into (2.55) and assuming that $(\mathrm{d}\varrho_{\mathrm{w,H}})/(\mathrm{d}t) \approx 0$ leads to

$$\frac{\mathrm{d}}{\mathrm{d}t}\bar{s}_{\mathrm{H}}(t) = \frac{\dot{m}_{\mathrm{v,C}}(t) + \dot{m}_{\mathrm{v,init}}(t) - \dot{m}_{\mathrm{v,con}}(t) - \dot{m}_{\mathrm{w}}(t)}{\varrho_{\mathrm{w,H}}(t)\pi\ell_{\mathrm{T}}\big(d_{\mathrm{T}} + 2\bar{s}_{\mathrm{H}}(t)\big)\sum\limits_{j=1}^{4} n_{\mathrm{T},j}}. \tag{2.57}$$

While the vapor flows $\dot{m}_{\mathrm{v,init}}$ and $\dot{m}_{\mathrm{v,con}}$ to control ϑ_{E} are modeled in Sec. 2.2.6, the vapor flow $\dot{m}_{\mathrm{v,C}}$ through the Compressor is known by (2.51). The derivation of the condensate flow $\dot{m}_{\mathrm{w}}$ leaving the Heat Chamber is based on [100] and leads to the following result:

$$\dot{m}_{\mathrm{w}}(t) = \frac{\pi\varrho_{\mathrm{w}}^2 g \sum\limits_{j=1}^{4} n_{\mathrm{T},j}}{8\eta_{\mathrm{w}}}\Big(4(r+s)^4\ln\tfrac{r+s}{r} + 4r^2(r+s)^2 - r^4 - 3(r+s)^4\Big),$$

(2.58)

where $\varrho_{\mathrm{w}} = \varrho_{\mathrm{w,H}}(t)$, $\eta_{\mathrm{w}} = \eta_{\mathrm{w,H}}(t)$, $r = d_{\mathrm{T}}/2$, and $s = \bar{s}_{\mathrm{H}}(t)$. Note that the derivation of (2.58) assumes steady flow and thus is – strictly speaking – not compatible with (2.57). However, since there is $(\mathrm{d}\bar{s}_{\mathrm{H}})/(\mathrm{d}t) \ll 1$, the error due to the noncompatibility of the assumptions in (2.57) and (2.58) is small.

Energy Balance

By considering the heat capacities of water and metal, the energy balance over the Heat Chamber leads to

$$\frac{\mathrm{d}}{\mathrm{d}t}\vartheta_{\mathrm{H}} = \frac{\dot{q}_{\mathrm{v,C}} + P_{\mathrm{C}} + \dot{q}_{\mathrm{v,init}} - \sum\limits_{j=1}^{4}\dot{q}_{\mathrm{T},j} - \dot{q}_{\mathrm{w}} - \dot{q}_{\mathrm{HA}} - \dot{q}_{\mathrm{v,con}} - \vartheta_{\mathrm{H}}\frac{\mathrm{d}m_{\mathrm{w,H}}}{\mathrm{d}t}c_{p,\mathrm{w,H}}}{m_{\mathrm{w,H}}c_{p,\mathrm{w}} + m_{\mathrm{met,H}}c_{p,\mathrm{met}}}, \tag{2.59}$$
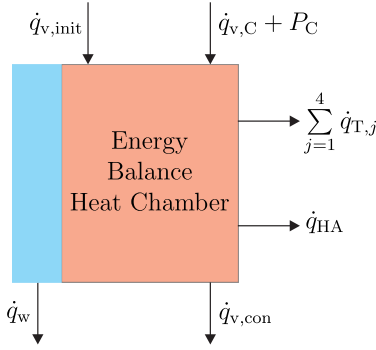
Figure 2.10: Energy balance over the Heat Chamber

where

$$\dot{q}_{\text{HA}}(t) = k_{\text{HA}} A_{\text{HA}} (\vartheta_{\text{H}}(t) - \vartheta_{\text{A}}), \tag{2.60a}$$

$$\dot{q}_{\text{w}}(t) = \dot{m}_{\text{w}}(t) c_{p,\text{w},\text{H}}(t) \vartheta_{\text{H}}(t), \tag{2.60b}$$

$$\dot{q}_{\text{v},\text{C}}(t) = \dot{m}_{\text{v},\text{C}}(t) \big(c_{p,\text{w},\text{E}}(t) \vartheta_{\text{E}}(t) + \Delta h_{v,\text{E}}(t) \big), \tag{2.60c}$$

$$\dot{q}_{\text{v},\text{con}}(t) = \dot{m}_{\text{v},\text{con}}(t) \big(c_{p,\text{w},\text{H}}(t) \vartheta_{\text{H}}(t) + \Delta h_{v,\text{H}}(t) \big), \tag{2.60d}$$

$$\dot{q}_{\text{v},\text{init}}(t) = \dot{m}_{\text{v},\text{init}}(t) \big(c_{p,\text{w},\text{H}}(t) \vartheta_{\text{H}}(t) + \Delta h_{v,\text{H}}(t) \big). \tag{2.60e}$$

Note that in (2.59), time dependencies are dropped[14] for the sake of compact notation.

Based on (2.1), the properties of water are

$$\varrho_{\text{w},\text{H}}(t) := \varrho(\vartheta_{\text{H}}(t), 0), \qquad \eta_{\text{w},\text{H}}(t) := \eta(\vartheta_{\text{H}}(t), 0),$$
$$c_{p,\text{w},\text{H}}(t) := c_{p,\text{w}}(\vartheta_{\text{H}}(t)), \quad \Delta h_{v,\text{H}}(t) := \Delta h_v(\vartheta_{\text{H}}(t)).$$

---

[14] Besides $m_{\text{met},\text{H}}$ and $c_{p,\text{met}}$, all quantities in (2.59) depend on time t.

2.2.6 Valves

To simulate the validation system as described in Sec. 2.4.1, two valves must be modeled: a valve to induce the live steam mass flow $\dot{m}_{\text{v,init}}$ and another valve to release the excess vapor mass flow $\dot{m}_{\text{v,con}}$. Since the positions of these valves are determined via split-range control, see Sec. 2.2.7, their models [10] convert the splitter outputs, namely the desired valve positions $\varphi_{11,d}$, $\varphi_{12,d} \in [0,1]$, into corresponding desired mass flows:

$$
\dot{m}_{\text{v,init},d} = 31.62
\begin{cases}
K_{v,1}(\varphi_{11,d})\left(\frac{v_{21}}{p_{11}-p_{12}}\right)^{-\frac{1}{2}}, & p_{12} > \frac{p_{11}}{2}, \\[2mm]
K_{v,1}(\varphi_{11,d})\left(\frac{2v_1^*}{p_{11}}\right)^{-\frac{1}{2}}, & p_{12} \leq \frac{p_{11}}{2},
\end{cases}
\tag{2.61a}
$$

$$
\dot{m}_{\text{v,con},d} = 31.62
\begin{cases}
K_{v,2}(\varphi_{12,d})\left(\frac{v_{22}}{p_{21}-p_{22}}\right)^{-\frac{1}{2}}, & p_{22} > \frac{p_{21}}{2}, \\[2mm]
K_{v,2}(\varphi_{12,d})\left(\frac{2v_2^*}{p_{21}}\right)^{-\frac{1}{2}}, & p_{22} \leq \frac{p_{21}}{2},
\end{cases}
\tag{2.61b}
$$

where the valve characteristics $K_{v,1}(\varphi_{11,d})$ and $K_{v,2}(\varphi_{12,d})$ are not further detailed to protect the reader from tedious technicalities. However, note that time dependencies are dropped in (2.61). The specific volumes $v_{2i} = v(p_{i2}, \vartheta_{i1})$ and $v_i^* = v(\frac{p_{i1}}{2}, \vartheta_{i1})$ with $i = 1, 2$ are calculated by the Matlab function *Xsteam.m*. In this context, p_{11} and ϑ_{11} denote the pressure and temperature in front of the live steam valve, and p_{12} and ϑ_{12} the pressure and temperature behind the live steam valve. Accordingly, p_{21} and ϑ_{21} are the pressure and temperature in front of the excess vapor valve, and p_{22} and ϑ_{22} the pressure and temperature behind the excess vapor valve.

The valve actuators are modeled by first-order low pass filters such that $\dot{m}_{\text{v,init}}$ and $\dot{m}_{\text{v,con}}$ are determined by

$$
\frac{\mathrm{d}}{\mathrm{d}t}\dot{m}_{\text{v,init}}(t) = \frac{1}{T_{\text{V},1}}\big(\dot{m}_{\text{v,init},d}(t) - \dot{m}_{\text{v,init}}(t)\big),
\tag{2.62a}
$$

$$
\frac{\mathrm{d}}{\mathrm{d}t}\dot{m}_{\text{v,con}}(t) = \frac{1}{T_{\text{V},2}}\big(\dot{m}_{\text{v,con},d}(t) - \dot{m}_{\text{v,con}}(t)\big).
\tag{2.62b}
$$

2.2.7 Controllers

In standard FFE plants, the following controllers are applied:

1. PI controller for setpoint control of the output density $\varrho_{o,R,4}$ via manipulation of the Compressor speed N_C.

2. PI plus split-range controller for setpoint control of the Effect temperature ϑ_E via manipulation of the live steam mass flow $\dot{m}_{v,init}$ and excess vapor mass flow $\dot{m}_{v,con}$, see Fig. 2.11 and Sec. 2.2.6.

3. PI controllers for setpoint control of the filling levels $h_{R,j}$ in the Reservoirs via manipulation of the corresponding output mass flows $\dot{m}_{o,R,j}$, see (2.41).
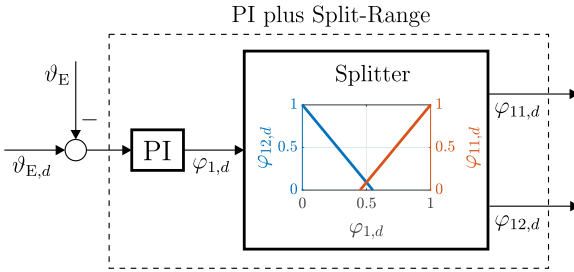
Figure 2.11: PI plus split-range controller

The PI controllers[15] are standard implementations and commonly equipped with anti-reset windup, cf. [80]. However, the PI plus split-range controller, see Item 2., requires some further explanation: As shown in Fig. 2.11, a PI controller generates the signal $\varphi_{1,d} \in [0,1]$, which is split into the live steam valve position $\varphi_{11,d} \in [0,1]$ and excess vapor valve position $\varphi_{12,d} \in [0,1]$ via the splitter characteristic

$$\varphi_{12,d} = -\frac{20}{11}\varphi_{1,d} + 1, \quad \varphi_{1,d} \in [0, 0.55], \tag{2.63a}$$

---

[15] All controller parameters were given by GEA Wiegand GmbH and relate to the FFE with project number 36004416, year 2015.

$$\varphi_{11,d} = \frac{20}{11}\varphi_{1,d} - \frac{9}{11}, \quad \varphi_{1,d} \in [0.45, 1]. \tag{2.63b}$$

The conversion of splitter outputs $\varphi_{11,d}$, $\varphi_{12,d}$ into vapor mass flows $\dot{m}_{\mathrm{v,init}}$, $\dot{m}_{\mathrm{v,con}}$ is treated in Sec. 2.2.6.

2.3 Implementation of the Plant Model
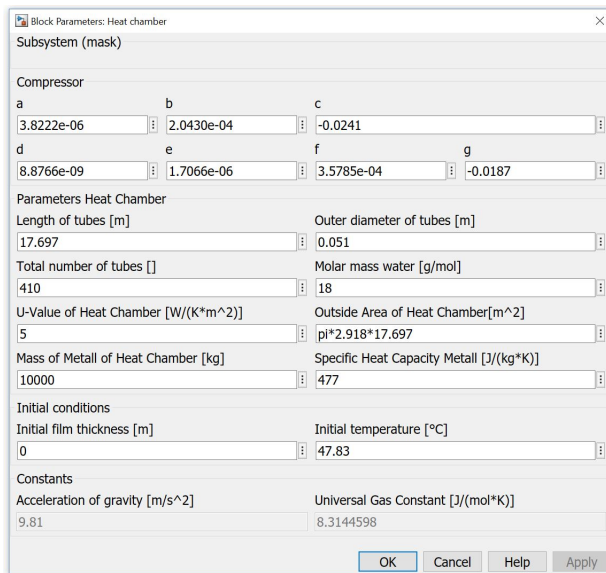
Figure 2.12: Simulink mask of a *Heat Chamber* module

In order to implement the subsystems from Sec. 2.2, Matlab/Simulink is used. An advantage of Simulink is to transfer the modular design of the mathematical model into a simulation model such that the corresponding parameters can be set via masks. Hence, masked modules for *Plate with Tubes*, *Energy Balance Effect*, *Heat Chamber*, *Reservoir*, and *Pipe* are developed. To give an example, Fig. 2.12 depicts the mask of the *Heat Chamber* module. Based on these modules, FFEs with arbitrary designs can be simulated in a simple manner. Note that the Plate and Tubes subsystems are combined under one mask,

43

since all Plate outputs only affect the downstream Tubes and the number of Plates corresponds to the number of passes. Additionally, the energy balance of the Effect is implemented as extra module, since it gets inputs from each pass.

As an FFE with four passes is considered, the plant model[16] consists of four *Plate with Tubes* modules, see (2.3)–(2.34), and four *Reservoir* modules, see (2.40)–(2.42). Despite the fourth *Reservoir* module, the first three ones are each connected by a *Pipe* module, see (2.43)–(2.46). Furthermore, there is one *Energy Balance Effect* module, see (2.35)–(2.39), and one *Heat Chamber* module, see (2.47)–(2.60).

2.4 Validation

In this section, the plant model is validated to obtain a digital twin. As not all actuator signals are measured, parts of the closed-loop system must be reconstructed. Therefore, the validation system is a combination of the open-loop and closed-loop system, which is detailed in Sec. 2.4.1. Corresponding results are shown in Sec. 2.4.2 and discussed in Sec. 2.4.3.

2.4.1 Validation System

The validation is performed via process data of the FFE sketched in Fig. 2.1. Relevant scenarios, namely **ramp-up** and **stationary operation**, are considered by comparing the measured signals being

(a) the Effect temperature ϑ_{E},

(b) Heat Chamber temperature ϑ_{H},

(c) outputs mass flow $\dot{m}_{o,\mathrm{R},4}$, and

(d) outputs density $\varrho_{o,\mathrm{R},4}$

---

[16] All model parameters were given by GEA Wiegand GmbH and relate to the FFE with project number 36004416, year 2015.

to the corresponding modeled ones which are marked by $\hat{(\cdot)}$. For this purpose, the plant's input signals, namely,

(i) the input density $\varrho_{i,\mathrm{P},1}$ (measured),

(ii) input mass flow $\dot{m}_{i,\mathrm{P},1}$ (measured),

(iii) input product temperature $\vartheta_{i,\mathrm{P},1}$ (measured),

(iv) Compressor speed N_{C} (not directly measured),

(v) live steam mass flow $\dot{m}_{\mathrm{v,init}}$ (not measured), and

(vi) excess vapor mass flow $\dot{m}_{\mathrm{v,con}}$ (not measured)

should be known. While the Inputs (i)–(iii) are known via measurements, the Inputs (iv)–(vi) must be modeled and thus are marked by $\hat{(\cdot)}$, which is illustrated in Fig. 2.13. As explained in Sec. 2.2.7, the output density $\varrho_{o,\mathrm{R},4}$ is controlled via Compressor speed N_{C}. Since the corresponding controller signal $N_{\mathrm{C},d}$ is measured by the variable frequency drive, the actuated signal $\hat{N}_{\mathrm{C}}$ is modeled by considering the dynamics of the slew rate limiter, see (2.54). However, no measurements of the vapor flows $\dot{m}_{\mathrm{v,init}}$ and $\dot{m}_{\mathrm{v,con}}$ are available. As the latter represent the actuated variables of the ϑ_{E}-loop, see Sec. 2.2.7, the corresponding closed-loop system is reconstructed.
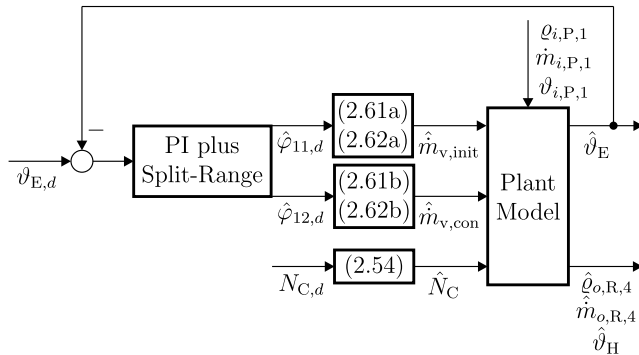
Figure 2.13: Validation system

2.4.2 Results

(a) Input mass flow

(b) Compressor speed

(c) Input temperature

(d) Vapor mass flows
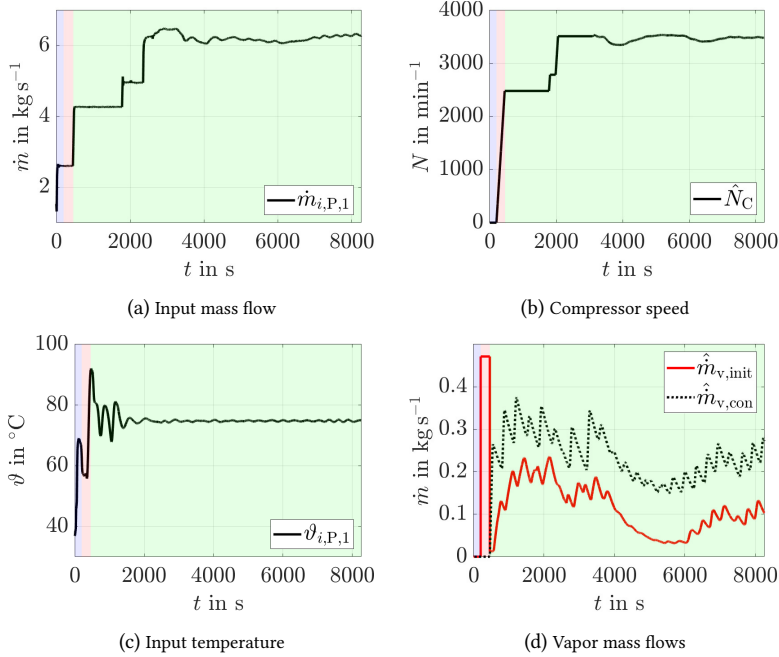
Figure 2.14: Inputs of the plant model

As being interested in the validation of the dynamic behavior, let us consider the following scenario which includes ramp-up and stationary operation:

1. $t \in [0, 200]$ s: Water enters Plate 1 and flows through all passes for cleaning purposes (blue).

2. $t \in (200, 460]$ s: The live steam valve is fully opened such that $\dot{m}_{v,init}$ is induced into the Heat Chamber. Additionally, the Compressor is ramped up (red).

3. $t \in (460, 8260]$ s: The Effect temperature control loop is active. Instead of water, product enters the FFE at $t = 2000$ s (green).

Firstly, note that the colors inside the parenthesis of Items 1. to 3. refer to the background colors in Fig. 2.14, which depicts the inputs of the plant model, and Fig. 2.15, which shows the results. Secondly, note that variables marked by $\hat{(\cdot)}$ are modeled outputs, otherwise the variable is measured.

(a) Effect temperature

(b) Heat Chamber temperature

(c) Output mass flow

(d) Input and output density
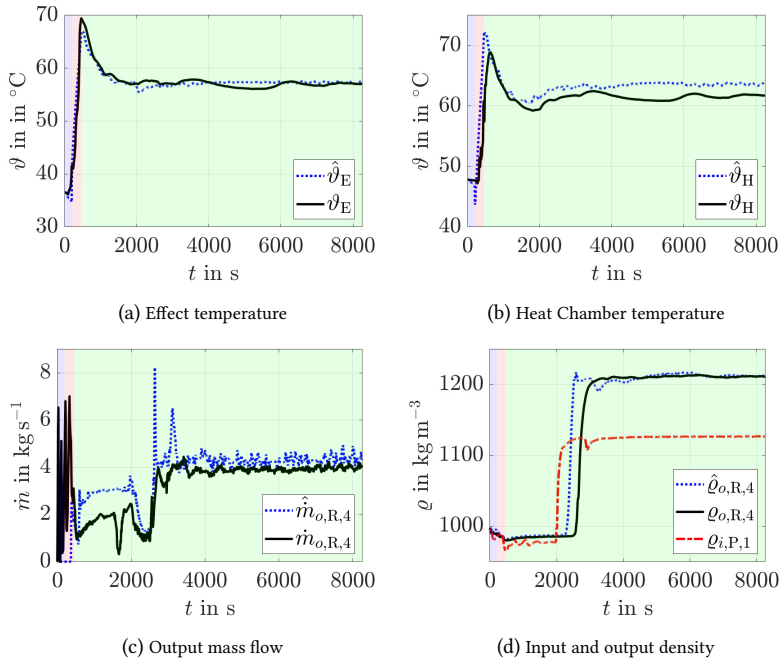
Figure 2.15: Validation of the plant model

2.4.3 Discussion

In Fig. 2.15a, it is observed that the measured temperature ϑ_{E} is well mapped by the modeled one $\hat{\vartheta}_{\mathrm{E}}$. Nonetheless, some discussions regarding temperature ϑ_{H}, see Fig. 2.15b, mass flow $\dot{m}_{o,\mathrm{R},4}$, see Fig. 2.15c, and density $\varrho_{o,\mathrm{R},4}$, see Fig. 2.15d, are required:

– Figure 2.15b: The deviation between modeled $\hat{\vartheta}_{\mathrm{H}}$ and measured ϑ_{H} is acceptably small since the temperature measurement is inaccurate and includes an uncertainty of approximately 1°C. Therefore, a general recommendation is to use the measurement of pressure p_{E} for the purpose of control as the former is more accurate than the measurement of ϑ_{E}.

– Figure 2.15c: During $t \in [0, 2000)$ s, the FFE is flooded by water for cleaning purposes. To keep the model as simple as possible, constant k-values (heat transfer coefficients) are applied and valid for the considered product, namely milk, but not for water. This fact explains the deviation between the measurement $\dot{m}_{o,\mathrm{R},4}$ and model $\hat{\dot{m}}_{o,\mathrm{R},4}$ observed during $t \in [0, 2000)$ s. However, the cleaning of the FFE is neither interesting from the control engineering perspective nor from the process engineering perspective. Thus, the observed deviation is acceptable. When product instead of water is applied during $t \in [2000, 8260]$ s, the modeled output $\hat{\dot{m}}_{o,\mathrm{R},4}$ exhibits wiggles that are not apparent in the corresponding measurement $\dot{m}_{o,\mathrm{R},4}$. This drawback is caused by the Discrete Conveyor Model introduced in Sec. 2.2.2. Although there is some kind of diffusion modeled via ξ, see (2.21), (2.29), there is still a lack of diffusion, which affects wiggles in the modeled output $\hat{\dot{m}}_{o,\mathrm{R},4}$. Additionally, it is difficult to use the Discrete Conveyor Model for control design or for further analyses. Hence, a "continuous version" of the Discrete Conveyor Model may mitigate these drawbacks. Moreover, note that there are also large wiggles in the measurement $\dot{m}_{o,\mathrm{R},4}$ during $t \in [0, 400]$ s. The reason for these wiggles is that the measurement device, a Coriolis flow meter, outputs a noise-corrupted signal when the actual output mass flow is approximately zero. Finally, observe that there is a small stationary deviation between $\dot{m}_{o,\mathrm{R},4}$ and $\hat{\dot{m}}_{o,\mathrm{R},4}$ during $t \in [2800, 8260]$ s. In this context, possible culprits are a small sensor bias and/or a small error of (2.1a) that relates w and ϱ; recall that model-internal masses and mass flows are basically determined by w, see (2.11) and (2.12). Nevertheless, this stationary deviation is such small that it is not of practical relevance.

– Figure 2.15d: Both, a delay-mismatch and a diffusion-mismatch, are observed. The latter may also be resolved by developing a continuous

version of the Discrete Conveyor Model. Regarding the delay-mismatch, there exist the following possibilities:

(A) Relation (2.14) underestimates the true delay of product in Tubes.

(B) Relation (2.44) underestimates the true delay of product in Pipes.

(C) There are additional unmodeled sources of delays. Especially, the assumption of perfect mixing in the Reservoir is debatable.

In the sequel, new Tube models are developed in Ch. 3 to mitigate the aforementioned drawbacks of the Discrete Conveyor Model. Moreover, a chosen new Tube model is identified and experimentally proven via pilot plant experiments, see Ch. 4. Thereby, resolving the problem of diffusion-mismatch is enabled. Additionally, deeper insights regarding the encountered sources for the delay-mismatch are obtained, see Items (A)–(C). In particular, the time delay of product in Tubes, see Item (A), is analyzed in detail.

2.5 Takeaways

Let us summarize the main results and highlights of this chapter:

– By decomposing the FFE into relevant subsystems, a large variety of different FFE designs and products can be modeled in a simple manner.

– As all subsystems are implemented under Simulink masks, the user is able to create complex FFE designs by only setting the masks' parameters and connecting inputs/outputs.

– To model overtaking of liquid particles, the Discrete Overtaking Conveyor Model is proposed.

– The validation shows that the plant model can be considered as digital twin.

3 New Models for Evaporating Liquid Films

Based on the physical conservation laws, new models of evaporating liquid films in Tubes are presented in this chapter. From the mathematical perspective, the derivation of these models yields systems of partial differential equations (PDEs) with boundary inputs and outputs. Since the PDEs are hyperbolic[1], the method of characteristics [32, 117] is applied to obtain corresponding time-delay relations. Although this chapter focuses on the transport of evaporating liquid films, the presented models may also be applied to other transport processes, e.g., in traffic flow [34, 28, 148], which is motivated via analogies.

Commonly, the evaporating mass flow is assumed to be uniformly distributed along the Tubes [141, 102, 107, 127]. However, in the present chapter, the plan is to develop models where evaporation is either proportional to the water content at any given point in the Tubes or localized to a single liquid element. Methodologically, models described by first-order quasilinear PDEs are preferred so that, after transformation into time-delay equations, the models represented by distributed delay equations are of special interest. The latter come up as equivalent i/o relations of the transport processes that are internally governed by the PDEs. Compared to PDEs, time-delay equations have the following advantages:

- They are easier to implement in complex process simulations.

- Delay elements are available in many simulation environments.

Parts of this chapter are reproduced from [155, 160].
[1] The definition of a hyperbolic PDE is, e.g., given in [32].

To develop the new models, let us proceed as follows. In Sec. 3.1, the observed input-output (i/o) behavior of evaporating liquid film in Tubes is qualitatively described. Subsequently, the two flow models, namely, Dynamic Plug Flow (DPF), see Sec. 3.2, and Overtaking Particle Flow (OPF), see Sec. 3.3, are introduced via their corresponding PDEs, where the sink terms for evaporation are, at first, not specified. However, in Sec. 3.4, models to consider evaporation are described so that technically useful combinations of flow and evaporation models are detailed in Sec. 3.5. Finally, based on the simulations in Sec. 3.6, the ability of these models to map the observed i/o behavior is evaluated.

Those readers, who are only interested in the models' behavior but not in the corresponding time-delay equations or further details, can skip Sections 3.2.2 and 3.2.3, Sections 3.3.2 and 3.3.3, and Section 3.5.

3.1 Preliminaries and Qualitative I/O Behavior

Let us focus on the dynamic behavior of evaporating liquid film in an FFE pass, which consists of serially connected Plate and Tubes[2], see Fig. 3.1. Since the Plate model is already detailed in Sec. 2.2.1 and not relevant w.r.t. the delay behavior, special attention is paid to the liquid transport in Tubes and evaporation modeling therein.
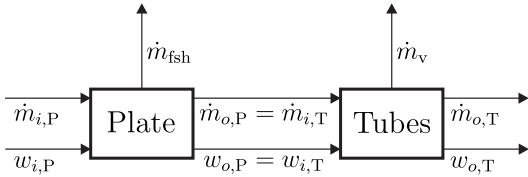
Figure 3.1: Flow diagram of an FFE pass

---

[2] A standalone consideration of only the Tubes' i/o behavior is technically not feasible because Plate and Tubes are always constructed as a single (combined) unit. However, the Reservoir does not need to be considered and is therefore excluded from the definition of an FFE pass in this chapter.

To this end, a relation for the average velocity $\bar{c}_{i,\mathrm{T}}$ at the Tubes' inputs is additionally needed. Therefore, let us recall (2.14) such that

$$\bar{c}_{i,\mathrm{T}}(t) := \frac{\ell_{\mathrm{T}}}{\tau_{\mathrm{T}}(t)} = \frac{\dot{m}_{i,\mathrm{T}}(t)}{n_{\mathrm{T}}\pi\big(d_{\mathrm{T}} - \bar{s}_{\mathrm{T}}(t)\big)\bar{s}_{\mathrm{T}}(t)\varrho_{i,\mathrm{T}}(t)} \tag{3.1}$$

can be introduced, where the average film thickness $\bar{s}_{\mathrm{T}}$ is determined by (2.15), (2.16).

(a) Qualitative behavior

(b) Data from an experiment with water
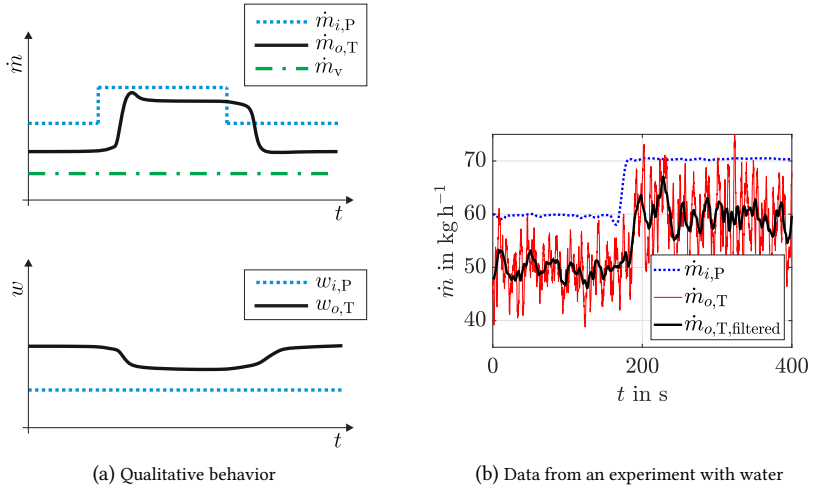
Figure 3.2: Input-output behavior of an FFE pass

To assess the quality of the new models, let us compare them qualitatively to the i/o behavior of an FFE pass which is observed in practice. The behavior is shown in Fig. 3.2a where changes in the output mass flow and dry matter content are shown in response to an up/down-step in the input mass flow, while evaporation mass flow and input dry matter content are kept constant. In case of an up-step, a delay in the response of the output mass flow with some overshoot is expected. In case of a down-step, there is also a delayed response. The overshoot is caused by wave-like effects [14, 4] and rather observed in the microscopical behavior. Regarding the dry matter content, the delay is similar to that of the output mass flow. Since larger input mass flow causes larger transport velocity and shorter residence of the liquid inside

53

the Tubes, it leads to less evaporation which can be concluded from both, the mass flow and dry matter content plots.

To justify the qualitative i/o behavior in Fig. 3.2a, let us present data from an up-step experiment in a one-Tube pilot plant with water and constant evaporation, see Fig. 3.2b. As no direct measurement of $\dot{m}_{o,T}$ is available, it is calculated via numerical differentiation of the water level in the Reservoir after the Tube and, to this end, basic moving average filter is used. In this experiment, both phenomena are observed: the delayed response and the overshoot. A detailed study with viscous product including identification and experimental proof of a certain model is presented in Ch. 4.

3.2 Dynamic Plug Flow

(a) $t = t_1$: Red plug appears at the input boundary ($x = 0$) with velocity $c(t_1, 0)$ and starts moving uniformly

(b) $t = t_2$: Blue plug follows with velocity $c(t_2, 0)$ while the red one has reached position x, keeping constant speed $c(t_1, 0)$

(c) Illustration of the FIFO principle: the fast (red) plug follows the slow (blue) one but cannot overtake it
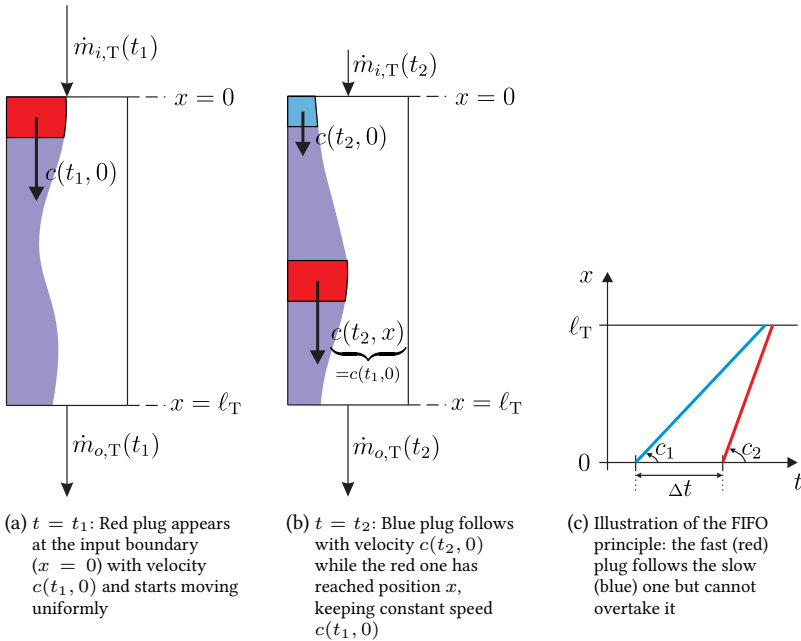
Figure 3.3: Sketches of DPF

Figures 3.3a and 3.3b serve as a kinematic diagram of the Dynamic Plug Flow (DPF) model. For convenience, water/dry content separation and evaporation is disregarded as well as only a single Tube of length ℓ_T is considered in Fig. 3.3. The model is based on the following assumptions:

1. Particles entering the Tube at time t achieve the same velocity $\bar{c}_{i,\mathrm{T}}(t)$ and move together, forming a plug. Function $\bar{c}_{i,\mathrm{T}}(t)$ is continuously differentiable.

2. Plugs may have different velocities, but the velocity of a single plug stays constant during its travel along the Tube.

3. Plugs cannot overtake each other, i.e., the first-in-first-out (FIFO) principle holds.

4. Plugs consist of separated, noninteracting parts: water and dry matter.

5. The flow is one-dimensional in space x.

6. There are neither internal nor external forces acting on the plugs.

7. The infinitesimal vapor mass flow $\dot{\mu}_\mathrm{v}(t, x)\,\mathrm{d}x$ evaporates from the water part of the plug at point x and time t. Thus, $\dot{\mu}_\mathrm{v}(t, x)$ is the linear density of the vapor mass flow distribution along the Tube. The SI unit of $\dot{\mu}_\mathrm{v}$ is $\mathrm{kg\,s^{-1}\,m^{-1}}$.

Assumptions 2. and 3. are common in the plug flow theory but may sound contradictory to the unfamiliar reader. To resolve this apparent contradiction, a simple thought experiment is presented in Remark 3.1.

Remark 3.1. Consider two plugs moving through the Tube as represented by Fig. 3.3c: Some time Δt after plug 1 entered the Tube with velocity c_1, plug 2 follows with higher velocity c_2. When plug 2 enters, plug 1 has already moved the distance $\Delta x_1 = c_1\,\Delta t$. Because of the head start, it is possible that plug 2 will not catch up with plug 1 during their travel through the Tube. To this end, the condition

$$\frac{\ell_\mathrm{T} - \Delta x_1}{c_1} < \frac{\ell_\mathrm{T}}{c_2}$$

should be satisfied. Substituting $\Delta x_1 = c_1 \Delta t$ and rearranging the terms yields

$$\frac{c_2 - c_1}{\Delta t} < \frac{c_1 \, c_2}{\ell_T}.$$

Taking the limit $\Delta t \to 0$, as continuous flow requires, leads to the restriction on the rate of change of the input flow velocity

$$\dot{c}(t) < \frac{c^2(t)}{\ell_T},$$

which is the same as (3.5) formally deduced in Sec. 3.2.2. The meaning of this condition is that the velocity of the incoming plugs should not increase too rapidly.

3.2.1 PDE Model

In order to obtain the PDEs of DPF, let us consider the Tube of length ℓ_T and introduce the spatial variable x measured along the Tube with $x = 0$ being the inlet and $x = \ell_T$ the outlet. The state variables $\xi_w(t, x)$ and $\xi_d(t, x)$ denote the linear density in $\mathrm{kg\,m^{-1}}$ of water and dry content, respectively, over all n_T Tubes of one pass (all Tubes behave exactly similarly). Moreover, $c(t, x)$ denotes the flow velocity at a given point.

The PDEs are derived from the mass balance and, because plugs may have different velocities (Assumption 2.), momentum balance. Thus, the following model is built, where $x \in [0, \ell_T]$, $t \geq t_0$:

$$\frac{\partial \xi_w(t, x)}{\partial t} + c(t, x)\frac{\partial \xi_w(t, x)}{\partial x} + \xi_w(t, x)\frac{\partial c(t, x)}{\partial x} = -\dot{\mu}_v(t, x), \quad \text{(3.2a)}$$

$$\text{IC: } \xi_w(t_0, x) = \xi_{w,0}(x),$$

$$\text{BC: } \xi_w(t, 0) = \frac{\dot{m}_{i,T}(t)\big(1 - w_{i,T}(t)\big)}{c(t, 0)},$$

$$\frac{\partial \xi_d(t, x)}{\partial t} + c(t, x)\frac{\partial \xi_d(t, x)}{\partial x} + \xi_d(t, x)\frac{\partial c(t, x)}{\partial x} = 0, \quad \text{(3.2b)}$$

$$\text{IC: } \xi_d(t_0, x) = \xi_{d,0}(x),$$

$$\text{BC: } \xi_{\mathrm{d}}(t,0) = \frac{\dot{m}_{i,\mathrm{T}}(t)w_{i,\mathrm{T}}(t)}{c(t,0)},$$

$$\frac{\partial c(t,x)}{\partial t} + c(t,x)\frac{\partial c(t,x)}{\partial x} = 0, \tag{3.2c}$$

$$\text{IC: } c(t_0,x) = c_0(x),$$

$$\text{BC: } c(t,0) = \bar{c}_{i,\mathrm{T}}(t),$$

$$\text{Output 1: } \dot{m}_{o,\mathrm{T}}(t) = \big(\xi_{\mathrm{w}}(t,\ell_{\mathrm{T}}) + \xi_{\mathrm{d}}(t,\ell_{\mathrm{T}})\big)c(t,\ell_{\mathrm{T}}),$$

$$\text{Output 2: } w_{o,\mathrm{T}}(t) = \frac{\xi_{\mathrm{d}}(t,\ell_{\mathrm{T}})}{\xi_{\mathrm{w}}(t,\ell_{\mathrm{T}}) + \xi_{\mathrm{d}}(t,\ell_{\mathrm{T}})}.$$

The mass balances for water and dry matter content yield (3.2a) and (3.2b); recall that $\dot{\mu}_{\mathrm{v}}(t,x)\,\mathrm{d}x$ denotes the infinitesimal evaporation mass flow from point x at time t. By assuming one-dimensional flow and neglecting interaction between the plugs as well as external forces (Assumption 5. and 6.), the momentum balance simplifies to (3.2c). The PDEs are equipped with initial conditions (ICs), boundary conditions (BCs) defined by the mass flow and dry mass content on the input boundary $x = 0$, and output values for mass flow and dry matter content taken at the output boundary $x = \ell_{\mathrm{T}}$.

Observe that (3.2c) is the inviscid Burger's equation [105, 117]. The solution of this equation may include singularities, so-called shock waves, that occur at the intersections of characteristics and must be treated as generalized solutions. Studying shock waves is not of the author's interest because they cannot physically appear in the real FFE due to the rather moderate and smooth nature of the falling film. Speaking about reality, the liquid flow always exhibits some diffusion, which can be modeled by adding the second-order term $D_f \frac{\partial^2 c(t,x)}{\partial x^2}$ to the right-hand side of (3.2c). The diffusion inhibits the formation of shock waves. However, adding it would be a divergence from the original plan of focusing on first-order PDEs and would make it impossible to obtain a time-delay representation of the i/o dynamics. Therefore, another way of avoiding the shock waves is chosen, namely, to exclude them by enforcing a constraint on the rate of change of the input flow velocity. This constraint, see (3.5), is specified in Sec. 3.2.2.

The general aim is to convert the PDE model (3.2) to the time-delay form by solving it via the method of characteristics. To this end, assumptions re-

garding the evaporation term $\dot{\mu}_{\mathrm{v}}$ are necessary and introduced in Sec. 3.4. Therefore, in Sections 3.5.1 and 3.5.2, uniform evaporation and evaporation proportional to the water content are specified for DPF.

3.2.2 Constraints on the Input Velocity

The PDE model (3.2) does not explicitly reflect Assumption 3. Hence, the question is, which conditions the initial profile $c_0(x)$ and the input velocity $\bar{c}_{i,\mathrm{T}}(t)$ should fulfill to satisfy Assumption 3. To this end, let us specify the following three conditions:

The first one is the matching condition

$$c_0(0) = \bar{c}_{i,\mathrm{T}}(t_0), \tag{3.3}$$

which ensures a continuous velocity profile $c(t, x)$ w.r.t. x.

The other two conditions[3] follow from the requirement that the output mass flow should be positive and finite. This requirement is satisfied if the denominators of (A.13a) and (3.39a) – similarly, (A.21a) and (3.48a) – are strictly positive. In view of (A.9), (A.8d), and (3.40), (3.41), this leads to the conditions

$$\frac{\mathrm{d}c_0(x)}{\mathrm{d}x} > \frac{c_0(x)}{x - \ell_{\mathrm{T}}}, \quad \forall x \in [0, \ell_{\mathrm{T}}) \tag{3.4}$$

and

$$\dot{\bar{c}}_{i,\mathrm{T}}(t) < \frac{\bar{c}_{i,\mathrm{T}}^{\,2}(t)}{\ell_{\mathrm{T}}}, \quad \forall t \geq t_0. \tag{3.5}$$

Constraint (3.4) ensures that the plugs from the initial profile do not overtake each other, whereas (3.5) guarantees the same about the plugs coming from the input mass flow.

Remark 3.2. The requirement that the output mass flow should be finite is equivalent to the "no overtaking" requirement of Assumption 3. In a nutshell,

---

[3] Although these conditions are based on the time-delay equations of DPF, see Sections 3.5.1 and 3.5.2, they do not depend on evaporation. Therefore, the reader can set $\dot{m}_{\mathrm{v}} \equiv 0$ when reading the equations of Sections 3.5.1 and 3.5.2 in the context of Sec. 3.2.2.

infinite output mass flow is caused by many infinitesimal plugs arriving at the output boundary simultaneously, integrating into infinite mass flow. This is the manifestation of overtaking or, rather, of its critical case of "catching up" which, however, always accompanies overtaking due to the continuity of the flow.

3.2.3 Constraints on the Input Mass Flow

In view of (3.1), recall that the flow velocity $\bar{c}_{i,\mathrm{T}}$ at the inlet of the Tubes depends on the mass flow $\dot{m}_{i,\mathrm{T}}$ into the Tubes which, according to Fig. 3.1, is the same as the mass flow $\dot{m}_{o,\mathrm{P}}$ out of the Plate. In this context, note that $\dot{m}_{o,\mathrm{P}}$ is the output of the dynamical system (2.3)–(2.8) whose input is the mass flow $\dot{m}_{i,\mathrm{P}}$ into the Plate. As $\dot{m}_{i,\mathrm{P}}$ is a manipulated variable, see Ch. 5, it is of interest to deduce constraints on $\dot{m}_{i,\mathrm{P}}$ that guarantee satisfaction of the constraints on $\bar{c}_{i,\mathrm{T}}$ developed in Sec. 3.2.2.

In the sequel, such constraints regarding steps of $\dot{m}_{i,\mathrm{P}}$ are presented. Since $\dot{m}_{\mathrm{fsh}} \ll \dot{m}_{i,\mathrm{P}}$, flash evaporation can be neglected, i.e., $\dot{m}_{\mathrm{fsh}} \approx 0$ is assumed in this discussion. Additionally, let us assume that $(\mathrm{d}\varrho_{i,\mathrm{P}}(t))/(\mathrm{d}t) \approx 0$ as already done in Sec. 2.2. Then, the i/o behavior of the Plate model (2.3)–(2.8) is condensed to

$$\frac{\mathrm{d}}{\mathrm{d}t}\dot{m}_{o,\mathrm{P}}(t) = \frac{g\varrho_{i,\mathrm{P}}(t)\bar{A}^2}{\dot{m}_{o,\mathrm{P}}(t)A_\mathrm{P}}\big(\dot{m}_{i,\mathrm{P}}(t) - \dot{m}_{o,\mathrm{P}}(t)\big). \tag{3.6}$$

By inserting (2.15), (2.16) into (3.1) and taking into account that $\dot{m}_{i,\mathrm{T}} = \dot{m}_{o,\mathrm{P}}$, it follows that

$$\bar{c}_{i,\mathrm{T}} = \bar{c}_{i,\mathrm{T}}(\dot{m}_{o,\mathrm{P}}) = \frac{\dot{m}_{o,\mathrm{P}}^{2/3}}{\varrho_{i,\mathrm{T}}\pi v_1\big(d_\mathrm{T} - v_1\dot{m}_{o,\mathrm{P}}^{1/3}\big)}, \tag{3.7}$$

where

$$v_1 = \left(\frac{3\eta_{i,\mathrm{T}}}{g\varrho_{i,\mathrm{T}}^2\pi d_\mathrm{T} n_\mathrm{T}}\right)^{1/3}. \tag{3.8}$$

Due to neglected flash evaporation, it can be assumed that $\varrho_{i,\mathrm{P}} \approx \varrho_{i,\mathrm{T}}$ and thus

$$\dot{\bar{c}}_{i,\mathrm{T}} = \frac{\mathrm{d}\bar{c}_{i,\mathrm{T}}}{\mathrm{d}\dot{m}_{o,\mathrm{P}}} \frac{\mathrm{d}\dot{m}_{o,\mathrm{P}}}{\mathrm{d}t} \overset{(3.6)}{=} \frac{2 v_2 \left(\dot{m}_{i,\mathrm{P}} - \dot{m}_{o,\mathrm{P}}\right) \left(d_{\mathrm{T}} - \frac{1}{2} v_1 \sqrt[3]{\dot{m}_{o,\mathrm{P}}}\right)}{3 \dot{m}_{o,\mathrm{P}}^{4/3} \varrho_{i,\mathrm{P}} \pi v_1 \left(d_{\mathrm{T}} - v_1 \sqrt[3]{\dot{m}_{o,\mathrm{P}}}\right)^2} \quad (3.9)$$

with

$$v_2 = \frac{g \varrho_{i,\mathrm{P}} \bar{A}^2}{A_{\mathrm{P}}}. \quad (3.10)$$

Note that, for conciseness, time dependencies are dropped in (3.7)–(3.10). Substituting (3.7) and (3.9) into (3.5) yields

$$\dot{m}_{i,\mathrm{P}}(t) - \dot{m}_{o,\mathrm{P}}(t) < \frac{3 \dot{m}_{o,\mathrm{P}}^{3/8}(t)}{2 \ell_{\mathrm{T}} \varrho_{i,\mathrm{P}}(t) \pi v_1(t) v_2(t) \left(d_{\mathrm{T}} - \dfrac{v_1(t) \dot{m}_{o,\mathrm{P}}^{1/3}(t)}{2}\right)}. \quad (3.11)$$

The right-hand side of (3.11) is the maximal admissible up-step of $\dot{m}_{i,\mathrm{P}}$ since the up-step is measured w.r.t. the current value of $\dot{m}_{o,\mathrm{P}}$. Furthermore, note that down-steps are not limited because they can only decrease the flow velocity which does not cause shock waves and cannot violate (3.5).

Based on the data from [161], the conclusion is that condition (3.11) is satisfied in the practice. The minimum stationary product mass flow out of the Plate is $\dot{m}_{o,\mathrm{P,min}} = 5\,\mathrm{kg\,s^{-1}}$ which, together with Table 3.2 and (3.11), leads to

$$\dot{m}_{i,\mathrm{P}}(t) - \dot{m}_{o,\mathrm{P}}(t) < 15.07\,\mathrm{kg\,s^{-1}}.$$

Hence, stepwise increases in $\dot{m}_{i,\mathrm{P}}$ that are less than $15.07\,\mathrm{kg\,s^{-1}}$ are allowed by the DPF model. Due to limitations of the actuator (pump), changes w.r.t. the operation point will never be larger than 30%. As the maximum stationary product mass flow out of the Plate $\dot{m}_{o,\mathrm{P,max}} = 6.6\,\mathrm{kg\,s^{-1}}$ yields a maximum step size of $2\,\mathrm{kg\,s^{-1}}$, it is ensured that (3.11) holds for the investigated process. Moreover, pure steps cannot be realized by the actuator, i.e., steps requested by the controller/operator will be smoothed in practice, which relaxes (3.11) even more.

However, if the velocity restrictions should be violated in other process configurations with other liquids, a model allowing overtaking is required. Therefore, in the following section, such a model is introduced.

3.3 Overtaking Particle Flow

To enable overtaking of particles, let us consider noninteracting particles moving in a two-dimensional space just like cars on a highway driving down parallel lanes, see Fig. 3.4. Instead of a few lanes, however, there is a continuum, i.e., the "lanes" are assigned specific velocities to them, ranging continuously from $c_{\min}$ to $c_{\max}$. In other words, the original spatial domain $[0, \ell_{\mathrm{T}}]$ is extended by adding the second coordinate $c \in [c_{\min}, c_{\max}]$. All particles having coordinate c move along the x-axis with the same velocity c. As they are restricted to a separate lane, they can overtake neighboring particles on the slower lanes[4], hence the name Overtaking Particle Flow (OPF).

The input boundary $x = 0$ is populated with particles of the input mass flow according to some velocity distribution function, which is generally time-varying and further detailed in Sec. 3.3.2. For instance, it is reasonable to suppose that a higher mass flow means predominantly faster particles which is represented by a distribution centered around a higher value of c. Accordingly, Fig. 3.4 shows the scenario when at time t_0 the input mass flow $\dot{m}_{i,\mathrm{T}}(t_0)$ is small. Its particles, colored blue, are assigned slower lanes, although some of them are a little faster than others. Later, at time t_1, the blue particles have moved some distance towards the output. Meanwhile, the input flow has increased and the new particles, colored red, are starting on the faster lanes. At time t_2, the fast particles have overtaken the slow ones and arrive at the output first, so that they appear in the output mass flow.

To consider evaporation, the mass flow is split into two parallel flows: one for dry matter and another for water. Both flows gain the same velocities on the input boundary. The only difference is that the water flow experiences evaporation.

---

[4] Of course, the lane itself cannot be slower but the particles on it have a smaller velocity.

(a) $t = t_0$ (b) $t = t_1$ (c) $t = t_2$
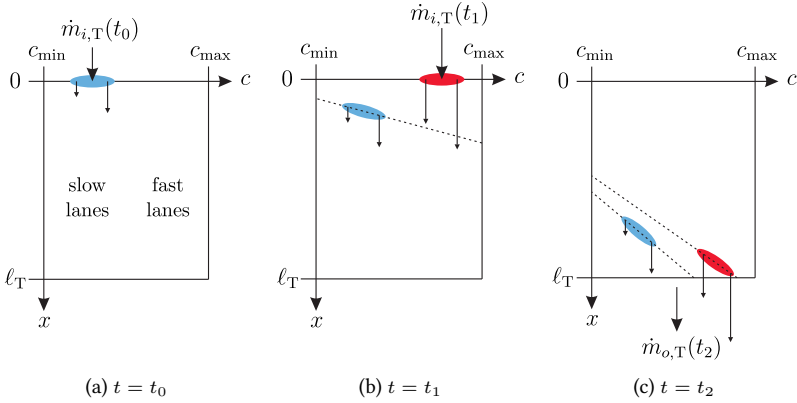
Figure 3.4: Sketches of OPF

3.3.1 PDE Model

Let us denote $\xi_{\mathrm{w}}(t, x, c)$ and $\xi_{\mathrm{d}}(t, x, c)$ the state of, respectively, water and dry matter flows. The value of $\xi_{\mathrm{w}}(t, x, c)$ represents the areal density of water in the point (x, c) at time t; analogously $\xi_{\mathrm{d}}(t, x, c)$ for dry matter. Areal density over the extended spatial domain $[0, \ell_{\mathrm{T}}] \times [c_{\min}, c_{\max}]$ is understood as "mass divided by length and by velocity". The SI unit of ξ_{w} and ξ_{d} is thus $\mathrm{kg\,s\,m}^{-2}$.

To develop the PDE description of OPF with evaporation, let us make the following assumptions:

1. The distribution of the input mass flow $\dot{m}_{i,\mathrm{T}}(t)$ along the input boundary $x = 0$ is specified by the time-varying "density" function $f(c, t)$ satisfying

$$\int_{c_{\min}}^{c_{\max}} f(c, t)\, \mathrm{d}c \equiv 1 \tag{3.12}$$

so that

$$\xi_{\mathrm{w}}(t, 0, c) + \xi_{\mathrm{d}}(t, 0, c) = f(c, t)\dot{m}_{i,\mathrm{T}}(t)/c. \tag{3.13}$$

2. The water and dry matter particles follow the same velocity distribution which, together with the previous assumption, yields

$$\xi_{\mathrm{w}}(t, 0, c) = f(c, t)\dot{m}_{i,\mathrm{T}}(t)\big(1 - w_{i,\mathrm{T}}(t)\big)/c, \qquad (3.14\mathrm{a})$$
$$\xi_{\mathrm{d}}(t, 0, c) = f(c, t)\dot{m}_{i,\mathrm{T}}(t)w_{i,\mathrm{T}}(t)/c. \qquad (3.14\mathrm{b})$$

3. The velocity of each particle stays constant.

4. The infinitesimal vapor mass flow in point x from the part of the water flow moving at velocity c is $\dot{\mu}_{\mathrm{v}}(t, x, c)\,\mathrm{d}x\,\mathrm{d}c$. Therefore, $\dot{\mu}_{\mathrm{v}}(t, x, c)$ is the areal density of the vapor mass flow distribution over the domain $[0, \ell_{\mathrm{T}}] \times [c_{\min}, c_{\max}]$. The dimensional unit of $\dot{\mu}_{\mathrm{v}}$ is $\mathrm{kg\,m^{-2}}$, i.e., mass flow divided by length and by velocity.

The mass balance yields the following PDEs, defined on $x \in [0, \ell_{\mathrm{T}}]$, $t \geq t_0$, $c \in [c_{\min}, c_{\max}]$:

$$\frac{\partial \xi_{\mathrm{w}}(t, x, c)}{\partial t} + c\frac{\partial \xi_{\mathrm{w}}(t, x, c)}{\partial x} = -\dot{\mu}_{\mathrm{v}}(t, x, c), \qquad (3.15\mathrm{a})$$
$$\text{IC: } \xi_{\mathrm{w}}(t_0, x, c) = \xi_{\mathrm{w},0}(x, c),$$
$$\text{BC: } \xi_{\mathrm{w}}(t, 0, c) = f(c, t)\dot{m}_{i,\mathrm{T}}(t)\big(1 - w_{i,\mathrm{T}}(t)\big)/c,$$

$$\frac{\partial \xi_{\mathrm{d}}(t, x, c)}{\partial t} + c\frac{\partial \xi_{\mathrm{d}}(t, x, c)}{\partial x} = 0, \qquad (3.15\mathrm{b})$$
$$\text{IC: } \xi_{\mathrm{d}}(t_0, x, c) = \xi_{\mathrm{d},0}(x, c),$$
$$\text{BC: } \xi_{\mathrm{d}}(t, 0, c) = f(c, t)\dot{m}_{i,\mathrm{T}}(t)w_{i,\mathrm{T}}(t)/c,$$

$$\text{Output 1: } \dot{m}_{o,\mathrm{T}}(t) = \int_{c_{\min}}^{c_{\max}} \big(\xi_{\mathrm{w}}(t, \ell_{\mathrm{T}}, c) + \xi_{\mathrm{d}}(t, \ell_{\mathrm{T}}, c)\big)c\,\mathrm{d}c, \qquad (3.15\mathrm{c})$$

$$\text{Output 2: } w_{o,\mathrm{T}}(t) = \frac{1}{\dot{m}_{o,\mathrm{T}}(t)} \int_{c_{\min}}^{c_{\max}} \xi_{\mathrm{d}}(t, \ell_{\mathrm{T}}, c)c\,\mathrm{d}c. \qquad (3.15\mathrm{d})$$

Different evaporation models specifying $\dot{\mu}_{\mathrm{v}}(t, x, c)$ are treated in Sections 3.5.3 and 3.5.4.

3.3.2 Choice of the Velocity Distribution Function

The input velocity distribution function $f(c, t)$ is to be determined experimentally using parameter identification techniques. Specifically, it can be assumed that $f(\cdot, t)$ belongs to a certain class of functions $[c_{\min}, c_{\max}] \to \mathbb{R}_{\geq 0}$ parametrized by a vector of time-varying parameters. The parameters may vary depending, e.g., on the input mass flow or dry matter content. The choice of the class of distribution functions can be based on phenomenological or fundamental reasons. Let us discuss some relevant ideas.

Thinking phenomenologically, a Gaussian distribution is a reasonable approach. It is loosely motivated by the fact that numerous stochastic variables affecting the flow can be aggregated, according to the central limit theorem, into a normally distributed variable. As the OPF model only accepts a limited range of velocities $[c_{\min}, c_{\max}]$, the Gaussian distribution has to be truncated[5] and approximated[6]. For example, in the simulations of Sec. 3.6, a cosine approximation is constructed as follows:

$$
f(c, t) = \begin{cases} \dfrac{1}{\delta} \left(1 + \cos \dfrac{2\pi(c - \bar{c}_{i,\mathrm{T}}(t))}{\delta} \right), & |c - \bar{c}_{i,\mathrm{T}}(t)| \leq \dfrac{\delta}{2}, \\ 0, & \text{otherwise,} \end{cases}
\tag{3.16}
$$

where $\bar{c}_{i,\mathrm{T}}(t)$ is the mean velocity, see Fig. 3.5. In the simulations, $\bar{c}_{i,\mathrm{T}}(t)$ depends on the input mass flow so that the larger the flow, the faster it is. The support of the distribution (3.16) is $\mathcal{C}(t) = [\bar{c}_{i,\mathrm{T}}(t) - \delta/2, \bar{c}_{i,\mathrm{T}}(t) + \delta/2]$. Thus, it must be ensured that $c_{\min}$ and $c_{\max}$ are such that $\mathcal{C}(t) \subset [c_{\min}, c_{\max}]$ at all times, i.e., for all realistically possible values of $\bar{c}_{i,\mathrm{T}}(t)$. Distribution (3.16) can be generalized, e.g., by considering time-varying dispersion $\delta = \delta(t)$

---

[5] Instead of truncating the Gaussian distribution, it is also possible to *censore* the Gaussian distribution such that the normalization condition (3.12) is satisfied. However, censoring necessarily leads to spikes in the distribution [130] and is therefore inferior to truncation.

[6] Strictly speaking, approximation of the Gaussian distribution is not required, but it is of advantage since it ensures that $f(c_{\min}, t) = f(c_{\max}, t) = 0$, which leads to sufficient smoothing of the output. Otherwise, there would be jumps at $f(c_{\min}, t)$ and $f(c_{\max}, t)$ that can lead to nonsmooth outputs.
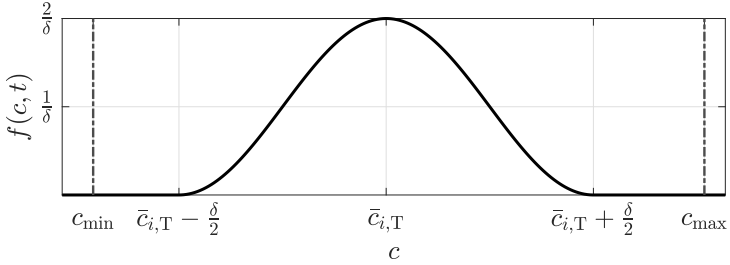
Figure 3.5: Shape of the velocity distribution function (3.16) for $t = \mathrm{const}$

or skewed distributions, cf. Sec. 4.3.1.[7] Furthermore, in some scenarios, the piecewise linear approximation may be more computationally efficient:

$$f(c,t) = \begin{cases} \dfrac{2}{\delta}\big(1 - |c - \bar{c}_{i,\mathrm{T}}(t)|\big), & |c - \bar{c}_{i,\mathrm{T}}(t)| \leq \dfrac{\delta}{2}, \\[2mm] 0, & \text{otherwise.} \end{cases} \tag{3.17}$$

Next, let us turn the attention to the idea of a fundamental (physical) derivation of the velocity distribution function.[8] The plan is to deduce the velocity distribution function $f(c,t)$ predicted by the Navier-Stokes equation (NSE) of momentum balance. In order to simplify the NSE, let us assume that the flow is stationary and laminar. For simplicity, a single Tube is considered again as shown in Fig. 3.6a. The inner radius of the Tube is $R = d/2$ and the film's average thickness is $\bar{s}$. Then, the momentum balance in cylindrical coordinates is

$$\frac{1}{r}\frac{\mathrm{d}}{\mathrm{d}r}\left(r\frac{\mathrm{d}c}{\mathrm{d}r}\right) = -\frac{\varrho g}{\eta}. \tag{3.18}$$

---

[7] Besides ensuring that the support of f is $\mathcal{C} \subset [c_{\min}, c_{\max}]$, the only other requirement to f is that the normalization condition (3.12) should be satisfied for all t.

[8] Note that subscript T indicating the Tubes is often skipped in the discussion on a physical velocity distribution function for the sake of better readability.

(a) Geometry

(b) NSE solution

(c) NSE solution with relaxed BCs

(d) Approximation
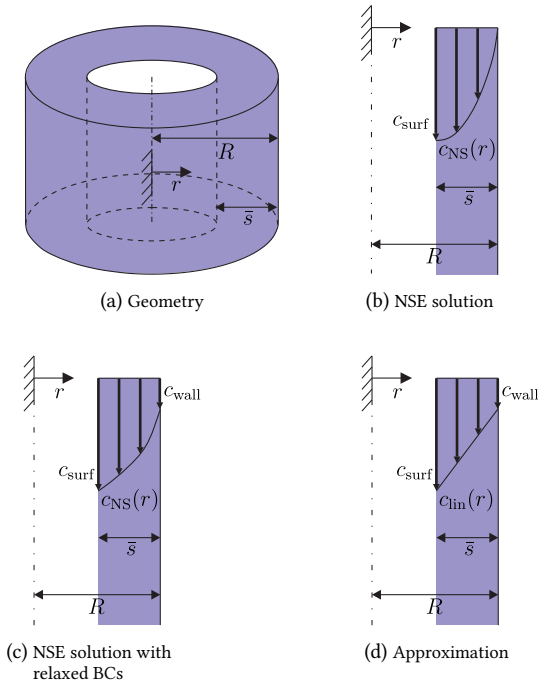
Figure 3.6: Sketches of physical velocity distribution functions

The unknown function is $c(r)$ which denotes the velocity profile along the radius of the Tube. Normally [100], the equation is equipped with the boundary conditions

BC 1: $c(R) = 0$,   "No-slip condition on the wall",   (3.19)

BC 2: $\left.\dfrac{\mathrm{d}c}{\mathrm{d}r}\right|_{R-\bar{s}} = 0$,   "No shear on the liquid-gas interface".   (3.20)

Let the velocity profile $c_{\mathrm{NS}}(r)$ be the solution of the Navier-Stokes boundary problem. It has the shape shown in Fig. 3.6b. Hence, it is possible to write down the mass flow through the inlet cross-section of the Tube as

$$\dot{m}_{i,\mathrm{T}}(t) = 2\pi\varrho \int\limits_{R-\bar{s}}^{R} r\, c_{\mathrm{NS}}(r)\,\mathrm{d}r. \tag{3.21}$$

In order to obtain the velocity distribution function $f(c,t)$, the integration variable in the integral of (3.21) has to be changed to c. Suppose the function $r_{\mathrm{NS}}(c)$ is the inverse of $c_{\mathrm{NS}}(r)$, then

$$\dot{m}_{i,\mathrm{T}}(t) = 2\pi\varrho \int\limits_{0}^{c_{\mathrm{surf}}} c\, r_{\mathrm{NS}}(c)\frac{\mathrm{d}r_{\mathrm{NS}}(c)}{\mathrm{d}c}\,\mathrm{d}c. \tag{3.22}$$

To derive (3.22), let us use the boundary condition (3.19) and $c_{\mathrm{surf}} := c_{\mathrm{NS}}(R-\bar{s})$, which is the velocity on the film's surface. Moreover, note that (3.22) corresponds to the stationary flow but let us formally apply it to time-varying flow so that $c_{\mathrm{surf}} := c_{\mathrm{surf}}(t)$, $r_{\mathrm{NS}}(c) := r_{\mathrm{NS}}(c,t)$, and $\varrho := \varrho(t)$:

$$\dot{m}_{i,\mathrm{T}}(t) = 2\pi\varrho(t) \int\limits_{0}^{c_{\mathrm{surf}}(t)} c\, r_{\mathrm{NS}}(c,t)\frac{\partial r_{\mathrm{NS}}(c,t)}{\partial c}\,\mathrm{d}c. \tag{3.23}$$

By comparing (3.23) to

$$\dot{m}_{i,\mathrm{T}}(t) = \int\limits_{c_{\min}}^{c_{\max}} \big(\xi_{\mathrm{w}}(t,0,c) + \xi_{\mathrm{d}}(t,0,c)\big) c\,\mathrm{d}c, \tag{3.24}$$

the input boundary condition for ξ_{w} is found as

$$\xi_{\mathrm{w}}(t,0,c) = \begin{cases} 2\pi\varrho(t)\big(1 - w_{i,\mathrm{T}}(t)\big)r_{\mathrm{NS}}(c,t)\dfrac{\partial r_{\mathrm{NS}}(c,t)}{\partial c}, & c \in [0, c_{\mathrm{surf}}(t)], \\ 0, & \text{otherwise}, \end{cases} \tag{3.25}$$

and for ξ_d it is similar but with $w_{i,\mathrm{T}}$ instead of $(1 - w_{i,\mathrm{T}})$. Comparing it to the BC of (3.15a), a certain parametrized shape of $f(c,t)$ can be deduced. However, there are two problems.

Firstly, the distribution assigns zero velocity to some particles, namely, to those that touch the wall, according to the BC (3.19). This phenomenon implies infinite time delay and leads to all kinds of problems, in particular, if the PDE model should be converted into time-delay equations. Hence, it would be more practical to describe such an "infinitely long aftereffect" by an ordinary differential or difference-differential equation rather than an infinite time-delay. However, it falls out of the scope of this thesis.

Secondly, the boundary condition (3.20) results in

$$\left. \frac{\partial r_\mathrm{NS}(c,t)}{\partial c} \right|_{c=c_\mathrm{surf}(t)} = \infty, \tag{3.26}$$

i.e., the velocity distribution function $f(c,t)$ will have an infinite spike at $c = c_\mathrm{surf}(t)$. It is not only a numerical difficulty but also a fundamental problem. Compare it to what happens when all particles in the input flow have the same velocity, say $\bar{c}(t)$. Then, the distribution also has an infinite spike: $f(c,t) = \delta(c - \bar{c}(t))$ where δ is the delta-function. Such a model, where all particles entering at the same time have the same velocity, is exactly the DPF model; the corresponding proof is given in App. A.5. Recalling that DPF does not allow overtaking and consequently requires constraints on the rate of change of the input velocity, it is not of surprise that OPF with the "spiky" velocity distribution suffers a similar problem. Without going into technical details, note that under special circumstances, the infinite spikes, which originated at different times at the input boundary $x = 0$, may reach the output boundary $x = \ell_\mathrm{T}$ simultaneously and, after integration, yield infinite output mass flow, cf. Remark 3.2. The culprit is the boundary condition (3.20): Indeed, it implies that the particles near the surface of the film have almost the same velocity which is similar to DPF. Such a distribution of velocities causes no trouble in the stationary flow but cannot be formally transferred to the time-varying scenario as it was planned to do.

A remedy to the issues just described may constitute in adjusting the boundary conditions (3.19) and (3.20). For example, they can be replaced by

$$\text{BC 1: } c(R) = c_{\text{wall}} > 0, \tag{3.27}$$

$$\text{BC 2: } \frac{\mathrm{d}c}{\mathrm{d}r}\bigg|_{R-\bar{s}} = c'_{\text{surf}} < 0. \tag{3.28}$$

The corresponding solution looks like Fig. 3.6c and has the shape

$$c(r) = C_1 + C_2 \ln r - \frac{\varrho g}{4\eta}r^2, \qquad C_1, C_2 = \text{const}, \tag{3.29}$$

where C_1 and C_2 are determined by the BCs (3.27), (3.28). Proceeding as described above, an adjusted version of (3.25) would be obtained and thus a velocity distribution function $f(c, t)$ should be identified experimentally. To spare the reader from tedious details, let us show a simplification of this approach.

To this end, instead of $c_{\text{NS}}(r)$, let us consider the linear velocity profile $c_{\text{lin}}(r)$, as shown in Fig. 3.6d:

$$c_{\text{lin}}(r) = \frac{(R - r)c_{\text{surf}} + (r - R + \bar{s})c_{\text{wall}}}{\bar{s}}. \tag{3.30}$$

It results in a version of (3.25) that looks like this:

$$\xi_{\text{w}}(t, 0, c) = \begin{cases} a_1(t)\big(c - a_2(t)\big), & c \in [c_{\text{wall}}(t), c_{\text{surf}}(t)], \\ 0, & \text{otherwise,} \end{cases} \tag{3.31}$$

where

$$a_1(t) = 2\pi\varrho_{i,\text{T}}(t)\big(1 - w_{i,\text{T}}(t)\big)\left(\frac{\bar{s}(t)}{c_{\text{surf}}(t) - c_{\text{wall}}(t)}\right)^2, \tag{3.32}$$

$$a_2(t) = c_{\text{wall}}(t) + \frac{R}{\bar{s}(t)}\big(c_{\text{surf}}(t) - c_{\text{wall}}(t)\big). \tag{3.33}$$

From (3.31), (3.12), it follows that the velocity distribution function is

$$
f(c,t) = \begin{cases} \dfrac{c\,(c - a_2(t))}{\displaystyle\int\limits_{c_{\text{wall}}(t)}^{c_{\text{surf}}(t)} c\,(c - a_2(t))\,\mathrm{d}c}, & c \in [c_{\text{wall}}(t), c_{\text{surf}}(t)], \\[4pt] 0, & \text{otherwise.} \end{cases}
\tag{3.34}
$$

Experimental data allow identification of the the boundary velocities $c_{\text{wall}}(t)$, $c_{\text{surf}}(t)$, and the average film thickness $\bar{s}(t)$.

To conclude, the choice of the velocity distribution function cannot be universal. It must be guided by the concrete application and motivated by the experimental evidence as the shape of the distribution directly affects the shape of the step response of the model.

3.3.3 Average Time Delay

The i/o representations of DPF (3.39) and (3.48) are time-delay systems with time-varying pointwise delay $\tau(t)$ meaning that all particles coming out of the Tubes at time t started their journey at the same time $t - \tau(t)$. OPF, on the other hand, converts to systems with distributed delays (3.55) and (3.63). Indeed, as the velocities of the simultaneously incoming particles in OPF are distributed, their travel time also varies.[9]

However, for the purpose of control design, it can be useful to define various pointwise approximations of the distributed delay, such as

$$
\bar{\tau}(t) := \frac{\ell_{\text{T}}}{\dot{m}_{o,\text{T}}(t)} \int\limits_{c_{\min}}^{c_{\max}} \left(\xi_{\text{d}}(t, \ell_{\text{T}}, c) + \xi_{\text{w}}(t, \ell_{\text{T}}, c) \right) \mathrm{d}c,
\tag{3.35}
$$

which represents the weighted average of the travel times of the output flow elements.

---

[9] As in Sec. 3.2.2, the reader can set $\dot{m}_{\text{v}} \equiv 0$ when considering the equations of Sec. 3.5 in the context of Sec. 3.3.3 since, in all models, the delay behavior does not depend on evaporation. Recall that each plug or particle moves with constant velocity assigned when it enters.

3.4 Evaporation Models
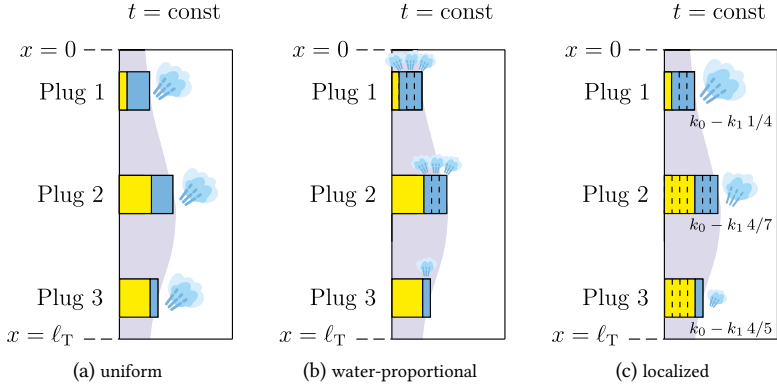
Figure 3.7: Evaporation models

Let us discuss some possibilities to model evaporation, i.e., the sink terms of the PDEs (3.2a) and (3.15a). To this end, the models of *uniform evaporation*, see Sec. 3.4.1, *water-proportional evaporation*, see Sec. 3.4.2, and *localized evaporation*, see Sec. 3.4.3, are described, whereas their mathematical formulations depend on the considered flow model (DPF or OPF). Therefore, the purpose of this section is to gather a qualitative understanding of each evaporation model, while corresponding mathematical models are given in combination with chosen flow models, see Sec. 3.5. All considered evaporation models are illustrated in Fig. 3.7 and, for simplicity, based on plug flow, where the yellow part of a plug corresponds to its dry matter content and the blue part to its water content.

3.4.1 Uniform Evaporation

The assumption of uniform evaporation is often applied in studies on modeling the dynamics of FFE Tubes [141, 102, 107, 127]. Its basic idea is shown in Fig. 3.7a meaning that the same amount of vapor evaporates from the water-part of each plug in the Tube. Thus, the mass flow $\dot{m}_v(t)$, which instan-

taneously evaporates from the liquid film, is uniformly distributed to each plug.

3.4.2 Water-Proportional Evaporation

Although the assumption of uniform evaporation is far-spread in the literature [141, 102, 107, 127], it is prone to failure. Indeed, the output mass flow may, in general, become negative and the output dry matter content may exceed 1. The origin of both problems becomes obvious by thinking about a plug containing a rather small amount of water. Nothing in the uniform evaporation model stops it from losing more water than it has ever contained because uniform evaporation disregards the water content of individual plugs.

To counter the problem, let us introduce a model where evaporation mass flow from a given plug is proportional to its water content. This assumption allows the following physical interpretation: Water molecules jump from liquid to vapor with equal probability, i.e., where there is more water there is more evaporation. Hence, the amount of evaporated water is proportional to the local amount of water in the Tube. A visualization of this concept is given in Fig. 3.7b.

3.4.3 Localized Evaporation

In this section, another evaporation model is introduced, namely, localized evaporation. Note that the previously discussed uniform and water-proportional evaporation models are based on the total vapor flow $\dot{m}_v$ from the whole Tube(s) and distribution thereof among the plugs (uniformly or proportionally to the water mass in a given plug).

The localized evaporation model, on the contrary, directly considers local evaporation from each plug separately, which is shown in Fig. 3.7c. An advantage of the localized approach is that the local vapor mass flow can depend on the local properties of the product. It is indeed reasonable as the heat transfer coefficient k_T goes down as the dry matter content $w \in [0, 1]$ increases which results in reduced evaporation [60]. In the frame of FFEs, this

notion was, e.g., applied by Winchester [141] assuming that k_T decreases linearly with increasing w, which is also implied by Fig. 3.7c.

3.5   Combinations of Flow and Evaporation Models

In Tab. 3.1, all possible combinations of the flow models (DPF, see Sec. 3.2, and OPF, see Sec. 3.3) and evaporation models (uniform, see Sec. 3.4.1, water-proportional, see Sec. 3.4.2, and localized, see Sec. 3.4.3) are shown. However, it must be distinguished between technically useful and useless combinations: If a combination is useful, then Tab. 3.1 references the corresponding section, where the evaporation model is specified for the considered flow model and the resulting PDE system is solved[10]. Otherwise, Remarks 3.3 and 3.4 explain why the corresponding combination is technically useless.

Evap. Flow	Uniform	Water-Proportional	Localized
DPF	Sec. 3.5.1	Sec. 3.5.2	Remark 3.3
OPF	Remark 3.4	Sec. 3.5.3	Sec. 3.5.4

Table 3.1: Combinations of flow and evaporation models

Remark 3.3. Besides OPF, the localized evaporation model can in principle be applied to the DPF model as well. However, the resulting PDEs are not solvable analytically. The difficulties arise essentially from the compressions and rarefactions in DPF due to varying plug velocities which complicates the dynamics of the dry matter content. The problem can be avoided in OPF because the flow is split into separate "lanes" with different velocities, cf. Fig. 3.4. Thus, the localized evaporation model is studied only in case of OPF.

---

[10] Note that the PDE systems are solved via the method characteristics. While the resulting time-delay equations are presented in Sections 3.5.1 to 3.5.4, corresponding calculations are given in Appendices A.1 to A.4.

Remark 3.4. The assumption of uniform evaporation, which is regarded in the context of DPF, is not suitable for OPF due to the fundamental reason that $\xi_{\mathrm{w}}(t, x, c) = 0$ in some points (x, c) is possible. Those points cannot evaporate any mass without ξ_{w} going negative which would not be physical.

3.5.1 Time-Delay Equations for DPF with Uniform Evaporation

At first, let us recall the formula for the vapor mass flow $\dot{m}_{\mathrm{v}}$ evaporating from the liquid film in the Tubes

$$\dot{m}_{\mathrm{v}}(t) = \frac{k_{\mathrm{T}} \pi d_{\mathrm{T}} \ell_{\mathrm{T}} n_{\mathrm{T}} \big(\vartheta_{\mathrm{H}}(t) - \vartheta_{\mathrm{T}}(t)\big)}{\Delta h_v(\vartheta_{\mathrm{T}}(t))} \tag{3.36}$$

which follows from the energy balance [137, 102, 141]. Note that ϑ_{T} denotes the boiling temperature of the liquid in the Tubes. By neglecting boiling point elevation, the assumption $\vartheta_{\mathrm{T}} \approx \vartheta_{\mathrm{E}}$ applies. Alternatively to considering boiling point elevation, it is possible to model the heat transfer coefficient k_{T} in (3.36) dependently on the dry matter content w of the liquid [60]. However, including this feature would not let us solve the PDEs analytically, cf. Remark 3.3. Thus, in this model, let us use (3.36) with constant k_{T} identified for stationary input dry matter content $w_{i,\mathrm{T}}$.

The assumption of uniform evaporation along the Tubes is modeled via

$$\dot{\mu}_{\mathrm{v}}(t, x) = q(t) \qquad \text{with} \qquad q(t) = \frac{\dot{m}_{\mathrm{v}}(t)}{\ell_{\mathrm{T}}}. \tag{3.37}$$

By substituting (3.37) into (3.2a), it is possible to solve (3.2) and thus the time-delay representation of the i/o dynamics is obtained. Basic calculations of the method of characteristics are shown in App. A.1. They yield the following result.

Input-output behavior of DPF with uniform evaporation
Consider the DPF model given by (3.2), (3.37). For

$$t \geq t_0 + \frac{\ell_{\mathrm{T}}}{c_0(0)}, \tag{3.38}$$

the outputs $\dot{m}_{o,\mathrm{T}}$ and $w_{o,\mathrm{T}}$ are independent of the initial conditions and are solely determined by the boundary conditions, i.e., by the input variables $\dot{m}_{i,\mathrm{T}}$, $w_{i,\mathrm{T}}$ and $\bar{c}_{i,\mathrm{T}}$. The i/o behavior is then described by the time-delay equations

$$
\dot{m}_{o,\mathrm{T}}(t) = \frac{\dot{m}_{i,\mathrm{T}}(\theta)}{\nu(t,\theta)} \left(1 - \frac{\bar{c}_{i,\mathrm{T}}(\theta)}{\dot{m}_{i,\mathrm{T}}(\theta)} \int_\theta^t q(\alpha)\nu(\alpha,\theta)\, \mathrm{d}\alpha \right) \Bigg|_{\theta=t-\tau(t)} , \quad (3.39\mathrm{a})
$$

$$
w_{o,\mathrm{T}}(t) = w_{i,\mathrm{T}}(\theta) \left(1 - \frac{\bar{c}_{i,\mathrm{T}}(\theta)}{\dot{m}_{i,\mathrm{T}}(\theta)} \int_\theta^t q(\alpha)\nu(\alpha,\theta)\, \mathrm{d}\alpha \right)^{-1} \Bigg|_{\theta=t-\tau(t)} , \quad (3.39\mathrm{b})
$$

where the mass dispersion factor $\nu(\alpha,\theta)$ is defined as

$$
\nu(\alpha,\theta) = 1 - \frac{\dot{\bar{c}}_{i,\mathrm{T}}(\theta)}{\bar{c}_{i,\mathrm{T}}(\theta)}(\alpha - \theta) \tag{3.40}
$$

and time delay $\tau(t)$ is implicitly defined by

$$
\tau(t) = \frac{\ell_{\mathrm{T}}}{\bar{c}_{i,\mathrm{T}}(t - \tau(t))}. \tag{3.41}
$$

Remark 3.5. For conciseness, (3.39)–(3.41) only show the i/o equations that are relevant "in the long run", i.e., after some time has passed since the initial time t_0 so that the initial conditions do not affect the outputs anymore. It should be enough for most practical purposes (computer simulation, control design, etc.). If needed, however, the complete solution of (3.2) valid for all $t \geq t_0$ can be found in App. A.1. Moreover, note that (3.39)–(3.41) are valid iff the constraints on the input velocity, see Sec. 3.2.2, are satisfied.

For simulation purposes, it is impractical to apply the implicit definition (3.41) of $\tau(t)$ directly. Instead, it can be resolved using the method of dynamic inversion [48]. The idea behind this method is to replace (3.41) with

$$
\frac{\mathrm{d}}{\mathrm{d}t}\Big(\tau(t)\bar{c}_{i,\mathrm{T}}\big(t - \tau(t)\big) - \ell_{\mathrm{T}} \Big) = -\gamma\Big(\tau(t)\bar{c}_{i,\mathrm{T}}\big(t - \tau(t)\big) - \ell_{\mathrm{T}} \Big), \quad (3.42)
$$

where $\gamma = \text{const} > 0$ ensures exponentially decreasing equation error. Evaluating the derivative in (3.42) leads to

$$
\frac{\mathrm{d}\tau(t)}{\mathrm{d}t} = \left. \frac{\tau(t)\dot{\bar{c}}_{i,\mathrm{T}}(\theta) + \gamma\big(\tau(t)\bar{c}_{i,\mathrm{T}}(\theta) - \ell_{\mathrm{T}}\big)}{\tau(t)\dot{\bar{c}}_{i,\mathrm{T}}(\theta) - \bar{c}_{i,\mathrm{T}}(\theta)} \right|_{\theta = t - \tau(t)} \, , \quad t \geq t_f ,
$$

$$
\tau(t_f) = t_f - t_0
$$

(3.43)

where t_f is such that $t_f - \tau(t_f) = t_0$, so by (3.41)

$$
t_f = t_0 + \frac{\ell_{\mathrm{T}}}{\bar{c}_{i,\mathrm{T}}(t_0)}.
$$

(3.44)

Remark 3.6. In [27], the time-delay formulation of DPF without evaporation is proposed for a general transportation system and is called *Dynamic Network Loading Model*. However, the relation to the corresponding PDE description, the implementation of (3.41), and the input velocity restrictions are not discussed therein.

3.5.2 Time-Delay Equations for DPF with Water-Proportional Evaporation

Mathematically, the assumption of water-proportional evaporation is, in case of DPF, described by

$$
\dot{\mu}_{\mathrm{v}}(t, x) = b(t)\xi_{\mathrm{w}}(t, x) \qquad \text{with} \qquad b(t) = \frac{\dot{m}_{\mathrm{v}}(t)}{m_{\mathrm{w}}(t)},
$$

(3.45)

where the total vapor mass flow $\dot{m}_{\mathrm{v}}$ is given by (3.36) and m_{w} is the total mass of water inside the Tubes:

$$
m_{\mathrm{w}}(t) = \int_0^{\ell_{\mathrm{T}}} \xi_{\mathrm{w}}(t, x) \, \mathrm{d}x.
$$

(3.46)

Note that the factor $b(t)$ in (3.45) may be called "instantaneous evaporation rate".

The full solution of the PDE system (3.2) under assumption (3.45) is derived in App. A.2 and yields the following result.

Input-output behavior of DPF with water-proportional evaporation
Consider the DPF model given by (3.2), (3.45). For

$$t \geq t_0 + \frac{\ell_{\mathrm{T}}}{c_0(0)}, \tag{3.47}$$

the outputs $\dot{m}_{o,\mathrm{T}}$ and $w_{o,\mathrm{T}}$ are independent of the initial conditions and are solely determined by the boundary conditions, i.e., by the input variables $\dot{m}_{i,\mathrm{T}}$, $w_{i,\mathrm{T}}$ and $\bar{c}_{i,\mathrm{T}}$. The i/o behavior is then described by the time-delay equations

$$\dot{m}_{o,\mathrm{T}}(t) = \left. \frac{\dot{m}_{i,\mathrm{T}}(\theta)\Big(w_{i,\mathrm{T}}(\theta) + \big(1 - w_{i,\mathrm{T}}(\theta)\big)\,\beta(\theta,t)\Big)}{\nu(t,\theta)} \right|_{\theta=t-\tau(t)} , \tag{3.48a}$$

$$w_{o,\mathrm{T}}(t) = \left. \frac{w_{i,\mathrm{T}}(\theta)}{w_{i,\mathrm{T}}(\theta) + \big(1 - w_{i,\mathrm{T}}(\theta)\big)\,\beta(\theta,t)} \right|_{\theta=t-\tau(t)} , \tag{3.48b}$$

where ν and τ are determined by (3.40) and (3.41), respectively. Note that the time delay τ can be still defined via (3.41) because in all presented models, evaporation does not affect the velocity of plugs. Moreover, the integral evaporation rate $\beta(\theta,t)$ is defined as

$$\beta(\theta,t) = \exp\left(-\int_\theta^t b(\alpha)\,\mathrm{d}\alpha\right). \tag{3.49}$$

The latter, via the definition (3.45) of $b(t)$, depends on the total water mass m_{w}, which is calculated as

$$m_{\mathrm{w}}(t) = \int_{t-\tau(t)}^t \dot{m}_{i,\mathrm{T}}(\theta)\big(1 - w_{i,\mathrm{T}}(\theta)\big)\beta(\theta,t)\,\mathrm{d}\theta. \tag{3.50}$$

Remark 3.7. Instead of (3.50), m_w can be obtained via the mass balance of water over the Tubes, i.e.,

$$\frac{\mathrm{d}m_\mathrm{w}(t)}{\mathrm{d}t} = \big(1 - w_{i,\mathrm{T}}(t)\big)\dot{m}_{i,\mathrm{T}}(t) - \big(1 - w_{o,\mathrm{T}}(t)\big)\dot{m}_{o,\mathrm{T}}(t) - \dot{m}_\mathrm{v}(t). \quad (3.51)$$

However, this approach may lead to accumulation of the numerical integration error. Thus, the finite-time integration formula (3.50) is numerically more advantageous than (3.51).

3.5.3 Time-Delay Equations for OPF with Water-Proportional Evaporation

According to Remark 3.4, let us skip the uniform evaporation model in case of OPF and, instead, study evaporation proportional to the water content. It is defined similarly to (3.45), i.e.,

$$\dot{\mu}_\mathrm{v}(t, x, c) = b(t)\xi_\mathrm{w}(t, x, c) \qquad \text{with} \qquad b(t) := \frac{\dot{m}_\mathrm{v}(t)}{m_\mathrm{w}(t)}, \qquad (3.52)$$

where the total vapor mass flow $\dot{m}_\mathrm{v}$ is given by (3.36) and the total mass of water is calculated as

$$m_\mathrm{w}(t) = \int_0^{\ell_\mathrm{T}} \int_{c_{\min}}^{c_{\max}} \xi_\mathrm{w}(t, x, c) \, \mathrm{d}c \, \mathrm{d}x. \qquad (3.53)$$

The full solution of the PDEs (3.15) under the evaporation model (3.52) is obtained in App. A.3. It leads to the following result.

Input-output behavior of OPF with water-proportional evaporation
Consider the OPF model (3.15), (3.52). For

$$t \geq t_0 + \frac{\ell_\mathrm{T}}{c_{\min}}, \qquad (3.54)$$

the outputs $\dot{m}_{o,\mathrm{T}}$ and $w_{o,\mathrm{T}}$ are independent of the initial conditions and are solely determined by the boundary conditions, i.e., by the input variables

$\dot{m}_{i,\mathrm{T}}$, $w_{i,\mathrm{T}}$, and input velocity distribution function f. The i/o relations are then given by the time-delay equations

$$\dot{m}_{o,\mathrm{T}}(t) = \int_{c_{\min}}^{c_{\max}} f(c,\theta)\,\dot{m}_{i,\mathrm{T}}(\theta)\Big(w_{i,\mathrm{T}}(\theta)$$

$$+ \big(1 - w_{i,\mathrm{T}}(\theta)\big)\beta(\theta,t)\Big)\Big|_{\theta=t-\ell_{\mathrm{T}}/c}\,\mathrm{d}c, \qquad (3.55\mathrm{a})$$

$$w_{o,\mathrm{T}}(t) = \frac{1}{\dot{m}_{o,\mathrm{T}}(t)} \int_{c_{\min}}^{c_{\max}} f(c,\theta)\,\dot{m}_{i,\mathrm{T}}(\theta)\,w_{i,\mathrm{T}}(\theta)\Big|_{\theta=t-\ell_{\mathrm{T}}/c}\,\mathrm{d}c, \qquad (3.55\mathrm{b})$$

where notation (3.49) is used and the total water mass $m_{\mathrm{w}}(t)$ is calculated as

$$m_{\mathrm{w}}(t) = \int_{0}^{\ell_{\mathrm{T}}} \int_{c_{\min}}^{c_{\max}} \frac{f(c,\theta)\,\dot{m}_{i,\mathrm{T}}(\theta)\big(1 - w_{i,\mathrm{T}}(\theta)\big)\beta(\theta,t)}{c}\Bigg|_{\theta=t-x/c}\,\mathrm{d}c\,\mathrm{d}x. \qquad (3.56)$$

3.5.4 Time-Delay Equations for OPF with Localized Evaporation

The following assumptions specify the localized evaporation model for OPF under the requirement that the resulting PDEs are explicitly solvable and thus convertible into time-delay equations:

1. To approximate the relationship between the heat transfer coefficient k_{T} and dry matter content w, let us adopt the linear model

$$k_{\mathrm{T}}(w) = k_0 - k_1 w, \qquad k_0, k_1 = \text{const} > 0 \qquad (3.57)$$

proposed by Winchester [141]. Obviously, this model only makes sense for $w \leq k_0/k_1$. As w increases and approaches its limit value k_0/k_1 from below, k_{T} turns to zero and evaporation halts. Note that the relation (3.57) applies to each infinitesimal flow element. Then, w corresponds to the local dry matter content, i.e., the ratio $\xi_{\mathrm{d}}/(\xi_{\mathrm{w}} + \xi_{\mathrm{d}})$.

Furthermore, linearity of (3.57) is crucial because it leads to a coupling between the PDEs for ξ_w and ξ_d in the form of a rational term which results in an integrable characteristic equation.

2. Let us call "siblings" the infinitesimal flow elements that originated on the input boundary $x = 0$ at the same time, say t_1, but with different c-coordinates. Thus, the assumption is that the vapor flow from the siblings is distributed between them proportionally to the same distribution function $f(c, t_1)$ that was used to distribute the input flow among them. This assumption simplifies the model by way of decoupling the dynamics of the group of siblings from the dynamics of other flow elements. Furthermore, it ensures that all siblings always have the same dry matter content, essentially decoupling them from each other.

By formalizing these ideas, the vapor mass flow density in the point (x, c) is specified as

$$\dot{\mu}_v(t, x, c) = \phi(t, x, c) k_T(t, x, c) p(t) \tag{3.58}$$

where, in accordance with (3.57), the local heat transfer coefficient $k_T(t, x, c)$ is

$$k_T(t, x, c) = k_0 - k_1 \frac{\xi_d(t, x, c)}{\xi_w(t, x, c) + \xi_d(t, x, c)}. \tag{3.59}$$

The distribution factor $\phi(t, x, c)$, following Assumption 2., is governed by the equations

$$\frac{\partial \phi(t, x, c)}{\partial t} + c \frac{\partial \phi(t, x, c)}{\partial x} = 0,$$
$$\text{IC: } \phi(0, x, c) = \phi_0(x, c), \tag{3.60}$$
$$\text{BC: } \phi(t, 0, c) = f(c, t),$$

and the coefficient $p(t)$ is chosen to match (3.58) with the total vapor mass flow formula (3.36):

$$p(t) = \frac{\pi d_T n_T \left(\vartheta_H(t) - \vartheta_T(t) \right)}{\Delta h_v(\vartheta_T(t))}. \tag{3.61}$$

The full solution of the PDEs (3.15) with (3.58)–(3.61) is obtained in App. A.4. It leads to the following result.

Input-output behavior of OPF with localized evaporation

Consider the OPF model (3.15), (3.58)–(3.61). For

$$t \geq t_0 + \frac{\ell_{\mathrm{T}}}{c_{\min}}, \tag{3.62}$$

the outputs $\dot{m}_{o,\mathrm{T}}$ and $w_{o,\mathrm{T}}$ are independent of the initial conditions and are solely determined by the boundary conditions, i.e., by the input variables $\dot{m}_{i,\mathrm{T}}$, $w_{i,\mathrm{T}}$, and input velocity distribution function f. The i/o relations are then given by the time-delay equations

$$\dot{m}_{o,\mathrm{T}}(t) = \int\limits_{c_{\min}}^{c_{\max}} f(c,\theta)\,\dot{m}_{i,\mathrm{T}}(\theta)\,w_{i,\mathrm{T}}(\theta)$$

$$\Omega\left(\frac{1}{w_{i,\mathrm{T}}(\theta)},\,\frac{c\,\varpi(\theta,t)}{\dot{m}_{i,\mathrm{T}}(\theta)w_{i,\mathrm{T}}(\theta)}\right)\Bigg|_{\theta=t-\ell_{\mathrm{T}}/c} \mathrm{d}c, \tag{3.63a}$$

$$w_{o,\mathrm{T}}(t) = \frac{1}{\dot{m}_{o,\mathrm{T}}(t)} \int\limits_{c_{\min}}^{c_{\max}} f(c,\theta)\,\dot{m}_{i,\mathrm{T}}(\theta)\,w_{i,\mathrm{T}}(\theta)\Bigg|_{\theta=t-\ell_{\mathrm{T}}/c} \mathrm{d}c, \tag{3.63b}$$

where the function Ω is defined via the Lambert W-function as

$$\Omega(a,b) = \frac{k_1}{k_0}\left(W\left(\left(\frac{k_0}{k_1}a-1\right)\exp\left(\frac{k_0}{k_1}a-1-\frac{k_0^2}{k_1}b\right)\right)+1\right). \tag{3.64}$$

Additionally, (3.63) uses the abbreviation

$$\varpi(\theta,t) = \int\limits_{\theta}^{t} p(\alpha)\,\mathrm{d}\alpha. \tag{3.65}$$

3.6 Simulation

To study the behavior of the new models, see Sec. 3.5, and their ability to map the qualitative i/o behavior, see Fig. 3.2a, they are compared via simulations of step-experiments in Sec. 3.6.1. Since the model *OPF with water-proportional*

evaporation will also be relevant in Ch. 4, its behavior is discussed in more detail by considering an animation in Sec. 3.6.2.

3.6.1 Comparison of the Models

To simulate realistic situations, up/down-steps of the mass flow into the Plate are executed between the levels $\dot{m}_{i,\mathrm{P0}}$ and $\dot{m}_{i,\mathrm{P1}}$. These scenarios occur during ramp-up of the FFE or when changing the operation point [161]. The parameters and constants used for this study are shown in Tab. 3.2 and refer to the first of four passes in the FFE used for milk powder production, see Ch. 2. Time-varying liquid properties of the milk, such as density ϱ or dynamic viscosity η, are calculated via (2.1) with the parameters of App. A.6.

The simulations of this study include the Plate dynamics (2.3)–(2.10). It dampens the input mass flow and ensures that velocity restrictions (3.3), (3.4), and (3.5) are satisfied as explained in Sec. 3.2.2.

All models are implemented in Simulink in the form of time-delay equations:

- – (3.39), (3.43) for DPF with uniform evaporation;
- – (3.48), (3.50), (3.43) for DPF with water-proportional evaporation;
- – (3.55), (3.56) for OPF with water-proportional evaporation;
- – (3.63) for OPF with localized evaporation.

All models assume the same average input velocity function (3.1), i.e., the larger the flow, the higher its velocity. For OPF, the cosine velocity distribution function (3.16) is used. The distributed delays in the models are approximated with finite sums, where the number of summands is selected empirically by taking into account how fast the processes are. Since the models have the structure of a finite-time integrator, the numerical error caused by this approximation is not accumulated.

Remark 3.8. Alternatively to the time-delay equations, PDE models (3.2) and (3.15) could be implemented in Simulink directly with the method developed in [159].

Symbol	Value	Unit
$\bar{A}$	0.005	m^2
A_P	2.14	m^2
c_max	0.44	m s^{-1}
c_min	0.22	m s^{-1}
d_T	0.05	m
g	9.81	m s^{-2}
k_T	1045	$\text{W m}^{-2}\,\text{K}^{-1}$
k_0	1896	$\text{W m}^{-2}\,\text{K}^{-1}$
k_1	2361	$\text{W m}^{-2}\,\text{K}^{-1}$

Symbol	Value	Unit
ℓ_T	17.7	m
n_T	131	–
$\dot{m}_{i,\text{P0}}$	5	kg s^{-1}
$\dot{m}_{i,\text{P1}}$	6.6	kg s^{-1}
$w_{i,\text{P}}$	0.36	kg kg^{-1}
γ	10	s^{-1}
δ	0.15	m s^{-1}
ϑ_H	57.3	$^\circ\text{C}$
$\vartheta_{i,\text{P}}$	72	$^\circ\text{C}$
ϑ_T	54.7	$^\circ\text{C}$

Table 3.2: Parameters and constants for the simulation-based model comparison

The simulation results are given in Fig. 3.8. To this end, the time-delay blocks in Simulink are initialized with arbitrary but realistic values. After $400\,\text{s}$ of simulation time, when the stationary flow has established, the up/down-steps of $\dot{m}_{i,\text{P}}$ are performed. Let us make some observations:

1. All models respond to an up-step in the input mass flow with an overshoot of the output mass flow. It qualitatively agrees with the expected behavior, see Fig. 3.2a.

2. The water-proportional evaporation model, both for DPF and OPF, causes immediate response to a change in $\dot{m}_{i,\text{T}}$, particularly in terms of $w_{o,\text{T}}$, see Fig. 3.8b. Indeed, an increase in the amount of incoming water immediately increases the evaporation mass flow near the inlet and decreases it near the outlet. As a result, the output dry matter content starts going down. The symmetric effect is present when the input mass flow decreases.

3. Uniform and localized evaporation models, on the other hand, exhibit a distinct delay followed by a transient, both in the output mass flow and output dry matter content, see Fig. 3.8a and Fig. 3.8c.

(a) Comparison of DPF with uniform (unif.) and water-proportional (w-pr.) evaporation models

(b) Comparison of DPF and OPF, both with water-proportional (w-pr.) evaporation model

(c) Comparison of OPF with water-proportional (w-pr.) and localized (loc.) evaporation models
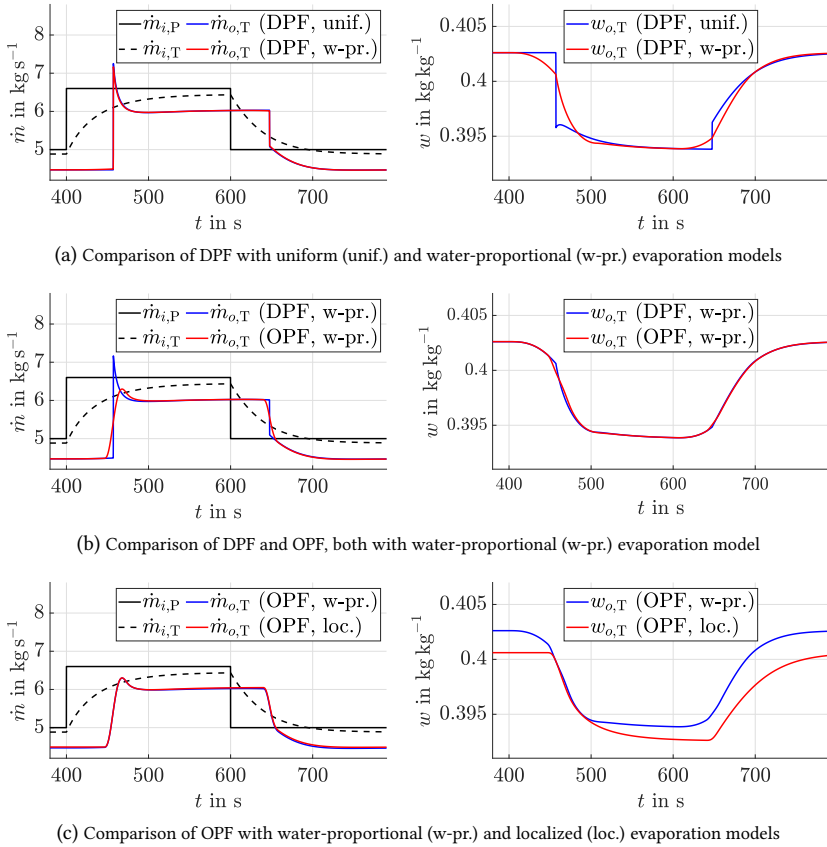
Figure 3.8: Simulations of DPF and OPF with different evaporation models

4. OPF exhibits smoother transients in $\dot{m}_{o,\mathrm{T}}$ compared to DPF, see Fig. 3.8b. It is explained by the diffusion-like properties of the velocity distribution function inside OPF.

5. Switching DPF to OPF, while using the same water-proportional evaporation model, affects $\dot{m}_{o,\mathrm{T}}$ more noticeably than $w_{o,\mathrm{T}}$, see Fig. 3.8b. Conversely, changing the evaporation model has more effect on $w_{o,\mathrm{T}}$ than on $\dot{m}_{o,\mathrm{T}}$, see Fig. 3.8a and Fig. 3.8c.

6. The lower $w_{o,\mathrm{T}}$ of OPF with localized evaporation compared to the other models, see Fig. 3.8c, is explained by the dependence (3.57) of the heat transfer coefficient on the local dry matter content: as the latter goes up, the former decreases, resulting in reduced local evaporation.

To sum up, the comparative simulations provide some insight into choosing the flow and evaporation models. The choice between the flow models (DPF vs. OPF) can be made knowing that OPF produces smoother output mass flow compared to DPF due to a diffusion-like effect. However, the amount of calculation associated with simulation of OPF is higher because of its distributed integral delay as opposed to the pointwise delay in DPF.

If DPF is selected, there are two alternatives for the evaporation model: uniform and water-proportional. The latter yields smoother transient in the output dry matter content. Another difference that should be taken into account: The uniform evaporation model exhibits a delayed initial response, whereas the water-proportional one responds immediately to any changes in the input mass flow. Arguably, the instant response at the output may be unrealistic. However, the main part of the transient is still delayed. Therefore, depending on whether the instant response is small enough to be regarded as a modeling error, the water-proportional evaporation model still proves useful.

If, on the other hand, OPF is the favored flow model, then the choice of the evaporation model is between water-proportional and localized. Unlike the water-proportional model, which responds instantly to any changes in the input mass flow, the localized evaporation demonstrates a purely delayed transient. Water-proportional model is more computationally expensive due to the need of calculating the total mass of water inside the Tube in the form of a double integral. Localized evaporation model, although simpler numerically, contains an important part that requires nontrivial experimental identification, namely, the heat transfer coefficient as a function of the dry matter content.

3.6.2 Animation of an Illustrative Example

In order to visualize the behavior of the OPF model with water-proportional evaporation, which is important in the sequel of the present thesis, let us consider an example. To this end, Fig. 3.9 shows several snapshots of a video

animating the combined "dry matter + water" PDE state $\xi_d + \xi_w$ as well as the mass flows $\dot{m}_{i,\mathrm{T}}$ and $\dot{m}_{o,\mathrm{T}}$.

The animation corresponds to the following scenario. Initially, the flow is stationary with input mass flow $\dot{m}_{i,\mathrm{T}} = 0.5$ and constant vapor mass flow $\dot{m}_v \equiv 0.2$. Some time later, two impulses appear in the input mass flow, a small one followed by a larger one, so that

$$\dot{m}_{i,\mathrm{T}}(t) = \begin{cases} 1, & 1 \leq t \leq 2, \\ 2, & 3 \leq t \leq 4, \\ 0.5, & \text{otherwise.} \end{cases}$$

The average flow velocity depends on the mass flow according to the formula

$$\bar{c}_{i,\mathrm{T}}(t) = 0.04 + 0.06\, \dot{m}_{i,\mathrm{T}}(t)$$

and the velocity distribution function is chosen to be cosine (3.16) with $\delta = 0.02$. The dry matter fraction of the incoming liquid is $w_{i,\mathrm{T}}(t) \equiv 0.36$ and the length of the Tube is $\ell_{\mathrm{T}} = 1$.

Let us point out a few features in Fig. 3.9:

1. Overtaking of the small and slow mass flow impulse by the large and fast one is apparent between Fig. 3.9c and 3.9d.

2. As the impulses are faster than the "normal" mass flow of $\dot{m}_{i,\mathrm{T}} = 0.5$, they take up positions with larger c-values and leave gaps in the area of small c. The gaps, when they arrive at the output boundary, appear as an undershoot in the output mass flow, see Fig. 3.9f. The undershoot is apparent in the output because the input steps are sharp. Compare it to the more realistic scenario in Fig. 3.8c where the input mass flow is filtered by the Plate and no undershoot is observed.

3. Water-proportional evaporation leads to an exponential shape of the stationary state function ξ_w which can be observed in Fig. 3.9a.

(a) $t = 0.5$: Initial stationary flow where the particles' velocities are distributed around $\bar{c}_{i,\mathrm{T}} = 0.07$.

(b) $t = 1.5$: Small impulse enters the tube with average velocity $\bar{c}_{i,\mathrm{T}} = 0.10$.

(c) $t = 3.5$: Large impulse enters with average velocity $\bar{c}_{i,\mathrm{T}} = 0.16$.

(d) $t = 9.5$: Large impulse, being faster, has overtaken the small one and reaches the outlet first.

(e) $t = 11.5$: Small impulse finally appears in the output mass flow.

(f) $t = 18$: Undershoot caused by the gaps in the flow of slowest particles with $\bar{c}_{i,\mathrm{T}} = 0.07$.

Figure 3.9: Still frames from the animation of the illustrative OPF example

3.7 Takeaways

Let us summarize the main results and highlights of this chapter:

– Two new PDE models based on the physical conservation laws for the transported instances, i.e., plugs and particles, are derived:

(a) *Dynamic Plug Flow (DPF)* considers plugs, i.e., a "bundle of particles" entering a Tube simultaneously, where the velocities of plugs inside the Tube are different but the velocity of a single plug stays constant; overtaking of plugs is not possible.

(b) *Overtaking Particle Flow (OPF)* considers particles with different but constant velocities, where overtaking of particles is possible. The velocities of particles entering the Tube are determined according to a distribution function which can either be phenomenologically motivated or physically derived.

– Both models are able to show advanced dynamic effects, such as wave phenomena or time-varying residence times. In particular, the OPF model has the remarkable property of modeling diffusion without the commonly used second-order spatial derivative term in the PDE.

– Besides the classical notion of *uniform evaporation*, two new approaches to model evaporation are developed:

(i) *Water-proportional evaporation*, where the total vapor mass flow from the liquid is distributed among the transported instances proportionally to their water contents.

(ii) *Localized evaporation*, where the vapor mass flow from each transported instance is calculated separately according to a linear relation between the Tube's heat transfer coefficient and the liquid's dry matter content.

– Technically motivated combinations of flow models (DPF, OPF) and evaporation models are transformed into time-delay equations via the method of characteristics. These combinations are simulated and discussed regarding their ability to map the observed qualitative i/o behavior of evaporating liquid film in FFE Tubes.

4 Identification of Distributed Delays and Experimental Proof of a New Model

Regarding FFE Tubes, there exist lots of experimental studies identifying relations for the liquid's film thickness and heat transfer coefficients [3, 2, 71] but, to the best of the author's knowledge, no results on time-delay relations are available. However, there are numerous methods on time-delay estimation techniques; overviews are given in [20, 110]. In this context, most of the algorithms apply for pointwise constant [133, 36, 109, 104, 151] or pointwise time-varying delays [42, 9, 26, 131, 153] and even a method to treat distributed delays [40] exists. Nevertheless, the problem is that algorithms for such complicated systems are commonly tested via academic examples so that the practical applicability is debatable. A further difficulty arises when measurements of the inputs and/or outputs of a system to be identified are not available.

To solve these challenges, it is, at first, necessary to choose a model from Sec. 3.5 and thus to find a compromise between the model's accuracy and identification effort due to cost/time constraints. Additionally, step-response based pilot plant experiments are conducted so that output error based least-squares can be used used to identify the intended delay relations. The advantage of this identification strategy is twofold: Firstly, although the delay relations are identified in the offline manner, they can be used to estimate the delays in online experiments. Secondly, since an output error based least-squares algorithm is applied, the system to be identified can be arbitrarily complex so that even nonlinear models with distributed delays may be con-

---

Parts of this chapter are reproduced from [158].

sidered. To take nonmeasurable inputs and outputs into account, let us estimate and thus "indirectly measure" them via additional models of the pilot plant's subsystems.

The plan of this chapter is as follows. In Sec. 4.1, advantages and disadvantages of the models from Sec. 3.5 are discussed, which leads to a well-founded choice of a certain model by taking the accuracy/effort trade-off into account. Next, the pilot plant set-up is explained in Sec. 4.2 and relations to indirectly measure relevant nonmeasured quantities are given. Sections 4.3 and 4.4 present the chapter's main results, namely, identification of the chosen model's distributed delay behavior and experimental proof of this model. In Sec. 4.5, the highlights of this chapter are summarized.

Those readers, who are only interested in the experimental proof of the chosen model, but not in details on the pilot plant and identification, can skip Sections 4.2 and 4.3, respectively.

4.1   Choice of a Model

In Ch. 3, new models were introduced to describe the dynamics of evaporating liquid film in FFE Tubes. Particularly, in Sec. 3.6, these models were compared via simulations by discussing relevant scenarios.
Based on this discussion, Tab. 4.1 summarizes advantages (+) and disadvantages (−) of the combined flow/evaporation models regarding identification and experimental proof. If a combination is not applicable (N/A), a reference to the corresponding remark is given. The criteria evaluated in Tab. 4.1 are:

1. Identification effort, where

    (a) "low ident. effort" means that identification is restricted to the delay behavior;

    (b) "high ident. effort" means that, besides the delay behavior, evaporation must additionally be identified.[1]

---

[1] In this case, the coefficients of the linear relation (3.57) must additionally be identified, which requires further expensive experiments. Otherwise, constant heat transfer coefficients can be taken from the literature [74, 60, 2].

2. Diffusion behavior, where

   (a) "diffusion" is related to the velocity distribution function $f(c, t)$, see Sec. 3.3.2, and thus appears only in case of OPF;

   (b) "no diffusion" is related to the assumption of plug flow and thus appears only in case of DPF.

3. Distinct delay behavior, where

   (a) "distinct delay" is related to the classical notion of delay, i.e., the output response to an input change is delayed;

   (b) "no distinct delay" means that there is a small instant output response to an input change, but the main part of the transient is is still delayed, which appears only in case of water-proportional evaporation, see Sec. 3.6.1.

Evap.⟍ Flow	Uniform	Water-Proportional	Localized
DPF	+ low ident. effort + distinct delay − no diffusion	+ low ident. effort − no distinct delay − no diffusion	N/A, see Remark 3.3
OPF	N/A, see Remark 3.4	+ low ident. effort + diffusion − no distinct delay	+ diffusion + distinct delay − high ident. effort

Table 4.1: Advantages and disadvantages of flow and evaporation models

Let us evaluate Tab. 4.1: Although DPF with water-proportional evaporation may be useful for control design, this model is less suitable than the other ones regarding identification and experimental proof since it has more disadvantages than advantages. However, all other possible model combinations have the same number of advantages and disadvantages. Therefore, it is necessary to introduce "weights"[2]:

---

[2] The term "weights" is written in quotation marks since it is only a qualitative weighting and not a quantitative (classical) one.

(i) Low identification effort is most important due to the following reasons: Firstly, costs and time for experiment design, implementation, procedure, and evaluation should be kept as low as possible. Secondly, it is desired to identify the delay behavior independently of evaporation.

(ii) Judging from the experiments with water, cf. Fig. 3.2b, and the simulation study to compare all models, see Fig. 3.8, the model error due to "no diffusion" is larger than the one due to "no distinct delays". In particular, the spiky response of DPF with uniform evaporation, see Fig. 3.8a, is expected to be unrealistic.

The aforementioned weighting yields the following qualitative result:

$$\text{OPF, w.-prop.} > \text{DPF, unif.} > \text{OPF, localized.} \tag{4.1}$$

Hence, the model *Overtaking Particle Flow with water-proportional evaporation* is chosen.

4.2 Pilot Plant Description and Measurements

Before performing the identification in Sec. 4.3 and experimental proof in Sec. 4.4, some technicalities w.r.t. the pilot plant, its operation modes and available direct/indirect measurements are discussed in this section.

The principle of the pilot plant is shown in Fig. 4.1, where the labels FI, DI, TI, and PI correspond to mass flow, density, temperature, and pressure identification, i.e., direct measurements (in green). Moreover, the switch represents switching between circulation and single-pass mode, which is detailed in Sec. 4.2.1 and Sec. 4.2.2, respectively.
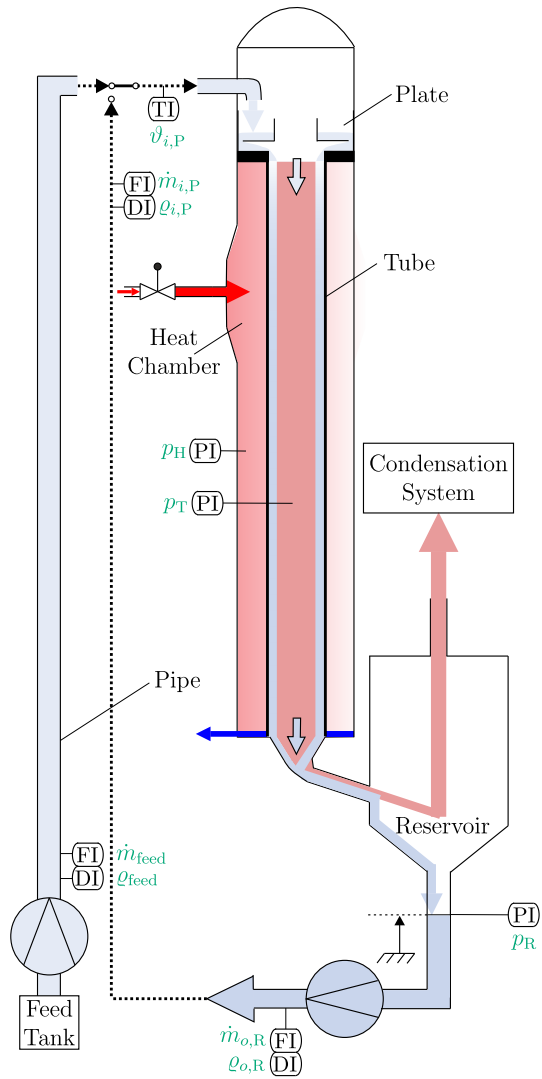
Figure 4.1: Sketch of the pilot plant

In both of these modes, the test liquid, dextrose with polyvinylpyrrolidone[3], is induced onto the Plate which distributes it such that a thin film forms on top of the Tube. When entering the Plate, flash evaporation can occur, i.e., a small amount of liquid evaporates as it undergoes a reduction in pressure, cf. Remark 4.2. Subsequently, the liquid film flows down the inner surface of the Tube and, in case of evaporation, live steam is introduced into the Heat Chamber, i.e., to the outside Tube surface. The live steam provides its enthalpy of condensation to the Tube and thus triggers evaporation of the liquid film inside the Tube. Consequently, the liquid's dry matter content is increased at the Tube's output. To ensure evaporation at low temperatures, partial vacuum is generated inside and outside the Tube. From the bottom of the Tube, the liquid flows into the Reservoir, see Remarks 4.4 and 4.5, and the vapor, see Remark 4.3, coming from the liquid film is gathered by the Condensation System. Downstream to the Reservoir, a pump conveys the liquid either back to the Plate (circulation) or out of the plant into some tank (single-pass). Both of the operation modes, circulation and single-pass, are used for the identification and experimental, respectively.

Note that all quantities shown in Fig. 4.1 are directly measured (printed in green). However, for the intended purposes, it is necessary to generate indirectly measured quantities (printed in blue) which are given in Tab. 4.2. If an indirect measurement requires further explanation, corresponding remarks or sections are referenced in Tab. 4.2.

Remark 4.1. By assuming saturated vapor conditions in the plant, the pressure measurements of vapor can be used to generate corresponding temperatures via the temperature-explicit form of Antoine's equation [125]. Hence, solving (2.48) w.r.t. ϑ leads to

$$\vartheta(p) = 39.72 + \frac{3984.92}{16.57 - \ln p}. \tag{4.2}$$

---

[3] Since the digital twin, see Ch. 2, has milk as product, the reader might ask why, in this chapter, dextrose with polyvinylpyrrolidone (and not milk) is used as product. The reasons are of practical nature: Firstly, dextrose with polyvinylpyrrolidone can be easily produced by GEA Wiegand GmbH and, therefore, does not need to be ordered from a customer (cost reason). Secondly, cleaning of the pilot plant is less cumbersome if dextrose with polyvinylpyrrolidone instead of milk is used (hygienic reason).

Quantity	Relation
$w_{\text{feed}}(t)$	(2.2) with $\varrho := \varrho_{\text{feed}}(t)$, $\vartheta := \vartheta_{i,\text{P}}(t)$, and coeff. from Tab. A.2
$\dot{m}_{o,\text{Pipe}}(t)$	lower case of (2.43) with $\dot{m}_{i,\text{Pipe}}(t) := \dot{m}_{\text{feed}}(t)$
$w_{o,\text{Pipe}}(t)$	(2.44), (2.46) with $w_{i,\text{Pipe}}(t) := w_{\text{feed}}(t)$, $\varrho_{i,\text{Pipe}}(t) := \varrho_{\text{feed}}(t)$
$\vartheta_{\text{T}}(t)$	(4.2) with $p := p_{\text{T}}(t)$, see Remark 4.1
$\dot{m}_{\text{fsh}}(t)$	(4.3), see Remark 4.2
$\dot{m}_{o,\text{P}}(t)$	(4.5), see Remark 4.2
$w_{o,\text{P}}(t)$	(4.8), see Remark 4.2
$\vartheta_{\text{H}}(t)$	(4.2) with $p := p_{\text{H}}(t)$, see Remark 4.1
$\dot{m}_{\text{v}}(t)$	(4.9), see Remark 4.3
$h_{\text{R}}(t)$	(4.10), see Remark 4.4
$\dot{m}_{o,\text{T}}(t)$	(4.13), see Remark 4.5 and Sec. 4.3
$w_{o,\text{R}}(t)$	(2.2) with $\varrho := \varrho_{o,\text{R}}(t)$, $\vartheta := \vartheta_{\text{T}}(t)$, and coeff. from Tab. A.2

Table 4.2: Relations for indirect measurements

Remark 4.2. Since no direct measurements at the Tube's input are available, corresponding indirect measurements are required. To this end, a model of the pilot plant's Plate is developed. The Plate is a tank with a small gap at its bottom having the purpose to distribute the liquid uniformly over the Tube. In addition to that, so-called flash evaporation occurs if the liquid undergoes fast pressure reduction, i.e., if there is partial vacuum[4] in the plant. To describe the i/o dynamics of the Plate, a similar model as the one presented in Sec. 2.2.1 is used. However, in the present chapter, the following assumptions are additionally made:

1. The liquid's temperature is approximately the same as the temperature of the vapor ϑ_{T} inside the Tube.

---

[4] Partial vacuum is generated by a vacuum pump when experiments *with evaporation* are conducted. Otherwise, i.e., in experiments *without evaporation*, there is ambient pressure inside the pilot plant so that no flash evaporation occurs.

2. The effect of the Plate's discharge coefficient is neglected and therefore, it is possible to substitute $\bar{A} = A_{o,\mathrm{P}}$ in (2.3) and (2.5), where $A_{o,\mathrm{P}}$ denotes the cross-sectional area at the Plate's outlet.

3. Since $\dot{m}_{\mathrm{fsh}} \ll \dot{m}_{i,\mathrm{P}}$, the liquid's density over the Plate can be approximated by the input density $\varrho_{i,\mathrm{P}}$, where $(\mathrm{d}\varrho_{i,\mathrm{P}})/(\mathrm{d}t) \approx 0$.

Assumption 1. simplifies (2.8) to[5]

$$\dot{m}_{\mathrm{fsh}}(t) = \max \left\{ \frac{\dot{m}_{i,\mathrm{P}}(t)c_p(t)\big(\vartheta_{i,\mathrm{P}}(t) - \vartheta_{\mathrm{T}}(t)\big)}{\big(c_{p,\mathrm{w}}(t) - c_p(t)\big)\vartheta_{\mathrm{T}}(t) + \Delta h_v(t)}, 0 \right\}, \qquad (4.3)$$

where the indirect measurements of $c_p(t)$, $c_{p,\mathrm{w}}(t)$, and $\Delta h_v(t)$ are explained in App. A.7. By disregarding technicalities for implementation purposes, i.e., $\max\{h_{\mathrm{P}}(t), 0\} := h_{\mathrm{P}}(t)$ and $\max\{h_{\mathrm{P}}(t), \varepsilon\} := h_{\mathrm{P}}(t)$, let us combine (2.3) and (2.5) such that Assumptions 2. and 3. lead to the relations[6]

$$\dot{m}_{i,\mathrm{liq}}(t) = \dot{m}_{i,\mathrm{P}}(t) - \dot{m}_{\mathrm{fsh}}(t), \qquad (4.4)$$

$$\frac{\mathrm{d}}{\mathrm{d}t}\dot{m}_{o,\mathrm{P}}(t) = \frac{g\varrho_{i,\mathrm{P}}(t)A_{o,\mathrm{P}}^2}{\dot{m}_{o,\mathrm{P}}(t)A_{\mathrm{P}}}\big(\dot{m}_{\mathrm{liq}}(t) - \dot{m}_{o,\mathrm{P}}(t)\big), \qquad (4.5)$$

$$h_{\mathrm{P}}(t) = \frac{1}{2g}\left(\frac{\dot{m}_{o,\mathrm{P}}(t)}{\varrho_{i,\mathrm{P}}(t)A_{o,\mathrm{P}}}\right)^2, \qquad (4.6)$$

$$w_{i,\mathrm{liq}}(t) = \frac{w_{i,\mathrm{P}}(t)\dot{m}_{i,\mathrm{P}}(t)}{\dot{m}_{i,\mathrm{liq}}(t)}, \qquad (4.7)$$

$$\frac{\mathrm{d}}{\mathrm{d}t}w_{o,\mathrm{P}}(t) = \frac{\dot{m}_{i,\mathrm{liq}}(t)}{\varrho_{i,\mathrm{P}}(t)A_{\mathrm{P}}h_{\mathrm{P}}(t)}\big(w_{i,\mathrm{liq}}(t) - w_{o,\mathrm{P}}(t)\big). \qquad (4.8)$$

---

[5] The input mass flow $\dot{m}_{i,\mathrm{P}}(t)$ is printed in black in (4.3), (4.4) since it depends on the operation mode whether $\dot{m}_{i,\mathrm{P}}(t)$ is directly or indirectly measured. In case of circulation mode, see Sec. 4.2.1, $\dot{m}_{i,\mathrm{P}}(t)$ is directly measured. In case of single-pass mode, see Sec. 4.2.2, $\dot{m}_{i,\mathrm{P}}(t)$ is indirectly measured via $\dot{m}_{o,\mathrm{Pipe}}(t)$.

[6] The indirect measurement of $w_{i,\mathrm{P}}(t)$ depends on the operation mode. In case of circulation mode, see Sec. 4.2.1, $w_{i,\mathrm{P}}(t)$ is indirectly measured via (2.2) with $\varrho := \varrho_{i,\mathrm{P}}(t)$, $\vartheta := \vartheta_{i,\mathrm{P}}(t)$, and coefficients from Tab. A.2. In case of single-pass mode, see Sec. 4.2.2, $w_{i,\mathrm{P}}(t)$ is indirectly measured via $w_{o,\mathrm{Pipe}}(t)$.

Note that, according to the operation mode, $\varrho_{i,\mathrm{P}}(t)$ is either directly measured (in circulation mode) or indirectly measured (in single-pass mode) and therefore printed in black; further details are given in App. A.7.

Remark 4.3. As described in Sec. 3.5.1, the mass flow $\dot{m}_{\mathrm{v}}$ evaporating from the liquid film can be calculated by

$$\dot{m}_{\mathrm{v}}(t) = \frac{k_{\mathrm{T}} \pi d_{\mathrm{T}} \ell_{\mathrm{T}} \big(\vartheta_{\mathrm{H}}(t) - \vartheta_{\mathrm{T}}(t) \big)}{\Delta h_v(\vartheta_{\mathrm{T}}(t))}, \tag{4.9}$$

where the calculation of $\Delta h_v(\vartheta_{\mathrm{T}}(t))$ follows from App. A.7. While the parameters d_{T} and ℓ_{T} are known from geometry, the identification of constant heat transfer coefficients k_{T} is not that simple but, nevertheless, feasible.[7]

Remark 4.4. The relation to indirectly measure the level $h_{\mathrm{R}}(t)$ follows from the hydrostatic pressure in the Reservoir:

$$h_{\mathrm{R}}(t) = \frac{p_{\mathrm{R}}(t)}{g\, \varrho_{o,\mathrm{R}}(t)}. \tag{4.10}$$

Note that the atmospheric pressure is already considered in the direct measurement of $p_{\mathrm{R}}(t)$.

Remark 4.5. Since the Tube's outputs $\dot{m}_{o,\mathrm{T}}$ and $w_{o,\mathrm{T}}$ cannot be measured with the available devices, the identification and experimental proof can only be performed by modeling the Reservoir whose outputs $\dot{m}_{o,\mathrm{R}}$ and $w_{o,\mathrm{R}}$ are directly and indirectly measured, respectively. The Reservoir represents a tank receiving inflow from the Tube, while the outflow is generated by a downstream pump. To model the Reservoir's dynamics, let us, at first, assume perfect mixing of the liquid. In this case, the liquid's density ϱ_{R} and dry

---

[7] GEA Wiegand GmbH has a method based on static experiments to identify k_{T} at specific values for the dry matter contents w of the liquid. To conduct the experimental proof in Sec. 4.4, constant values for k_{T} at $w = 0.15\,\mathrm{kg\,kg}^{-1}$ and $w = 0.30\,\mathrm{kg\,kg}^{-1}$ are given.

matter content w_R are uniformly distributed such that $\varrho_\mathrm{R}(t) = \varrho_{o,\mathrm{R}}(t)$ and $w_\mathrm{R}(t) = w_{o,\mathrm{R}}(t)$. Then, the mass balance over the Reservoir yields

$$\dot{m}_{o,\mathrm{R}}(t) = \dot{m}_{o,\mathrm{T}}(t) - A_\mathrm{R} \left(h_\mathrm{R}(t) \frac{\mathrm{d}\varrho_{o,\mathrm{R}}(t)}{\mathrm{d}t} + \frac{\mathrm{d}h_\mathrm{R}(t)}{\mathrm{d}t} \varrho_{o,\mathrm{R}}(t) \right) \quad (4.11)$$

and the corresponding dry matter balance leads to

$$\frac{\mathrm{d}}{\mathrm{d}t} w_{o,\mathrm{R}}(t) = \frac{\dot{m}_{o,\mathrm{T}}(t)}{\varrho_{o,\mathrm{R}}(t) A_\mathrm{R} h_\mathrm{R}(t)} \big(w_{o,\mathrm{T}}(t) - w_{o,\mathrm{R}}(t) \big). \quad (4.12)$$

However, there are two open questions:

1. Is it convenient to assume perfect mixing in the Reservoir?

2. Can (4.11) and (4.12) be used to indirectly measure the Tube's outputs $\dot{m}_{o,\mathrm{T}}(t)$ and $w_{o,\mathrm{T}}(t)$?

The answers to these questions require additional insight and are therefore given in Sections 4.3 and 4.4.[8]

4.2.1 Circulation Mode

The flow diagram of the pilot plant in circulation mode (lower switch position in Fig. 4.1) is sketched in Fig. 4.2. When operating in this mode, $\dot{m}_{i,\mathrm{P}}$ is directly measured on the top, right before the liquid enters the Plate, see Fig. 4.1. Moreover, there is neither partial vacuum generated nor live steam induced in this mode, which leads to *no evaporation*, i.e., $\dot{m}_\mathrm{fsh} = \dot{m}_\mathrm{v} \equiv 0$ such that dry matter content w, density ϱ, and dynamic viscosity η of the liquid stay constant. Thus, this operation mode enables identification of the Tube model's distributed delays at constant w, ϱ, and η, but varying mass flows $\dot{m}$, see Sec. 4.3. Since w stays constant in this mode, the mass flow $\dot{m}$ is the only relevant transported quantity. As described in Sec. 2.2.4, the Pipe is a feedthrough w.r.t. mass flow which has the following consequences: Firstly, the Pipe's dynamics do not need to be considered in circulation mode.

---

[8] The reader might have already seen in Tab. 4.2 that the indirect measurement of $\dot{m}_{o,\mathrm{T}}$ is possible since it is printed in blue therein.
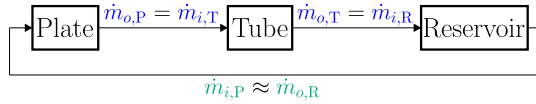
Figure 4.2: Pilot plant in circulation mode

Secondly, the direct measurements of the mass flow out of the Reservoir $\dot{m}_{o,R}$ and mass flow into the Plate $\dot{m}_{i,P}$ are approximately the same.

In a nutshell, *circulation mode* is preferred for the *identification* due to the following reasons:

(a) In this mode, the time-delay behavior to be identified is solely determined by the Tube.

(b) Compared to single-pass mode, see Sec. 4.2.2, there is less experimental effort since the product is directly reused.[9]

4.2.2 Single-Pass Mode

Besides circulation mode, the pilot plant can also be operated in single-pass mode (upper switch position in Fig. 4.1). The corresponding flow diagram is depicted in Fig. 4.3.[10] In this mode, the feed's mass flow $\dot{m}_{\text{feed}}$ and dry matter content w_{feed} are (directly and indirectly) measured at the bottom, right after the pump conveying the liquid through the Pipe from the Feed Tank to the Plate. Furthermore, live steam induction and partial vacuum generation are both active, which yields *evaporation*, i.e., $\dot{m}_{\text{v}} > \dot{m}_{\text{fsh}} > 0$. Hence, dry matter content w, density ϱ, and dynamic viscosity η of the liquid increase when it flows down the Tube. Therefore, note that, besides mass flow $\dot{m}$, the dry

---

[9] In single-pass mode, the output product must be caught in an output tank and is often not reusable anymore due to layering in the output tank. However, in circulation mode, the product is "automatically" reused as being directly pumped back to the top of the plant, i.e., from the Reservoir's output to the Plate's input.

[10] In view of Fig. 4.3, the reader might wonder why $w_{o,T} = w_{i,R}$ is printed in black. The reason is that $w_{o,T}$ cannot be indirectly measured in a meaningful way, which is detailed in Sec. 4.4.2.
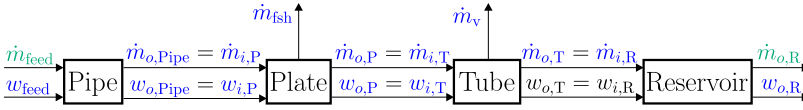
Figure 4.3: Pilot plant in single-pass mode

matter content w is another relevant transported quantity in this mode since evaporation is active.

To sum up, *single-pass mode* is preferred for the *experimental proof* due to the following reasons:

(a) Evaporation can additionally be considered in this mode.

(b) Experimental conditions are close to reality as most of the industrial FFE plants are operated in this mode.

4.3 Identification of Distributed Delays

Next, let us identify the distributed delays of the Tube model via output error based least-squares. As explained in Sec. 4.2.1, the experiments are conducted in *circulation mode without evaporation*. To this end, measurements of the input and output mass flows of the Tube are required. The input mass flow $\dot{m}_{i,\mathrm{T}}$ is indirectly measured via the Plate model, see Remark 4.2 and Fig. 4.2. The output mass flow $\dot{m}_{o,\mathrm{T}}$ can be indirectly measured via the Reservoir model by solving (4.11) w.r.t. $\dot{m}_{o,\mathrm{T}}$, i.e.,

$$\dot{m}_{o,\mathrm{T}}(t) = \dot{m}_{o,\mathrm{R}}(t) + A_{\mathrm{R}}\left(h_{\mathrm{R}}(t)\frac{\mathrm{d}\varrho_{o,\mathrm{R}}(t)}{\mathrm{d}t} + \frac{\mathrm{d}h_{\mathrm{R}}(t)}{\mathrm{d}t}\varrho_{o,\mathrm{R}}(t)\right). \quad (4.13)$$

However, as written in Remark 4.5, the indirect measurement (4.13) can only be regarded as useful if the perfect mixing assumption is justified. Since circulation mode without evaporation at constant dry matter contents and densities is applied, see Sec. 4.3.3, the experiments are independent on assumptions on mixing as it does not appear.

To keep numerical noise small, all derivatives in (4.13) are filtered via some basic moving average filter, where a window length of $T_f = 3\,\mathrm{s}$ is sufficient. Hence, the corresponding signals are delayed by the average filter delay $\tau_f = T_f/2 = 1.5\,\mathrm{s}$. However, since τ_f is negligibly small compared to the delays to be identified, further investigation of its influence is not required. Hence, (4.13) can be used as indirect measurement of $\dot{m}_{o,\mathrm{T}}$.

In the sequel, let us proceed as follows. In Sec. 4.3.1, the Tube model, whose distributed delay behavior should be identified, is explained. Subsequently, it is clarified how to use the method of output error based least-squares in this context, see Sec. 4.3.2, whereas the experimental procedure is shown in Sec. 4.3.3. Finally, the results are presented in Sec. 4.3.4.

Readers being familiar with output error based least-squares and/or not interested in details on the experiments may skip Sec. 4.3.2 and/or Sec. 4.3.3.

4.3.1 Model for Identification

As detailed in Sec. 4.1, the model *Overtaking Particle Flow* (OPF) *with water-proportional evaporation* is chosen. While evaporation is only considered for the experimental proof in Sec. 4.4.3, let us firstly focus on OPF without evaporation, which is needed for identification in circulation mode, cf. Fig. 4.2. Due to the lack of evaporation, i.e. $\dot{m}_{\mathrm{v}} = \dot{m}_{\mathrm{fsh}} \equiv 0$, the only relevant transported quantity is the mass flow $\dot{m}$.

In the sequel, it is *no more* distinguished between directly and indirectly measured quantities. Instead, let us distinguish between *measured*[11] inputs/outputs $(\cdot)$ and *modeled* ones $(\hat{\cdot})$.

For the purpose of identification, the transport of $\dot{m}$ in the Tube is based on the OPF model without evaporation, i.e.,

$$\hat{\dot{m}}_{o,\mathrm{T}}(t) = \int\limits_{c_{\min}(t)}^{c_{\max}(t)} f(c,\sigma)\dot{m}_{i,\mathrm{T}}(\sigma)\Big|_{\sigma=t-\ell_{\mathrm{T}}/c}\,\mathrm{d}c. \tag{4.14}$$

---

[11] Measured inputs/outputs are either directly or indirectly measured.
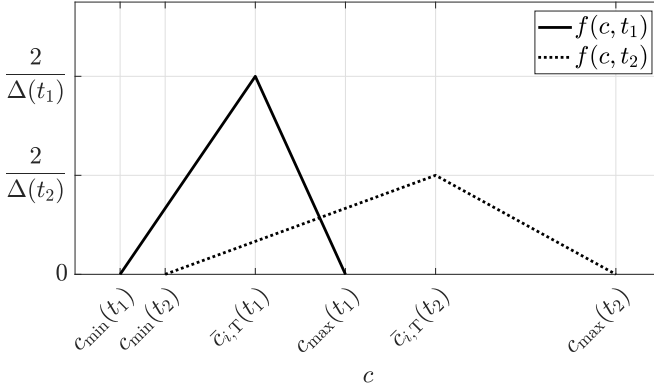
Figure 4.4: Visualization of the velocity distribution function (4.15)

It describes overtaking of liquid particles by considering their velocity c as another independent variable in addition to space x and time t, see Sec. 3.3. A special feature of OPF is that, besides time-varying delay behavior, it allows diffusion modeling which is achieved by distributing the particles' velocities according to a probability-like distribution function $f(c, t)$. Thereafter, the triangular distribution

$$f(c,t) = \begin{cases} \dfrac{2\big(c - c_{\min}(t)\big)}{\big(\bar{c}_{i,\mathrm{T}}(t) - c_{\min}(t)\big)\Delta(t)}, & c \in [c_{\min}(t), \bar{c}_{i,\mathrm{T}}(t)], \\ \dfrac{2\big(c_{\max}(t) - c\big)}{\big(c_{\max}(t) - \bar{c}_{i,\mathrm{T}}(t)\big)\Delta(t)}, & c \in (\bar{c}_{i,\mathrm{T}}(t), c_{\max}(t)], \\ 0, & \text{otherwise,} \end{cases} \tag{4.15a}$$

$$\Delta(t) := c_{\max}(t) - c_{\min}(t) \tag{4.15b}$$

is considered, where the relations between the velocities and delays are given by:

$$c_{\min}(t) = \frac{\ell_{\mathrm{T}}}{\tau_{\max}(t)}, \tag{4.16a}$$
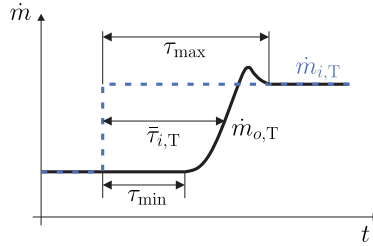
Figure 4.5: Input-output behavior of OPF with (4.15); no evaporation

$$\bar{c}_{i,\mathrm{T}}(t) = \frac{\ell_{\mathrm{T}}}{\bar{\tau}_{i,\mathrm{T}}(t)}, \tag{4.16b}$$

$$c_{\max}(t) = \frac{\ell_{\mathrm{T}}}{\tau_{\min}(t)}. \tag{4.16c}$$

The triangular distribution function[12] (4.15) is chosen to restrict identification to the OPF delays $\tau_{\min}(t)$, $\bar{\tau}_{i,\mathrm{T}}(t)$, and $\tau_{\max}(t)$; Figure 4.4 visualizes (4.15). In this context, it gets evident that the normalization condition (3.12) is satisfied.

In Fig. 4.5, a physical interpretation of the OPF delays is given by sketching the step-response of OPF with distribution function (4.15) but without evaporation. Observe that an input step affects a $\tau_{\min}$-delayed output reaction. After $\tau_{\max}$, all particles of the lower input flow have arrived at the output.

4.3.2 Methodology

In order to use the maximum of information from available measurements, the plan is to identify relations for the OPF delays $\tau_{\min}$, $\bar{\tau}_{i,\mathrm{T}}$, and $\tau_{\max}$ by applying output error based least-squares [54] in the *offline* manner, i.e., identification is performed *after* the experiment. Note that all other parameters apart from the OPF delays are either known by geometry or from preliminary

---

[12] Other possibilities to choose $f(c,t)$ are discussed in Sec. 3.3.2. However, those options require identification of additional parameters besides the OPF delays. Thus, to keep the identification effort as low as possible, the triangular distribution (4.15) is chosen.

experiments.[13] At first, let us consider ansatzfunctions for the OPF delays to represent them as relations of the flow and liquid properties. According to [2, 3] and references therein, liquid film flow can be characterized via the Reynolds number defined by

$$Re(t) = \frac{\dot{m}_{i,\mathrm{T}}(t)}{\pi d_{\mathrm{T}} \eta(t)}, \tag{4.17}$$

where the measurement of $\eta(t)$ is explained in App. A.7. Thus, identification of the ansatzfunctions

$$\tau_{\min}(t) = a_{\min} Re(t)^{b_{\min}}, \tag{4.18a}$$

$$\bar{\tau}_{i,\mathrm{T}}(t) = \bar{a} Re(t)^{\bar{b}}, \tag{4.18b}$$

$$\tau_{\max}(t) = a_{\max} Re(t)^{b_{\max}} \tag{4.18c}$$

is convenient and the parameter vector is

$$\theta = \begin{bmatrix} a_{\min}, & b_{\min}, & \bar{a}, & \bar{b}, & a_{\max}, & b_{\max} \end{bmatrix}^{\top}. \tag{4.19}$$

Furthermore, let us consider the output error

$$e_j = \dot{m}_{o,\mathrm{T}}(t_j; \theta) - \hat{\dot{m}}_{o,\mathrm{T}}(t_j; \hat{\theta}), \quad j = 1, 2, \ldots, N, \tag{4.20}$$

where $\dot{m}_{o,\mathrm{T}}$ is measured according to (4.13), $\hat{\dot{m}}_{o,\mathrm{T}}$ is the model output according to (4.14), and N denotes the number of samples. Note that the estimated parameter vector $\hat{\theta}$ is plugged into (4.14) via (4.15)–(4.18). The model and pilot plant are both fed by the same measured input $\dot{m}_{i,\mathrm{P}}$. Furthermore, the objective function

$$\min_{\hat{\theta}} \sum_{j=1}^{N} e_j^2 \tag{4.21}$$

is considered. In the present thesis, the Matlab/Simulink implementation of the trust-region reflective algorithm is used for the purpose of minimization.

---

[13] More precisely, apart from the identified delays, all the other parameters were given by GEA Wiegand GmbH and relate to dextrose with polyvinylpyrrolidone as well as to their FFE pilot plant with project number 34-09-00015, year 2009.

No.	w in $\mathrm{kg\,kg^{-1}}$	η in $\mathrm{mPa\,s}$	ϱ in $\mathrm{kg\,m^{-3}}$
1	0.42	43.053	1162
2	0.30	12.199	1107
3	0.14	2.2344	1039

Table 4.3: Properties of the test liquid in identification experiments

4.3.3 Experiment Design

To identify $\hat{\theta}$, let us apply three different mixtures of the test liquid, dextrose with polyvinylpyrrolidone, at the constant temperature $\vartheta_{i,\mathrm{P}} = \vartheta_{\mathrm{T}} = 60°\mathrm{C}$, see Tab. 4.3. For each of these three mixtures, the following experiment is conducted:

(i) Operate the pilot plant in circulation mode.

(ii) Wait until the process is stationary, i.e.,
$\dot{m} := \dot{m}_{i,\mathrm{P}} = \dot{m}_{i,\mathrm{T}} = \dot{m}_{i,\mathrm{R}} = \dot{m}_{o,\mathrm{R}} = \mathrm{const}$, and $h_{\mathrm{R}} = \mathrm{const}$.

(iii) By rapidly increasing/decreasing the pump's rotational speed, apply an up/down step to $\dot{m}_{i,\mathrm{P}}$ and measure the decrease/increase of h_{R}.

(iv) Repeat (ii) and (iii).

(v) Terminate the experiment when the mass flow range
$\dot{m} \in [60, 120]\,\mathrm{kg\,h^{-1}}$ is covered by up/down steps.

Since there is no evaporation, the product properties w, η, and ϱ shown in Tab. 4.3 remain constant during each experiment (i)–(v). To visualize the identification procedure (i)–(v), Fig. 4.6 demonstrates the results for mixture No. 1 of Tab. 4.3.

4.3.4 Results

Table 4.4 shows the identified parameters for each experiment, where the numbering (No.) corresponds to the one in Tab. 4.3. Based on these parameters, Fig. 4.7 illustrates the OPF delays as functions of mass flow $\dot{m}$ and dy-
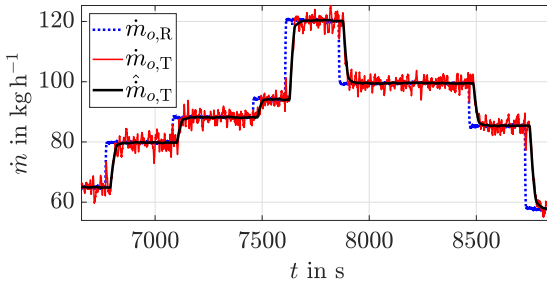
Figure 4.6: Identification procedure (i)–(v) for mixture No. 1 of Tab. 4.3

No.	Re-range	$a_{\min}$	$b_{\min}$	$\bar{a}$	$\bar{b}$	$a_{\max}$	$b_{\max}$
1	$[3.1, 6.1]$	29.4	-0.25	80.3	-0.38	239.6	-0.054
2	$[7.3, 19]$	12.7	0.02	25.8	-0.11	42.1	-0.001
3	$[40, 128]$	8.94	-0.04	17.4	-0.03	58.4	-0.25

Table 4.4: Identified parameters

namic viscosity η. The gaps between the identification data are interpolated via Matlab's *poly12*.

As intuitively expected, the delays increase with increasing η and decrease with increasing $\dot{m}$. Furthermore, it can be observed that the impact of viscosity on the delays is larger than the one of mass flow, in particular for $\tau_{\max}$.

Finally, the author emphasizes that all results are liquid-dependent and refer to dextrose with polyvinylpyrrolidone. If another liquid is considered, the results for the identified delays may differ from the obtained ones although being valid in similar Re-ranges. The reason for this fact is that Re essentially relates $\dot{m}_{i,\mathrm{T}}$ to η, see (4.17), such that further liquid properties, like surface tension or thermal conductivity, remain unconsidered although they may affect the liquid's time-delay behavior. To consider this issue, there exists the option to include additional characteristic numbers, such as Kapitza or Prandtl number, into the ansatzfunctions (4.18), cf. [66]. However, in this case, the number of parameters to be identified increases and relations for the further liquid properties must be identified in additional experiments.
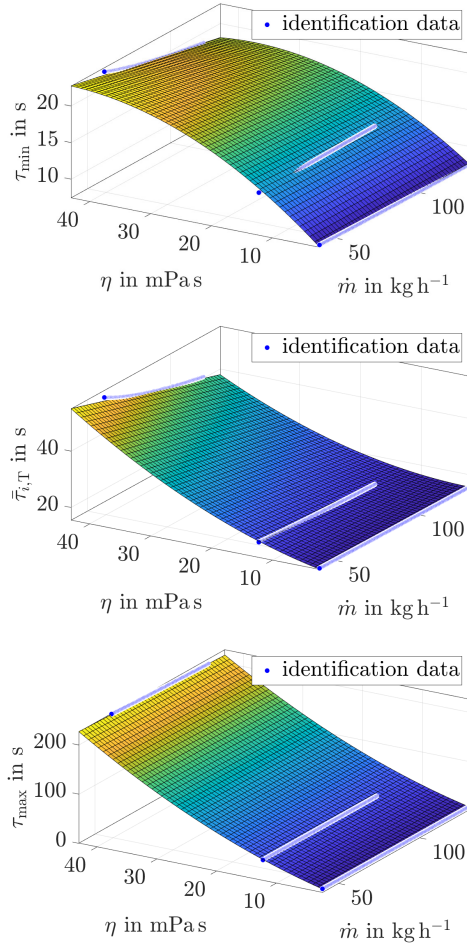
Figure 4.7: Identified OPF delays as functions of $\dot{m}$ and η

Due to these drawbacks, identification is restricted to Re since it is the most significant characteristic number to investigate liquid film flow [3].

4.4 Experimental Proof

In this section, the identified OPF delays are tested by conducting additional experiments. Since industrial FFEs usually operate in single-pass mode, the experimental proof is performed in this mode.

4.4.1 OPF without Evaporation

At first, let us conduct experiments without evaporation. To this end, similar step-experiments as described by the Items (ii)–(iv) in Sec. 4.3.3 are applied. The corresponding results are depicted in Fig. 4.8. As delays get smaller with decreasing dry matter content w, the scale is correspondingly modified in each subfigure of Fig. 4.8. To sum up, it can be seen that the modeled Tube output $\hat{\dot{m}}_{o,\mathrm{T}}$ and the measured one $\dot{m}_{o,\mathrm{T}}$ are in very good accordance.

4.4.2 Preliminaries for Evaporation

As soon as evaporation is included, besides the transport of mass flow $\dot{m}$, the dry matter content w is additionally relevant. To this end, let us reconsider the model of the Reservoir, see Remark 4.5. This model is based on the assumption of perfect mixing. In view of (4.13), it follows that the transport of $\dot{m}$ is almost unaffected by this assumption since changes of $\dot{m}_{o,\mathrm{T}}$ are basically driven by changes of $\dot{m}_{o,\mathrm{R}}$ and $\mathrm{d}h_{\mathrm{R}}/\mathrm{d}t$, whereas changes of the Reservoir's output density $\varrho_{o,\mathrm{R}}$ are comparatively small and slow.

In contrast, the transport of w is essentially determined by changes of ϱ and therefore assumptions on mixing in the Reservoir are decisive. Hence, step-experiments w.r.t. the dry matter content[14] in single-pass mode are shown

---

[14] Practically, an up-step of w_{feed} is realized via a quick change from a feed tank with liquid of *low* dry matter content to a feed tank with liquid of *higher* dry matter content.

(a) $w = 0.45\,\mathrm{kg\,kg^{-1}}$

(b) $w = 0.30\,\mathrm{kg\,kg^{-1}}$

(c) $w = 0.15\,\mathrm{kg\,kg^{-1}}$
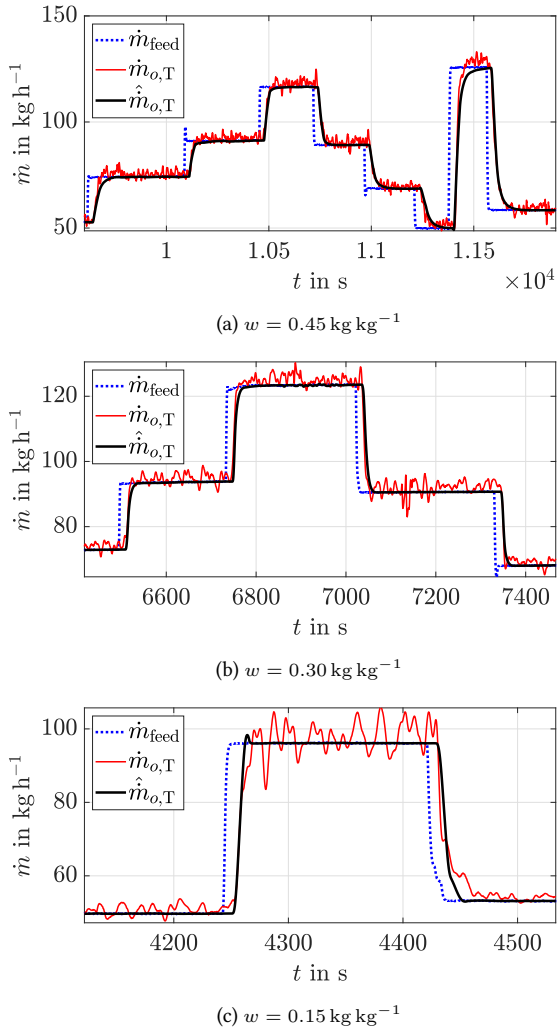
Figure 4.8: Experimental proof of OPF without evaporation

(a) Perfect mixing: (4.22), $\hat{\zeta}_{\text{mix}} = 1$ (b) Imperfect mixing: (4.22), $\hat{\zeta}_{\text{mix}} = 0.38$
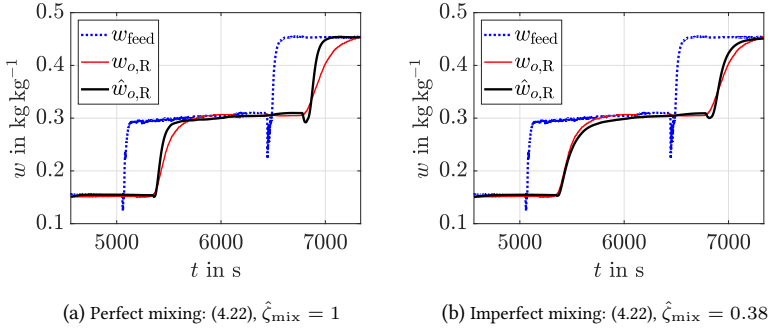
Figure 4.9: Step-experiments w.r.t. w in single-pass mode

in Fig. 4.9. While the delay behavior is basically determined by the Pipe and Tube, the transient behavior is mostly affected by the mixing behavior in the Reservoir. As can be seen in Fig. 4.9a, the assumption of perfect mixing, cf. (4.12), is not very good since the transients of the model $\hat{w}_{o,\text{R}}$ are much faster than the ones of the measurement $w_{o,\text{R}}$. Therefore, the factor $\hat{\zeta}_{\text{mix}} \in (0, 1]$ is introduced in (4.12) to model imperfect mixing such that

$$\frac{\mathrm{d}}{\mathrm{d}t}\hat{w}_{o,\text{R}}(t) = \frac{\hat{\zeta}_{\text{mix}}\,\hat{m}_{o,\text{T}}(t)}{\varrho_{o,\text{R}}(t)A_{\text{R}}h_{\text{R}}(t)}\left(\hat{w}_{o,\text{T}}(t) - \hat{w}_{o,\text{R}}(t)\right) \qquad (4.22)$$

is obtained. Firstly, note that $\hat{\zeta}_{\text{mix}} = 1$ corresponds to perfect mixing. Secondly, note that, based on the data of Fig. 4.9, $\hat{\zeta}_{\text{mix}} = 0.38$ is identified via output error based least-squares, see Fig. 4.9b. Thirdly, note that, instead of (4.22), it is also possible to consider more elaborate approaches [89] to model imperfect mixing. Nevertheless, in the latter case, the computational and identification effort are much larger compared to the author's approach.

Since $w_{o,\text{R}}$ and $\dot{m}_{o,\text{T}}$ are also measured, see Tab. 4.2, it seems convenient to solve (4.22) w.r.t. $\hat{w}_{o,\text{T}}$ and thus obtain an indirect measurement. However, such an approach leads to a strongly noise-corrupted signal so that additional filtering would be required. As additional filtering would manipulate the delay behavior, see Sec. 4.3, it is not convenient to use (4.22) for an indirect measurement of $w_{o,\text{T}}$. Instead, let us utilize the "inherent low-pass filtering"

of (4.22) by considering it as an additional model equation receiving inputs from the outputs of the Tube model, namely, $\hat{\dot{m}}_{o,\mathrm{T}}$ and $\hat{w}_{o,\mathrm{T}}$.

4.4.3 OPF with Water-Proportional Evaporation

To model evaporation, it is assumed proportional to the local mass of water in the Tube, i.e., where there is more water there is more evaporation, see Sec. 3.4.2. Hence, the Tube model *OPF with water-proportional evaporation* is proven via experiments in this section; corresponding model equations are given in Sec 3.5.3. Since constant heat transfer coefficients k_{T} for specific values $w = \mathrm{const}$ are given by GEA Wiegand GmbH, the mass flow $\dot{m}_{\mathrm{v}}$ evaporating from the liquid is indirectly measured, see Remark 4.3. Therefore, the evaporation model does not require any further identification: It simply distributes $\dot{m}_{\mathrm{v}}$ proportionally to the water content of a liquid particle in the Tube.

As detailed in Sec. 4.4.2, besides mass flow $\dot{m}_{o,\mathrm{T}}$, the dry matter content $w_{o,\mathrm{R}}$ is another important output. Both of them are modeled $(\hat{\cdot})$ as well as measured $(\cdot)$ so that they can be used for the experimental proof of the model; corresponding results are shown in Fig. 4.10. From the plots for $\dot{m}$, it follows that the influence of evaporation on the liquid film's time-delay behavior is negligible since $\dot{m}_{o,\mathrm{T}}$ and $\hat{\dot{m}}_{o,\mathrm{T}}$ still coincide well although the OPF delays were identified in experiments without evaporation. In other words, the comparatively small increase of the liquid's dynamic viscosity η, density ϱ, and dry matter content w due to evaporation does not significantly affect the delay behavior in the Tube.

Similarly, the results for w also reveal that model and experiment are in good accordance. The only remarkable deviation is observed in Fig. 4.10b during $t \in [2400, 2680]\,\mathrm{s}$. The reason for this deviation is the indirect measurement of $\dot{m}_{\mathrm{v}}$ via (4.9), where a constant heat transfer coefficient k_{T} is assumed. However, according to [141], k_{T} decreases with increasing w since heat transfer worsens. Thus, as the model assumes constant k_{T}-values, evaporation is overestimated to some extent during the aforementioned time span. Nevertheless, despite this small model error, evaporation is mostly modeled well as shown by Fig. 4.10a, where $w_{o,\mathrm{R}}$ and $\hat{w}_{o,\mathrm{R}}$ are in very good agreement. Broadly speaking, the considered model is well capable to describe

(a) $w_{\text{feed}} = 0.30\,\text{kg}\,\text{kg}^{-1}$

(b) $w_{\text{feed}} = 0.15\,\text{kg}\,\text{kg}^{-1}$
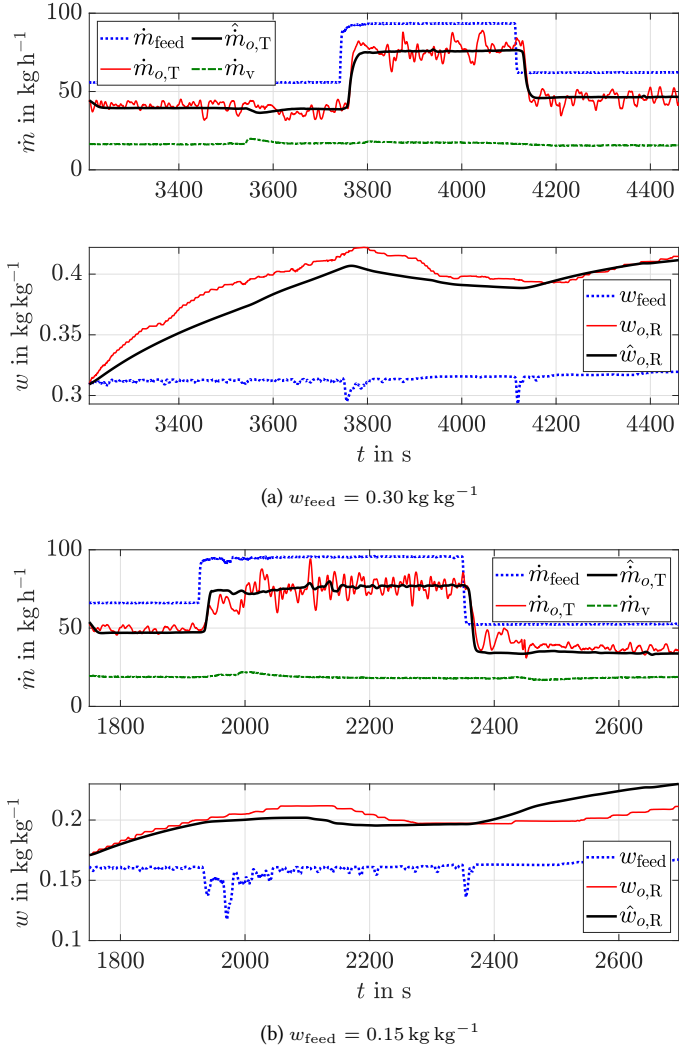
Figure 4.10: Experimental proof of OPF with water-proportional evaporation

the real FFE process and therefore the experimental proof is completed. Finally, note that even better results, particularly w.r.t. the delay behavior of w, may be achieved by applying OPF with localized evaporation as Tube model, see Sec. 3.5.4, and/or by detailed PDE-based modeling of the Reservoir [89]. However, in both cases, the identification effort would increase drastically compared to the proposed approach.

4.5 Takeaways

Let us summarize the main results and highlights of this chapter:

– Based on pilot plant experiments, a novel method to identify time-delay relations for the distributed delays behavior of the Overtaking Particle Flow model has been developed.

– The model *Overtaking Particle Flow with water-proportional evaporation* is experimentally proven and thus can be readily implemented in digital twins to simulate the complicated dynamics of liquid films in FFE Tubes.

– Although the time-delay relations are identified in experiments without evaporation, they yield good results in both of the experimental proofs, with and without evaporation. Thus, the influence of evaporation on the liquid's delay behavior can be neglected.[15]

---

[15] Thereafter, the basic assumption of all our models from Ch. 3, namely that the velocity of liquid particles/plugs solely depends on their input properties but not on evaporation, is experimentally verified.

5 A New Multivariable Control Concept for Falling Film Evaporators

The literature review in Sec. 1.2.2 led to a gap regarding multivariable control of the FFE process. In particular, there is only Van Wijck et al. [136] who consider multivariable control of the output dry matter content w_o and output mass flow $\dot{m}_o$ although the corresponding loops are strongly coupled [142]. However, in [136], this problem is only solved implicitly by setting different speeds of the corresponding loop responses[1].

To fill this gap, let us proceed as follows. In Sec. 5.1, a control-oriented model is derived, which condenses the plant model of Ch. 2 to simplified i/o relations. Subsequently, the loop pairing problem is solved in Sec. 5.2 and a new multivariable control concept is developed in Sec. 5.3.

Those readers, who are familiar with the analysis methods from Sec. 5.2, may restrict themselves to the results in the corresponding subsections.

5.1 Control-Oriented Modeling

The aim of this section is to derive a control-oriented model of the FFE process. For this purpose, Fig. 5.1 shows the manipulated inputs P_C (Compressor power), $\dot{m}_i$ (input mass flow), $\dot{m}_{v,con}$ (excess vapor mass flow), controlled

---

Parts of this chapter are reproduced from [156, 157].

[1] The speeds of the loop responses are adjusted by the parameters of the IMC controller in [136].
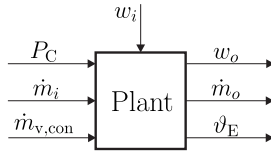
Figure 5.1: Control-oriented i/o block diagram of the plant

outputs w_o (output dry matter content), $\dot{m}_o$ (output mass flow), ϑ_{E} (Effect temperature), and disturbance w_i (input dry matter content).

Remark 5.1. As detailed in Sec. 2.4, the live steam mass flow $\dot{m}_{\mathrm{v,init}}$ is actually an additional manipulated input. However, in the framework of this chapter, $\dot{m}_{\mathrm{v,init}}$ is disregarded since it is most important to heat up the FFE. Apart from that, $\dot{m}_{\mathrm{v,con}}$ dominates $\dot{m}_{\mathrm{v,init}}$ since the additional energy supplied by P_{C} must be released to enable setpoint control of ϑ_{E}, cf. Fig. 2.14d.

As origin, let us consider the plant model presented in Ch. 2. However, since this model is too detailed for the present control problem, simplifications are required.

At first, the liquid flow through the FFE is focused, which is affected by the dynamics of Pipes, see Sec. 5.1.1, Tubes, see Sec. 5.1.2, as well as Reservoirs and Plates, see Sec. 5.1.3. By combining the dynamics of these subsystems in Sec. 5.1.4, relations for the outputs w_o and $\dot{m}_o$ are obtained. To derive a relation for the remaining output ϑ_{E}, it necessary to simplify the energy balances of the Effect and Heat Chamber, see Sec. 5.1.5.

Regarding the outputs w_o and $\dot{m}_o$, the idea of aggregating the dynamics of Pipes, Tubes, Reservoirs and Plates leads to the rearranged flow diagram in Fig. 5.2. Therefore, Remark 5.2 explains why this rearrangements is justified from the modeling perspective.

Remark 5.2. The reader might have noticed that the rearranged flow diagram in Fig. 5.2, which focuses on the transport of w and $\dot{m}$, deviates from the physical structure of the considered FFE, see Fig. 2.1. By modeling the FFE process as shown in Fig. 5.2, the basic idea consists in rearranging the FFE's subsystems so that the overall *i/o behavior* is essentially *conserved*, but the *number of states* is kept as *small* as possible.
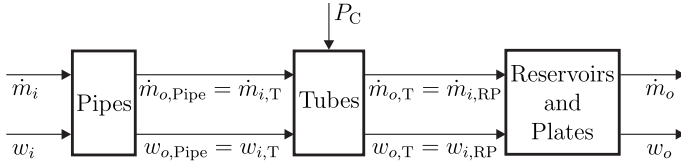
Figure 5.2: Rearranged flow diagram of the transport of w and $\dot{m}$

In a nutshell, the modeling procedure presented in the sequel will show that all outputs w_o, $\dot{m}_o$, ϑ_{E} are, at the same time, states. The only state, which is additionally required, is the Heat Chamber temperature ϑ_{H}.

5.1.1 Simplification of Pipes

As shown in Sec. 2.2.4, the Pipes can be modeled as feedthrough w.r.t. mass flow[2], i.e.,

$$\dot{m}_{o,\mathrm{Pipe}}(t) = \dot{m}_i(t). \tag{5.1}$$

Although the transport of dry matter content through the Pipes is described via variable transport delay, see (2.44), it is convenient for control design to approximate it via constant transport delay such that

$$w_{o,\mathrm{Pipe}}(t) = w_i(t - \tau_{\mathrm{Pipe}}). \tag{5.2}$$

Further explanations on modeling constant τ_{Pipe} are given in Remark 5.3. Moreover, note that, in the framework of this chapter, τ_{Pipe} is the sum of all single Pipe delays. Since the FFE considered in Ch. 2 consists of three Pipes, there is $\tau_{\mathrm{Pipe}} := \sum_{l=1}^{3} \tau_{\mathrm{Pipe},l}$.

---

[2] For convenience, the upper case of (2.43), which represents filling of the Pipe, is neglected.

5.1.2 Simplification of Tubes

A simplified model for the i/o dynamics of FFE Tubes [141, 102, 107] is given by

$$\dot{m}_{o,\mathrm{T}}(t) = \dot{m}_{i,\mathrm{T}}(t - \tau_{\mathrm{T}}) - \frac{1}{\tau_{\mathrm{T}}} \int\limits_{t-\tau_{\mathrm{T}}}^{t} \dot{m}_{\mathrm{v}}(\theta) \, \mathrm{d}\theta \tag{5.3}$$

for the mass flow and

$$w_{o,\mathrm{T}}(t) = \frac{\dot{m}_{i,\mathrm{T}}(t - \tau_{\mathrm{T}}) w_{i,\mathrm{T}}(t - \tau_{\mathrm{T}})}{\dot{m}_{o,\mathrm{T}}(t)} \tag{5.4}$$

for the dry matter content. As with the Pipe delay, the Tube delay τ_{T} denotes the sum of the delays in all (in this case, four) passes, i.e., $\tau_{\mathrm{T}} := \sum_{j=1}^{4} \tau_{\mathrm{T},j}$. Remark 5.3 explains why modeling constant τ_{T} is justified for the intended purpose.

Remark 5.3. While the Pipe delay τ_{Pipe} is of the "hydraulic type" [29], the Tube delay τ_{T} is more complicated because the Tubes, unlike Pipes, are not completely filled with liquid which may lead to wave formation, mixing of the flow, and other effects [4, 14]. As shown in Ch. 3, the Tube delay can be modeled by the concepts of Dynamic Plug Flow or Overtaking Particle Flow. The latter represents a nonlinear distributed delay model further complicated by evaporation. Additionally, there are other advanced models to describe the behavior of evaporating liquid film inside the Tubes based on coupled Navier-Stokes equations for the liquid and vapor phase [77, 38]. In general, both of the delays, τ_{Pipe} and τ_{T}, depend, e.g., on the liquid's dry matter content and mass flow [161, 158] which vary due to controller action. However, in the present chapter, let us assume constant τ_{Pipe} and τ_{T}. In practical investigations with the digital twin from Ch. 2, it is observed that controller action causes changes of τ_{T} by at most $\pm 20\,\%$ and τ_{P} by at most $\pm 10\,\%$ w.r.t. their nominal values. Moreover, as will be discussed in Sec. 5.3, the proposed control concept combines some useful features with basic PID and PI controllers, which are robust against delay changes [16]. Due to these reasons, modeling constant delays is justified for the intended purpose.

To take evaporation into account, let us evaluate the stationary energy balance over the Compressor with efficiency factor η_C so that the relation[3]

$$\dot{m}_v(t) = \bar{q}P_C(t) \text{ with } \bar{q} = \frac{\varrho_{v,E}\,\eta_C}{p_H - p_E} \tag{5.5}$$

is obtained. By considering the same vapor mass flow $\dot{m}_v$ in (5.3) as in (5.5), it is assumed that the vapor mass flow conveyed by the Compressor $\dot{m}_{v,C}$, see (2.51), is equal to the mass flow evaporating from the liquid. This assumption is physically justified by the stationary mass balance of vapor over the Effect, which yields $\sum_{j=1}^{4} \dot{m}_{v,j} = \dot{m}_{v,C} := \dot{m}_v$ if the small amount of flash vapor $\sum_{j=1}^{4} \dot{m}_{\text{fsh},j}$ is neglected, see also Remark 2.5.

Since a slew rate limiter prevents fast changes of $\dot{m}_v$, see Remark 5.4, the moving average filter term in (5.3) can be approximated by

$$\frac{1}{\tau_T} \int_{t-\tau_T}^{t} \dot{m}_v(\theta)\,\mathrm{d}\theta \approx \dot{m}_v(t) \stackrel{(5.5)}{=} \bar{q}P_C(t). \tag{5.6}$$

To sum up, the advantage of modeling $\dot{m}_v$ according to (5.5) is that there is a linear relation between the vapor mass flow $\dot{m}_v$ and Compressor power P_C. In contrast, the relation between $\dot{m}_v$ and Compressor speed N_C is nonlinear, see (2.50), (2.51). Hence, it is more convenient to choose P_C as a manipulated variable in place of N_C.

Remark 5.4. In fact, the power P_C is manipulated by the controller and therefore not necessarily slow. However, as shown in App. A.8, P_C is converted into the Compressor's rotational speed N_C via a variable frequency drive and the rate of change of N_C is then limited by a slew rate limiter. The latter has the effect that changes of the vapor mass flow $\dot{m}_v$ are slow, which justifies the approximation (5.6).

---

[3] Note that (5.5) can also be interpreted as a linear fit of the corresponding compressor map, cf. Fig. 2.9b.

5.1.3 Simplification of Reservoirs and Plates

By neglecting flash evaporation, which is small compared to other mass flows, and taking into account that FFEs essentially work around their operation point, the dynamics of Reservoirs and Plates can be modeled via low-pass filters. In this context, it is common to approximate a serial connection of low pass filters by a single low pass filter with an additional delay element [46]. This additional delay is formally assigned to the Tubes and Pipes since their delays are dominant with regard to the whole process. Hence, the dynamics of Reservoirs and Plates are summed up by a low-pass filter w.r.t. mass flow such that

$$\frac{\mathrm{d}}{\mathrm{d}t}\dot{m}_o(t) = \frac{1}{T_2}\big(\dot{m}_{i,\mathrm{RP}}(t) - \dot{m}_o(t)\big) \tag{5.7}$$

and a low pass filter w.r.t. dry matter content such that

$$\frac{\mathrm{d}}{\mathrm{d}t}w_o(t) = \frac{1}{T_1}\big(w_{i,\mathrm{RP}}(t) - w_o(t)\big). \tag{5.8}$$

5.1.4 Combination of Simplified Pipes, Tubes, Reservoirs and Plates

In view of Fig. 5.2, let us combine (5.1)–(5.8) which yields the i/o relations

$$\frac{\mathrm{d}}{\mathrm{d}t}w_o(t) = \frac{1}{T_1}\left(\frac{w_i(t-\tau_1)\dot{m}_i(t-\tau_2)}{\dot{m}_i(t-\tau_2) - \bar{q}P_{\mathrm{C}}(t)} - w_o(t)\right), \tag{5.9a}$$

$$\frac{\mathrm{d}}{\mathrm{d}t}\dot{m}_o(t) = \frac{1}{T_2}\left(\dot{m}_i(t-\tau_2) - \bar{q}P_{\mathrm{C}}(t) - \dot{m}_o(t)\right) \tag{5.9b}$$

with $\tau_1 := \tau_{\mathrm{T}} + \tau_{\mathrm{Pipe}}$ and $\tau_2 := \tau_{\mathrm{T}}$.

5.1.5 Simplification of Effect and Heat Chamber

Finally, simplified evaluations of the Effect's and Heat Chamber's energy balances are presented. Compared to Ch. 2, the simplifications are as follows:

- The properties c_p, Δh_v, and m of liquid, water, and vapor are assumed constant and valid around the operation point.

- The Tubes of all four passes are bundled such that the sum of all Tube surfaces $A_{\Sigma,\mathrm{T}} = \sum_{j=1}^{4} A_{\mathrm{T},j}$, the average heat transfer coefficient $\bar{k}_{\mathrm{T}} = \sum_{j=1}^{4} k_{\mathrm{T},j}/4$, and the average specific heat capacity $\bar{c}_p = (c_{p,i} + c_{p,o})/2$ apply.

- The live steam mass flow $\dot{m}_{\mathrm{v,init}}$ to initialize the process is neglected, see Remark 5.1.

- Heat losses to the ambience are neglected since they are small compared to all other energy flows.

- Boiling point elevation of the liquid is neglected for convenience.

Consequently, the energy balances yield

$$\frac{\mathrm{d}}{\mathrm{d}t}\vartheta_{\mathrm{E}}(t) = \frac{\dot{q}_{i,\mathrm{E}}(t) + \dot{q}_{\mathrm{T}}(t) - \dot{q}_{o,\mathrm{E}}(t) - \dot{q}_{\mathrm{v,C}}(t)}{m_{\mathrm{E}}\bar{c}_p + m_{\mathrm{met,E}}c_{p,\mathrm{met}}}, \tag{5.10}$$

$$\frac{\mathrm{d}}{\mathrm{d}t}\vartheta_{\mathrm{H}}(t) = \frac{\dot{q}_{\mathrm{v,C}}(t) + P_{\mathrm{C}}(t) - \dot{q}_{\mathrm{T}}(t) - \dot{q}_{\mathrm{v,con}}(t) - \dot{q}_{\mathrm{w,H}}(t)}{m_{\mathrm{w,H}}c_{p,\mathrm{w,H}} + m_{\mathrm{met,H}}c_{p,\mathrm{met}}}, \tag{5.11}$$

where

$$\dot{q}_{i,\mathrm{E}}(t) = \dot{m}_i(t)c_{p,i}\vartheta_{\mathrm{E}}(t), \tag{5.12a}$$

$$\dot{q}_{\mathrm{T}}(t) = \bar{k}_{\mathrm{T}}A_{\Sigma,\mathrm{T}}\big(\vartheta_{\mathrm{H}}(t) - \vartheta_{\mathrm{E}}(t)\big), \tag{5.12b}$$

$$\dot{q}_{o,\mathrm{E}}(t) = \dot{m}_o(t)c_{p,o}\vartheta_{\mathrm{E}}(t), \tag{5.12c}$$

$$\dot{q}_{\mathrm{v,C}}(t) = \bar{q}P_{\mathrm{C}}(t)\big(c_{p,\mathrm{w,E}}\vartheta_{\mathrm{E}}(t) + \Delta h_{v,\mathrm{E}}\big), \tag{5.12d}$$

$$\dot{q}_{\mathrm{v,con}}(t) = \dot{m}_{\mathrm{v,con}}(t)\big(c_{p,\mathrm{w,H}}\vartheta_{\mathrm{H}}(t) + \Delta h_{v,\mathrm{H}}\big), \tag{5.12e}$$

$$\dot{q}_{\mathrm{w,H}}(t) = \big(\bar{q}P_{\mathrm{C}}(t) - \dot{m}_{\mathrm{v,con}}(t)\big)c_{p,\mathrm{w,H}}\vartheta_{\mathrm{H}}(t). \tag{5.12f}$$

Remark 5.5. Readers being familiar with FFEs might be surprised that the temperature ϑ_i of the superheated liquid entering the FFE has no (disturbing) influence. The reason is the flash process in the Plate, see Sec. 2.2.1, which rapidly cools down the liquid to (approximately) the Effect temperature ϑ_{E}.

Summing up, the simplified (but nonlinear) i/o model of the FFE process is composed of (5.9)–(5.12).

5.2 Control Loop Pairing and Interaction Analyses

Numerous process engineering applications are designed as multiple-inputs-multiple-outputs (MIMO) plants. After classifying the inputs into manipulated variables and disturbances, the pairing problem of controlled and manipulated variables naturally arises. Practically, this problem is often solved intuitively by applying a decentralized multiloop single-input-single-output (SISO) control architecture which, however, can lead to poor performance [118]. Nevertheless, a deep analysis of the pairing problem and investigating possible loop interactions help to find a more efficient multivariable control structure [123, 43]. To this end, the following questions should be answered:

1) Which pairing choice of the controlled and manipulated variables is best for multiloop SISO control?

2) Is this pairing choice stable[4] over the plant's operation frequency domain?

3) Is this pairing choice feasible regarding stability of the multiloop SISO control system?

4) Is it better to design a multivariable controller instead of multiloop SISO controllers?

5) If yes, how should this multivariable controller be structured?

By inventing the relative gain array (RGA), Bristol [25] presented a steady-state measure giving an answer to Question 1). Subsequently, many extensions of the RGA were created, cf. [47, 64, 99]. In this context, substituting the steady-state gain matrix by the transfer function matrix in Bristol's RGA is

---

[4] In this context, the term "stable" means that the pairing recommendation is unique in all relevant operation frequencies of a plant. Note that there may be plants where this property is not satisfied, cf. [154].

most common [123] and solves Question 2). The latter approach is referenced as dynamic relative gain array (DRGA) throughout this thesis. Although the RGA and DRGA are often applied to various processes [120, 101], Question 3) cannot be answered by these methods. To remedy this issue, there exist the notions of decentralized integral controllability (DIC) [123, 15] and the Niederlinski index (NI) [96]. Since all of the aforementioned process measures assume multiloop SISO control, it is debatable whether a multivariable controller achieves better performance, see Question 4). Therefore, modern approaches, such as the participation matrix (PM) [30] or Hankel interaction index array (HIIA) [144], use the Gramian controllability and observability matrices to quantify process interactions. Consequently, recommendations on the structure of a multivariable controller are obtained, which answers Question 5).

In this section, Questions 1) – 5) are solved for the FFE process by applying RGA, DRGA, NI, DIC, normalized PM, and HIIA. The work coming closest to the present one is [142], where RGA and DRGA are used to decide which manipulated variable is best to control the output dry matter content of the FFE process. Based on a different model than the one presented in [142], the results obtained therein are verified and extended by investigating the feasibility of a chosen pairing for multiloop SISO control. Furthermore, it is analyzed if a multivariable controller may achieve better results than multi-loop SISO controllers. Finally, recommendations w.r.t. a possible structure of the multivariable controller are given.

The plan of this section is as follows. In Sec. 5.2.1, the simplified nonlinear FFE model resulting from Sec. 5.1 is linearized around the FFE's standard operation point to obtain a transfer function matrix of the plant. The main contribution is presented in Sections 5.2.2 to 5.2.6, where all relevant methods are recalled, applied to the linearized FFE model and thus the pairing problem is solved. In Sec. 5.2.7, all important results are summarized.

	u_1	P_C
manipulated inputs u	u_2	$\dot{m}_i$
	u_3	$\dot{m}_\mathrm{v,con}$
disturbance input	z	w_i
	x_1	w_o
states x	x_2	$\dot{m}_o$
	x_3	ϑ_E
	x_4	ϑ_H
	y_1	w_o
controlled outputs y	y_2	$\dot{m}_o$
	y_3	ϑ_E

Table 5.1: Control nomenclature in Sec. 5.2

5.2.1 Preliminaries

Throughout Sec. 5.2, the control nomenclature in Tab. 5.1 is used so that the controlled outputs are given by

$$y = \begin{bmatrix} y_1 \\ y_2 \\ y_3 \end{bmatrix} = \underbrace{\begin{bmatrix} 1 & 0 & 0 & 0 \\ 0 & 1 & 0 & 0 \\ 0 & 0 & 1 & 0 \end{bmatrix}}_{=C} x. \tag{5.13}$$

Hence, the model composed of (5.9)–(5.12) can be compactly denoted by

$$\frac{\mathrm{d}}{\mathrm{d}t} x(t) = f\big(x(t), u(t), u(t - \tau_2), z(t - \tau_1)\big), \tag{5.14a}$$

$$y(t) = Cx(t), \tag{5.14b}$$

which represents a nonlinear state space with input delays but linear output equation. Note that initial values do not need to be specified since they are not relevant for the intended analyses.

Linearization of (5.14) about the operation point (OP) with subsequent Laplace transformation yields the transfer function matrix

$$G(s) = C\left(sI_4 - f_x\right)^{-1}\left(f_u + f_{u_{\tau_2}}\,\mathrm{e}^{-s\tau_2}\right) \tag{5.15}$$

and disturbance transfer function matrix

$$G_z(s) = C\left(sI_4 - f_x\right)^{-1} f_{z_{\tau_1}}\,\mathrm{e}^{-s\tau_1}, \tag{5.16}$$

where $f_{(\cdot)} := \partial f/\partial(\cdot)|_{\mathrm{OP}}$, $u_{\tau_2} := u(t-\tau_2)$, and $z_{\tau_1} := z(t-\tau_1)$ are abbreviations.

In the sequel, let us focus on $G(s)$ according to (5.15) by applying the parameters and operation point data given in [156]. Moreover, some of the analyses performed in Sections 5.2.2 to 5.2.6 depend on appropriate scaling[5] of $G(s)$. To realize such scaling, there exist various opportunities [123]. Since FFEs basically work around their standard operation point, it is useful to scale the linearized outputs $\Delta y_i = y_i - y_{i,\mathrm{OP}}$ w.r.t. the largest allowed control error $\Delta e_{i,\mathrm{max}}$, i.e.,

$$\Delta\tilde{y}_i = \frac{\Delta y_i}{\Delta e_{i,\mathrm{max}}}, \quad i = 1,2,3, \tag{5.17}$$

where $\tilde{(\cdot)}$ indicates that the variable $(\cdot)$ is scaled and

$$\begin{bmatrix}\Delta e_{1,\mathrm{max}} \\ \Delta e_{2,\mathrm{max}} \\ \Delta e_{3,\mathrm{max}}\end{bmatrix} = \begin{bmatrix}0.01\,\mathrm{kg\,kg^{-1}} \\ 0.2\,\mathrm{kg\,s^{-1}} \\ 1\,\mathrm{K}\end{bmatrix}. \tag{5.18}$$

The linearized inputs $\Delta u_j = u_j - u_{j,\mathrm{OP}}$ are scaled w.r.t. the largest allowed deviation $\Delta u_{j,\mathrm{max}}$ from the operation point, i.e.,

$$\Delta\tilde{u}_j = \frac{\Delta u_j}{\Delta u_{j,\mathrm{max}}}, \quad j = 1,2,3 \tag{5.19}$$

---

[5] In general, scaling of $G(s)$ simplifies the model analysis [123]. While the relative gain array, see Sec. 5.2.2, or the Niederlinki index, see Sec. 5.2.3, are scaling-independent, the Gramian-based interaction measures, see Sections 5.2.5 and 5.2.6, depend on suitable scaling [58].

with

$$\begin{bmatrix} \Delta u_{1,\text{max}} \\ \Delta u_{2,\text{max}} \\ \Delta u_{3,\text{max}} \end{bmatrix} = \begin{bmatrix} 10\,\text{kW} \\ 1\,\text{kg}\,\text{s}^{-1} \\ 0.1\,\text{kg}\,\text{s}^{-1} \end{bmatrix}. \tag{5.20}$$

To get an impression of the plant dynamics, the scaled (3×3) transfer function matrix

$$\tilde{G}(s) = [\tilde{g}_{ij}(s)] \tag{5.21}$$

with

$$\tilde{g}_{11}(s) = \frac{\tilde{\alpha}_1}{\tilde{\alpha}_2(\tilde{\alpha}_3 s + 1)}, \tag{5.22a}$$

$$\tilde{g}_{12}(s) = -\frac{\tilde{\alpha}_4\,\mathrm{e}^{-\tilde{\alpha}_5 s}}{\tilde{\alpha}_6(\tilde{\alpha}_3 s + 1)}, \tag{5.22b}$$

$$\tilde{g}_{13}(s) = 0, \tag{5.22c}$$

$$\tilde{g}_{21}(s) = -\frac{\tilde{\beta}_1}{\tilde{\beta}_2(\tilde{\beta}_3 s + 1)}, \tag{5.22d}$$

$$\tilde{g}_{22}(s) = \frac{\mathrm{e}^{-\tilde{\alpha}_5 s}}{\tilde{\beta}_3 s + 1}, \tag{5.22e}$$

$$\tilde{g}_{23}(s) = 0, \tag{5.22f}$$

$$\tilde{g}_{31}(s) = -\frac{\tilde{\gamma}_1 s^2 + \tilde{\gamma}_2 s + \tilde{\gamma}_3}{\tilde{\gamma}_4 s^3 + \tilde{\gamma}_5 s^2 + \tilde{\gamma}_6 s + \tilde{\gamma}_7}, \tag{5.22g}$$

$$\tilde{g}_{32}(s) = \frac{\tilde{\gamma}_8 s^2 + \tilde{\gamma}_9 s + \tilde{\gamma}_{10} - (\tilde{\gamma}_{11} s + \tilde{\gamma}_{12})\,\mathrm{e}^{-\tilde{\alpha}_5 s}}{\tilde{\gamma}_{13} s^3 + \tilde{\gamma}_{14} s^2 + \tilde{\gamma}_{15} s + \tilde{\gamma}_{16}}, \tag{5.22h}$$

$$\tilde{g}_{33}(s) = -\frac{\tilde{\gamma}_{17}}{\tilde{\gamma}_{18} s^2 + \tilde{\gamma}_{19} s + \tilde{\gamma}_{20}} \tag{5.22i}$$

is considered, where $\tilde{\alpha}_i$, $\tilde{\beta}_j$, $\tilde{\gamma}_k$ denote positive constants. Analyzing (5.22a)–(5.22i) shows that all denominator polynomials are Hurwitz. While

the coefficients of the transfer functions $\tilde{g}_{ij}$ are not given for the sake of compact notation, the scaled steady-state gain matrix

$$\tilde{G}(0) = \begin{bmatrix} 3.12 & -2.95 & 0 \\ -1.48 & 5 & 0 \\ -2.54 \cdot 10^5 & 2.38 \cdot 10^5 & -4.93 \cdot 10^5 \end{bmatrix}. \tag{5.23}$$

is explicitly presented. Let us briefly discuss the physical meaning of the *negative* elements in (5.23):

- $\tilde{g}_{12}(0)$: Increasing $\triangle \tilde{u}_2$, while keeping $\triangle \tilde{u}_1$ constant, yields a larger denominator in (5.4) and thus decreases $\triangle \tilde{y}_1$ see (5.3), (5.4), (5.5).

- $\tilde{g}_{21}(0)$: Increasing $\triangle \tilde{u}_1$, while keeping $\triangle \tilde{u}_2$ constant, decreases $\triangle \tilde{y}_2$, see (5.3), (5.5).

- $\tilde{g}_{31}(0)$: Increasing $\triangle \tilde{u}_1$ initiates an energy flow from the Effect to the Heat Chamber, which, while keeping $\triangle \tilde{u}_2$ and $\triangle \tilde{u}_3$ constant, decreases $\triangle \tilde{y}_3$, see (5.10), (5.12d).

- $\tilde{g}_{33}(0)$: Increasing $\triangle \tilde{u}_3$ initiates an energy flow out the Heat Chamber, see (5.11), (5.12e), which, while keeping $\triangle \tilde{u}_1$ and $\triangle \tilde{u}_2$ constant, decreases $\triangle \tilde{y}_3$, see (5.10), (5.12b).

The Bode plots of the non-zero elements in (5.21) are depicted in Fig. 5.3. Firstly, it is observed that the inertia of $\triangle \tilde{y}_3$ is much larger than the one of $\triangle \tilde{y}_1$ and $\triangle \tilde{y}_2$. Secondly, according to (5.22h), $\tilde{g}_{32}$ is composed of a delayed part and a delay-free part. Since the delay-free part dominates the delayed part, the typical behavior of a delay element cannot be detected from the phase plot of $\tilde{g}_{32}$, see Fig. 5.3. Thirdly, it can be seen that the plant crosses the phase angle of $180°$ at $\omega_{\mathrm{crit}} = 0.0114\,\mathrm{rad\,s^{-1}}$ for the first time, see the black vertical line in Fig. 5.3. As mentioned in [142], ω_{crit} can be interpreted as the plant's crossover frequency and serves as rough orientation for the relevant operation domain, namely, at lower frequencies than ω_{crit}.
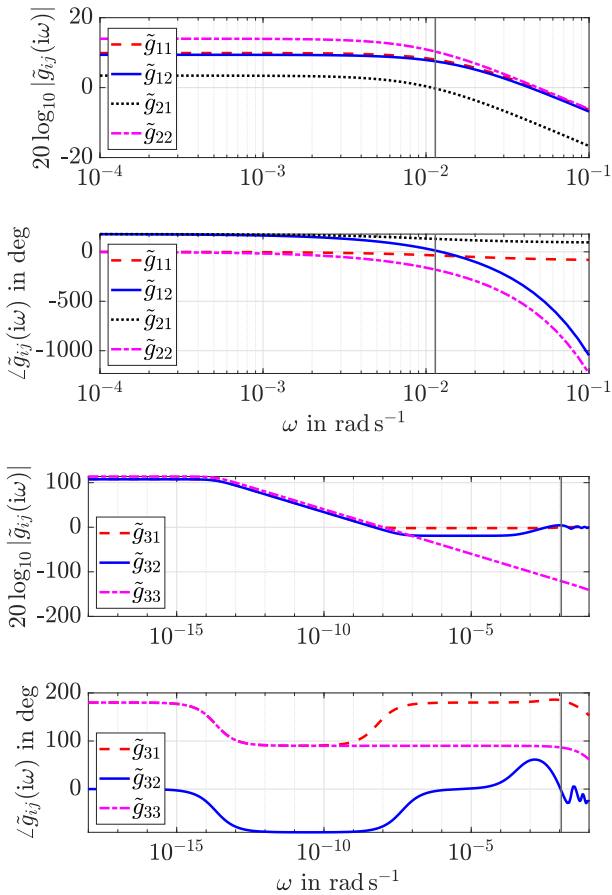
Figure 5.3: Bode plots of the non-zero elements in $\tilde{G}(i\omega)$

5.2.2 Relative Gain Array

The relative gain array (RGA) of a nonsingular square transfer function matrix $G(s)$ being stable is determined by

$$R(s) = G(s) \circ \left(G(s)^{-1}\right)^\top, \qquad (5.24)$$

where $\circ$ denotes the Hadamard product, i.e., elementwise multiplication.

In this context, it is distinguished between the the steady-state RGA $R(s = 0)$, cf. [25, 123], and DRGA $R(s = \mathrm{i}\omega)$, cf. [123, 58]. Regarding DRGA, some advice on determining the relevant frequency domain of a plant is given in Sec. 5.2.1 and in [154]. To practically evaluate $R(\mathrm{i}\omega)$, it is common to consider the magnitude of its elements $|r_{ij}(\mathrm{i}\omega)|$ over ω. In this case, the normalization property of the RGA, see Remark 5.6, is not valid anymore. Furthermore, negative RGA-elements are no more possible, which may lead to misinterpretations. However, these drawbacks can be mitigated by comparing $|R(\mathrm{i}\omega)|$ to the steady-state RGA.

Remark 5.6. Let us make some important remarks on the properties and interpretation of the RGA:

– The essential recommendation is to prefer pairings with RGA-elements close to one and to avoid parings with negative RGA-elements [123].

– The RGA is normalized such that the sum of each column, as well as the sum of each row, is equal to one (normalization property).

– The RGA is independent of the scaling of $G(s)$.

– The RGA can be directly applied to $G(s)$ with time delays [121].

– The RGA enables conclusions on the existence of right half-plane (RHP) transmission zeros in $G(s)$ or RHP-zeros in its elements $g_{ij}(s)$, see [62].

– Generalizations of the RGA to unstable $G(s)$ are known [61].

Application of the steady-state RGA to (5.23) yields

$$R(0) = \begin{bmatrix} 1.39 & -0.39 & 0 \\ -0.39 & 1.39 & 0 \\ 0 & 0 & 1 \end{bmatrix} \tag{5.25}$$

and thus recommends the diagonal pairing, i.e.,

$$y_1 \leftrightarrow u_1, \quad y_2 \leftrightarrow u_2, \quad y_3 \leftrightarrow u_3. \tag{5.26}$$

Regarding DRGA, there are cancellations of all frequency-dependent terms due to the special structure of the plant (5.21). Therefore, the evaluation of the RGA (5.24) for the plant (5.21) leads to

$$R(s) = \begin{bmatrix} \dfrac{\tilde{\alpha}_1 \tilde{\beta}_2 \tilde{\alpha}_6}{\tilde{\alpha}_1 \tilde{\beta}_2 \tilde{\alpha}_6 - \tilde{\alpha}_2 \tilde{\beta}_1 \tilde{\alpha}_4} & \dfrac{\tilde{\alpha}_2 \tilde{\beta}_1 \tilde{\alpha}_4}{\tilde{\alpha}_2 \tilde{\beta}_1 \tilde{\alpha}_4 - \tilde{\alpha}_1 \tilde{\beta}_2 \tilde{\alpha}_6} & 0 \\ \dfrac{\tilde{\alpha}_2 \tilde{\beta}_1 \tilde{\alpha}_4}{\tilde{\alpha}_2 \tilde{\beta}_1 \tilde{\alpha}_4 - \tilde{\alpha}_1 \tilde{\beta}_2 \tilde{\alpha}_6} & \dfrac{\tilde{\alpha}_1 \tilde{\beta}_2 \tilde{\alpha}_6}{\tilde{\alpha}_1 \tilde{\beta}_2 \tilde{\alpha}_6 - \tilde{\alpha}_2 \tilde{\beta}_1 \tilde{\alpha}_4} & 0 \\ 0 & 0 & 1 \end{bmatrix} = \text{const} \tag{5.27}$$

for all s. Thus, by plugging the numerical values of the coefficients $\tilde{\alpha}_k$, $\tilde{\beta}_l$ into (5.27), the same result as in (5.25) is obtained. To conclude, the RGA analysis confirms the result in [142], where a similarly constructed FFE but a different model is investigated.

5.2.3 Niederlinski Index

The following theorem was originally introduced in [96].

Theorem 5.1 (Niederlinski's theorem, refined version [55]).
Consider a closed-loop system composed of the square plant $G(s)$ and the diagonal controller

$$C(s) = \frac{k}{s} \underbrace{\text{diag}\,(\tilde{c}_1(s), \tilde{c}_2(s), \dots, \tilde{c}_m(s))}_{=\tilde{C}(s)}, \quad k > 0, \tag{5.28}$$

where m is the number of plant inputs being equal to the number of plant outputs and $\tilde{c}_j(s)$, $j = 1, 2, \ldots, m$ denotes controllers without integrators. Let us assume that the following conditions hold:

(a) $G(s)$ is stable[6],

(b) $H(s) = G(s)\tilde{C}(s)$ is rational[7] and proper,

(c) each individual control loop is stable if any of the other loops is opened.

Then, a sufficient condition for instability of the closed-loop system is

$$\frac{\det G(0)}{\prod\limits_{j=1}^{m} g_{jj}(0)} < 0. \tag{5.29}$$

Thus, Theorem 5.1 excludes unfeasible pairings in multiloop SISO control systems. Firstly, note that the left-hand side of (5.29) is called Niederlinski index (NI) and is independent of the scaling of $G(s)$, cf. [11]. Secondly, note that NI > 0 is a necessary condition for stability of the multiloop SISO control system [55]. Thirdly, note that the diagonal proper controller $C(s)$ in (5.28) represents all controllers of integrating type, e.g., I, PI or PID [96]. Hence, a cancellation of the zero-pole in $C(s)$ is not allowed. Fourthly, note that Condition (c) of Theorem 5.1 is also referenced as integrity [19].

Evaluating NI of the paring (5.26) leads to

$$\text{NI} = 0.72, \tag{5.30}$$

which is greater than zero and thus allows the conclusion that the pairing (5.26) may yield a stable multiloop SISO control system.

---

[6] Huang et al. [63] have shown that the Niederlinski index can also be applied to plants with *unstable poles* in their diagonal elements.
[7] Huang et al. [63] have shown that the Niederlinski index can also be applied to plants with *time delays*, which is an important result regarding the plant (5.21).

5.2.4 Decentralized Integral Controllability

Definition 5.1 (Decentralized Integral Controllability [122]).
The square plant $G(s)$ is decentralized integral controllable (DIC) if there exists a diagonal controller $C(s)$ with integral action in each loop such that the closed-loop system is stable and such that each individual loop may be detuned independently by a factor ε_j, $0 \leq \varepsilon_j \leq 1$, $j = 1, 2, \ldots, m$ without introducing instability.

To present the criteria for DIC, let us define the structured value μ as follows [39]:

$$\mu(M) = \begin{cases} 0, & \text{if no } \Delta \in X_\infty \text{ solves } \det(I_n + M\Delta) = 0, \\ \left(\min_{\Delta \in X_\infty} \left\{ \sigma_{\max}(\Delta) \,\middle|\, \det(I_n + M\Delta) = 0 \right\} \right)^{-1}, & \text{otherwise,} \end{cases} \tag{5.31}$$

where $M \in \mathbb{C}^{n \times n}$ is a squared complex matrix, $\sigma_{\max}(\Delta)$ the maximum singular value of the block-diagonal perturbation $\Delta \in X_\infty$, and $X_\infty \subset \mathbb{C}^{n \times n}$.[8] Additionally, the matrix $E(0)$ is given by

$$E(0) = \big(G(0) - G_{\text{diag}}(0)\big) G_{\text{diag}}(0)^{-1} \tag{5.32}$$

with

$$G_{\text{diag}}(0) = \text{diag}\big(g_{11}(0), g_{22}(0), \ldots, g_{mm}(0)\big). \tag{5.33}$$

Hence, the following criteria, cf. [122], can be readily introduced and hold for stable $G(s)$: While a necessary condition for DIC

$$r_{jj}(0) \geq 0, \quad j = 1, 2, \ldots, m \tag{5.34}$$

uses the diagonal elements $r_{jj}(0)$ of $R(0)$, a sufficient one

$$\mu\big(E(0)\big) < 1 \tag{5.35}$$

---

[8] More precisely, the numerical solution of the optimization problem (5.31) generally leads to an upper bound $\bar{\mu}$ and a lower bound $\underline{\mu}$ of the structured singular value. In the framework of this thesis, the upper bound is meant when considering the structured singular value, i.e., $\mu(\cdot) := \bar{\mu}(\cdot)$.

is based on the structured singular value μ of the matrix $E(0)$. Firstly, note that $\mu(E(0))$ can be determined numerically in Matlab via *mussv(E,ones(size(E,1),2))* since μ is computed w.r.t. the structure of $C(s)$, see (5.28) and [122]. Secondly, note that there are also other criteria for (2×2) and (3×3) plants, cf. [123]. Thirdly, note that DIC can be related to the concept of passivity, which is detailed in [15].

Remark 5.7. While Niederlinski's theorem [96, 55] provides a sufficient condition for instability of the multiloop SISO control system, the notion of DIC makes a statement on the existence of a stabilizing diagonal controller with integral action. The relation between both concepts is precised in [122].

Let us evaluate the DIC criteria for $\tilde{G}(0)$ according to (5.23). From (5.25), it follows that the necessary condition (5.34) for DIC is fulfilled. The sufficient DIC condition (5.35) is also satisfied since

$$\mu\big(E(0)\big) = 0.53, \tag{5.36}$$

which shows that the plant[9] with pairing (5.26) is DIC. Hence, it is verified that multiloop SISO control with pairing (5.26) is feasible.

5.2.5 Participation Matrix

At first, let us recall the definitions of the Gramian controllability matrix

$$P = \int\limits_0^\infty \mathrm{e}^{A\theta} B B^\top \, \mathrm{e}^{A^\top \theta} \, \mathrm{d}\theta \tag{5.37}$$

---

[9] The same result (5.36) is obtained for the scaled plant $\tilde{G}(0)$ and for the unscaled one $G(0)$. Hence, there are two possibilities: Either, besides the necessary condition (5.34), the sufficient condition (5.35) for DIC is also invariant under scaling or it's a specialty of the considered plant.

and Gramian observability matrix

$$Q = \int_0^\infty e^{A^\top \theta} C^\top C \, e^{A\theta} \, d\theta, \tag{5.38}$$

where the matrices $A \in \mathbb{R}^{n \times n}$, $B \in \mathbb{R}^{n \times m}$ and $C \in \mathbb{R}^{m \times n}$ correspond to the minimal state space representation of the stable plant $G(s)$. Thus, the first Gramian-based interaction measure can be introduced, namely the participation matrix (PM) Φ, see [30], whose elements ϕ_{ij} are given by

$$\phi_{ij} = \frac{\mathrm{tr}(P_j Q_i)}{\mathrm{tr}(PQ)}. \tag{5.39}$$

Note that P_j and Q_i denote the controllability Gramian and observability Gramian, respectively, for the subsystem (i, j), i.e., $g_{ij}(s)$. To enable a comparison of Φ to other Gramian-based measures, see Sec. 5.2.6, the normalization [58]

$$\bar{\phi}_{ij} = \frac{\sqrt{\phi_{ij}}}{\sum\limits_{l=1}^{m} \sum\limits_{k=1}^{m} \sqrt{\phi_{kl}}} \tag{5.40}$$

is used in the sequel and referenced as normalized PM $\bar{\Phi}$. Since the interpretation of $\bar{\Phi}$ is the same as for the other Gramian-based measure (Hankel interaction index array), evaluation of both of these measures is performed in the following subsection.

5.2.6 Hankel Interaction Index Array

Let us start by recapitulating the Hankel singular values (HSVs) of $G(s)$ with Gramians P and Q. The HSVs are given by

$$\sigma_{H,i} = \sqrt{\lambda_i(PQ)}, \quad i = 1, 2, \ldots, n, \tag{5.41}$$

where λ_i are the eigenvalues. The Matlab command to calculate the HSVs of a system *sys* is *hsvd(sys)*. Furthermore, the Hankel seminorm[10] of $G(s)$ is determined by

$$||G(s)||_H = \max_{1 \leq i \leq n} \sigma_{H,i}. \tag{5.42}$$

Let $||g_{ij}(s)||_H$ denote the Hankel seminorm of the (i,j)-subsystem of $G(s)$. Then, according to [144], the (i,j)-th element of the Hankel interaction index array (HIIA) H[11] is determined by

$$h_{ij} = \frac{||g_{ij}(s)||_H}{\sum\limits_{l=1}^{m} \sum\limits_{k=1}^{m} ||g_{kl}(s)||_H}. \tag{5.43}$$

To interpret both of the Gramian-based interaction measures, $\bar{\Phi}$ and H (measure matrices), let us consider the following recommendations [58]:

– The larger the element of the measure matrix, the larger is the impact of the corresponding input on the corresponding output.

– The sum of the measure matrix' elements, which is close to one, determines the control structure.

Since the measure matrices were originally introduced for delay-free $G(s)$, it is convenient to approximate delay terms $e^{-s\tau}$ via Padé approximations [58]. Most importantly, note that the measure matrices *depend* on appropriate *scaling* of the plant model. Thus, the evaluation of the measure matrices requires the scaled plant $\tilde{G}(s)$.

Next, let us calculate $\bar{\Phi}$ and H for $\tilde{G}(s)$ according to (5.21). However, before doing that, notice that Fig. 5.3 reveals strong interaction between $\tilde{g}_{11}$, $\tilde{g}_{12}$, $\tilde{g}_{21}$, and $\tilde{g}_{22}$ while (5.23), (5.25) indicate that controlling y_3 by u_3 is

---

[10] A *norm* gets zero if and only if the zero element is considered (positive definiteness); recall that the remaining properties of a norm are absolute homogeneity and triangle inequality. However, in case of a *seminorm*, positive definiteness is not required, i.e., a seminorm can also get zero if other elements than the zero element are considered. The Hankel norm is a seminorm due to the following reason: If the largest eigenvalue of the matrix PQ is zero, the transfer function matrix $G(s)$ is not necessarily zero.

[11] Note that H is normed by its definition (5.43).

the only possibility. Therefore, the interaction analyses are restricted to the $(w_o, \dot{m}_o)$-plant

$$\tilde{G}_{\mathrm{red}}(s) = \begin{bmatrix} \tilde{g}_{11}(s) & \tilde{g}_{12}(s) \\ \tilde{g}_{21}(s) & \tilde{g}_{22}(s) \end{bmatrix}. \tag{5.44}$$

Furthermore, as recommended in [142], the delay terms in $\tilde{G}_{\mathrm{red}}(s)$ are approximated via a fifth-order Padé approximation which enables application of the Gramian-based interaction measures.

Evaluating the normalized PM, see Sec. 5.2.5, for (5.44) leads to

$$\bar{\Phi} = \begin{bmatrix} 0.1383 & 0.3248 \\ 0.0657 & 0.4712 \end{bmatrix}. \tag{5.45}$$

The sum of the upper triangular in $\bar{\Phi}$ is 0.9343. However, before interpreting this result, let us also evaluate the measure matrix H.

Evaluating the HIIA for (5.44) yields

$$H = \begin{bmatrix} 0.1728 & 0.2876 \\ 0.0821 & 0.4574 \end{bmatrix}. \tag{5.46}$$

Hence, the sum of the upper triangular in H is 0.9179.

To conclude, both of the interaction measures, normalized PM and HIIA, recommend the sparse multivariable controller

$$C(s) = \begin{bmatrix} C_1(s) & C_3(s) \\ 0 & C_2(s) \end{bmatrix} \tag{5.47}$$

with upper triangular structure. In this case, it seems beneficial to design $C_3(s)$ as decoupling feedforward [58].

5.2.7 Summary of Results

The results are twofold: On the one hand, it is shown via RGA, DRGA, NI, and DIC that multiple SISO loop control with the pairing (5.26) is feasible but, on

the other hand, it follows from PM and HIIA that the upper triangular multivariable controller (5.47) may be better to control the strongly interacting $(w_o, \dot{m}_o)$-plant (5.44). Hence, in the following section, it is planned to design such a multivariable controller for the $(w_o, \dot{m}_o)$-plant, while the control of ϑ_{E} is well realizable as SISO loop with $\dot{m}_{\mathrm{v,con}}$ as manipulated variable.[12]

5.3 New Control Concept

Based on the results of Sec. 5.2, a multivariable controller for the $(w_o, \dot{m}_o)$-plant is designed in this section. To design the controller, a model of the $(w_o, \dot{m}_o)$-plant is required. However, the model (5.44) has the following *drawbacks*:

1. (5.44) is based on a linearization about the FFE's standard operation point and therefore this model's range of application is limited.

2. (5.44) only regards manipulated variables and controlled outputs but not the disturbance due to time-varying w_i.

To counter these problems, let us proceed as follows. At first, a *modified* model for the $(w_o, \dot{m}_o)$-plant is introduced in Sec. 5.3.1. Subsequently, in Sec. 5.3.2, the new control concept is derived. Moreover, by taking the actuators' limits into account, the domain of feasible setpoints is calculated. Finally, the influence of parameter uncertainties is considered in Sec. 5.3.3 while Sec. 5.3.4 validates the concept by connecting it to the digital twin of the plant. Thereby, structural uncertainties are investigated.

Remark 5.8. Throughout this section, it is assumed that measurements of the dry matter content w or, more precisely, of w_i and w_o are available. In fact, these variables are indirectly measured via a well-identified static estimator, see Remark 2.1.

---

[12] More precisely, recall from Ch. 2 that ϑ_{E} is controlled via split-range of $\dot{m}_{\mathrm{v,init}}$ and $\dot{m}_{\mathrm{v,con}}$. However, in the framework of Ch. 5, $\dot{m}_{\mathrm{v,init}}$ is neglected, see also Remark 5.1.

5.3.1 Preliminaries

In view of the model (5.9), it is observed that

$$\frac{\mathrm{d}}{\mathrm{d}t}\dot{m}_o(t) = \frac{1}{T_2}\left(\dot{m}_i(t-\tau_2) - \bar{q}P_{\mathrm{C}}(t) - \dot{m}_o(t)\right), \quad \tau_2 := \tau_{\mathrm{T}} \qquad (5.9b)$$

is a *linear* i/o relation w.r.t. the $\dot{m}$-transport through the FFE. Hence, the application of linear control design methods is enabled for (5.9b). However, by recalling

$$\frac{\mathrm{d}}{\mathrm{d}t}w_o(t) = \frac{1}{T_1}\left(\frac{w_i(t-\tau_1)\dot{m}_i(t-\tau_2)}{\dot{m}_i(t-\tau_2) - \bar{q}P_{\mathrm{C}}(t)} - w_o(t)\right), \quad \tau_1 := \tau_{\mathrm{T}} + \tau_{\mathrm{Pipe}}, \ (5.9a)$$

it gets evident that the w-transport is described by a *nonlinear* i/o relation, which prevents us from direct application of linear control methods.

A remedy to this problem without using linearization is described in the following. Instead of considering the dry matter balances, it is also possible to evaluate the dry matter *flow* balances over the corresponding subsystems:

(a) The dry matter flow balance over the *Pipes* is obtained via multiplication of (5.1) by (5.2), which yields

$$\dot{m}_{o,\mathrm{Pipe}}(t)w_{o,\mathrm{Pipe}}(t) = \dot{m}_i(t)w_i(t-\tau_{\mathrm{Pipe}}). \qquad (5.48)$$

(b) The dry matter flow balance over the *Tubes* is obtained via multiplication of (5.4) by $\dot{m}_{o,\mathrm{T}}(t)$, which yields

$$\dot{m}_{o,\mathrm{T}}(t)w_{o,\mathrm{T}}(t) = \dot{m}_{i,\mathrm{T}}(t-\tau_{\mathrm{T}})w_{i,\mathrm{T}}(t-\tau_{\mathrm{T}}). \qquad (5.49)$$

(c) The dry matter flow balance over the *Reservoirs and Plates* can be modeled via low-pass filtering, i.e.,

$$\frac{\mathrm{d}}{\mathrm{d}t}\left(\dot{m}_o(t)w_o(t)\right) = \frac{1}{T_1}\left(\dot{m}_{i,\mathrm{RP}}(t)w_{i,\mathrm{RP}}(t) - \dot{m}_o(t)w_o(t)\right), \qquad (5.50)$$

see Sec. 5.1.3 for further explanations.

In view of Fig. 5.2, it is possible to substitute (5.48) into (5.49) into (5.50), which leads to

$$\frac{\mathrm{d}}{\mathrm{d}t}\big(\dot{m}_o(t)w_o(t)\big) = \frac{1}{T_1}\big(\dot{m}_i(t - \tau_2)w_i(t - \tau_1) - \dot{m}_o(t)w_o(t)\big), \qquad (5.51)$$

where the abbreviations τ_1 and τ_2, see (5.9a) and (5.9b), are used. Moreover, let us approximate (5.51) by

$$\frac{\mathrm{d}}{\mathrm{d}t}\big(\dot{m}_o(t)w_o(t)\big) \approx \frac{1}{T_1}\big(\dot{m}_i(t - \tau_1)w_i(t - \tau_1) - \dot{m}_o(t)w_o(t)\big). \qquad (5.52)$$

By comparing (5.51) and (5.52), it can be seen that $\dot{m}_i(t-\tau_2)$ is substituted by $\dot{m}_i(t-\tau_1)$. This approximation is advantageous regarding the control design in Sec. 5.3.2.

manipulated inputs u	u_1	$\dot{m}_i$
	u_2	P_{C}
disturbance input	z	w_i
states x	x_1	$\dot{m}_o w_o$
	x_2	$\dot{m}_o$
controlled outputs y	y_1	w_o
	y_2	$\dot{m}_o$

Table 5.2: Control nomenclature in Sec. 5.3

To sum up, the i/o dynamics of the $(w_o, \dot{m}_o)$-plant can be modeled via (5.52), (5.9b) which, despite some approximations, turns out to be a useful approach.[13] In the sequel, the control nomenclature in Tab. 5.2 is considered. Then, together with (5.52), (5.9b), the state-space model

---

[13] In identification experiments with real-world data, it is observed that the i/o dynamics of the $(w_o, \dot{m}_o)$-plant are well modeled via (5.52), (5.9b). To spare the reader from further details, these experiments are not discussed in this thesis, but shown in [157].

$$\begin{bmatrix} \dot{x}_1(t) \\ \dot{x}_2(t) \end{bmatrix} = \begin{bmatrix} -\frac{1}{T_1} & 0 \\ 0 & -\frac{1}{T_2} \end{bmatrix} \begin{bmatrix} x_1(t) \\ x_2(t) \end{bmatrix} + \begin{bmatrix} 0 \\ \frac{1}{T_2} \end{bmatrix} u_1(t - \tau_2)$$

$$+ \begin{bmatrix} \frac{1}{T_1} \\ 0 \end{bmatrix} u_1(t - \tau_1)z(t - \tau_1) + \begin{bmatrix} 0 \\ -\frac{\bar{q}}{T_2} \end{bmatrix} u_2(t), \qquad (5.53a)$$

$$\begin{bmatrix} y_1(t) \\ y_2(t) \end{bmatrix} = \begin{bmatrix} x_1(t) \,/\, x_2(t) \\ x_2(t) \end{bmatrix} \qquad (5.53b)$$

is obtained. Let us make some remarks on (5.53).

Remark 5.9. In fact, (5.53) is linear in the state equations (5.53a)[14], but has a nonlinear output equation (5.53b). Although the state matrix of (5.53a) is decoupled, the inputs u_1 and u_2 both affect the $\dot{x}_2$-equation. Additionally, the states x_1 and x_2 are coupled by the output equation (5.53b). Finally, note that the disturbance z couples into (5.53a) via multiplication.

Remark 5.10. Compared to the model (5.9), the advantage of (5.53) is that the nonlinearity is "transferred" from the *dynamic state* equation (5.9a) to the *static output* equation (5.53b).[15] Therefore, instead of linearizing the state equations as in Sec. 5.2.1, an output transformation can be applied to "remove" the nonlinearity, see Sec. 5.3.2.

Application of the Laplace transformation (initial values neglected) to (5.53a) leads to the transfer functions

$$P_{11}(s) = \frac{X_1(s)}{\tilde{U}_1(s)} = \frac{e^{-\tau_1 s}}{1 + T_1 s}, \qquad (5.54a)$$

$$P_{21}(s) = \frac{X_{21}(s)}{U_1(s)} = \frac{e^{-\tau_2 s}}{1 + T_2 s}, \qquad (5.54b)$$

$$P_{22}(s) = \frac{X_{22}(s)}{U_2(s)} = -\frac{\bar{q}}{1 + T_2 s} \qquad (5.54c)$$

---

[14] The nonlinearity $u_1 z$ may be interpreted as pseudo-input $\tilde{u}_1$, see Fig. 5.4. With this notion, it gets obvious that the states and inputs are connected via linear relations in (5.53a).

[15] This "transfer of the nonlinearity" was enabled by considering the *dry matter flow balances* instead of dry matter balances.

of the block diagram in Fig. 5.4, which is an alternative realization of (5.53).
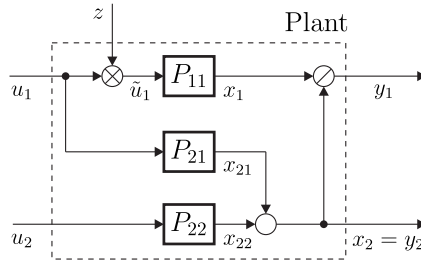
Figure 5.4: Block diagram representation of the plant for control design

5.3.2 Derivation and Design

In the following, all features of the concept are presented, where nonexact plant parameters marked by $\hat{(\cdot)}$ are explicitly considered in the derivation. The latter is composed of the following steps: output transformation, decoupling compensator, feedforward compensators, disturbance rejection, feedback controllers, and consideration of actuator limits.

Output Transformation
Instead of directly controlling the nonlinear output equation (5.53b), it is better to design the controller based on the linear state equations (5.53a). To this end, let us introduce the following output transformation:

$$\begin{bmatrix} x_1 \\ x_2 \end{bmatrix} = \begin{bmatrix} y_1 y_2 \\ y_2 \end{bmatrix} := \Phi(y_1, y_2). \tag{5.55}$$

Hence, as shown in Fig. 5.5, the controller $\mathcal{C}$ becomes a state-based feedback controller and will be designed in the sequel.

Decoupling Compensator
In Fig. 5.4, it gets obvious that y_2 is affected by u_1 via P_{21}. The latter may be interpreted as output disturbance to P_{22}. Hence, it is possible to apply classical disturbance compensation for the purpose of decoupling such that

$$Q_{21}(s)\,\hat{P}_{22}(s) = \hat{P}_{21}(s) \tag{5.56}$$
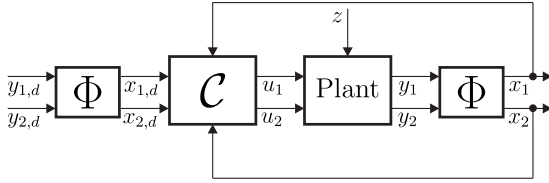
Figure 5.5: Closed-loop system with output transformation Φ and controller $\mathcal{C}$ to be designed

which yields the decoupling compensator

$$Q_{21}(s) = \frac{\hat{P}_{21}(s)}{\hat{P}_{22}(s)} = -\frac{\mathrm{e}^{-\hat{\tau}_2 s}}{\hat{\hat{q}}}.$$
(5.57)

The closed-loop system with decoupling compensator is shown in Fig. 5.6, where the controllers $\mathcal{C}_1$ and $\mathcal{C}_2$ are specified later in this subsection since they include the feedback controllers, feedforward compensators, and disturbance rejection. Note that the closed-loop system in Fig. 5.6 is closely related to the multivariable controller recommended in (5.47).[16]
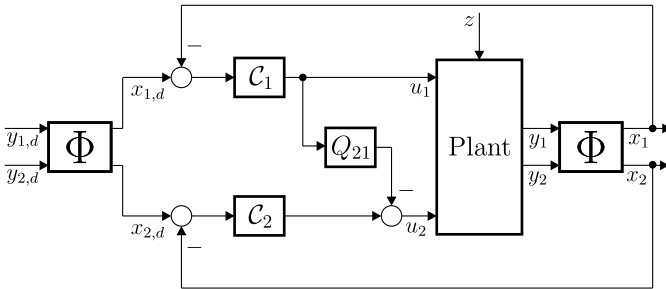
Figure 5.6: Closed-loop system with output transformation Φ, decoupling compensator Q_{21}, and controllers $\mathcal{C}_1$ and $\mathcal{C}_2$ to be designed

---

[16] Indeed, the scheme in Fig. 5.6 directly follows the recommendation from (5.47) since P_{C} is calculated via $\mathcal{C}_2$ and Q_{21}, whereas $\dot{m}_i$ is calculated via $\mathcal{C}_1$. Note that, in Sec. 5.3, the manipulated inputs u are coded via Tab. 5.2 while, in Sec. 5.2, a different coding of u was used, see Tab. 5.1.

Feedforward Compensators

To achieve good reference tracking of $x_{1,d}$, the corresponding feedforward is designed based on P_{11} according to (5.54a). Since P_{11} has a delay, its inverse cannot be calculated directly as noncausal behavior would be the consequence. Instead, let us apply an idea of Kreisselmeier et al. [82] and "split the inverse" into a pre-filter W_{11} and a compensator Q_{11}. To this end, P_{11} is split such that

$$P_{11}(s) = P_{11,0}(s)\, e^{-\tau_1 s}, \tag{5.58}$$

where

$$P_{11,0}(s) = \frac{1}{1 + T_1 s} \tag{5.59}$$

is the delay-free part and $e^{-\tau_1 s}$ is the delayed part. Thus, the compensator Q_{11} is determined by the inverse of $\hat{P}_{11,0}$ while the first-order low-pass filter F with time constant T_f[17] enables properness, i.e.,

$$Q_{11}(s) = \hat{P}_{11,0}^{-1}(s)F(s) = \frac{1 + \hat{T}_1 s}{1 + T_f s}. \tag{5.60}$$

The pre-filter W_{11} is applied to $x_{1,d}$ and composed of the delayed part $e^{-\hat{\tau}_1 s}$ of $\hat{P}_{11}$ as well as of the filter F, cf. [82], such that

$$W_{11}(s) = e^{-\hat{\tau}_1 s} F(s) = \frac{e^{-\hat{\tau}_1 s}}{1 + T_f s}. \tag{5.61}$$

Thereby, it is ensured that x_1 being delayed by P_{11} and $x_{1,d}$ being comparably delayed by W_{11} "meet at the right time". Consequently, $x_{1,d}$ is not controlled. Instead, $\tilde{x}_{1,d}$ is controlled, which corresponds to $x_{1,d}$ delayed and filtered by W_{11}. However, as setpoint control is of interest, the resulting shift between $\tilde{x}_{1,d}$ and $x_{1,d}$ has no practical consequences.

To design the feedforward for P_{22}, let us consider the closed-loop system in Fig. 5.6. Due to the transformation Φ, changes of $y_{2,d}$ affect both control loops, the first and second one. Hence, the same filter W_{11} as applied to $x_{1,d}$

---

[17] Explanations on the choice of T_f are given in Sec. 5.3.3.

must also be applied to $x_{2,d}$ leading to $\tilde{x}_{2,d}$. This issue needs to be considered for the design of the second loop's compensator Q_{22}. From

$$X_2(s) = W_{11}(s)X_{2,d}(s) = Q_{22}(s)\hat{P}_{22}(s)X_{2,d}(s), \qquad (5.62)$$

it follows that

$$Q_{22}(s) = \frac{W_{11}(s)}{\hat{P}_{22}(s)} = -\frac{\mathrm{e}^{-\hat{\tau}_1 s}}{1+T_{\mathrm{f}}s}\frac{1+\hat{T}_2 s}{\hat{\hat{q}}}. \qquad (5.63)$$

Disturbance Rejection
According to Fig. 5.4, the disturbance z couples into the plant via multiplication in front of P_{11}. Hence, the disturbance due to z can be easily rejected by an appropriate division[18], which is shown in Fig. 5.7.[19] The latter depicts the complete control concept.

As interim conclusion, let us reconsider the plant in Fig. 5.4 and recapitulate some results from the previous considerations, namely that

- the nonlinearity (division) at the plant's output is canceled by the output transformation Φ (via multiplication),

- the influence of u_1 via P_{21} on y_2 is canceled by the decoupling compensator Q_{21},

- the influence of z is canceled via division, see Fig. 5.7.

Thus, the design of the feedback controllers C_1 and C_2 can be restricted to P_{11} and P_{22}, respectively.

Feedback Controllers
From internal model control (IMC) theory [93], it is known that P_{11} representing "low-pass filter plus delay" should be controlled by a PI controller

---

[18] The case "division by $z = 0\,\mathrm{kg\,kg^{-1}}$" can appear in practice when the FFE is flooded by water (for cleaning purposes) instead of product. To catch this case, z must be suitably saturated, which is discussed in Sec. 5.3.4.

[19] The disturbance rejection in Fig. 5.7 is a slight improvement to the version in [157]: While the disturbance rejection in [157] only affects the feedforward path, the version in Fig. 5.7 affects both, the feedforward and feedback path.
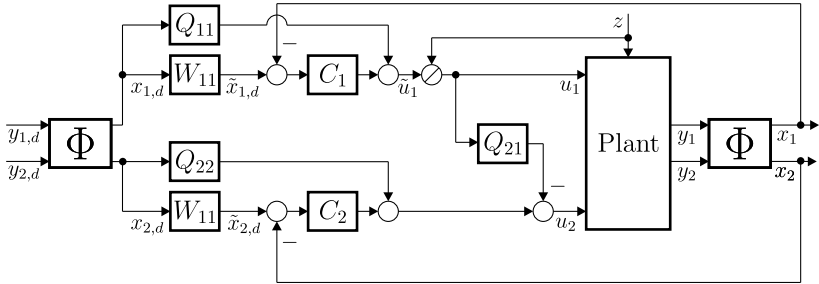
Figure 5.7: Complete control concept consisting of the output tranformation Φ, decoupling compensator Q_{21}, feedforward compensators Q_{11} and Q_{22}, pre-filter W_{11}, disturbance rejection, and controllers C_1 and C_2

with Smith predictor (PI-S).[20] Recalling that the Smith predictor lacks robustness to plant-model mismatches [138], it is not recommendable to implement PI-S. However, there are two alternatives:

1. Modifications of the Smith predictor for unstable plants [88] or for plant models with parameter uncertainty [85, 87] are known.

2. Instead of PI-S, it is possible to apply a PID controller which may outperform PI-S w.r.t. performance-robustness tradeoff [53]. In this case, the derivative action of a PID controller adds a similar effect as the Smith predictor part of PI-S.

As shown in Chapters 3 and 4, the FFE process is well modeled as a system with distributed delays such that the approximation as a system with pointwise delays, see Fig. 5.4 with (5.54), naturally leads to some *structural* model error. Therefore, let us use Alternative 2 in the sequel since it is expected to be superior to Alternative 1 regarding robustness to structural plant-model mismatches. Thus, to control P_{11}, the PID controller

$$C_1(s) = k_{p,1} + \frac{k_{i,1}}{s} + k_{d,1}s \tag{5.64}$$

---

[20] Strictly speaking, the IMC theory leads to PI-S for P_{11} if and only if steps are considered as reference signals [111, 93].

is considered. For realization purposes, the D-part needs to be approximated via low-pass filtering, i.e.,

$$k_{d,1}\, s \approx \frac{k_{d,1}\beta_1 s}{s + \beta_1}. \tag{5.65}$$

As P_{22} represents a simple low-pass filter element, the PI controller

$$C_2(s) = k_{p,2} + \frac{k_{i,2}}{s} \tag{5.66}$$

is applied.[21] In the following, all features without the feedback controllers C_1 and C_2 are referenced as *feedforward structure*.

Remark 5.11. In the proposed control concept, decoupling of the controlled variables is *explicitly* achieved by the feedforward structure. In contrast, the *implicit* solution for another type of FFE via different speeds of control loop responses, see [136], is insufficient for the present FFE configuration. This insufficiency is manifested in closed-loop simulations with the digital twin[22], where large oscillations are observed, especially of $\dot{m}_o$, attributed to only implicit decoupling via controller gains.

Consideration of Actuator Limits
As FFEs usually operate with constant setpoints for long time spans, it is important to ensure that the actuators are kept away from their limits during stationary process. Therefore, a map of feasible setpoint pairs $(y_{1,d}, y_{2,d})$ is developed in this section.
At first, let us consider the stationary i/o equations

$$y_{1,d} = \frac{u_{1,d}\,\bar{z}}{y_{2,d}} \quad \text{and} \quad y_{2,d} = u_{1,d} - \bar{q}\, u_{2,d} \tag{5.67}$$

which can be reformulated by

$$u_{1,d} = \frac{y_{1,d}\, y_{2,d}}{\bar{z}} \quad \text{and} \quad u_{2,d} = \frac{y_{2,d}(y_{1,d} - \bar{z})}{\bar{q}\,\bar{z}}. \tag{5.68}$$

---

[21] The choice of the controller parameters for C_1, see (5.64), (5.65), and C_2, see (5.66), is discussed in Sec. 5.3.3.
[22] Corresponding results are not shown explicitly for the sake of compact representation.

The actuator limits affect that

$$u_{1,d} \in [u_{1,d,\min}, u_{1,d,\max}] = [0, 6.6]\,\mathrm{kg\,s^{-1}}, \tag{5.69a}$$

$$u_{2,d} \in [u_{2,d,\min}, u_{2,d,\max}] = [60, 200]\,\mathrm{kW}. \tag{5.69b}$$

In this context, note that, generally, the Compressor is able to operate at lower power than $60\,\mathrm{kW}$. However, in this case, there would be operation below the critical point, which is not recommended. Furthermore, the maximum value of $u_{1,d}$ corresponds to the fully opened input mass flow control valve, i.e., $\varphi = 1$ in (A.60).

Observe that combining (5.68) with (5.69) yields a system of inequalities, which can be solved analytically so that

$$y_{1,d} \leq \frac{u_{1,d,\max}\,\bar{z}}{y_{2,d}}, \tag{5.70}$$

$$y_{1,d} \leq \frac{\bar{z}(y_{2,d} + \bar{q}\,u_{2,d,\max})}{y_{2,d}}, \tag{5.71}$$

$$y_{1,d} \geq \frac{\bar{z}(y_{2,d} + \bar{q}\,u_{2,d,\min})}{y_{2,d}}. \tag{5.72}$$

Based on (5.70), (5.72), the domain of admissible pairs $(y_{1,d}, y_{2,d})$ is plotted in green for the interesting ranges of $y_{1,d}$, $y_{2,d}$ in Fig. 5.8, where $\bar{z} = 0.35\,\mathrm{kg\,kg^{-1}}$ and $\bar{q} = 0.024\,\mathrm{kg\,kW^{-1}\,s^{-1}}$. Note that, in the ranges of $y_{1,d}, y_{2,d}$ shown in Fig. 5.8, the inequality (5.71) is inactive and can therefore be ignored. Hence, the following choice of setpoints is feasible:

  – Setpoint 1: $y_{1,d} = 0.51\,\mathrm{kg\,kg^{-1}}$, $y_{2,d} = 4.3\,\mathrm{kg\,s^{-1}}$,

  – Setpoint 2: $y_{1,d} = 0.55\,\mathrm{kg\,kg^{-1}}$, $y_{2,d} = 3.8\,\mathrm{kg\,s^{-1}}$.

This choice is considered for the simulations in Sections 5.3.3 and 5.3.4.

5.3.3 Robustness to Parameter Uncertainties

In this section, the simulation model is composed of the plant in Fig. 5.4 and the control structure in Fig. 5.7. Additionally, consider the parameters in Tab. 5.3, where the uncertainties of plant parameters are given in parenthe-
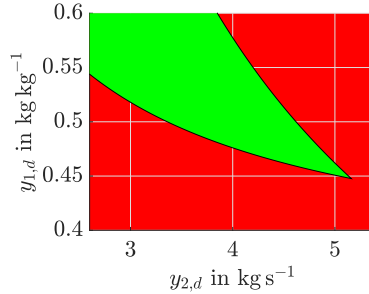
Figure 5.8: Feasible (green) and unfeasible (red) setpoint domains

ses and marked by $(\hat{\cdot})$. Note that all *plant parameters* are identified via output error based least-squares using the digital twin being specified in Sec. 5.3.4. As identification is not in the scope of this chapter, this topic is not detailed any further. Nevertheless, choosing suitable *controller parameters* is important and therefore discussed in Remarks 5.12 and 5.13. In this context, Remark 5.12 shows how to find a suitable value for the filter time constant T_f, whereas Remark 5.13 offers a possibility to determine the parameters of C_1 and C_2.

Remark 5.12. To design the filter time constant T_f, let us consider the feedforward compensators Q_{11} and Q_{22} since they are both affected by T_f. By evaluating the initial value theorem for each Q_{11} and Q_{22}, the gains of the setpoint steps $\triangle x_{1,d}$ and $\triangle x_{2,d}$ (inputs to Q_{11} and Q_{22}) are determined by

$$\lim_{s \to \infty} Q_{11}(s) = \lim_{s \to \infty} \frac{1 + \hat{T}_1 s}{1 + T_f s} = \frac{\hat{T}_1}{T_f},$$

$$\lim_{s \to \infty} Q_{22,0}(s) = \lim_{s \to \infty} -\frac{1 + \hat{T}_2 s}{\hat{q}(1 + T_f s)} = -\frac{\hat{T}_2}{\hat{q} T_f}.$$

Note that, in case of Q_{22}, the delay-free part $Q_{22,0}$ must be considered since delaying has no effect on the gain behavior. Together with the corresponding maximum allowed feedforward steps $\triangle \tilde{u}_{1,ff}$ and $\triangle u_{2,ff}$ (outputs of Q_{11} and Q_{22}), a lower bound of T_f is found.

symbol	value	unit
T_1 ($\hat{T}_1 = 1.4\,T_1$)	70.36 (98.50)	s
T_2 ($\hat{T}_2 = 0.6\,T_2$)	154.1 (92.47)	s
τ_1 ($\hat{\tau}_1 = 1.4\,\tau_1$)	251.0 (351.4)	s
τ_2 ($\hat{\tau}_2 = 0.6\,\tau_2$)	185.0 (111.0)	s
$\bar{q}$ ($\hat{\bar{q}} = 1.4\,\bar{q}$)	0.024 (0.034)	$\mathrm{kg\,kW^{-1}\,s^{-1}}$
T_f	127.3	s
$k_{p,1}$	0.506	—
$k_{i,1}$	0.001	$\mathrm{s^{-1}}$
$k_{d,1}$	-196.7	s
β_1	0.002	$\mathrm{s^{-1}}$
$k_{p,2}$	-61.17	—
$k_{i,2}$	-0.397	$\mathrm{s^{-1}}$

Table 5.3: Parameters for the simulation of the new control concept

Remark 5.13. Since T_f is designed as a lower bound, see Remark 5.12, high speed of the control concept is enabled by the feedforward structure. Hence, there is robustness reserve with regard to the gains of the feedback controllers C_1 and C_2. Via Simulink's built in *PID Tuner*, the robustness reserve can be easily exploited by tuning the transient behavior to be robust. This approach yields the controller gains shown in Tab. 5.3. In this context, it is ensured that overshoots are small to avoid fouling and product losses. Moreover, parametric uncertainties can cause imperfect decoupling. Therefore, the settings of C_1 and C_2 can influence each other and thus iterative tuning is required. Finally, the reader might be surprised that some controller gains are negative which is explained as follows: Firstly, $k_{d,1}$ may be negative since it must be considered *together* with the low-pass filter parameter β_1 leading to stable zeros of the PID controller.[23] Secondly, $k_{p,2}$ and $k_{i,2}$ are negative due to the negative gain of P_{22}, see (5.54c).

---

[23] see also https://de.mathworks.com/help/slcontrol/ug/when-tuning-the-pid-controller-the-d-gain-has-a-different-sign-from-the-i-gain.html, retrieved, July 14, 2021, 10:28.

Before the concept can be simulated, a suitable test signal for the disturbance $z = w_i$ (input dry matter content) must be defined. To this end, the following scenario is considered: The liquid fed into the FFE comes from a feed tank, where the dry matter content at the bottom is larger than at the top due to imperfect mixing and sedimentation. Since the tank's outlet is at the bottom, w_i is initially higher than its average $\bar{w}_i$ and then lowers until the tank is empty. After approximately two hours, the feed tank is empty and gets replaced by a new one so that w_i increases fast. In the sequel, this behavior is simulated as a sawtooth wave for w_i, which falls from $0.36\,\mathrm{kg\,kg^{-1}}$ to $0.34\,\mathrm{kg\,kg^{-1}}$ within two hours and then steps back to $0.36\,\mathrm{kg\,kg^{-1}}$.

Next, let us consider the following simulation steps:

1. $t = 0\,\mathrm{s}$: Start from the stationary state.

2. $t = 2000\,\mathrm{s}$: Step from Setpoint 1 to Setpoint 2.

3. $t = 4600\,\mathrm{s}$: Step from Setpoint 2 to Setpoint 1.

4. $t = 7200\,\mathrm{s}$: Step of disturbance z due to feed tank exchange.

All simulations are performed with ideal initial conditions. Furthermore, actuator dynamics, see App. A.8, are neglected. The corresponding results are shown in Fig. 5.9.

Observe that, in case of no plant-model mismatches, i.e., the control structure's $(\hat{\cdot})$-parameters exactly match the plant's parameters, y_1, y_2 overlap $\tilde{y}_{1,d}$, $\tilde{y}_{2,d}$, where the latter correspond to $y_{1,d}$, $y_{2,d}$ filtered by W_{11}, see (5.61). In this case, the closed-loop behavior is completely determined by the feedforward structure such that there is no contribution of the controllers C_1 and C_2. If there are plant-model mismatches, i.e., the control structure's $(\hat{\cdot})$-parameters are different from the plant parameters as shown in Tab. 5.3, the tracking and disturbance response of $\hat{y}_1$, $\hat{y}_2$ is still good although the parameter uncertainties are $\pm 40\,\%$. This fact emphasizes the apparent robustness of the present concept.

Finally, let as discuss two artifacts observed in Fig. 5.9: Firstly, note that u_1 and $\hat{u}_1$ initially match exactly while there is an initial mismatch between u_2 and $\hat{u}_2$. The reason for this behavior is that, $\hat{u}_1$ is only affected by the nonexact time constant $\hat{T}_1$, see (5.60), which has no disturbing effects in case of

(a) Dry matter content

(b) Input mass flow

(c) Output mass flow

(d) Compressor power
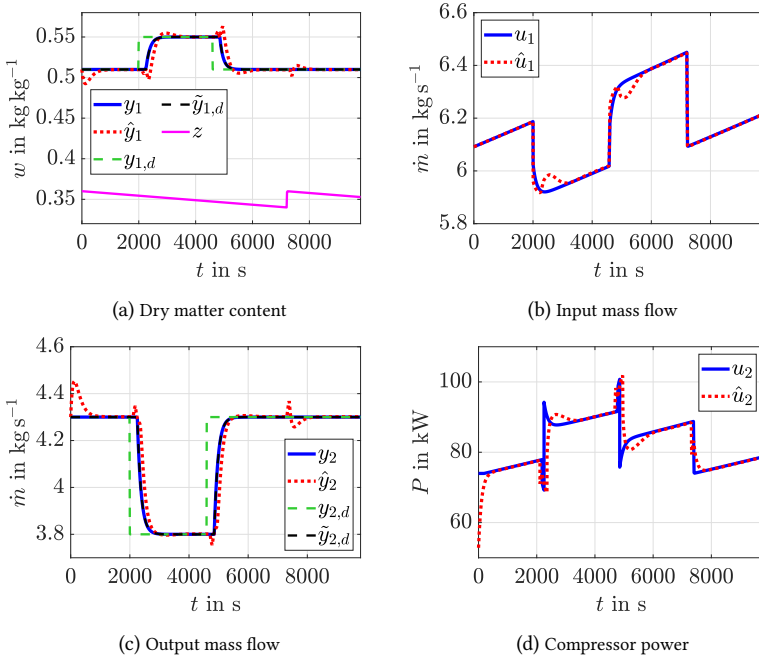
Figure 5.9: Simulation of the control concept for exact and nonexact plant parameters

ideal initial conditions. However, $\hat{u}_2$ is additionally affected by the nonexact parameter $\hat{\tilde{q}}$ leading to a gain mismatch in the feedforward structure, see (5.57) and (5.63), and thus causes the initial mismatch of u_2 and $\hat{u}_2$. Secondly, in Fig. 5.9d, it can be seen that u_2 exhibits wiggles during setpoint changes. To explain this behavior, let us consider the up-step of $y_{2,d}$ at $t = 4600\,\mathrm{s}$ with ideal parameters: Due to this step of $y_{2,d}$, the manipulated variable u_1 directly (without delay) reacts via the feedforward compensator Q_{11}. After the time τ_2, the decoupling compensator Q_{21} compensates the reaction of u_1 by increasing u_2. Subsequently, after the time $\tau_1 - \tau_2$, the feedforward compensator Q_{22} decreases u_2 to finally adjust the new (higher) desired output mass flow. Practically, these wiggles of u_2 are strongly mitigated due to the slew rate limiter acting on the Compressor's speed N_C, see App. A.8.

5.3.4 Validation via Digital Twin

In this section, the control structure in Fig. 5.7 is connected to the plant which basically consists in the digital twin from Ch. 2. More precisely, compared to Ch. 2, the following modifications are implemented in the digital twin of the present chapter:

1. Since the Tubes' model in Ch. 2 has numerical drawbacks due to its discrete-time representation, it is replaced by the Overtaking Particle Flow (OPF) model with water-proportional evaporation which is introduced in Ch. 3 and experimentally proven in Ch. 4. Note that OPF has similar behavior as the discrete-time model in Ch. 2, but has better numerical stability due to its continuous-time nature.

2. The actuator dynamics described in App. A.8 are additionally included in the digital twin.

The controller parameters correspond to the ones in Tab. 5.3, where the exact parameters T_1, T_2, τ_1, τ_2, and $\bar{q}$ are applied since structural plant-model mismatches are investigated in this section.

Before the control structure is initialized, the FFE is flooded by water for cleaning purposes during $t \in [0, 2000)$ s. At $t = 2000$ s, the liquid to be concentrated (product) enters the FFE which is recognized by a large step of z, see Fig. 5.10a. During the operation with water, there is $z = 0 \, \text{kg} \, \text{kg}^{-1}$, which would affect division by zero in the feedforward structure, see Fig. 5.7. This problem is avoided by setting the lower bound of z to $z_{\min} = 0.34 \, \text{kg} \, \text{kg}^{-1}$, which corresponds to the minimum possible value for z during operation with product.

To validate the proposed control concept, let us consider the following scenario, which implies a ramp-up strategy for the FFE process:

(a) $t = 200$ s: Ramp up the Compressor power by stepping from its initial value $u_{2,0} = 0 \, \text{kW}$ to $u_{2,d}$ calculated by (5.68) with $\bar{z} := z_{\min}$ and $y_{1,d}, y_{2,d}$ according to Setpoint 1.

(b) $t = 460$ s: Ramp up the input mass flow by stepping from its initial value $u_{1,0} = 2.7 \, \text{kg} \, \text{s}^{-1}$ to $u_{1,d}$ calculated by (5.68) with $\bar{z} := z_{\min}$ and $y_{1,d}, y_{2,d}$ according to Setpoint 1.

(a) Dry matter content

(b) Input mass flow

(c) Output mass flow

(d) Compressor power
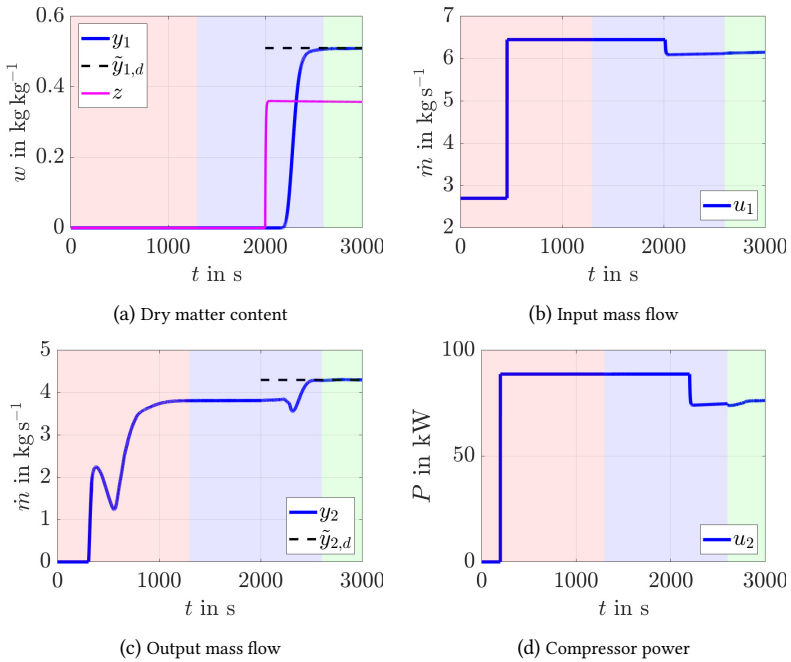
Figure 5.10: Validation of the ramp-up strategy via digital twin

(c) $t = 1300\,\text{s}$: Switch to u_1, u_2 calculated by the feedforward structure some time before the product enters the FFE at $t = 2000\,\text{s}$.

(d) $t = 2600\,\text{s}$: Additionally, switch on the feedback controllers C_1, C_2 when y_1, y_2 are close to their operation points.

(e) $t = 4000\,\text{s}$: Step from Setpoint 1 to Setpoint 2.

(f) $t = 7000\,\text{s}$: Step from Setpoint 2 to Setpoint 1.

(g) $t = 9200\,\text{s}$: Step of disturbance z due to feed tank exchange.

The corresponding results are depicted in Fig. 5.10 and Fig. 5.11, where Fig. 5.10 shows the ramp-up process and Fig. 5.11 the setpoint changes

(a) Dry matter content

(b) Input mass flow

(c) Output mass flow
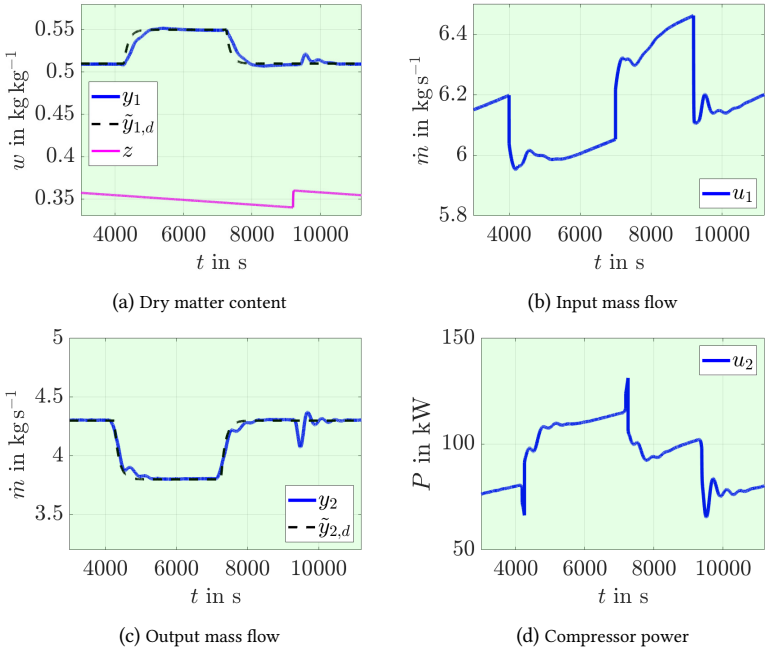
(d) Compressor power

Figure 5.11: Validation of the tracking and disturbance response via digital twin

and disturbance response. Note that the background colors in Fig. 5.10 and Fig. 5.11 have the following meanings:

- The red area corresponds to ramp-up of Compressor power and input mass flow, i.e., Items (a), (b).

- The blue area corresponds to control under pure feedforward structure, i.e., Item (c).

- The green area corresponds to control under feedforward structure plus feedback controllers, i.e., Items (d)–(g).

In Fig. 5.10a and Fig. 5.10c, it gets evident that the idea to ramp-up the process via pure feedforward structure yields a well-controlled transient behav-

ior when product instead of water is introduced into the FFE at $t = 2000$ s. Furthermore, in Fig. 5.11a and Fig. 5.11c, it can be seen that both, the tracking and disturbance response, have satisfying behavior. Thus, the proposed concept is considered to be validated.

5.4 Takeaways

Let us summarize the main results and highlights of this chapter:

– Via RGA, NI, and DIC, it is verified that multiloop SISO control of the FFE process with loop pairing (5.26) is feasible.

– Via PM and HIIA, it is found that a multiviable controller with triangular structure outperforms multiloop SISO control of the $(w_o, \dot{m}_o)$-plant.

– A new multivariable control concept is developed, which actively addresses the major challenges encountered in control of FFEs: large transport delays, additional control of the output mass flow, strong plant couplings, and disturbances due to time-varying input dry matter content.

– Robustness of the concept w.r.t. *parametric* plant-model mismatch is shown in a simulation study.

– Robustness of the concept w.r.t. *structural* plant-model mismatch is shown via the digital twin of the plant.

– A new automated ramp-up strategy for the FFE process is proposed and validated.

– Simple implementation of the concept to standard digital control systems is possible due to block diagram representation.

6 Summary and Outlook

Motivated by a request from GEA Wiegand GmbH, the essential aim of this thesis was to develop new transport models for evaporating liquid films and a new control concept for the falling film evaporator (FFE) process. To connect and thus reach both of these aims, the basic plan consisted in acquiring a deep understanding of the process and required a close cooperation with the industry. In the framework of this cooperation, the author made the experience that there is a large gap between the industrial practice and science. Hence, the present thesis had the intention to minimize this gap as far as allowed by the time constraints on a dissertation.

Based on the open problems and objectives specified in Ch. 1, the challenges and corresponding solutions are, in the following, compactly summarized for each chapter. To this end, the thesis' main results are consecutively enumerated, see Items 1. to 11., but attributed to each chapter.[1]

Chapter 2 – A Digital Twin for a Falling Film Evaporator
While the literature mainly considers dynamic models with constant delays, a dynamic FFE model enabling the simulation of time-varying delay behavior is developed in this chapter.
To easily model the dynamics of various designs, the FFE process is divided into connectable subsystems. Via real-world data of a certain FFE design (one Effect, four passes, mechanical vapor recompression), the corresponding plant model is validated so that a digital twin is generated.
Hence, the main results of this chapter are as follows:

1. Development of dynamic models for subsystems of FFEs.

2. Implementation of the subsystem models to Matlab/Simulink, where parameters are set via user-friendly interfaces.

---

[1] Smaller intermediate results are described in the takeaways at the end of each chapter.

3. Validation of a certain FFE model to obtain a digital twin of the plant.

In this context, it is observed that the dynamic behavior of evaporating liquid film in the FFE's Tubes requires further research, which is conducted in Ch. 3.

Chapter 3 – New Models for Evaporating Liquid Films
Unlike the liquid transport in completely filled Pipes, modeling of evaporating falling film in Tubes is challenging. Since a control engineer is most notably interested in the input-output (i/o) behavior, the method of characteristics offers a possibility to transform hyperbolic PDEs into time-delay relations.
To this end, fundamental balance equations of transported instances, i.e. plugs or particles, are evaluated so that systems of first-order quasilinear PDEs are derived. The latter may be interpreted as special formulations of the transport equation with a sink term representing evaporation. More precisely, the following new flow models are obtained:

(a) Dynamic Plug Flow (DPF): Transported instances move without overtaking such that the First-In-First-Out (FIFO) principle holds. The instances may have different velocities, but the velocity of a single instance stays constant during its travel.

(b) Overtaking Particle Flow (OPF): Transported instances can overtake one another. At the input, they assume different velocities according to a probability-like distribution function but still, each instance's velocity stays constant during its travel.

To model the sink term, the following approaches are presented:

(i) Uniform evaporation: The total vapor mass flow from the Tube is distributed uniformly among the transported instances.

(ii) Water-proportional evaporation: The total vapor mass flow from the Tube is distributed among the transported instances proportionally to their water contents.

(iii) Localized evaporation: The vapor mass flow from each transported instance is calculated separately.

While uniform evaporation is known from the literature, water-proportional evaporation and localized evaporation are new models. By considering tech-

nically reasonable combinations of transport PDEs (a), (b) and sink terms (i), (ii), (iii), the method of characteristics is applied to obtain the corresponding time-delay relations. Finally, these models are implemented in Matlab/Simulink and their ability to map the qualitatively observed i/o behavior is discussed.

Summing up, the main contributions of this chapter are:

4. Derivation of two new PDE-based transport models with three different ways to model the sink term (evaporation).

5. Transformation of certain new PDE models into time-delay models via the method of characteristics.

6. Implementation of the time-delay models to Matlab/Simulink and discussion of each model's specific behavior.

To show the practical significance of the proposed approach, a chosen time-delay model is further treated in Ch. 4.

Chapter 4 – Identification of Distributed Delays and Experimental Proof of a New Model

By taking the effort-accuracy tradeoff into account, the *OPF model with water-proportional evaporation* is chosen for identification and experimental proof. As shown in Ch. 3, the time-delay representation of this model is a system with distributed delays. Since the literature only investigates academic examples to estimate distributed delays, a practically applicable method should be developed.

For this purpose, pilot plant experiments without evaporation are conducted. Via output error based least-squares, relations for the parameters specifying the model's distributed delay behavior are identified. In experiments with evaporation, the identified model reveals its ability to simulate real-world FFE conditions. This fact leads us to the conclusion that the influence of evaporation on the liquid film's delay behavior can be neglected.

Thus, this chapter's main results are:

7. Identification of a chosen model's distributed delay behavior.

8. Experimental proof of the identified model.

As the thesis' modeling part is finished by these results, Ch. 5 deals with control of the FFE process.

Chapter 5 – A New Multivariable Control Concept for Falling Film Evaporators

Before developing a new control concept, some analyses of the plant are required. To this end, the plant model from Ch. 2 is simplified and condensed to the i/o dynamics of the manipulated and controlled variables, as well as disturbances. In this context, first analyses reveal that it is sufficient to only focus on the plant with the output dry matter content w_o and output mass flow $\dot{m}_o$ as controlled variables, i.e., the $(w_o, \dot{m}_o)$-plant. While the literature found that the $(w_o, \dot{m}_o)$-plant is strongly coupled, this thesis' analyses extend this result by the recommendation to design a multivariable controller with upper triangular structure. Motivated by this notion and the fact that decoupling of the $(w_o, \dot{m}_o)$-plant is only solved implicitly in the literature, the aim is to develop an explicit solution.

Based on a simplified but still nonlinear plant model, an output transformation enables linearization so that classical methods such as decoupling, feedforward design, and disturbance rejection are applied. As the feedforward structure is responsible for fast performance of the concept, the feedback controllers are designed as robust PI(D) controllers. By investigating structural model uncertainties via the digital twin, it is shown that the concept can be readily implemented in the practice.

In conclusion, the main results of this chapter are:

9. Development of new control-oriented i/o models for the FFE process.

10. Solution of the loop pairing problem and analysis of plant interactions for the FFE process.

11. Design and validation of a new multivariable control concept for the FFE process.

These promising results motivate future research which should generally tend to keep on closing the gap between the recent theoretical ideas and industrial practice. For this purpose, **three directions** are possible:

(A) Predictive control techniques [8, 83] can be extended and applied to the new transport models presented in Ch. 3. According to the author's experience with such approaches, special challenges should consist in sufficient robustness w.r.t. structural model uncertainties and in implementation to digital control systems. Additionally, teaching of opera-

tors would be very important to acquire understanding and acceptance among the plant personnel.

(B) Since the presented method to identify distributed delays, see Ch. 4, requires tedious experiments, application of online time-delay estimation algorithms is desired. In this context, the question of sufficient excitation is of importance. As many process engineering applications operate in stationary states over long time spans, methods, which are able to estimate the delay although the excitation is low, should be developed and applied.

(C) Developping soft sensors gets more and more important in modern process engineering. Regarding FFEs, an idea is the early detection of fouling via degradation of the Tubes' heat transfer coefficients.

From the practical perspective, implementation of the control concept presented in Ch. 5 to real-world falling film evaporators is planned. However, to do this, long-lasting tests with a pilot plant must be conducted in advance. Due to limited time resources, the corresponding results are no more part of the present thesis.

A Appendix

A.1 Solution of the PDEs of DPF with Uniform Evaporation

In this appendix, the DPF equations (3.2) are solved under the uniform evaporation assumption (3.37) using the method of characteristics. Direct application of this method to (3.2) is not possible due to the terms $\xi_{\mathrm{w}}\frac{\partial c}{\partial x}$ in (3.2a) and $\xi_{\mathrm{d}}\frac{\partial c}{\partial x}$ in (3.2b). However, by introducing the variable $\zeta(t,x) := \frac{\partial c(t,x)}{\partial x}$, the system (3.2) of three PDEs with assumption (3.37) can be transformed into the following system of four PDEs:

$$\frac{\partial \xi_{\mathrm{w}}(t,x)}{\partial t} + c(t,x)\frac{\partial \xi_{\mathrm{w}}(t,x)}{\partial x} = -\xi_{\mathrm{w}}(t,x)\zeta(t,x) - q(t), \qquad \text{(A.1a)}$$

$$\text{IC: } \xi_{\mathrm{w}}(t_0,x) = \xi_{\mathrm{w},0}(x),$$

$$\text{BC: } \xi_{\mathrm{w}}(t,0) = \frac{\dot{m}_{i,\mathrm{T}}(t)\big(1 - w_{i,\mathrm{T}}(t)\big)}{c(t,0)},$$

$$\frac{\partial \xi_{\mathrm{d}}(t,x)}{\partial t} + c(t,x)\frac{\partial \xi_{\mathrm{d}}(t,x)}{\partial x} = -\xi_{\mathrm{d}}(t,x)\zeta(t,x), \qquad \text{(A.1b)}$$

$$\text{IC: } \xi_{\mathrm{d}}(t_0,x) = \xi_{\mathrm{d},0}(x),$$

$$\text{BC: } \xi_{\mathrm{d}}(t,0) = \frac{\dot{m}_{i,\mathrm{T}}(t)w_{i,\mathrm{T}}(t)}{c(t,0)},$$

$$\frac{\partial c(t,x)}{\partial t} + c(t,x)\frac{\partial c(t,x)}{\partial x} = 0, \qquad \text{(A.1c)}$$

$$\text{IC: } c(t_0,x) = c_0(x),$$

$$\text{BC: } c(t,0) = \bar{c}_{i,\mathrm{T}}(t),$$

163

$$\frac{\partial \zeta(t,x)}{\partial t} + c(t,x)\frac{\partial \zeta(t,x)}{\partial x} = -\zeta^2(t,x), \tag{A.1d}$$

$$\text{IC: } \zeta(t_0, x) = \frac{\mathrm{d}c_0(x)}{\mathrm{d}x},$$

$$\text{BC: } \zeta(t,0) = -\frac{\dot{\bar{c}}_{i,\mathrm{T}}(t)}{\bar{c}_{i,\mathrm{T}}(t)} \quad \text{with} \quad \dot{\bar{c}}_{i,\mathrm{T}}(t) := \frac{\mathrm{d}}{\mathrm{d}t}\bar{c}_{i,\mathrm{T}}(t),$$

$$\text{Output 1: } \dot{m}_{o,\mathrm{T}}(t) = \big(\xi_\mathrm{w}(t,\ell_\mathrm{T}) + \xi_\mathrm{d}(t,\ell_\mathrm{T})\big)c(t,\ell_\mathrm{T}),$$

$$\text{Output 2: } w_{o,\mathrm{T}}(t) = \frac{\xi_\mathrm{d}(t,\ell_\mathrm{T})}{\xi_\mathrm{w}(t,\ell_\mathrm{T}) + \xi_\mathrm{d}(t,\ell_\mathrm{T})}.$$

Let us introduce the parameterization $(\tilde{t}(\sigma), \tilde{x}(\sigma))$, $\sigma \geq 0$ of the characteristic time-space curves and denote the values of the dependent variables on the curves using the abbreviation

$$\tilde{\square}(\sigma) = \square\big(\tilde{t}(\sigma), \tilde{x}(\sigma)\big), \tag{A.2}$$

where $\square$ is ξ_w, ξ_d, c, or ζ. Comparing the coefficients of the identity

$$\frac{\mathrm{d}\tilde{t}}{\mathrm{d}\sigma}\frac{\partial\tilde{\square}}{\partial\tilde{t}} + \frac{\mathrm{d}\tilde{x}}{\mathrm{d}\sigma}\frac{\partial\tilde{\square}}{\partial\tilde{x}} = \frac{\mathrm{d}\tilde{\square}}{\mathrm{d}\sigma} \tag{A.3}$$

to the PDEs (A.1), the following system of characteristic equations is obtained:

$$\frac{\mathrm{d}\tilde{t}(\sigma)}{\mathrm{d}\sigma} = 1, \quad \tilde{t}(0) = \tilde{t}_0 \tag{A.4a}$$

$$\frac{\mathrm{d}\tilde{x}(\sigma)}{\mathrm{d}\sigma} = \tilde{c}(\sigma), \quad \tilde{x}(0) = \tilde{x}_0 \tag{A.4b}$$

$$\frac{\mathrm{d}\tilde{\xi}_\mathrm{w}(\sigma)}{\mathrm{d}\sigma} = -\tilde{\xi}_\mathrm{w}(\sigma)\tilde{\zeta}(\sigma) - q(\tilde{t}(\sigma)), \quad \tilde{\xi}_\mathrm{w}(0) = \tilde{\xi}_{\mathrm{w},0} \tag{A.4c}$$

$$\frac{\mathrm{d}\tilde{\xi}_\mathrm{d}(\sigma)}{\mathrm{d}\sigma} = -\tilde{\xi}_\mathrm{d}(\sigma)\tilde{\zeta}(\sigma), \quad \tilde{\xi}_\mathrm{d}(0) = \tilde{\xi}_{\mathrm{d},0} \tag{A.4d}$$

$$\frac{\mathrm{d}\tilde{c}(\sigma)}{\mathrm{d}\sigma} = 0, \quad \tilde{c}(0) = \tilde{c}_0 \tag{A.4e}$$

$$\frac{\mathrm{d}\tilde{\zeta}(\sigma)}{\mathrm{d}\sigma} = -\tilde{\zeta}^2(\sigma), \quad \tilde{\zeta}(0) = \tilde{\zeta}_0. \tag{A.4f}$$

The solution of the ODEs (A.4) is

$$\tilde{t}(\sigma) = \tilde{t}_0 + \sigma, \tag{A.5a}$$

$$\tilde{x}(\sigma) = \tilde{x}_0 + \tilde{c}_0\sigma, \tag{A.5b}$$

$$\tilde{\xi}_{\mathrm{w}}(\sigma) = \frac{1}{1 + \tilde{\zeta}_0\sigma} \left(\tilde{\xi}_{\mathrm{w},0} - \int_{\tilde{t}_0}^{\tilde{t}_0+\sigma} q(\alpha)\big(1 + \tilde{\zeta}_0(\alpha - \tilde{t}_0)\big)\,\mathrm{d}\alpha \right), \tag{A.5c}$$

$$\tilde{\xi}_{\mathrm{d}}(\sigma) = \frac{\tilde{\xi}_{\mathrm{d},0}}{1 + \tilde{\zeta}_0\sigma}, \tag{A.5d}$$

$$\tilde{c}(\sigma) = \tilde{c}_0, \tag{A.5e}$$

$$\tilde{\zeta}(\sigma) = \frac{\tilde{\zeta}_0}{1 + \tilde{\zeta}_0\sigma}. \tag{A.5f}$$

Looking to find the solution of the PDEs (A.1) in a given point (t, x), the characteristic curve satisfying the boundary conditions

$$\tilde{t}(\sigma) = t, \qquad \tilde{x}(\sigma) = x \tag{A.6}$$

is of interest. As for the other boundary condition $(\tilde{t}_0, \tilde{x}_0)$, recall that, in terms of plug flow, the characteristic curve $(\tilde{t}(\sigma), \tilde{x}(\sigma))$ is the trajectory of a single plug. Therefore, let us consider two cases:

1. Suppose the plug crossing the point x at time t originated from the initial mass distribution. Let the initial (at $t = t_0$) position of that plug be denoted $x_i(t, x) \in [0, \ell_{\mathrm{T}}]$. In this case, the characteristic curve satisfying the boundary conditions

$$\tilde{t}_0 = t_0, \qquad \tilde{x}_0 = x_i(t, x) \tag{A.7}$$

is of interest. Substituting (A.6) and (A.7) into (A.5), unwrapping the notation (A.2), and using the initial conditions of the PDEs (A.1) yields the solution

$$\xi_{\mathrm{w}}(t, x) = \frac{1}{\mu(t, x)} \left(\xi_{\mathrm{w},0}\big(x_i(t, x)\big) - \int_{t_0}^{t} q(\alpha)\mu(\alpha, x)\,\mathrm{d}\alpha \right), \tag{A.8a}$$

165

$$\xi_{\mathrm{d}}(t, x) = \frac{\xi_{\mathrm{d},0}\big(x_i(t, x)\big)}{\mu(t, x)}, \tag{A.8b}$$

$$c(t, x) = c_0\big(x_i(t, x)\big), \tag{A.8c}$$

$$x_i(t, x) = x - c_0\big(x_i(t, x)\big)(t - t_0), \tag{A.8d}$$

where

$$\mu(t, x) := 1 + \left.\frac{\mathrm{d}c_0(x)}{\mathrm{d}x}\right|_{x_i(t,x)} (t - t_0). \tag{A.9}$$

2. Suppose the plug crossing the point x at time t originated from the input mass flow. Let $t_i(t, x) \geq t_0$ be the time when this plug enters through the input boundary $x = 0$. Then the boundary condition for the corresponding characteristic is

$$\tilde{t}_0 = t_i(t, x), \qquad \tilde{x}_0 = 0. \tag{A.10}$$

Similarly to the previous case, the solution

$$\xi_{\mathrm{w}}(t, x) = \frac{1}{\nu(t, \theta)} \left(\frac{\dot{m}_{i,\mathrm{T}}(\theta)\left(1 - w_{i,\mathrm{T}}(\theta)\right)}{\bar{c}_{i,\mathrm{T}}(\theta)} \right.$$
$$\left. - \int_{\theta}^{t} q(\alpha)\nu(\alpha, \theta)\,\mathrm{d}\alpha \right)\Bigg|_{\theta = t_i(t,x)}, \tag{A.11a}$$

$$\xi_{\mathrm{d}}(t, x) = \left.\frac{\dot{m}_{i,\mathrm{T}}(\theta)\,w_{i,\mathrm{T}}(\theta)}{\nu(t, \theta)\,\bar{c}_{i,\mathrm{T}}(\theta)}\right|_{\theta = t_i(t,x)}, \tag{A.11b}$$

$$c(t, x) = \bar{c}_{i,\mathrm{T}}\big(t_i(t, x)\big), \tag{A.11c}$$

$$t_i(t, x) = t - \frac{x}{\bar{c}_{i,\mathrm{T}}\big(t_i(t, x)\big)} \tag{A.11d}$$

is obtained, where

$$\nu(t,\theta) := 1 - \frac{\dot{\bar{c}}_{i,\mathrm{T}}(\theta)}{\bar{c}_{i,\mathrm{T}}(\theta)}(t-\theta). \tag{A.12}$$

Remark A.1. Solution (A.8) is valid while $x_i(t,x) \geq 0$, i.e., for $t_0 \leq t \leq t_0 + x/c_0(0)$. Solution (A.11) applies when $t_i(t,x) > t_0$, i.e., for $t > t_0 + x/c_0(0)$. Thus, cases (A.8) and (A.11) cover all $t \geq t_0$.

Remark A.2. The values μ and ν may be called "mass dispersion factors" as they are responsible for the gradual changes in the linear density profile due to the velocity differences of the neighboring plugs.

Finally, substituting $x = \ell_{\mathrm{T}}$ into the solutions (A.8) and (A.11), the outputs of the model (3.2), (3.37) are obtained as follows:

1. For $t \in \left[t_0, t_0 + \frac{\ell_{\mathrm{T}}}{c_0(0)}\right]$ (when output is defined by initial conditions):

$$\dot{m}_{o,\mathrm{T}}(t) = \frac{c_0(\chi)}{\mu(t,\ell_{\mathrm{T}})}\Bigg(\xi_{\mathrm{d},0}(\chi) + \xi_{\mathrm{w},0}(\chi)$$
$$- \int_{t_0}^{t} q(\alpha)\mu(\alpha,\ell_{\mathrm{T}})\,\mathrm{d}\alpha\Bigg)\Bigg|_{\chi=x_i(t,\ell_{\mathrm{T}})}, \tag{A.13a}$$

$$w_{o,\mathrm{T}}(t) = \xi_{\mathrm{d},0}(\chi)\Bigg(\xi_{\mathrm{d},0}(\chi) + \xi_{\mathrm{w},0}(\chi)$$
$$- \int_{t_0}^{t} q(\alpha)\mu(\alpha,\ell_{\mathrm{T}})\,\mathrm{d}\alpha\Bigg)^{-1}\Bigg|_{\chi=x_i(t,\ell_{\mathrm{T}})}. \tag{A.13b}$$

2. For $t > t_0 + \frac{\ell_{\mathrm{T}}}{c_0(0)}$ (when output is independent of initial conditions):

$$\dot{m}_{o,\mathrm{T}}(t) = \frac{\dot{m}_{i,\mathrm{T}}(\theta)}{\nu(t,\theta)}\Bigg(1 - \frac{\bar{c}_{i,\mathrm{T}}(\theta)}{\dot{m}_{i,\mathrm{T}}(\theta)}\int_{\theta}^{t} q(\alpha)\nu(\alpha,\theta)\,\mathrm{d}\alpha\Bigg)\Bigg|_{\theta=t_i(t,\ell_{\mathrm{T}})}, \tag{A.14a}$$

$$w_{o,\mathrm{T}}(t) = w_{i,\mathrm{T}}(\theta)\left(1 - \frac{\bar{c}_{i,\mathrm{T}}(\theta)}{\dot{m}_{i,\mathrm{T}}(\theta)}\int_{\theta}^{t} q(\alpha)\nu(\alpha,\theta)\,\mathrm{d}\alpha\right)^{-1}\Bigg|_{\theta=t_i(t,\ell_{\mathrm{T}})}.$$
(A.14b)

To highlight the time-delay nature of the equations (A.14), time delay $\tau(t)$ can be introduced. It is related to the function $t_i(t, \ell_{\mathrm{T}})$ by

$$t_i(t, \ell_{\mathrm{T}}) = t - \tau(t).$$
(A.15)

A.2 Solution of the PDEs of DPF with Water-Proportional Evaporation

The PDEs (3.2) of DPF under water-proportional evaporation (3.45) are solved similarly to the case of uniform evaporation (A.1). The only difference is in the behavior of ξ_{w}. Its corresponding characteristic equation changes to

$$\frac{\mathrm{d}\tilde{\xi}_{\mathrm{w}}(\sigma)}{\mathrm{d}\sigma} = -\tilde{\xi}_{\mathrm{w}}(\sigma)\big(b(\tilde{t}(\sigma)) + \tilde{\zeta}(\sigma)\big)$$
(A.16)

with the general solution

$$\tilde{\xi}_{\mathrm{w}}(\sigma) = \frac{\tilde{\xi}_{\mathrm{w},0}\,\beta\big(\tilde{t}_0, \tilde{t}_0 + \sigma\big)}{1 + \tilde{\zeta}_0\sigma},$$
(A.17)

where

$$\beta(t_1, t_2) := \exp\left(-\int_{t_1}^{t_2} b(\alpha)\,\mathrm{d}\alpha\right).$$
(A.18)

This results in the following differences regarding the PDE solution (A.8), (A.11):

1. (A.8a) changes to

$$\xi_{\mathrm{w}}(t, x) = \frac{\xi_{\mathrm{w},0}\big(x_i(t,x)\big)\,\beta(t_0, t)}{\mu(t, x)}.$$
(A.19)

2. (A.11a) now reads

$$\xi_{\mathrm{w}}(t,x) = \left.\frac{\dot{m}_{i,\mathrm{T}}(\theta)\left(1 - w_{i,\mathrm{T}}(\theta)\right)\beta(\theta,t)}{\nu(t,\theta)\,\bar{c}_{i,\mathrm{T}}(\theta)}\right|_{\theta=t_i(t,x)}. \qquad \text{(A.20)}$$

Substitution $x = \ell_{\mathrm{T}}$ yields the outputs of the model (3.2), (3.45):

1. For $t \in \left[t_0, t_0 + \frac{\ell_{\mathrm{T}}}{c_0(0)}\right]$ (when output is defined by initial conditions):

$$\dot{m}_{o,\mathrm{T}}(t) = \left.\frac{c_0(\chi)\big(\xi_{\mathrm{d},0}(\chi) + \xi_{\mathrm{w},0}(\chi)\beta(t_0,t)\big)}{\mu(t,\ell_{\mathrm{T}})}\right|_{\chi=x_i(t,\ell_{\mathrm{T}})}, \qquad \text{(A.21a)}$$

$$w_{o,\mathrm{T}}(t) = \left.\frac{\xi_{\mathrm{d},0}(\chi)}{\xi_{\mathrm{d},0}(\chi) + \xi_{\mathrm{w},0}(\chi)\beta(t_0,t)}\right|_{\chi=x_i(t,\ell_{\mathrm{T}})}. \qquad \text{(A.21b)}$$

2. For $t > t_0 + \frac{\ell_{\mathrm{T}}}{c_0(0)}$ (when output is independent of initial conditions):

$$\dot{m}_{o,\mathrm{T}}(t) = \left.\frac{\dot{m}_{i,\mathrm{T}}(\theta)\big(w_{i,\mathrm{T}}(\theta) + \big(1 - w_{i,\mathrm{T}}(\theta)\big)\beta(\theta,t)\big)}{\nu(t,\theta)}\right|_{\theta=t_i(t,\ell_{\mathrm{T}})},$$

$$\text{(A.22a)}$$

$$w_{o,\mathrm{T}}(t) = \left.\frac{w_{i,\mathrm{T}}(\theta)}{w_{i,\mathrm{T}}(\theta) + \big(1 - w_{i,\mathrm{T}}(\theta)\big)\beta(\theta,t)}\right|_{\theta=t_i(t,\ell_{\mathrm{T}})}. \qquad \text{(A.22b)}$$

Equations (A.21) and (A.22) implicitly – via β – contain the total water mass $m_{\mathrm{w}}(t)$, which is obtained by using (A.19) and (A.20) in (3.46):

$$m_{\mathrm{w}}(t) = \int_{t_*(t)}^{t} \dot{m}_{i,\mathrm{T}}(\theta)\big(1 - w_{i,\mathrm{T}}(\theta)\big)\beta(\theta,t)\,\mathrm{d}\theta$$

$$+ \int_{x_*(t)}^{\ell_{\mathrm{T}}} \frac{\xi_{\mathrm{w},0}\big(x_i(t,x)\big)\beta(t_0,t)}{\mu(t,x)}\,\mathrm{d}x, \qquad \text{(A.23)}$$

where $x_*(t) = \min\{\ell_\mathrm{T}, tc_0(0)\}$ and $t_*(t) = \max\{t_0, t - \tau(t)\}$.

A.3 Solution of the PDEs of OPF with Water-Proportional Evaporation

In the sequel, let us use the method of characteristics to solve the PDEs (3.15) of OPF subject to the evaporation model (3.52) introduced in Sec. 3.5.3. As (3.15) is a system of 2-dimensional PDEs (in space[1]), the characteristic curve is defined in the 3-dimensional time-space as $\big(\tilde{t}(\sigma), \tilde{x}(\sigma), \tilde{c}(\sigma)\big)$. Extending the notation (A.2) to the 3-dimensional case and proceeding in the same way as in App. A.1, the characteristic system

$$\frac{\mathrm{d}\tilde{t}(\sigma)}{\mathrm{d}\sigma} = 1, \quad \tilde{t}(0) = \tilde{t}_0, \tag{A.24a}$$

$$\frac{\mathrm{d}\tilde{x}(\sigma)}{\mathrm{d}\sigma} = \tilde{c}(\sigma), \quad \tilde{x}(0) = \tilde{x}_0, \tag{A.24b}$$

$$\frac{\mathrm{d}\tilde{c}(\sigma)}{\mathrm{d}\sigma} = 0, \quad \tilde{c}(0) = \tilde{c}_0, \tag{A.24c}$$

$$\frac{\mathrm{d}\tilde{\xi}_\mathrm{w}(\sigma)}{\mathrm{d}\sigma} = -b\big(\tilde{t}(\sigma)\big)\,\tilde{\xi}_\mathrm{w}(\sigma), \quad \tilde{\xi}_\mathrm{w}(0) = \tilde{\xi}_{\mathrm{w},0}, \tag{A.24d}$$

$$\frac{\mathrm{d}\tilde{\xi}_\mathrm{d}(\sigma)}{\mathrm{d}\sigma} = 0, \quad \tilde{\xi}_\mathrm{d}(0) = \tilde{\xi}_{\mathrm{d},0} \tag{A.24e}$$

is obtained. The general solution of the ODEs (A.24) is

$$\tilde{t}(\sigma) = \tilde{t}_0 + \sigma, \tag{A.25a}$$

$$\tilde{x}(\sigma) = \tilde{x}_0 + \tilde{c}_0\sigma, \tag{A.25b}$$

$$\tilde{c}(\sigma) = \tilde{c}_0, \tag{A.25c}$$

$$\tilde{\xi}_\mathrm{w}(\sigma) = \tilde{\xi}_{\mathrm{w},0}\,\beta\big(\tilde{t}_0, \tilde{t}(\sigma)\big), \tag{A.25d}$$

$$\tilde{\xi}_\mathrm{d}(\sigma) = \tilde{\xi}_{\mathrm{d},0}, \tag{A.25e}$$

---

[1] In this case, the coordinate c is formally interpreted as another space coordinate besides x.

where

$$\beta(t_1, t_2) := \exp\left(-\int_{t_1}^{t_2} b(\alpha)\, d\alpha\right). \tag{A.26}$$

Similarly to App. A.1, two boundary conditions are imposed on the characteristic curve, the first being

$$\tilde{t}(\sigma) = t, \qquad \tilde{x}(\sigma) = x, \qquad \tilde{c}(\sigma) = c \tag{A.27}$$

and with regards to the second boundary condition, it is required to distinguish between two cases:

1. If $t_0 \leq t < t_0 + x/c$, then

$$\tilde{t}_0 = t_0, \qquad \tilde{x}_0 = (x - (t - t_0)c) \in (0, x], \qquad \tilde{c}_0 = c \tag{A.28}$$

which yields, using the initial conditions from the PDEs (3.15),

$$\xi_{\mathrm{w}}(t, x, c) = \xi_{\mathrm{w},0}\big(x - (t - t_0)c, c\big)\,\beta(t_0, t), \tag{A.29a}$$
$$\xi_{\mathrm{d}}(t, x, c) = \xi_{\mathrm{d},0}\big(x - (t - t_0)c, c\big). \tag{A.29b}$$

2. If $t \geq t_0 + x/c$, then

$$\tilde{t}_0 = t - x/c \geq t_0, \qquad \tilde{x}_0 = 0, \qquad \tilde{c}_0 = c \tag{A.30}$$

which yields, using the boundary conditions from the PDEs (3.15),

$$\xi_{\mathrm{w}}(t, x, c) = f(c, \theta)\dot{m}_{i,\mathrm{T}}(\theta)\big(1 - w_{i,\mathrm{T}}(\theta)\big)\beta(\theta, t)/c\Big|_{\theta = t - x/c}, \tag{A.31a}$$

$$\xi_{\mathrm{d}}(t, x, c) = f(c, \theta)\dot{m}_{i,\mathrm{T}}(\theta)w_{i,\mathrm{T}}(\theta)/c\Big|_{\theta = t - x/c}. \tag{A.31b}$$

Finally, the outputs of the PDEs (3.15) are obtained as

$$\dot{m}_{o,\mathrm{T}}(t) = \int\limits_{c_{\min}}^{c_*(t,\ell_{\mathrm{T}})} \big(\xi_{\mathrm{d},0}(\chi,c) + \xi_{\mathrm{w},0}(\chi,c)\beta(t_0,t)\big)\big|_{\chi=\ell_{\mathrm{T}}-(t-t_0)c}\, c\,\mathrm{d}c$$

$$+ \int\limits_{c_*(t,\ell_{\mathrm{T}})}^{c_{\max}} \Big(f(c,\theta)\,\dot{m}_{i,\mathrm{T}}(\theta)\,w_{i,\mathrm{T}}(\theta)$$

$$+ f(c,\theta)\,\dot{m}_{i,\mathrm{T}}(\theta)\big(1-w_{i,\mathrm{T}}(\theta)\big)\beta(\theta,t)\Big)\Big|_{\theta=t-\ell_{\mathrm{T}}/c}\,\mathrm{d}c, \quad \text{(A.32a)}$$

$$w_{o,\mathrm{T}}(t) = \left(\int\limits_{c_{\min}}^{c_*(t,\ell_{\mathrm{T}})} \xi_{\mathrm{d},0}(\ell_{\mathrm{T}}-(t-t_0)c,c)c\,\mathrm{d}c\right.$$

$$\left. + \int\limits_{c_*(t,\ell_{\mathrm{T}})}^{c_{\max}} f(c,\theta)\,\dot{m}_{i,\mathrm{T}}(\theta)\,w_{i,\mathrm{T}}(\theta)\big|_{\theta=t-\ell_{\mathrm{T}}/c}\,\mathrm{d}c\right)\Big/\dot{m}_{o,\mathrm{T}}(t)\ \text{(A.32b)}$$

where

$$c_*(t,x) = \begin{cases} c_{\min}, & \dfrac{x}{t-t_0} < c_{\min}, \\[2mm] c_{\max}, & \dfrac{x}{t-t_0} > c_{\max}, \\[2mm] \dfrac{x}{t-t_0}, & \text{otherwise.} \end{cases} \qquad \text{(A.33)}$$

Evaluation of (3.53) to determine the total mass of water in the tubes leads to

$$m_{\mathrm{w}}(t) = \int\limits_0^{\ell_{\mathrm{T}}}\int\limits_{c_{\min}}^{c_*(t,x)} \xi_{\mathrm{w},0}(x-(t-t_0)c,c)\beta(t_0,t)\,\mathrm{d}c\,\mathrm{d}x$$

$$+ \int\limits_0^{\ell_{\mathrm{T}}}\int\limits_{c_*(t,x)}^{c_{\max}} \frac{f(c,\theta)\,\dot{m}_{i,\mathrm{T}}(\theta)\big(1-w_{i,\mathrm{T}}(\theta)\big)\beta(\theta,t)}{c}\bigg|_{\theta=t-x/c}\,\mathrm{d}c\,\mathrm{d}x.$$

$$\text{(A.34)}$$

A.4 Solution of the PDEs of OPF with Localized Evaporation

The PDEs (3.15) of OPF with localized evaporation model (3.58)–(3.61) are solved similarly to the case of water-proportional evaporation, see App. A.3. The only difference is in the behavior of ξ_w and in the additional PDE (3.60). The corresponding characteristic equations for $\tilde{\xi}_w$ and $\tilde{\phi}$ are

$$\frac{d\tilde{\xi}_w(\sigma)}{d\sigma} = -\tilde{\phi}(\sigma)\left(k_0 - k_1 \frac{\tilde{\xi}_d(\sigma)}{\tilde{\xi}_w(\sigma) + \tilde{\xi}_d(\sigma)}\right) p(\tilde{t}(\sigma)), \qquad \text{(A.35a)}$$

$$\frac{d\tilde{\phi}(\sigma)}{d\sigma} = 0. \qquad \text{(A.35b)}$$

To solve the system of characteristic equations, let us introduce the new variable

$$\tilde{\omega}(\sigma) := \frac{\tilde{\xi}_w(\sigma)}{\tilde{\xi}_d(\sigma)} + 1 \qquad \text{(A.36)}$$

which satisfies

$$\frac{d\tilde{\omega}(\sigma)}{d\sigma} = -\frac{\tilde{\phi}(\sigma)p(\tilde{t}(\sigma))}{\tilde{\xi}_d(\sigma)} \frac{k_0\,\tilde{\omega}(\sigma) - k_1}{\tilde{\omega}(\sigma)}, \quad \tilde{\omega}(0) = \tilde{\omega}_0. \qquad \text{(A.37)}$$

Solving it together with the rest of the system (A.24) yields the general solution

$$\tilde{\omega}(\sigma) = \Omega\left(\frac{\tilde{\xi}_{w,0}}{\tilde{\xi}_{d,0}} + 1, \frac{\tilde{\phi}_0}{\tilde{\xi}_{d,0}}\varpi(\tilde{t}_0, \tilde{t}_0 + \sigma)\right), \qquad \text{(A.38)}$$

where the function Ω is defined via the Lambert W-function as

$$\Omega(a, b) = \frac{k_1}{k_0}\left(W\left(\left(\frac{k_0}{k_1}a - 1\right)\exp\left(\frac{k_0}{k_1}a - 1 - \frac{k_0^2}{k_1}b\right)\right) + 1\right) \qquad \text{(A.39)}$$

and additionally the abbreviation

$$\varpi(t_1, t_2) = \int_{t_1}^{t_2} p(\alpha)\,d\alpha \qquad \text{(A.40)}$$

is used.

To obtain the general solution of the PDEs, two boundary conditions are imposed on the characteristic curve, the first being

$$\tilde{t}(\sigma) = t, \qquad \tilde{x}(\sigma) = x, \qquad \tilde{c}(\sigma) = c \qquad (A.41)$$

and with regards to the second boundary condition, let us distinguish two cases:

1. If $t_0 \leq t < t_0 + x/c$, then

$$\tilde{t}_0 = t_0, \qquad \tilde{x}_0 = (x - (t - t_0)c) \in (0, x], \qquad \tilde{c}_0 = c \qquad (A.42)$$

which yields, using the initial conditions from the PDEs (3.15),

$$\omega(t, x, c) = \Omega \left(\frac{\xi_{w,0}(\chi, c)}{\xi_{d,0}(\chi, c)} + 1, \ \frac{\phi_0(\chi, c)\,\varpi(t_0, t)}{\xi_{d,0}(\chi, c)} \right) \Bigg|_{\chi = x - (t-t_0)c}, \qquad (A.43)$$

where $\omega(t, x, c)$ is connected to $\tilde{\omega}(\sigma)$ by the extension of the notation scheme (A.2).

2. If $t \geq t_0 + x/c$, then

$$\tilde{t}_0 = t - x/c \geq t_0, \qquad \tilde{x}_0 = 0, \qquad \tilde{c}_0 = c \qquad (A.44)$$

which yields, using the boundary conditions from the PDEs (3.15),

$$\omega(t, x, c) = \Omega \left(\frac{1}{w_{i,T}(\theta)}, \ \frac{c\,\varpi(\theta, t)}{\dot{m}_{i,T}(\theta)\,w_{i,T}(\theta)} \right) \Bigg|_{\theta = t - x/c}. \qquad (A.45)$$

Using relations

$$\dot{m}_{o,T}(t) = \int_{c_{min}}^{c_{max}} \xi_d(t, \ell_T, c)\,\omega(t, \ell_T, c)\,c\,\mathrm{d}c, \qquad (A.46)$$

$$w_{o,T}(t) = \frac{1}{\dot{m}_{o,T}(t)} \int_{c_{min}}^{c_{max}} \xi_d(t, \ell_T, c)\,c\,\mathrm{d}c, \qquad (A.47)$$

and the solution for ξ_{d} from App. A.3, the outputs of the model are finally obtained as

$$
\dot{m}_{o,\mathrm{T}}(t) = \int_{c_{\min}}^{c_*(t,\ell_{\mathrm{T}})} \xi_{\mathrm{d},0}(\chi,c)
$$

$$
\Omega \left(\frac{\xi_{\mathrm{w},0}(\chi,c)}{\xi_{\mathrm{d},0}(\chi,c)} + 1, \; \frac{\phi_0(\chi,c)\,\varpi(t_0,t)}{\xi_{\mathrm{d},0}(\chi,c)} \right) \bigg|_{\chi=\ell_{\mathrm{T}}-(t-t_0)c} c\,\mathrm{d}c
$$

$$
+ \int_{c_*(t,\ell_{\mathrm{T}})}^{c_{\max}} f(c,\theta)\,\dot{m}_{i,\mathrm{T}}(\theta)\,w_{i,\mathrm{T}}(\theta)
$$

$$
\Omega \left(\frac{1}{w_{i,\mathrm{T}}(\theta)}, \; \frac{c\,\varpi(\theta,t)}{\dot{m}_{i,\mathrm{T}}(\theta)w_{i,\mathrm{T}}(\theta)} \right) \bigg|_{\theta=t-\ell_{\mathrm{T}}/c} \mathrm{d}c, \tag{A.48a}
$$

$$
w_{o,\mathrm{T}}(t) = \left(\int_{c_{\min}}^{c_*(t,\ell_{\mathrm{T}})} \xi_{\mathrm{d},0}(\ell_{\mathrm{T}} - (t-t_0)c, c)c\,\mathrm{d}c \right.
$$

$$
\left. + \int_{c_*(t,\ell_{\mathrm{T}})}^{c_{\max}} f(c,\theta)\,\dot{m}_{i,\mathrm{T}}(\theta)\,w_{i,\mathrm{T}}(\theta)\big|_{\theta=t-\ell_{\mathrm{T}}/c} \mathrm{d}c \right) / \dot{m}_{o,\mathrm{T}}(t) \tag{A.48b}
$$

where

$$
c_*(t,x) = \begin{cases} c_{\min}, & \frac{x}{t-t_0} < c_{\min}, \\ c_{\max}, & \frac{x}{t-t_0} > c_{\max}, \\ \frac{x}{t-t_0}, & \text{otherwise.} \end{cases} \tag{A.49}
$$

A.5 Relation between OPF and DPF

Consider the i/o relation of the OPF model without evaporation, i.e.,

$$
\dot{m}_{o,\mathrm{T}}(t) = \int_{c_{\min}}^{c_{\max}} f(c,\sigma)\dot{m}_{i,\mathrm{T}}(\sigma)\bigg|_{\sigma=t-\ell_{\mathrm{T}}/c} \mathrm{d}c. \tag{A.50}
$$

By modeling the distribution function $f(c, t)$ via the delta-function such that

$$f(c, t) = \delta(c - \bar{c}_{i,\mathrm{T}}(t)), \tag{A.51}$$

it remains to be shown that the i/o relation of the DPF model without evaporation

$$\dot{m}_{o,\mathrm{T}}(t) = \frac{\bar{c}_{i,\mathrm{T}}(t - \tau(t))\dot{m}_{i,\mathrm{T}}(t - \tau(t))}{\bar{c}_{i,\mathrm{T}}(t - \tau(t)) - \dot{\bar{c}}_{i,\mathrm{T}}(t - \tau(t))\tau(t)},$$

$$\tau(t) = \frac{\ell_{\mathrm{T}}}{\bar{c}_{i,\mathrm{T}}(t - \tau(t))} \tag{A.52}$$

follows.

Proof A.1. Substitute (A.51) in (A.50):

$$\dot{m}_{o,\mathrm{T}}(t) = \int_{c_{\min}}^{c_{\max}} \delta\big(c - \bar{c}_{i,\mathrm{T}}(t - \ell_{\mathrm{T}}/c)\big)\dot{m}_{i,\mathrm{T}}(t - \ell_{\mathrm{T}}/c)\,\mathrm{d}c. \tag{A.53}$$

Introduce the new variable α by the relation

$$\alpha = c - \bar{c}_{i,\mathrm{T}}(t - \ell_{\mathrm{T}}/c). \tag{A.54}$$

Then, there is

$$\mathrm{d}c = \left(1 - \dot{\bar{c}}_{i,\mathrm{T}}\big(t - \ell_{\mathrm{T}}/c(\alpha)\big)\frac{\ell_{\mathrm{T}}}{c^2(\alpha)}\right)^{-1}\mathrm{d}\alpha, \tag{A.55}$$

where $c(\alpha)$ denotes the inverse of the relation (A.54). Hence, (A.53) takes form

$$\dot{m}_{o,\mathrm{T}}(t) = \int_{\alpha(c_{\min})}^{\alpha(c_{\max})} \delta(\alpha)\dot{m}_{i,\mathrm{T}}\big(t - \ell_{\mathrm{T}}/c(\alpha)\big)$$

$$\left(1 - \dot{\bar{c}}_{i,\mathrm{T}}\big(t - \ell_{\mathrm{T}}/c(\alpha)\big)\frac{\ell_{\mathrm{T}}}{c^2(\alpha)}\right)^{-1}\mathrm{d}\alpha. \tag{A.56}$$

By definition of the δ-function, the result

$$\dot{m}_{o,\mathrm{T}}(t) = \dot{m}_{i,\mathrm{T}}\big(t - \ell_{\mathrm{T}}/c(0)\big)\left(1 - \dot{\bar{c}}_{i,\mathrm{T}}\big(t - \ell_{\mathrm{T}}/c(0)\big)\frac{\ell_{\mathrm{T}}}{c^2(0)}\right)^{-1} \quad \text{(A.57)}$$

is obtained, which can be transformed into (A.52) using the relation

$$c(0) = \bar{c}_{i,\mathrm{T}}\big(t - \ell_{\mathrm{T}}/c(0)\big) \quad \Rightarrow \quad \frac{\ell_{\mathrm{T}}}{c(0)} = \tau(t). \quad \text{(A.58)}$$

A.6 Properties of Milk

Property	Formula	Parameters
$\varrho(\vartheta, w)$	(2.1a)	$A_{\varrho,\mathrm{w}} = 629.498,\ B_{\varrho,\mathrm{w}} = 2.64029,$ $C_{\varrho,\mathrm{w}} = -0.0047,\ A_{\varrho} = 0.507725,$ $B_{\varrho} = 1.164633$
$\Delta h_v(\vartheta)$	(2.1b)	$A_h = 323.15,\ B_h = 2382,$ $C_h = 0.324$
$c_p(\vartheta, w)$	(2.1c)	$A_{c,\mathrm{w}} = 5.647,\ B_{c,\mathrm{w}} = -0.00905,$ $C_{c,\mathrm{w}} = 1.4 \cdot 10^{-5},\ A_c = 1.716541,$ $B_c = -0.000137$
$\eta(\vartheta, w)$	(2.1d)	$A_\eta = 27.825563,\ B_\eta = 0.00549,$ $C_\eta = 4.311571,\ D_\eta = 2.810654,$ $E_\eta = -5.703782475,\ F_\eta = -1.203972904,$ $G_\eta = 0.018,\ \vartheta_{\mathrm{A}} = 293.15\,\mathrm{K}$
$\Delta\vartheta(\vartheta, w)$	(2.1e)	$A_\Delta = 7.177653,\ B_\Delta = 2.275225,$ $C_\Delta = -0.029483$

Table A.1: Liquid properties of milk

The FFE modeled and validated in Ch. 2 is fed by pre-concentrated milk. Its properties are given Tab. A.1.

A.7 Properties of Dextrose with Polyvinylpyrrolidone

Property	Formula	Parameters
$\varrho(\vartheta, w)$	(2.1a)	$A_{\varrho,\mathrm{w}} = 629.498,\ \ B_{\varrho,\mathrm{w}} = 2.64029,$ $C_{\varrho,\mathrm{w}} = -0.0047,\ \ A_{\varrho} = 0.368857,$ $B_{\varrho} = 0.137827$
$\Delta h_v(\vartheta)$	(2.1b)	$A_h = 323.15,\ \ B_h = 2382,$ $C_h = 0.324$
$c_p(\vartheta, w)$	(2.1c)	$A_{c,\mathrm{w}} = 5.647,\ \ B_{c,\mathrm{w}} = -0.00905,$ $C_{c,\mathrm{w}} = 1.4 \cdot 10^{-5},\ \ A_c = 7.266476,$ $B_c = -0.016612$
$\eta(\vartheta, w)$	(2.1d)	$A_\eta = 11.248094,\ \ B_\eta = 0.021970,$ $C_\eta = 0.123447,\ \ D_\eta = 0.983533,$ $E_\eta = -5.703782475,\ \ F_\eta = -1.203972904,$ $G_\eta = 0.018,\ \ \vartheta_\mathrm{A} = 293.15\,\mathrm{K}$

Table A.2: Liquid properties of dextrose with polyvinylpyrrolidone

To conduct the experiments in Ch. 4, dextrose with polyvinylpyrrolidone is used as test liquid whose properties are given in Tab. A.2. In this context, the variables ϑ and w, which are both functions of time t, should be chosen according to the sensor which is closest to the place of interest in the plant. For simplicity, in Ch. 4, almost all liquid properties are defined as functions of t but, in this appendix, they are specified for each relevant equation[2]:

- In (4.3): $c_p(t) := c_p(\vartheta_\mathrm{T}(t), w_{i,\mathrm{P}}(t)),\ c_{p,\mathrm{w}}(t) := c_{p,\mathrm{w}}(\vartheta_\mathrm{T}(t)),$
 $\Delta h_v(t) := \Delta h_v(\vartheta_\mathrm{T}(t)).$

- In (4.5), (4.6), (4.8): $\varrho_{i,\mathrm{P}}(t)$ in circulation mode,
 $\varrho_{i,\mathrm{P}}(t) := \varrho(\vartheta_{i,\mathrm{P}}(t), w_{o,\mathrm{Pipe}}(t))$ in single-pass mode.

- In (4.17): $\eta(t) := \eta(\vartheta_\mathrm{T}(t), w_{i,\mathrm{P}}(t)).$

---

[2] Variables in green are directly measured and variables in blue are indirectly measured.

A.8 Actuator Dynamics

Although actuator dynamics were neglected during the control design in Sec. 5.3, they are part of the real-world plant. Therefore, the actuator dynamics are modeled in this section and are included in the digital twin used for validation of the concept, see Sec. 5.3.4. As observed in Sec. 5.3, the multivariable controller outputs the power P_C and input mass flow $\dot{m}_i$. However, in fact, the multivariable controller outputs the corresponding desired values, i.e. $\dot{m}_{i,d}$ and $P_{C,d}$, since direct actuation of $\dot{m}_i$ and P_C is not possible. For the sake of clarity, let us disregard the control nomenclature introduced in Sec. 5.3.1 and instead consider all variables in physical nomenclature throughout this section.

At first, it is necessary to clarify how $\dot{m}_{i,d}$ is adjusted via a control Valve. Based on the deviation $\dot{m}_{i,d} - \dot{m}_i$, the PI controller

$$C_V(s) = k_{p,V} + \frac{k_{i,V}}{s} \tag{A.59}$$

calculates the desired Valve position $\varphi_d \in [0,1]$, which is the input to the control Valve modeled by

$$\frac{\mathrm{d}}{\mathrm{d}t}\varphi(t) = \frac{1}{T_V}\big(\varphi_d(t) - \varphi(t)\big), \tag{A.60a}$$

$$K_v(t) = \begin{cases} 0, & \varphi(t) \in [0, 0.02), \\ K_{v,s}\, n^{1-\varphi(t)}, & \varphi(t) \in [0.02, 1], \end{cases} \tag{A.60b}$$

$$\dot{m}_i(t) = K_v(t)\sqrt{1000\, \varrho_i(t)\big(p_{i,V}(t) - p_{o,V}(t)\big)}, \tag{A.60c}$$

cf. [10]. The pressures $p_{i,V}$, $p_{o,V}$, and input density ϱ_i are known via measurements. The constants $K_{v,s}$ and n determine the Valve's equal percentage characteristic curve, whereas the time constant T_V is known from preliminary identification experiments. Note that (A.60c) represents a quantity equation, i.e., all quantities in (A.60c) are divided by their physical units, where $\dot{m}_i$ in $\mathrm{kg\,h^{-1}}$, K_v in $\mathrm{kg\,h^{-1}}$, ϱ_i in $\mathrm{kg\,m^{-3}}$, $p_{i,V}$ and $p_{o,V}$ in $\mathrm{bar\,abs}$.
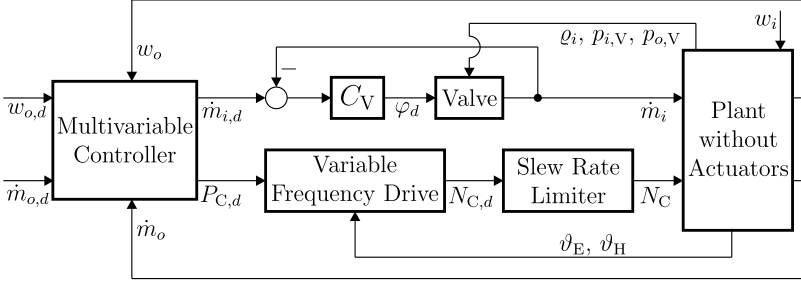
Figure A.1: Closed-loop system with actuator dynamics

To explain how the desired power $P_{C,d}$ is converted into the rotational speed N_C, let us recall the calculation of P_C from the Compressor model, see (2.53), which can be compactly rewritten by

$$P_C(t) = P_C\big(N_C(t), \vartheta_E(t), \vartheta_H(t)\big). \tag{A.61}$$

From the practical perspective, the programming of the Compressor's actuator, a variable frequency drive, needs to be modified to manipulate P_C instead of N_C. As detailed modeling of the variable frequency drive is out of the thesis' scope, let us instead use the estimator

$$\frac{\mathrm{d}}{\mathrm{d}t} N_{C,d}(t) = \frac{\dot{P}_{C,d}(t) - \frac{\partial P_C}{\partial \vartheta_E}(t)\dot{\vartheta}_E(t) - \frac{\partial P_C}{\partial \vartheta_H}(t)\dot{\vartheta}_H(t) - \gamma\big(P_C(t) - P_{C,d}(t)\big)}{\frac{\partial P_C}{\partial N_{C,d}}(t)} \tag{A.62}$$

with $\gamma > 0$ to determine the Compressor's desired rotational speed $N_{C,d}$. Firstly, note that (A.62) is based on the method of dynamic inversion [48] applied to (A.61) with $N_C := N_{C,d}$, i.e., (A.62) is obtained from

$$\frac{\mathrm{d}}{\mathrm{d}t}\Big(P_C\big(N_{C,d}(t), \vartheta_E(t), \vartheta_H(t)\big) - P_{C,d}(t)\Big) = -\gamma\Big(P_C(t) - P_{C,d}(t)\Big). \tag{A.63}$$

Secondly, note that in (A.62), the derivatives $\dot{(\cdot)}$ w.r.t. time t are implemented in combination with low-pass filters to enable noise suppression. Thirdly, note that in (A.62), P_C and its partial derivatives are calculated via the Compressor model, see (2.47)–(2.53).
Downstream to the variable frequency drive, the slew rate limiter (2.54) con-

verts $N_{C,d}$ into the actual rotational speed N_C. Thus, the slew rate limiter ensures that steps required by the controller are converted into ramps. The closed-loop system with explicit distinction between plant and actuators is shown in Fig. A.1. In the upper loop of Fig. A.1, a serial cascade control structure is observed.

References

[1] W. Addison. Large falling film evaporators and vapour compression. In *Proceedings of The South African Sugar Technologists' Association*, volume 55, pages 56–58, Durban, South Africa, 1981. SASTA.

[2] A. Åkesjö. *Hydrodynamics and heat transfer in vertical falling films with smooth and modified heat-transfer surfaces: an experimental and numerical investigation.* PhD thesis, Chalmers University of Technology, Gothenburg, Sweden, 2018.

[3] F. Al-Sibai. *Experimentelle Untersuchung der Strömungscharakteristik und des Wärmeübergangs bei welligen Rieselfilmen.* Cuvillier Verlag, Göttingen, Germany, 2006.

[4] C. Albert, H. Marschall, and D. Bothe. Direct numerical simulation of interfacial mass transfer into falling films. *International Journal of Heat and Mass Transfer*, 69:343–357, 2014.

[5] J. A. Andersen, L. W. A. Glasson, and F. P. Lees. The control of a single-effect concentrating evaporator. *Transactions of the Society of Instrument Technology*, 13(1):21, 1961.

[6] H. Andre and R. A. Ritter. Dynamic response of a double effect evaporator. *The Canadian Journal of Chemical Engineering*, 46(4):259–264, 1968.

[7] S. Angeletti and M. Moresi. Modelling of multiple-effect falling-film evaporators. *International Journal of Food Science & Technology*, 18(5):539–563, 1983.

[8] Z. Artstein. Linear systems with delayed controls: a reduction. *IEEE Transactions on Automatic control*, 27(4):869–879, 1982.

[9] A. Atitallah, S. Bedoui, and K. Abderrahim. Time delay estimation for a class of block-oriented nonlinear models. In *International Conference on Sciences and Techniques of Automatic Control and Computer Engineering*, volume 15, pages 1061–1066, Hammamet, Tunisia, 2014. IEEE.

[10] H. Auinger, J. Ehmann, L. Grütesen, J. Heinrich, M. Huk, K. Jürgens, W. Klein, A. Kuhn, B. Kujawski, D. Metz, A. Muschet, A. Nagel, H. Peters, R. Rölli, C. Schindler, K. Scholl, M. Schwind, J. Seckler, V. Seppendorf, F. Valentin-Rumpel, and M. Voß. VDI-Richtlinien, VDI 2173: Strömungstechnische Kenngrößen von Stellgeräten und deren Bestimmung. Technical Report ICS 23.060.40, Verein Deutscher Ingenieure, 2018.

[11] A. Avvalabadi and A. Shahmansourian. A new mathematical approach for input-output pairing in MIMO square systems. In *Iranian Conference on Electrical Engineering*, volume 22, pages 1244–1247, Tehran, Iran, 2014. IEEE.

[12] M. M. Awad. Fouling of heat transfer surfaces. In *Heat transfer-theoretical analysis, experimental investigations and industrial systems*. IntechOpen, London, UK, 2011.

[13] H. H. C. Bakker, C. Marsh, S. Paramalingam, and H. Chen. Cascade controller design for concentration control in a falling-film evaporator. *Food Control*, 17(5):325–330, 2006.

[14] P. Bandi, M. Modigell, S. Groß, A. Reusken, L. Zhang, Y. Heng, W. Marquardt, and A. Mhamdi. On reduced modeling of mass transport in wavy falling films. *American Institute of Chemical Engineers Journal*, 64(6):2265–2276, 2018.

[15] J. Bao, P. J. McLellan, and J. F. Forbes. A passivity-based analysis for decentralized integral controllability. *Automatica*, 38(2):243–247, 2002.

[16] J. Barraud, Y. Creff, and N. Petit. PI controllers performance for a process model with varying delay. In *United Kingdom Automatic Control Council International Conference on Control*, Bath, UK, 2004. URL https://cas.mines-paristech.fr/~petit/papers/IEE-Control04/main.pdf. Retrieved September 27 2021, 16:06.

[17] N. Bekiaris-Liberis and M. Krstic. *Nonlinear control under nonconstant delays*. Society for Industrial and Applied Mathematics, Philadelphia, Pennsylvania, USA, 2013.

[18] N. Bekiaris-Liberis and M. Krstic. Stability of predictor-based feedback for nonlinear systems with distributed input delay. *Automatica*, 70:195–203, 2016.

[19] J. J. Belletrutti and A. G. J. MacFarlane. Characteristic loci techniques in multivariable-control-system design. *Proceedings of the Institution of Electrical Engineers*, 118(9):1291–1297, 1971.

[20] S. Bjorklund and L. Ljung. A review of time-delay estimation techniques. In *Conference on Decision and Control*, volume 42, pages 2502–2507, Maui, Hawaii, USA, 2003. IEEE.

[21] F. M. Bojnourd, M. A. Fanaei, and H. Zohreie. Mathematical modelling and dynamic simulation of multi-effect falling-film evaporator for milk powder production. *Mathematical and Computer Modelling of Dynamical Systems*, 21(4):336–358, 2015.

[22] U. Bolmstedt. Simulation of the steady-state and dynamic behaviour of multiple effect evaporation plants part 2: dynamic behaviour. *Computer-Aided Design*, 9(1):29–40, 1977.

[23] D. Bresch-Pietri and N. Petit. Implicit integral equations for modeling systems with a transport delay. In *Recent Results on Time-Delay Systems*, pages 3–21. Springer, Cham, Switzerland, 2016.

[24] D. Bresch-Pietri, J. Chauvin, and N. Petit. Adaptive control scheme for uncertain time-delay systems. *Automatica*, 48(8):1536–1552, 2012.

[25] E. Bristol. On a new measure of interaction for multivariable process control. *IEEE Transactions on Automatic Control*, 11(1):133–134, 1966.

[26] F. Cacace, F. Conte, and A. Germani. State feedback stabilization of linear systems with unknown input time delay. *IFAC-PapersOnLine*, 50(1):1245–1250, 2017.

[27] E. Cascetta. *Transportation systems engineering: theory and methods*, volume 49. Springer Science & Business Media, Luxembourg, 2013.

[28] M. Čičić and K. H. Johansson. Traffic regulation via individually controlled automated vehicles: a cell transmission model approach. In *International Conference on Intelligent Transportation Systems*, volume 21, pages 766–771, Maui, Hawaii, USA, 2018. IEEE.

[29] C. H. Clerget and N. Petit. Dynamic optimization of processes with time varying hydraulic delays. *Journal of Process Control*, 83:20–29, 2019.

[30] A. Conley and M. E. Salgado. Gramian based interaction measure. In *Conference on Decision and Control*, volume 39, pages 5020–5022, Sydney, Australia, 2000. IEEE.

[31] A. O. S. Costa and E. L. Lima. Modelling and control of an industrial multiple-effect evaporator system. *Canadian Journal of Chemical Engineering*, 81(5):1032–1040, 2003.

[32] R. Courant and D. Hilbert. *Methods of mathematical physics: partial differential equations*, volume 2. Wiley, Weinheim, Germany, 1989.

[33] R. V. Craster and O. K. Matar. Dynamics and stability of thin liquid films. *Reviews of modern physics*, 81(3):1131–1198, 2009.

[34] C. F. Daganzo. The cell transmission model: a dynamic representation of highway traffic consistent with the hydrodynamic theory. *Transportation Research Part B: Methodological*, 28(4):269–287, 1994.

[35] C. O. Díaz-Ovalle, G. González-Alatorre, and J. F. J. Alvarado. Analysis of the dynamic response of falling-film evaporators considering fouling. *Food and Bioproducts Processing*, 104:124–136, 2017.

[36] S. Diop, I. Kolmanovsky, P. E. Moraal, and M. Van Nieuwstadt. Preserving stability/performance when facing an unknown time-delay. *Control Engineering Practice*, 9 (12):1319–1325, 2001.

[37] L. Dobos, J. Jäschke, J. Abonyi, and S. Skogestad. Dynamic model and control of heat exchanger networks for district heating. *Hungarian Journal of Industry and Chemistry*, 37 (1):37–49, 2009.

[38] A. Donaldson and A. Thimmaiah. Process modelling and optimization of design parameters in a falling film plate and frame evaporator. In *COMSOL Conference*, pages 1–9, Bangalore, India, 2016.

[39] J. Doyle. Analysis of feedback systems with structured uncertainties. *IEE Proceedings D (Control Theory and Applications)*, 129(6):242–250, 1982.

[40] S. V. Drakunov, W. Perruquetti, J. P. Richard, and L. Belkoura. Delay identification in time-delay systems using variable structure observers. *Annual Reviews in Control*, 30(2): 143–158, 2006.

[41] R. Early. *The Technology of Dairy Products*. Blackie Academic & Professional, an imprint of Thomas Science, London, UK, 1998.

[42] A. Elnaggar, G. A. Dumont, and A. L. Elshafei. Recursive estimation for system of unknown delay. In *Conference on Decision and Control*, volume 28, pages 1809–1810, Tampa, Florida, USA, 1989. IEEE.

[43] S. Engell. Feedback control for optimal process operation. *Journal of Process Control*, 17 (3):203–219, 2007.

[44] S. Evesque, A. Annaswamy, S. Niculescu, and A. Dowling. Adaptive control of a class of time-delay systems. *Journal of Dynamic Systems, Measurement, and Control*, 125(2): 186–193, 2003.

[45] M. Farsi and A. Jahanmiri. A new control algorithm for concentration control in three effect falling film evaporators. *Iranian Journal of Science & Technology, Transaction B, Engineering*, 33(B5):387–396, 2009.

[46] O. Föllinger, U. Konigorski, B. Lohmann, G. Roppenecker, and A. Trächtler. *Regelungstechnik*. VDE-Verlag, Offenbach, Germany, 2016.

[47] J. P. Gagnepain and D. E. Seborg. Analysis of process interactions with applications to multiloop control system design. *Industrial & Engineering Chemistry Process Design and Development*, 21(1):5–11, 1982.

[48] N. E. Getz and J. E. Marsden. A dynamic inverse for nonlinear maps. In *Conference on Decision and Control*, volume 34, pages 4218–4223, New Orleans, Louisiana, USA, 1995. IEEE.

[49] P. D. Gossen, G. R. Sriniwas, and F. J. Schork. Determining residence time distributions in complex process systems: a simple method. *Chemical Engineering Education*, 29(2): 106–111, 1995.

[50] M. Gourdon and E. Mura. Performance evaluation of falling film evaporators in the dairy industry. *Food and Bioproducts Processing*, 101:22–31, 2017.

[51] M. Gourdon, F. Innings, A. Jongsma, and L. Vamling. Qualitative investigation of the flow behaviour during falling film evaporation of a dairy product. *Experimental Thermal and Fluid Science*, 60:9–19, 2015.

[52] J. Grifoll, J. M. Gastó, and Y. Cohen. Non-isothermal soil water transport and evaporation. *Advances in Water Resources*, 28(11):1254–1266, 2005.

[53] C. Grimholt and S. Skogestad. Should we forget the Smith Predictor? *IFAC-PapersOnLine*, 51(4):769–774, 2018.

[54] L. Gröll. *Methodik zur Integration von Vorwissen in die Modellbildung*, volume 52. KIT Scientific Publishing, Karlsruhe, Germany, 2015.

[55] P. Grosdidier, M. Morari, and B. R. Holt. Closed-loop properties from steady-state gain information. *Industrial & Engineering Chemistry Fundamentals*, 24(2):221–235, 1985.

[56] A. Haasbroek, L. Auret, and W. H. Steyn. A comparison of control techniques for dairy falling film evaporators. *IFAC Proceedings Volumes*, 46(32):253–258, 2013.

[57] A. Haasbroek, W. H. Steyn, and L. Auret. Advanced control with fundamental and data-based modeling for falling film evaporators. In *International Conference on Industrial Technology*, pages 46–51, Cape Town, South Africa, 2013. IEEE.

[58] B. Halvarsson. *Interaction analysis in multivariable control systems: applications to bioreactors for nitrogen removal.* PhD thesis, Uppsala University, Uppsala, Sweden, 2010.

[59] C. Hirsch. *Numerical computation of internal and external flows, volume 1: fundamentals of numerical discretization.* John Wiley and Sons, Hoboken, New Jersey, USA, 1988.

[60] J. P. Holman. *Heat Transfer.* McGraw-Hill Higher Education, New York City, New York, USA, 1989.

[61] M. Hovd and S. Skogestad. Controllability analysis for unstable processes. In *Interactions Between Process Design and Process Control*, IFAC Postprint Volume, pages 49–54. Pergamon, Oxford, UK, 1992.

[62] M. Hovd and S. Skogestad. Simple frequency-dependent tools for control system analysis, structure selection and design. *Automatica*, 28(5):989–996, 1992.

[63] H. P. Huang and M. L. Roan. A complement to Niederlinski's index for multiloop integral control systems. *Chemical Engineering Communications*, 119(1):125–133, 1993.

[64] H. P. Huang, M. Ohshima, and I. Hashimoto. Dynamic interaction and multiloop control system design. *Journal of Process Control*, 4(1):15–27, 1994.

[65] P. S. Hussey. A digital computer model of a multiple effect evaporator. In *Proceedings of The South African Sugar Technologists' Association*, pages 70–76, South Africa, 1973. SASTA.

[66] S. Jani. Simulation of heat and mass transfer process in falling film single tube absorption generator. *International Journal of Science and Engineering Investigations*, 1(3):79–84, 2012.

[67] A. Jernqvist, G. Olgard, and B. Hedstrom. A digital computer program for multiple effect evaporation. *Swedish Paper Journal*, 69(15):477, 1966.

[68] D. E. Johnson. Simulation and analysis improve evaporator control. *ISA Journal*, 7(7):46, 1960.

[69] I. Karafyllis and M. Krstic. On the relation of delay equations to first-order hyperbolic partial differential equations. *European Series in Applied and Industrial Mathematics: Control, Optimisation and Calculus of Variations*, 20(3):894–923, 2014.

[70] I. Karafyllis and M. Krstic. Stability results for the continuity equation. *Systems & Control Letters*, 135:104594, 2020.

[71] T. D. Karapantsios and A. J. Karabelas. Longitudinal characteristics of wavy falling films. *International Journal of Multiphase Flow*, 21(1):119–127, 1995.

[72] M. Karimi and A. Jahanmiri. Nonlinear modeling and cascade control design for multi effect falling film evaporators. *Iranian Journal of Chemical Engineering*, 3(2):52–63, 2006.

[73] M. Karimi, A. Jahanmiri, and M. Azarmi. Inferential cascade control of multi-effect falling-film evaporator. *Food Control*, 18(9):1036–1042, 2007.

[74] E. Karlsson, M. Gourdon, L. Olausson, and L. Vamling. Heat transfer for falling film evaporation of black liquor up to very high prandtl numbers. *International Journal of Heat and Mass Transfer*, 65:907–918, 2013.

[75] S. Khanam and B. Mohanty. Energy reduction schemes for multiple effect evaporator systems. *Applied Energy*, 87(4):1102–1111, 2010.

[76] S. Khanam and B. Mohanty. Development of a new model for multiple effect evaporator system. *Computers & Chemical Engineering*, 35(10):1983–1993, 2011.

[77] C. R. Kharangate, H. Lee, and I. Mudawar. Computational modeling of turbulent evaporating falling films. *International Journal of Heat and Mass Transfer*, 81:52–62, 2015.

[78] R. Kicsiny. New delay differential equation models for heating systems with pipes. *International Journal of Heat and Mass Transfer*, 79:807–815, 2014.

[79] F. W. Koko and D. D. Joye. Design calculations for multiple-effect evaporators. 2. Comparison of linear and nonlinear methods. *Industrial & Engineering Chemistry Research*, 26 (1):104–107, 1987.

[80] M. V. Kothare, P. J. Campo, M. Morari, and C. N. Nett. A unified framework for the study of anti-windup designs. *Automatica*, 30(12):1869–1883, 1994.

[81] M. Kraume. *Transportvorgänge in der Verfahrenstechnik*. Springer-Vieweg, Wiesbaden, Germany, 2004.

[82] G. Kreisselmeier. Two-degree-of-freedom control structure (in German). *at-Automatisierungstechnik*, 47(6):266–269, 1999.

[83] M. Krstic. *Delay compensation for nonlinear, adaptive, and PDE systems*. Springer, Basel, Switzerland, 2009.

[84] S. T. Lahtinen. Identification of fuzzy controller for use with a falling-film evaporator. *Food Control*, 12(3):175–180, 2001.

[85] D. L. Laughlin, D. E. Rivera, and M. Morari. Smith predictor design for robust performance. *International Journal of Control*, 46(2):477–504, 1987.

[86] V. Léchappé, E. Moulay, F. Plestan, A. Glumineau, and A. Chriette. New predictive scheme for the control of LTI systems with input delay and unknown disturbances. *Automatica*, 52:179–184, 2015.

[87] D. Lee, M. Lee, S. Sung, and I. Lee. Robust PID tuning for Smith predictor in the presence of model uncertainty. *Journal of Process Control*, 9(1):79–85, 1999.

[88] T. Liu, Y. Z. Cai, D. Y. Gu, and W. D. Zhang. New modified smith predictor scheme for integrating and unstable processes with time delay. *IEE Proceedings – Control Theory and Applications*, 152(2):238–246, 2005.

[89] E. M. Marshall and A. Bakker. *Handbook of industrial mixing: science and practice*. John Wiley & Sons, Hoboken, New Jersey, USA, 2004.

[90] M. R. Matausek and A. D. Micic. A modified smith predictor for controlling a process with an integrator and long dead-time. *IEEE Transactions on Automatic Control*, 41(8): 1199–1203, 1996.

[91] Q. Meng, H. Zhang, and M. Howarth. Performances comparison between real-time auto-tuning PID and conventional PID controller for a dairy industrial evaporation process control. In *International Conference on Artificial Intelligence, Control and Automation Engineering*, Wuhan, China, 2019. DEStech Publications, Inc.

[92] W. Michiels and S. I. Niculescu. On the delay sensitivity of smith predictors. *International journal of systems science*, 34(8-9):543–551, 2003.

[93] M. Morari. Robust process control. *Chemical Engineering Research & Design*, 65(6):462–479, 1987.

[94] M. Munir, Y. Zhang, D. Wilson, W. Yu, and B. Young. Modelling of a falling film evaporator for dairy processes. In *Chemeca: Processing Excellence; Powering Our Future*, pages 174–181, Perth, Australia, 2014. Engineers Australia.

[95] R. B. Newell and D. G. Fisher. Model development, reduction, and experimental evaluation for an evaporator. *Industrial & Engineering Chemistry Process Design and Development*, 11 (2):213–221, 1972.

[96] A. Niederlinski. A heuristic approach to the design of linear multivariable interacting control systems. *Automatica*, 7(6):691–701, 1971.

[97] A. J. Niemi. Residence time distributions of variable flow processes. *The International Journal of Applied Radiation and Isotopes*, 28(10-11):855–860, 1977.

[98] D. O'Callaghan and P. Cunningham. Modern process control techniques in the production of dried milk products – a review. *Le Lait*, 85(4-5):335–342, 2005.

[99] J. Oldenburg, H. J. Pallasch, C. Carroll, V. Hagenmeyer, S. Arora, K. Jacobsen, J. Birk, A. Polt, and P. van den Abeel. Decision support for control structure selection during plant design. In *Computer Aided Chemical Engineering*, volume 25, pages 973–978. Elsevier, Amsterdam, Netherlands, 2008.

[100] A. Padmanaban. Film thickness measurements in falling annular films. Master's thesis, University of Saskatchewan, Saskatoon, Canada, 2006.

[101] A. Papadourakis, M. F. Doherty, and J. M. Douglas. Relative gain array for units in plants with recycle. *Industrial & Engineering Chemistry Research*, 26(6):1259–1262, 1987.

[102] S. Paramalingam. *Modelling, optimisation and control of a falling-film evaporator*. PhD thesis, Massey University, Palmerston North, New Zealand, 2004.

[103] S. Paramalingam, J. Winchester, and C. Marsh. On the fouling of falling film evaporators due to film break-up. *Food and Bioproducts Processing*, 78(2):79–84, 2000.

[104] A. E. Pearson and C. Y. Wuu. Decoupled delay estimation in the identification of differential delay systems. *Automatica*, 20(6):761–772, 1984.

[105] A. D. Polyanin and V. F. Zaitsev. *Handbook of nonlinear partial differential equations*. Chapman and Hall, London, UK, 2016.

[106] A. Ponomarev. Nonlinear predictor feedback for input-affine systems with distributed input delays. *IEEE Transactions on Automatic Control*, 61(9):2591–2596, 2015.

[107] P. Quaak, M. P. C. M. van Wijck, and J. J. van Haren. Comparison of process identification and physical modelling for falling-film evaporators. *Food Control*, 5(2):73–82, 1994.

[108] C. A. Ramirez, M. Patel, and K. Blok. From fluid milk to milk powder: energy use and energy efficiency in the european dairy industry. *Energy*, 31(12):1984–2004, 2006.

[109] X. M. Ren, A. B. Rad, P. T. Chan, and W. L. Lo. Online identification of continuous-time systems with unknown time delay. *IEEE Transactions on Automatic Control*, 50(9):1418–1422, 2005.

[110] J. P. Richard. Time-delay systems: an overview of some recent advances and open problems. *Automatica*, 39(10):1667–1694, 2003.

[111] D. E. Rivera. Internal model control: a comprehensive view. Technical report, Department of Chemical, Bio and Materials Engineering, College of Engineering and Applied Sciences, Arizona State University, Tempe, Arizona, USA, 1999.

[112] D. F. N. Rodriguez, E. Witrant, and O. Sename. Control-oriented modeling of fluid networks: a time-delay approach. In *Recent Results on Nonlinear Delay Control Systems*, pages 275–289. Springer, Wiesbaden, Germany, 2016.

[113] Q. Ruan, H. Jiang, M. Nian, and Z. Yan. Mathematical modeling and simulation of countercurrent multiple effect evaporation for fruit juice concentration. *Journal of Food Engineering*, 146:243–251, 2015.

[114] N. T. Russell. *Dynamic modelling of a falling-film evaporator for model predictive control*. PhD thesis, Massey University, Palmerston North, New Zealand, 1997.

[115] N. T. Russell, H. H. C. Bakker, and R. I. Chaplin. A comparison of dynamic models for an evaporation process. *Chemical Engineering Research and Design*, 78(8):1120–1128, 2000.

[116] C. Ruyer-Quil and P. Manneville. Improved modeling of flows down inclined planes. *The European Physical Journal B – Condensed Matter and Complex Systems*, 15(2):357–369, 2000.

[117] S. A. Sarra. The method of characteristics with applications to conservation laws. *Journal of Online Mathematics and its Applications*, 3:1–16, 2003.

[118] D. E. Seborg, T. F. Edgar, D. A. Mellichamp, and F. J. Doyle III. *Process dynamics and control.* John Wiley & Sons, Hoboken, New Jersey, USA, 2010.

[119] H. Semat and R. Katz. Physics, Chapter 9: Hydrodynamics (Fluids in Motion). *Research Papers in Physics and Astronomy, Robert Katz Publications*, 143:165–181, 1958.

[120] F. G. Shinskey. Predict distillation column response using relative gains. *Hydrocarbon Processing*, 60(5):196–200, 1981.

[121] S. Skogestad and M. Hovd. Use of frequency-dependent RGA for control structure selection. In *American Control Conference*, pages 2133–2139, San Diego, California, USA, 1990. IEEE.

[122] S. Skogestad and M. Morari. Variable selection for decentralized control. *Modeling, Identification and Control*, 13(2):113–125, 1992.

[123] S. Skogestad and I. Postlethwaite. *Multivariable feedback control: analysis and design.* John Wiley & Sons, Hoboken, New Jersey, USA, 2007.

[124] O. J. M. Smith. A controller to overcome dead time. *ISA Journal*, 6:28–33, 1959.

[125] J. G. Speight. *Lange's Handbook of Chemistry*. McGraw-Hill Education, New York City, New York, USA, 17th edition, 2017.

[126] D. Srivastava, B. Mohanty, and R. Bhargava. Modeling and simulation of MEE system used in the sugar industry. *Chemical Engineering Communications*, 200(8):1089–1101, 2013.

[127] Z. I. Stefanov and K. A. Hoo. A distributed-parameter model of black liquor falling film evaporators. Part I. Modeling of a single plate. *Industrial & Engineering Chemistry Research*, 42(9):1925–1937, 2003.

[128] Z. I. Stefanov and K. A. Hoo. Distributed parameter model of black liquor falling film evaporators. Part II. Modeling of a multiple-effect evaporator plant. *Industrial & Engineering Chemistry Research*, 43(25):8117–8132, 2004.

[129] Z. I. Stefanov and K. A. Hoo. Control of a multiple-effect falling-film evaporator plant. *Industrial & Engineering Chemistry Research*, 44(9):3146–3158, 2005.

[130] T. Y. Thanoon and R. Adnan. Model comparison of linear and nonlinear bayesian structural equation models with dichotomous data. *Communications in Statistics-Simulation and Computation*, 46(6):4578–4599, 2017.

[131] Y. C. Tian and F. Gao. Compensation of dominant and variable delay in process systems. *Industrial & Engineering Chemistry Research*, 37(3):982–986, 1998.

[132] S. M. Tonelli, J. A. Romagnoli, and J. A. Porras. Computer package for transient analysis of industrial multiple-effect evaporators. *Journal of Food Engineering*, 12(4):267–281, 1990.

[133] J. Tuch, A. Feuer, and Z. J. Palmor. Time delay estimation in continuous linear time-invariant systems. *IEEE Transactions on Automatic Control*, 39(4):823–827, 1994.

[134] GEA Wiegand GmbH. Evaporation Technology. https://www.gea.com/en/binaries/ev aporation-falling-film-forced-circulation-vapor-recompression-gea_tcm11-34893.pdf, 2016. Retrieved September 28 2021, 11:19.

[135] M. T. Van Genuchten. Analytical solutions of the one-dimensional convective-dispersive solute transport equation. Technical Report 1661, US Department of Agriculture, Agricultural Research Service, Washington, District of Columbia, USA, 1982.

[136] M. P. C. M. Van Wijck, P. Quaak, and J. J. Van Haren. Multivariable supervisory control of a four-effect falling-film evaporator. *Food Control*, 5(2):83–89, 1994.

[137] Verein Deutscher Ingenieure. *VDI-Wärmeatlas*. Springer Nature Switzerland AG, Cham, Switzerland, 11th edition, 2013.

[138] D. Vrancic, D. Vrecko, D. Juricic, and S. Strmcnik. Automatic tuning of the flexible smith predictor controller. In *American Control Conference*, volume 6, pages 3853–3857, San Diego, California, USA, 1999. IEEE.

[139] X. Wang, C. Li, and X. Chen. Disturbance rejection control for multiple-effect falling-film evaporator based on disturbance observer. *Transactions of the Institute of Measurement and Control*, 38(6):773–783, 2016.

[140] A. W. Westerberg and J. B. Hillenbrand. The synthesis of multiple-effect evaporator systems using minimum utility insights – II. Liquid flowpattern selection. *Computers & Chemical Engineering*, 12(7):625–636, 1988.

[141] J. Winchester. *Model based analysis of the operation and control of falling-film evaporators*. PhD thesis, Massey University, Palmerston North, New Zealand, 2000.

[142] J. A. Winchester and C. Marsh. Dynamics and control of falling film evaporators with mechanical vapour recompression. *Chemical Engineering Research and Design*, 77(5):357–371, 1999.

[143] E. Witrant and S. I. Niculescu. Modeling and control of large convective flows with time-delays. *Mathematics in Engineering, Science and Aerospace*, 1(2):191–205, 2010.

[144] B. Wittenmark and M. E. Salgado. Hankel-norm based interaction measure for input-output pairing. *IFAC Proceedings Volumes*, 35(1):429–434, 2002.

[145] O. S. Zain and S. Kumar. Simulation of a multiple effect evaporator for concentrating caustic soda solution – computational aspects. *Journal of Chemical Engineering of Japan*, 29(5):889–893, 1996.

[146] K. Zenger and R. Ylinen. Simulation of variable delays in material transport models. *Mathematics and Computers in Simulation*, 37(1):57–72, 1994.

[147] F. Zhang and M. Yeddanapudi. Modeling and simulation of time-varying delays. In *Symposium on Theory of Modeling and Simulation*, pages 1–8, Article No.: 34, Orlando, Florida, USA, 2012. Society for Computer Simulation International.

[148] H. M. Zhang. A theory of nonequilibrium traffic flow. *Transportation Research Part B: Methodological*, 32(7):485–498, 1998.

[149] Y. Zhang, M. Munir, I. Udugama, W. Yu, and B. R. Young. Modelling of a milk powder falling film evaporator for predicting process trends and comparison of energy consumption. *Journal of Food Engineering*, 225:26–33, 2018.

[150] C. Zheng and G. D. Bennett. *Applied contaminant transport modeling.* John Wiley & Sons, Hoboken, New Jersey, USA, 2002.

[151] G. Zheng, A. Polyakov, and A. Levant. Delay estimation via sliding mode for nonlinear time-delay systems. *Automatica*, 89:266–273, 2018.

[152] Q. C. Zhong. *Robust control of time-delay systems.* Springer Science & Business Media, Luxembourg, 2006.

[153] D. H. Zhou and P. M. Frank. A real-time estimation approach to time-varying time delay and parameters of NARX processes. *Computers & Chemical Engineering*, 23(11-12):1763–1772, 2000.

List of the Author's Publications

[154] J. Hofmann, H. C. Holz, and L. Gröll. Relative gain array and singular value analysis to improve the control in a biomass pyrolysis process. In *International Conference on Control and Automation*, volume 15, pages 596–603, Edinburgh, UK, 2019. IEEE.

[155] J. Hofmann, A. Ponomarev, V. Hagenmeyer, and L. Gröll. Transport models for liquid films (in German). *at-Automatisierungstechnik*, 68(8):625–640, 2020.

[156] J. Hofmann, L. Gröll, and V. Hagenmeyer. Control loop pairing and interaction analyses of the falling film evaporator process. In *International Conference on Process Control*, volume 23, pages 186–193, Strbske Pleso, Slovakia, 2021. IEEE.

[157] J. Hofmann, A. Ponomarev, V. Hagenmeyer, and L. Gröll. A new multivariable control concept for the falling film evaporator process. *Journal of Process Control*, 106:72–83, 2021.

[158] J. Hofmann, A. Ponomarev, V. Hagenmeyer, and L. Gröll. Time-delay identification and validation of a liquid film transport model based on pilot plant experiments. *IFAC-PapersOnLine*, 54(3):401–408, 2021.

[159] A. Ponomarev, J. Hofmann, and L. Gröll. Characteristics-based Simulink implementation of first-order quasilinear partial differential equations. In *International Conference on Simulation and Modeling Methodologies, Technologies and Applications*, volume 10, pages 139–146, Paris, France, 2020.

[160] A. Ponomarev, J. Hofmann, and L. Gröll. Novel control-oriented models for liquid transport in falling film evaporator tubes. *Computers & Chemical Engineering*, 152:107376, 2021.

[161] C. Schwaer, J. Hofmann, M. Mühlpfordt, A. Frank, and L. Gröll. Modular simulation model for falling film evaporators with novel approach to manage dominant time-varying transport delays. *Computers & Chemical Engineering*, 132:106604, 2020.